

Neuronal microtubule organization: from minus end to plus end

ISBN: 978-90-393-6551-9

The studies described in this thesis were performed at the Department of Neuroscience of the Erasmus MC in Rotterdam and at the division of Cell Biology at the Faculty of Science of the Utrecht University in Utrecht, the Netherlands.

Layout and Cover ('Baby Corn and Strawberry Jam') by Kah Wai Yau

Bottom picture on the cover was kindly provided by Presmann (Thailand) Co., Ltd.

Printed by Uitgeverij BOXPress|Proefschriftmaken.nl

© 2016 by Kah Wai Yau

# **Neuronal microtubule organization: from minus end to plus end**

Neuronale microtubulus organisatie: van min eind tot plus eind  
(met een samenvatting in het Nederlands)

Proefschrift

ter verkrijging van de graad van doctor aan de Universiteit Utrecht op gezag van de rector magnificus, prof.dr. G.J. van der Zwaan, ingevolge het besluit van het college voor promoties in het openbaar te verdedigen op woensdag 18 mei 2016 des middags te 12.45 uur

door

Kah Wai Yau

geboren op 31 mei 1985 te Heemskerk

Promotor: Prof.dr. C.C. Hoogenraad

Copromotor: Dr. L.C. Kapitein

## Contents

<b>Chapter 1</b>	
<b>General Introduction.....</b>	<b>7</b>
<b>Chapter 2</b>	
<b>Microtubule Dynamics in Dendritic Spines.....</b>	<b>19</b>
<b>Chapter 3</b>	
<b>NMDA Receptor Activation Suppresses Microtubule Growth and Spine Entry.....</b>	<b>39</b>
<b>Chapter 4</b>	
<b>Microtubule Minus-End Stabilization by Polymerization-Driven CAMSAP Deposition.....</b>	<b>67</b>
<b>Chapter 5</b>	
<b>Microtubule Minus-End Binding Protein CAMSAP2 Controls Axon Specification and Dendrite Development.....</b>	<b>89</b>
<b>Chapter 6</b>	
<b>Dendrites In Vitro and In Vivo Contain Microtubules of Opposite Polarity and Axon Formation Correlates with Uniform Plus-End-Out Microtubule Orientation.....</b>	<b>131</b>
<b>Chapter 7</b>	
<b>General Discussion.....</b>	<b>153</b>
<b>Addendum.....</b>	<b>163</b>



# Chapter 1

## General Introduction

The human body consists of trillions of cells (Luckey, 1972). There are different types of cells, each of them playing a specific role in the body, such as muscle cells and neurons. The typical human cell - as described in a textbook - is in the order of tens of micron in size and enclosed by the plasma membrane. Other membraneous compartments are present inside the cell, which are involved in energy production (mitochondria). For import and export of nutrients/waste products different routes are known that go from or to the plasma membrane (endocytic and secretory pathways). On the membrane compartments of the rough endoplasmic reticulum (RER) proteins are synthesized via ribosomes. After that the proteins are transported to the Golgi apparatus, where proteins are modified and directed to other destinations in the cell (Alberts, 2004).

To traffic cargos between different membrane compartments, intracellular transport mechanisms are needed to make this actively happen (Klann et al., 2012). Motor proteins are the driving forces of the transport machinery and drive cargo trafficking along the 'railroad' tracks in the cell (Schlager and Hoogenraad, 2009; van Spronsen and Hoogenraad, 2010). Such tracks are called actin filaments and microtubules and the motor proteins that utilize the tracks are myosins and kinesins / dynein respectively. Intermediate filaments are also part of the cellular cytoskeleton. In contrast to actin and microtubules, intermediate filaments are not polarized and there is no trafficking along these filaments. Microtubules and actin both exhibit a polarized architecture, meaning that they are built up of components that face in a similar direction when these structures are elongating. Together the intermediate filaments, actin filaments and microtubules form the cytoskeleton which is able to give the cell its shape and internal organization.

### Roads inside a cell: Microtubules

Microtubules are hollow tubes that consist of 13 protofilaments that are made up from two types of subunits called  $\alpha$ -tubulin and  $\beta$ -tubulin. These tubulin subunits form a heterodimer that binds sequentially in a head to tail fashion creating a polarized structure. Subsequently the GTP on the  $\beta$ -tubulin is hydrolysed to GDP, introducing strain on the microtubule structure (Alushin et al., 2014). The addition of a tubulin heterodimer happens faster on one side of the microtubule which is called the plus end. The minus-end of the microtubule is usually depolymerizing when free or stable when capped or anchored (Akhmanova and Steinmetz, 2008).

The specific switching between phases of growth and shrinkage of the microtubules in cells is known as dynamic instability (Mitchison and Kirschner, 1984). When a microtubule is growing and subsequently shrinks it is called catastrophe. The reverse transition is known as rescue. While the microtubule plus end is growing, other molecules, called End Binding proteins (EB1, 3) (Su et al., 1995), bind to the plus end of the microtubule (Morrison et al., 1998). Over the years it has been discovered that EB proteins are actually the core proteins on microtubule plus ends and other proteins bind to these core proteins via different ways (Jiang and Akhmanova, 2011). One of the ways other microtubule plus-end-binding proteins can track the growing microtubule is via a conserved SxIP motif, which binds to the EB proteins (Honnappa et al., 2009). There is a great variety of different proteins which contain this conserved SxIP motif (Jiang et al., 2012). Using these properties, a short polypeptide was constructed from one of the microtubule plus-end-tracking protein, called microtubule actin

cross-linking factor (MACF). Together with some adaptations, this short 18-residue MACF fragment with the SxIP motif was able to track microtubule plus ends by hitchhiking on EB proteins in cells (Honnappa et al., 2009).

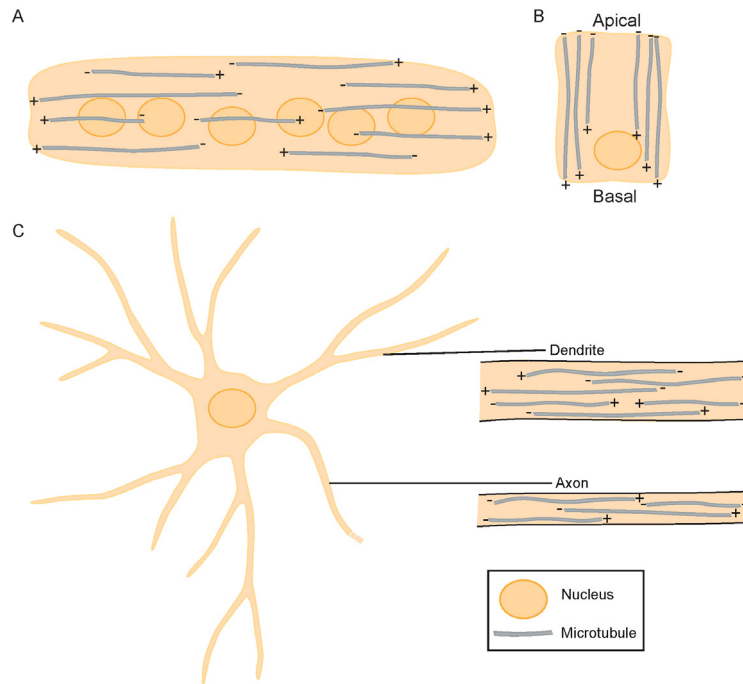


**Figure 1. Noncentrosomal Microtubule Organization**

For three different cell types the noncentrosomal microtubule organization is shown (A-C)

(A) Schematic drawing of a myotube with multiple nuclei and noncentrosomal microtubule organization.

(B) Schematic drawing of an epithelial cell with noncentrosomal microtubule organization

(C) Schematic drawing of a neuron with an inset of a section of a dendrite and axon showing noncentrosomal microtubule organization.

In some mammalian cells the microtubules are organized radially from the centre of the cell. Many of the microtubules are then nucleated in the centre of the cell and anchored with their minus-end on the centrosome. This so-called microtubule organizing centre (MTOC) is typical for these cells. But there are also different cell types that do not display a radial microtubule array and instead have more noncentrosomal microtubules. Besides epithelial cells and muscle cells neurons are such examples that exhibit a noncentrosomal microtubule organization (Kuijpers and Hoogenraad, 2011; Stiess et al., 2010) (Figure 1).

### Neuronal microtubule organization

Neurons are highly polarized cells and consist of different compartments, namely axon and dendrites. Axons (presynaptic region) transmit electrochemical signals to other neurons, which are received through their dendritic compartments (postsynaptic region, spines). These connections and signalling can be studied in neuronal culture systems. But before neurons can send and receive signals from other neurons that regulate synaptic plasticity, they go through several developmental stages, (Figure 2). 1) The first stage in neuronal culture systems involves neurons (days *in vitro*, DIV, 0.25) starting off as round cells with lamellipodia that spread around the cell and initiate formation of neurites (Flynn et al., 2012). 2) In the second stage of neuronal development (DIV0.5), outgrowth of minor processes is observed and these

processes tend to reach a length of 10-15 micron. 3) A couple of hours after stage 2, the axon starts to develop from one of the minor processes (DIV1.5). This process will rapidly grow to a much greater length than the other processes. The outgrowth of the axon defines the polarity of the neuronal cell. 4) At the final stages of neuronal development (DIV4) the dendrites start to develop from the remaining processes which have not become an axon. 5) Further maturation of the dendrites, formation of synapses happens at stage 5 (DIV >7)(Dotti et al., 1988).

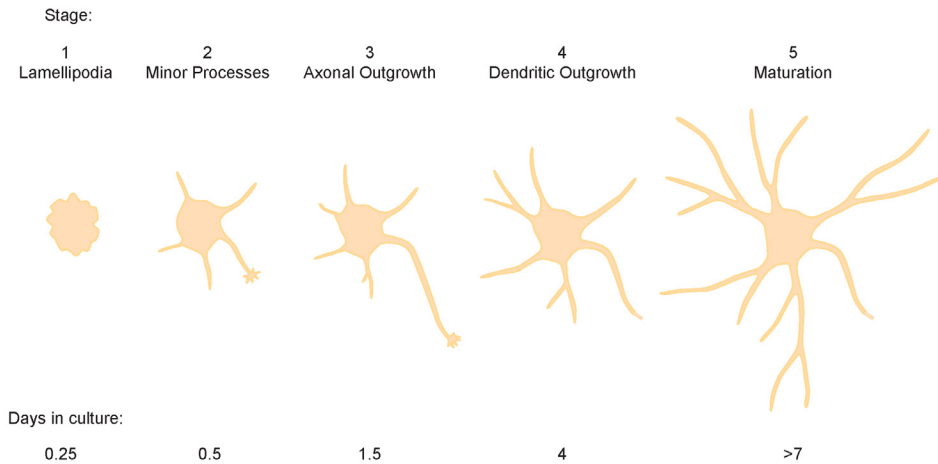


Figure 2. Stages of Development of Hippocampal Neurons in Culture  
The approximate times at which cells enter each of the stages is indicated. (Adapted from Dotti, C. G., C. A. Sullivan, et al. (1988). "The establishment of polarity by hippocampal neurons in culture." *J Neurosci* 8(4): 1454-1468.)

During these neuronal developmental stages the microtubule organization changes drastically. While stage 1 and 2 neurons might exhibit a centrosomal microtubule organization, there are already changes happening in the second stage of neuronal development, just before the outgrowth of an axon. For example, it has been shown that the centrosome is not needed for axonal outgrowth (Stiess et al., 2010). This means that the microtubules in the axon are most likely not attached to the centrosome or do not originate from the centrosome, in contrast to microtubules in many other mammalian cells. During later neuronal developmental stages the centrosome gradually loses its function as an MTOC (Kuijpers and Hoogenraad, 2011).

Electron microscopy studies in the '80s showed that dendrites in rat hippocampal neurons have a mixed microtubule organization. This was first shown in mature dendrites where Baas et al. used a polymerization assay (Baas et al., 1988; Heidemann, 1982). In this assay neurons were permeabilized and extra tubulin was added to the neuronal culture together with a buffer to aid in microtubule polymerization. After fixation procedures cross-sections were made from dendrites and axons and visualized under the electron microscope. It was then observed that "hooks" had appeared on the side of the microtubule cross-sections. The microtubule orientation determined whether the "hooks" turned left-handed or right-handed This means that the hooks on microtubules, that have their minus-end pointed toward the cell body, are different from the hooks on microtubules that have the minus-end pointing away from the cell body (Baas et al., 1988).

Studies by Baas et al. have shown that microtubules in mature dendrites have a mixed orientation at proximal sites and in the mid region. This meant that ~50% of the microtubules in proximal and mid region of the dendrite had the plus end pointing away from the cell

body. Another study that has been performed on mitral cell dendrites from bullfrogs also showed a mixed population of microtubules. However, when distal sites of dendrites of rat hippocampal neurons were analyzed, it was observed that the microtubules had an almost uniform orientation, pointing outwards with their plus end (Figure 3). This is similar to the case in axons, which have microtubules uniformly pointing in one direction. Studies by the same group showed that dendrites only had mixed microtubules from stage 4 of the neuronal development and onward (Baas et al., 1989), which was supported by second-harmonic generation (SHG) microscopy studies (Dombeck et al., 2003) and imaging studies which used GFP-EB3 (Stepanova et al., 2003).

**Origin of mixed microtubules**

Since mature neurons lack an active centrosome, a different mechanism is needed to maintain the mixed microtubules in dendrites and unidirectional microtubules in the axon. A possible candidate for microtubule anchoring and nucleation might be from membrane compartments in the cell such as the Golgi apparatus (Miller et al., 2009; Ori-McKenney et al., 2012). Another way to create additional microtubules is via severing of existing microtubules with microtubule-severing proteins. Proteins such as spastin and katanin use ATP hydrolysis to sever microtubules (Hartman et al., 1998; McNally and Vale, 1993; Roll-Mecak and Vale, 2008). Spastin was previously studied because of mutations found in patients with hereditary spastic paraplegia, hence the name. Although detailed structural information is known about spastin, it is still not certain how the severing of microtubules takes place.

Organisms such as the *Drosophila melanogaster* (common fruit fly) or *Caenorhabditis elegans* (roundworm), have a uniform microtubule organization in the dendrites (Chalfie and Thomson, 1979; Hill et al., 2012; Stone et al., 2008; Yan et al., 2013; Zheng et al., 2008). The microtubules in those dendrites have all MT minus-ends pointing away from the cell body.

Although mammalian dendrites have a mixed microtubule organization, it has been shown that transport can occur efficiently in mature dendrites (Kapitein and Hoogenraad, 2011; Kapitein et al., 2010). It has been proposed that dynein is the main motor protein that utilizes the mixed microtubules to initiate transport of cargo into the shaft of the dendrites, whereas subsequently other motor proteins might aid in the transport of cargo further into the dendrite. For instance, KIF17 is suggested to distribute cargo further into the dendritic shaft (Kapitein et al., 2010).

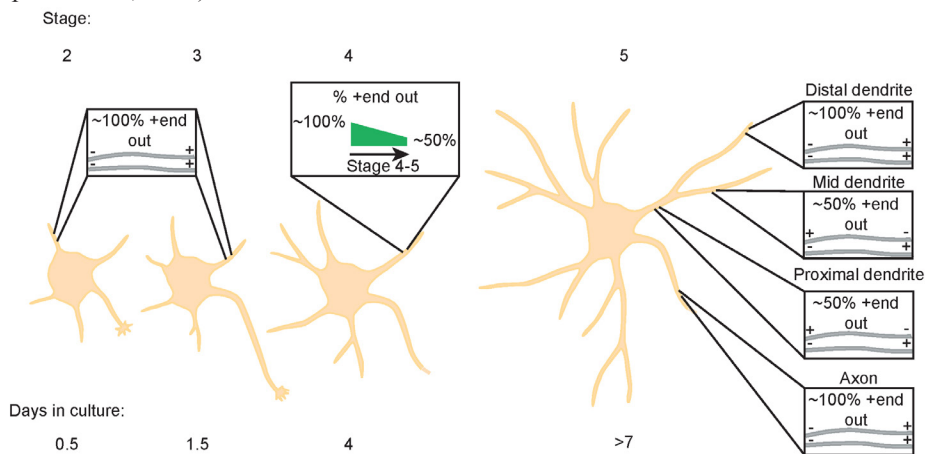


Figure 3. Microtubule Organization During Developmental Stages of Hippocampal Neurons in Culture  
The microtubule organization during the different developmental stages based on EM studies.

**Microtubules and synaptic plasticity**

Neuronal cells form synaptic contacts between each other with axons and dendrites. These contacts are formed by small protrusions on the dendritic shaft called spines (Bourne and Harris, 2008). Spines come in a variety of shapes that range from stubby, mushroom to thin spines. In contrast to the dendritic shaft, dendritic spines are abundant in actin (Sekino et al., 2007). Therefore, myosins are most likely important motors to regulate transport in these small dendritic compartments. It is well known that myosin V moves to the plus-end of actin filaments and myosin VI moves to the minus-end of actin filaments (De La Cruz et al., 1999; Wells et al., 1999). More recent studies have shown that myosin Vb moves cargo into spines (Wang et al., 2008) and have also suggested that myosin VI might be able to move cargo out of spines (Osterweil et al., 2005).

Apart from the actin cytoskeleton it has also been shown that microtubules can regulate postsynaptic plasticity (Jaworski et al., 2009). EB3 can concentrate on the plus-ends of microtubules entering the spines and regulate the localization of p140Cap, which in turn regulates actin dynamics and increases the spine size (Jaworski et al., 2009). An increase in spine size is indicative of increased synaptic transmission, the reverse corresponds with a reduction in synaptic transmission. These types of plasticity are also known as long-term potentiation (LTP) and long-term depression (LTD) respectively (Malenka and Bear, 2004). Not only do spines increase or shrink in size during LTP or LTD respectively, the key determinant for either type of plasticity is the insertion of extra receptors or removal of receptors. In case of N-methyl-D-aspartate (NMDA)-type glutamate receptor activation, extra  $\alpha$ -amino-3-hydroxy-5-methyl-4-isoxazolepropionic acid (AMPA)-type glutamate receptors are inserted during LTP and during LTD these are removed. Both situations allow influx of  $\text{Ca}^{2+}$  although during LTD this is reduced.

Only a subset of dendritic spines are entered by microtubules and studies have shown that roughly 10% of the spines are targeted per hour in an activity-dependent manner (Hu et al., 2008). Treatments to stimulate neuronal activity increased the number of microtubule invasions into spines (Hu et al., 2011). Hu et al. also hypothesised that drebrin, a protein that may act as a linker between actin and microtubules, controls microtubule entry into dendritic spines. Recent evidence suggests that kinesin-3 KIF1C can transport cargo into spines via microtubules (Esteves da Silva, 2015). However, the functional role of microtubule-based transport into spines has yet to be determined. Since actin is an abundant component of dendritic spines, it is more likely that myosins are responsible for the majority of transport into and out of spines along the cytoskeleton.

The dendritic and axonal compartments do not only differ in their microtubule organization and signalling properties, but also in microtubule associated proteins. The observed difference in microtubule associated proteins is often used as a marker to distinguish the axonal compartment and dendritic compartment. Two of the best known examples are the polarized microtubule associated protein 2 (MAP2) and tau. Tau is located in the axon whereas MAP2 has been discovered to bind to the side of microtubules in dendrites. Both tau and MAP2 bind longitudinally on the protofilaments of microtubules (Al-Bassam et al., 2002). Early studies have shown that microtubules are spaced differently, when bound by MAP2 or tau. MAP2 creates a larger spacing between microtubules than tau (Chen et al., 1992). Previous studies have also shown that activation of NMDA receptors affects the underlying microtubule cytoskeleton (Halpain and Greengard, 1990; Sanchez et al., 2000). Halpain et al. suggest that through activation of NMDA receptors MAP2 is dephosphorylated and in turn may modulate the neuronal microtubule cytoskeleton. Consistently, MAP2 was found to be a substrate for several protein kinases and phosphatases (Sontag et al., 2012).

### **Microtubule minus-end binding proteins**

Microtubules depolymerize in cells when the minus-end is not stabilized or anchored (Vorobjev et al., 1999), although recent studies have shown that various factors can stabilize or anchor microtubules to organizing centres other than the centrosome (Goodwin and Vale, 2010; Meng et al., 2008; Mogensen et al., 2000; Zheng et al., 2013). A few of these recent studies are focused on a family of proteins called CAMSAP which is short for calmodulin-regulated spectrin-associated protein. The name originated from the interactions found by a group that first characterized the CAMSAP family in 2009 (Baines et al., 2009), although the interactions with calmodulin and spectrin were not published until beginning of 2014 (King et al., 2014). These interactions have only been investigated for CAMSAP1 and one of the predicted coiled-coil regions of this protein appears to be responsible for the interactions with calmodulin and spectrin.

Several labs have reported that CAMSAP family members are microtubule minus-end binding proteins (Goodwin and Vale, 2010; Meng et al., 2008; Zheng et al., 2013). CAMSAP3 (KIAA1543, Nezha) was first described as a microtubule minus-end binding protein (Meng et al., 2008) This is consistent with the finding about the *Drosophila* ortholog Patronin which was picked up from a genetic screen. In this screen proteins were depleted and mitotic spindles were examined via high throughput microscopy. One phenotype that was observed, was the length of the mitotic spindle. Known candidates that created short spindles were confirmed in the screen and one of them, termed Ssp4, caused pronounced microtubule severing in interphase cells. (Goshima et al., 2007). In a latter study Goodwin et al. proposed to rename Ssp4 to Patronin and showed Patronin had a protective function for the microtubule minus-end by capping the microtubule minus-end. Patronin would thus physically prevent microtubule depolymerizing proteins from reaching the microtubule minus-end. A follow up study from the lab that first published about CAMSAP3, showed that CAMSAP2 and CAMSAP3 cooperate in organizing noncentrosomal microtubules in epithelial cells. Depletion studies of CAMSAP2/3 in epithelial cells, together with a depolymerizing assay, not only reduced the amount of growing microtubules but also caused more growth of microtubules at the centrosome (Tanaka et al., 2012).

Two back-to-back papers in *eLife* also described the function of CAMSAP/Patronin in another model system, *C. elegans*. Their focus was on microtubule organization in roundworm neurons and how microtubule stabilization by the roundworm ortholog, PTRN-1, is important for neuronal morphology (Marcette et al., 2014; Richardson et al., 2014). Not only did the microtubule stabilization appear to be important for neuronal morphology, but Chuang et al. showed that PTRN-1 is important for axon regeneration in *C. elegans* (Chuang et al., 2014). More recent studies revealed that NOCA-1 (protein with homology to vertebrate ninein) functions redundantly with PTRN-1 to assemble a microtubule array essential for worm growth and morphogenesis (Wang et al., 2015).

### **The tubulin-code**

In addition to the proteins that can bind directly to microtubules, there is another way to mark microtubules. One of these ways is by modifying individual tubulin subunits on the MTs. Several examples of tubulin modifications are known through modifying  $\alpha$ -tubulin or  $\beta$ -tubulin (Janke and Kneussel, 2010). The type of modification can often be related with the property and/or characteristic of a microtubule. For instance, long-lived microtubules are marked by acetylation or detyrosination. Acetylated/detyrosinated microtubules are known to have a higher binding affinity for kinesin-1, KIF5, whereas other kinesins like kinesin-2, KIF17 and kinesin-3, KIF1A, do not show this type of selectivity (Cai et al., 2009). Another study recently used *in vitro* assays to demonstrate that microtubule post-translational

modifications and isotypes influence motor proteins such as kinesin-1 (motility is increased by polyglutamylated) and kinesin-2 (requires detyrosination for motility) (Sirajuddin et al., 2014).

Acetylation of microtubules occurs on the lumen of stable and long-lived microtubules. However acetylation does not directly contribute to the stabilization of the microtubule. In neurons it has been found that decreased tubulin acetylation leads to impaired neuronal development (Creppe et al., 2009; Ohkawa et al., 2008; Park and Szostak, 1992). Tubulin glutamylated is a modification that appears on the outside of the microtubule at the C-terminal tails of tubulin. In particular neuronal microtubules exhibit polyglutamylated microtubules (Wolff et al., 1992), where glutamate side chains of different lengths can be formed (van Dijk et al., 2007). The different lengths of glutamate side chains have been suggested to be directly involved in activity-dependent signalling in neurons (Maas et al., 2009). Detyrosination occurs on  $\alpha$ -tubulin by removing the C-terminal tyrosine (Barra et al., 1973). The removal of the C-terminal tyrosine can be reversed by tyrosine ligase (re-tyrosination) (Raybin and Flavin, 1977). Detyrosination is often associated with microtubules that are long-lived. Tyrosination, which is thought to be important for binding proteins with cytoskeleton-associated glycine-rich (CAP-Gly) domain (Weisbrich et al., 2007), is associated with dynamic microtubules.

### Scope of this thesis

In this thesis, microtubule organization in cultured neurons was studied by using a large variety of techniques, such as laser microsurgery, super resolution microscopy and organotypical slice cultures. The neurons used here are most of the time hippocampal neurons from rat embryos. These neurons are plated on glass coverslips and allowed to develop over time, whereby they form synaptic connections with each other. To directly visualize the microtubule organization and its underlying role in neuronal activity two different microscopy methods are used together with viral infection or transfection techniques to express fluorescent microtubule plus-end markers. In **chapter 2** the two microscopy methods and viral techniques are described. The use of a virus makes it easier to have older neurons express the protein of interest. To visualize the protein of interest, it is coupled with a green fluorescent protein (GFP) or a different fluorescent protein. With a fluorescence microscope these proteins can then be imaged with a sensitive camera. One technique which is described in chapter 2 is total internal reflection (TIRF) microscopy. With this technique high contrast imaging of fluorescent proteins close to the coverslip can be achieved. Another microscopy technique is called spinning disk microscopy, which combines the z-stack scanning capabilities of a confocal microscope but has a faster acquisition rate which is suitable for live-cell imaging. To investigate the effect of neuronal activity on the microtubule cytoskeleton, glutamate receptors were activated via chemical stimulation. These experiments are described in **chapter 3**. Previous studies have shown that microtubules regulate spine morphology. In chapter 3 a follow up study is performed showing the effect of neuronal activity on the microtubule cytoskeleton. In **chapter 4** we describe the dynamics of a family of proteins, CAMSAPs, that bind to the microtubule minus-end. Using microscopy methods described in chapter 2 together with laser microsurgery techniques, the dynamics of CAMSAPs on microtubule minus-ends have been investigated. From the CAMSAP family, only CAMSAP2 is abundant in hippocampal neurons and is used to investigate their role in noncentrosomal microtubule organization in neurons. Using similar methods as in chapter 4, CAMSAP2 dynamics are investigated in neurons in **chapter 5**. In addition to the CAMSAP2 dynamics, the function of this protein on neuronal development is scrutinized. In these studies some light has been shed on the maintenance of microtubule minus-ends in neurons.

A fundamental question to be solved is about the orientation of microtubules in neurons.

Although there is a general consensus about the unidirectionality of microtubules in axons, in dendrites it is not as trivial. In different model systems, dendrites have been shown to contain a unidirectional microtubule orientation. In cultured rat hippocampal neurons, however, the dendrites are not unidirectional as shown with electron microscopy studies by Baas et al. In **chapter 6** we describe the microtubule orientation in axons and dendrites of hippocampal dissociated cultures, organotypic slice cultures and *in vivo* mice brain cortex. Using laser microsurgery techniques we are able to describe the MT orientation in dendrites during neuronal development. Future directions are discussed in **chapter 7**. In that chapter we highlight the model of neuronal microtubule organization that emerged from the previous chapters and existing literature. Future experiments are also discussed that might aid in solving remaining questions and further testing our hypothesis.

### REFERENCES

- Akhmanova, A., and Steinmetz, M.O. (2008). Tracking the ends: a dynamic protein network controls the fate of microtubule tips. *Nature reviews Molecular cell biology* 9, 309-322.
- Al-Bassam, J., Ozer, R.S., Safer, D., Halpain, S., and Milligan, R.A. (2002). MAP2 and tau bind longitudinally along the outer ridges of microtubule protofilaments. *The Journal of cell biology* 157, 1187-1196.
- Alberts, B. (2004). *Essential cell biology*, 2nd edn (New York, NY: Garland Science Pub.).
- Alushin, G.M., Lander, G.C., Kellogg, E.H., Zhang, R., Baker, D., and Nogales, E. (2014). High-resolution microtubule structures reveal the structural transitions in alpha-tubulin upon GTP hydrolysis. *Cell* 157, 1117-1129.
- Baas, P.W., Black, M.M., and Banker, G.A. (1989). Changes in microtubule polarity orientation during the development of hippocampal neurons in culture. *The Journal of cell biology* 109, 3085-3094.
- Baas, P.W., Deitch, J.S., Black, M.M., and Banker, G.A. (1988). Polarity orientation of microtubules in hippocampal neurons: uniformity in the axon and nonuniformity in the dendrite. *Proceedings of the National Academy of Sciences of the United States of America* 85, 8335-8339.
- Baines, A.J., Bignone, P.A., King, M.D., Maggs, A.M., Bennett, P.M., Pinder, J.C., and Phillips, G.W. (2009). The CKK domain (DUF1781) binds microtubules and defines the CAMSAP/ssp4 family of animal proteins. *Molecular biology and evolution* 26, 2005-2014.
- Barra, H.S., Rodriguez, J.A., Arce, C.A., and Caputto, R. (1973). A soluble preparation from rat brain that incorporates into its own proteins (14 C)arginine by a ribonuclease-sensitive system and (14 C)tyrosine by a ribonuclease-insensitive system. *Journal of neurochemistry* 20, 97-108.
- Bourne, J.N., and Harris, K.M. (2008). Balancing structure and function at hippocampal dendritic spines. *Annual review of neuroscience* 31, 47-67.
- Cai, D., McEwen, D.P., Martens, J.R., Meyhofer, E., and Verhey, K.J. (2009). Single molecule imaging reveals differences in microtubule track selection between Kinesin motors. *PLoS biology* 7, e1000216.
- Chalfie, M., and Thomson, J.N. (1979). Organization of neuronal microtubules in the nematode *Caenorhabditis elegans*. *The Journal of cell biology* 82, 278-289.
- Chen, J., Kanai, Y., Cowan, N.J., and Hirokawa, N. (1992). Projection domains of MAP2 and tau determine spacings between microtubules in dendrites and axons. *Nature* 360, 674-677.
- Chuang, M., Goncharov, A., Wang, S., Oegema, K., Jin, Y., and Chisholm, A.D. (2014). The microtubule minus-end-binding protein patronin/PTRN-1 is required for axon regeneration in *C. elegans*. *Cell reports* 9, 874-883.
- Creppe, C., Malinetskaya, L., Volvert, M.L., Gillard, M., Close, P., Malaise, O., Laguesse, S., Cornez, I., Rahmouni, S., Ormenese, S., et al. (2009). Elongator controls the migration and differentiation of cortical neurons through acetylation of alpha-tubulin. *Cell* 136, 551-564.
- De La Cruz, E.M., Wells, A.L., Rosenfeld, S.S., Ostap, E.M., and Sweeney, H.L. (1999). The kinetic mechanism of myosin V. *Proceedings of the National Academy of Sciences of the United States of America* 96, 13726-13731.
- Dombeck, D.A., Kasischke, K.A., Vishwasrao, H.D., Ingelsson, M., Hyman, B.T., and Webb, W.W. (2003). Uniform polarity microtubule assemblies imaged in native brain tissue by second-harmonic generation microscopy. *Proceedings of the National Academy of Sciences of the United States of America* 100, 7081-7086.
- Dotti, C.G., Sullivan, C.A., and Banker, G.A. (1988). The establishment of polarity by hippocampal neurons in culture. *The Journal of neuroscience : the official journal of the Society for Neuroscience* 8, 1454-1468.
- Esteves da Silva, M.A., M. Schatzle, P. Lipka, J. Watanabe, T. Cho, S. Futai, K. Wierenga, C. J. Kapitein, L. C. Hoogenraad, C. C. (2015). Positioning of AMPA receptor-containing endosomes regulates synapse

- architecture. *Cell reports* 13, 933-943.
- Flynn, K.C., Hellal, F., Neukirchen, D., Jacob, S., Tahirovic, S., Dupraz, S., Stern, S., Garvalov, B.K., Gurniak, C., Shaw, A.E., et al. (2012). ADF/cofilin-mediated actin retrograde flow directs neurite formation in the developing brain. *Neuron* 76, 1091-1107.
- Goodwin, S.S., and Vale, R.D. (2010). Patronin regulates the microtubule network by protecting microtubule minus ends. *Cell* 143, 263-274.
- Goshima, G., Wollman, R., Goodwin, S.S., Zhang, N., Scholey, J.M., Vale, R.D., and Stuurman, N. (2007). Genes required for mitotic spindle assembly in *Drosophila* S2 cells. *Science* 316, 417-421.
- Halpain, S., and Greengard, P. (1990). Activation of NMDA receptors induces rapid dephosphorylation of the cytoskeletal protein MAP2. *Neuron* 5, 237-246.
- Hartman, J.J., Mahr, J., McNally, K., Okawa, K., Iwamatsu, A., Thomas, S., Cheesman, S., Heuser, J., Vale, R.D., and McNally, F.J. (1998). Katanin, a microtubule-severing protein, is a novel AAA ATPase that targets to the centrosome using a WD40-containing subunit. *Cell* 93, 277-287.
- Heidemann, S.R.E., U. (1982). Microtubule polarity determination based on conditions for tubulin assembly in vitro. In *Methods in cell biology*, p. 10.
- Hill, S.E., Parmar, M., Gheres, K.W., Guignet, M.A., Huang, Y., Jackson, F.R., and Rolls, M.M. (2012). Development of dendrite polarity in *Drosophila* neurons. *Neural development* 7, 34.
- Honnappa, S., Gouveia, S.M., Weisbrich, A., Damberger, F.F., Bhavesh, N.S., Jawhari, H., Grigoriev, I., van Rijssel, F.J., Buey, R.M., Lawera, A., et al. (2009). An EB1-binding motif acts as a microtubule tip localization signal. *Cell* 138, 366-376.
- Hu, X., Ballo, L., Pietila, L., Viesselmann, C., Ballweg, J., Lombard, D., Stevenson, M., Merriam, E., and Dent, E.W. (2011). BDNF-induced increase of PSD-95 in dendritic spines requires dynamic microtubule invasions. *The Journal of neuroscience : the official journal of the Society for Neuroscience* 31, 15597-15603.
- Hu, X., Viesselmann, C., Nam, S., Merriam, E., and Dent, E.W. (2008). Activity-dependent dynamic microtubule invasion of dendritic spines. *The Journal of neuroscience : the official journal of the Society for Neuroscience* 28, 13094-13105.
- Janke, C., and Kneussel, M. (2010). Tubulin post-translational modifications: encoding functions on the neuronal microtubule cytoskeleton. *Trends in neurosciences* 33, 362-372.
- Jaworski, J., Kapitein, L.C., Gouveia, S.M., Dortland, B.R., Wulf, P.S., Grigoriev, I., Camera, P., Spangler, S.A., Di Stefano, P., Demmers, J., et al. (2009). Dynamic microtubules regulate dendritic spine morphology and synaptic plasticity. *Neuron* 61, 85-100.
- Jiang, K., and Akhmanova, A. (2011). Microtubule tip-interacting proteins: a view from both ends. *Current opinion in cell biology* 23, 94-101.
- Jiang, K., Toedt, G., Montenegro Gouveia, S., Davey, N.E., Hua, S., van der Vaart, B., Grigoriev, I., Larsen, J., Pedersen, L.B., Bezstarosti, K., et al. (2012). A Proteome-wide screen for mammalian SxIP motif-containing microtubule plus-end tracking proteins. *Current biology : CB* 22, 1800-1807.
- Kapitein, L.C., and Hoogenraad, C.C. (2011). Which way to go? Cytoskeletal organization and polarized transport in neurons. *Molecular and cellular neurosciences* 46, 9-20.
- Kapitein, L.C., Schlager, M.A., Kuijpers, M., Wulf, P.S., van Spronsen, M., MacKintosh, F.C., and Hoogenraad, C.C. (2010). Mixed microtubules steer dynein-driven cargo transport into dendrites. *Current biology : CB* 20, 290-299.
- King, M.D., Phillips, G.W., Bignone, P.A., Hayes, N.V., Pinder, J.C., and Baines, A.J. (2014). A conserved sequence in calmodulin regulated spectrin-associated protein 1 links its interaction with spectrin and calmodulin to neurite outgrowth. *Journal of neurochemistry* 128, 391-402.
- Klann, M., Koepl, H., and Reuss, M. (2012). Spatial modeling of vesicle transport and the cytoskeleton: the challenge of hitting the right road. *PloS one* 7, e29645.
- Kuijpers, M., and Hoogenraad, C.C. (2011). Centrosomes, microtubules and neuronal development. *Molecular and cellular neurosciences* 48, 349-358.
- Luckey, T.D. (1972). Introduction to intestinal microecology. *The American journal of clinical nutrition* 25, 1292-1294.
- Maas, C., Belgardt, D., Lee, H.K., Heisler, F.F., Lappe-Siefke, C., Magiera, M.M., van Dijk, J., Hausrat, T.J., Janke, C., and Kneussel, M. (2009). Synaptic activation modifies microtubules underlying transport of postsynaptic cargo. *Proceedings of the National Academy of Sciences of the United States of America* 106, 8731-8736.
- Malenka, R.C., and Bear, M.F. (2004). LTP and LTD: an embarrassment of riches. *Neuron* 44, 5-21.
- Marcette, J.D., Chen, J.J., and Nonet, M.L. (2014). The *Caenorhabditis elegans* microtubule minus-end binding homolog PTRN-1 stabilizes synapses and neurites. *eLife* 3, e01637.
- McNally, F.J., and Vale, R.D. (1993). Identification of katanin, an ATPase that severs and disassembles stable microtubules. *Cell* 75, 419-429.

## Chapter 1

---

- Meng, W., Mushika, Y., Ichii, T., and Takeichi, M. (2008). Anchorage of microtubule minus ends to adherens junctions regulates epithelial cell-cell contacts. *Cell* 135, 948-959.
- Miller, P.M., Folkmann, A.W., Maia, A.R., Efimova, N., Efimov, A., and Kaverina, I. (2009). Golgi-derived CLASP-dependent microtubules control Golgi organization and polarized trafficking in motile cells. *Nature cell biology* 11, 1069-1080.
- Mitchison, T., and Kirschner, M. (1984). Dynamic instability of microtubule growth. *Nature* 312, 237-242.
- Mogensen, M.M., Malik, A., Piel, M., Bouckson-Castaing, V., and Bornens, M. (2000). Microtubule minus-end anchorage at centrosomal and non-centrosomal sites: the role of ninein. *Journal of cell science* 113 ( Pt 17), 3013-3023.
- Morrison, E.E., Wardleworth, B.N., Askham, J.M., Markham, A.F., and Meredith, D.M. (1998). EB1, a protein which interacts with the APC tumour suppressor, is associated with the microtubule cytoskeleton throughout the cell cycle. *Oncogene* 17, 3471-3477.
- Ohkawa, N., Sugisaki, S., Tokunaga, E., Fujitani, K., Hayasaka, T., Setou, M., and Inokuchi, K. (2008). N-acetyltransferase ARD1-NAT1 regulates neuronal dendritic development. *Genes to cells : devoted to molecular & cellular mechanisms* 13, 1171-1183.
- Ori-McKenney, K.M., Jan, L.Y., and Jan, Y.N. (2012). Golgi outposts shape dendrite morphology by functioning as sites of acentrosomal microtubule nucleation in neurons. *Neuron* 76, 921-930.
- Osterweil, E., Wells, D.G., and Mooseker, M.S. (2005). A role for myosin VI in postsynaptic structure and glutamate receptor endocytosis. *The Journal of cell biology* 168, 329-338.
- Park, E.C., and Szostak, J.W. (1992). ARD1 and NAT1 proteins form a complex that has N-terminal acetyltransferase activity. *The EMBO journal* 11, 2087-2093.
- Raybin, D., and Flavim, M. (1977). Enzyme which specifically adds tyrosine to the alpha chain of tubulin. *Biochemistry* 16, 2189-2194.
- Richardson, C.E., Spilker, K.A., Cueva, J.G., Perrino, J., Goodman, M.B., and Shen, K. (2014). PTRN-1, a microtubule minus end-binding CAMSAP homolog, promotes microtubule function in *Caenorhabditis elegans* neurons. *eLife* 3, e01498.
- Roll-Mecak, A., and Vale, R.D. (2008). Structural basis of microtubule severing by the hereditary spastic paraplegia protein spastin. *Nature* 451, 363-367.
- Sanchez, C., Diaz-Nido, J., and Avila, J. (2000). Phosphorylation of microtubule-associated protein 2 (MAP2) and its relevance for the regulation of the neuronal cytoskeleton function. *Progress in neurobiology* 61, 133-168.
- Schlager, M.A., and Hoogenraad, C.C. (2009). Basic mechanisms for recognition and transport of synaptic cargos. *Molecular brain* 2, 25.
- Sekino, Y., Kojima, N., and Shirao, T. (2007). Role of actin cytoskeleton in dendritic spine morphogenesis. *Neurochemistry international* 51, 92-104.
- Sirajuddin, M., Rice, L.M., and Vale, R.D. (2014). Regulation of microtubule motors by tubulin isotypes and post-translational modifications. *Nature cell biology* 16, 335-344.
- Sontag, J.M., Nunbhakdi-Craig, V., White, C.L., 3rd, Halpain, S., and Sontag, E. (2012). The protein phosphatase PP2A/Balpha binds to the microtubule-associated proteins Tau and MAP2 at a motif also recognized by the kinase Fyn: implications for tauopathies. *The Journal of biological chemistry* 287, 14984-14993.
- Stepanova, T., Slemmer, J., Hoogenraad, C.C., Lansbergen, G., Dortland, B., De Zeeuw, C.I., Grosveld, F., van Cappellen, G., Akhmanova, A., and Galjart, N. (2003). Visualization of microtubule growth in cultured neurons via the use of EB3-GFP (end-binding protein 3-green fluorescent protein). *The Journal of neuroscience : the official journal of the Society for Neuroscience* 23, 2655-2664.
- Stiess, M., Maghelli, N., Kapitein, L.C., Gomis-Ruth, S., Wilsch-Brauninger, M., Hoogenraad, C.C., Tolic-Norrelykke, I.M., and Bradke, F. (2010). Axon extension occurs independently of centrosomal microtubule nucleation. *Science* 327, 704-707.
- Stone, M.C., Roegiers, F., and Rolls, M.M. (2008). Microtubules have opposite orientation in axons and dendrites of *Drosophila* neurons. *Molecular biology of the cell* 19, 4122-4129.
- Su, L.K., Burrell, M., Hill, D.E., Gyuris, J., Brent, R., Wiltshire, R., Trent, J., Vogelstein, B., and Kinzler, K.W. (1995). APC binds to the novel protein EB1. *Cancer research* 55, 2972-2977.
- Tanaka, N., Meng, W., Nagae, S., and Takeichi, M. (2012). Nezha/CAMSAP3 and CAMSAP2 cooperate in epithelial-specific organization of noncentrosomal microtubules. *Proceedings of the National Academy of Sciences of the United States of America* 109, 20029-20034.
- van Dijk, J., Rogowski, K., Miro, J., Lacroix, B., Edde, B., and Janke, C. (2007). A targeted multienzyme mechanism for selective microtubule polyglutamylation. *Molecular cell* 26, 437-448.
- van Spronsen, M., and Hoogenraad, C.C. (2010). Synapse pathology in psychiatric and neurologic disease. *Current neurology and neuroscience reports* 10, 207-214.
- Vorobjev, I.A., Rodionov, V.I., Maly, I.V., and Borisy, G.G. (1999). Contribution of plus and minus end pathways to

- microtubule turnover. *Journal of cell science* 112 ( Pt 14), 2277-2289.
- Wang, S., Wu, D., Quintin, S., Green, R.A., Cheerambathur, D.K., Ochoa, S.D., Desai, A., and Oegema, K. (2015). NOCA-1 functions with gamma-tubulin and in parallel to Patronin to assemble non-centrosomal microtubule arrays in *C. elegans*. *eLife* 4.
- Wang, Z., Edwards, J.G., Riley, N., Provance, D.W., Jr., Karcher, R., Li, X.D., Davison, I.G., Ikebe, M., Mercer, J.A., Kauer, J.A., and Ehlers, M.D. (2008). Myosin Vb mobilizes recycling endosomes and AMPA receptors for postsynaptic plasticity. *Cell* 135, 535-548.
- Weisbrich, A., Honnappa, S., Jaussi, R., Okhrimenko, O., Frey, D., Jelesarov, I., Akhmanova, A., and Steinmetz, M.O. (2007). Structure-function relationship of CAP-Gly domains. *Nature structural & molecular biology* 14, 959-967.
- Wells, A.L., Lin, A.W., Chen, L.Q., Safer, D., Cain, S.M., Hasson, T., Carragher, B.O., Milligan, R.A., and Sweeney, H.L. (1999). Myosin VI is an actin-based motor that moves backwards. *Nature* 401, 505-508.
- Wolff, A., de Nechaud, B., Chillet, D., Mazarguil, H., Desbruyeres, E., Audebert, S., Edde, B., Gros, F., and Denoulet, P. (1992). Distribution of glutamylated alpha and beta-tubulin in mouse tissues using a specific monoclonal antibody, GT335. *European journal of cell biology* 59, 425-432.
- Yan, J., Chao, D.L., Toba, S., Koyasako, K., Yasunaga, T., Hirotsune, S., and Shen, K. (2013). Kinesin-1 regulates dendrite microtubule polarity in *Caenorhabditis elegans*. *eLife* 2, e00133.
- Zheng, J., Furness, D., Duan, C., Miller, K.K., Edge, R.M., Chen, J., Homma, K., Hackney, C.M., Dallos, P., and Cheatham, M.A. (2013). Marshalin, a microtubule minus-end binding protein, regulates cytoskeletal structure in the organ of Corti. *Biology open* 2, 1192-1202.
- Zheng, Y., Wildonger, J., Ye, B., Zhang, Y., Kita, A., Younger, S.H., Zimmerman, S., Jan, L.Y., and Jan, Y.N. (2008). Dynein is required for polarized dendritic transport and uniform microtubule orientation in axons. *Nature cell biology* 10, 1172-1180.



## Chapter 2

### Microtubule Dynamics in Dendritic Spines

Lukas C. Kapitein, Kah Wai Yau, and Casper C. Hoogenraad  
Department of Neuroscience, Erasmus Medical Center, 3015 GE, Rotterdam, The Netherlands

#### ABSTRACT

Neuronal microtubules recently emerged as temporal and spatial regulators of dendritic spines, the major sites of excitatory synaptic input. By imaging microtubules in cultured mature primary hippocampal neurons using fluorescently tagged tubulin and microtubule plus-end binding (EB) protein EB3, dynamic microtubules were found to regularly depart from the dendritic shaft and enter dendritic spines. Evidence indicates that microtubule invasions into spines regulate spine actin dynamics and induce transient morphological changes, such as the formation of spine head protrusion and spine growth. Because alterations in spine morphology play an important role in synaptic plasticity and have been linked to learning and memory formation, it is possible that dynamic microtubules are engaged in adaptive processes in the adult brain. This chapter provides detailed methods for live imaging of dynamic microtubules in mature hippocampal neurons in culture. We describe protocols for culturing and transfecting mature hippocampal neurons and visualizing microtubules and microtubule plus-EB proteins by total internal reflection fluorescence microscopy and spinning disk confocal microscopy.

*Methods Cell Biol.* 2010;97:111-32

### I. INTRODUCTION

Neurons are electrically excitable polarized cells and typically composed of a cell body, one axon, and multiple highly branched dendrites. Signal transmission from the axon of one neuron toward dendrites of other neurons occurs at specialized junctions called synapses. Neuronal differentiation and maintenance of neuronal function in a brain network requires a well-organized interplay of many cellular processes, in many of which the microtubule cytoskeleton plays an important role (Conde and Caceres, 2009; Hoogenraad and Bradke, 2009; Lowery and Van Vactor, 2009). Our understanding of neuronal structure and function has increased tremendously through the use of primary culture techniques that allow neurons to develop axons and dendrites *in vitro*, as well as specialized subdomains such as growth cones, axon initial segment, dendritic spines, and inhibitory and excitatory synapses. Culturing primary neurons has become an important tool in neuronal cell biology, especially when combined with the ability to express exogenous genes, stain endogenous molecules using immunocytochemistry, and perform live cell imaging to address the function of specific proteins in their native cellular context. For instance, most of our knowledge of regulated exocytosis (Sudhof and Rothman, 2009), long-distance microtubule-based transport (Hirokawa and Takemura, 2004), receptor dynamics (Newpher and Ehlers, 2008; Sheng and Hoogenraad, 2007), and local mRNA translation (Bramham, 2008; Lin and Holt, 2008) comes from experiments performed in cultured neuronal cells. In general, insight into the basic cellular mechanisms of neurons in culture will help to better understand how the brain functions in an entire animal.

Most cellular studies of mammalian microtubule behavior and function have been focused on cultured fibroblasts (Cheeseman and Desai, 2008; Howard and Hyman, 2009; Steinmetz and Akhmanova, 2008). However, recent experimental evidence shows that microtubules and their plus-end binding (EB) proteins, also named +TIPs, play essential roles in the process of neuronal differentiation as well as in diverse aspects of mature neuronal functioning (Conde and Caceres, 2009; Hoogenraad and Bradke, 2009). Several plus-EB proteins, including cytoplasmic linker proteins (CLIPs), CLIP-associated proteins, EB family members, navigator family proteins, and Lissencephaly 1 (LIS1), have been shown to be important during several stages of neuronal development (Jaworski et al., 2008), such as in the formation and growth of axons (Lee et al., 2004; Martinez-Lopez et al., 2005; Tsai et al., 2005; Zhou et al., 2004) and proper signaling in more mature neurons (Gu et al., 2006). Recently, dynamic microtubules and the microtubule plus-EB protein EB3 were shown to be important for dynamic changes in structure and function of dendritic spines (Jaworski et al., 2009).

Microtubule arrays within neuronal processes appear highly organized with respect to their intrinsic polarity (Baas et al., 1988, 1989; Dombeck et al., 2003). Ultrastructural studies show that in axons, microtubules are generally long and uniformly oriented with their plus-ends distal to the cell body, whereas in proximal dendrites microtubules are much shorter and exhibit mixed polarity. More distal thinner dendrites of higher order, however, contain unipolar microtubules oriented the same way as the axonal ones (Baas et al., 1989). Since a major role of microtubules in mature neurons is to act as transport routes (Hirokawa and Takemura, 2005), distinct patterns of microtubule polarity orientation can generate asymmetries in the composition of each neuronal compartment by promoting specific motor protein motility (Kapitein et al., 2010). The specialized microtubule organization has recently been captured in action by visualizing fluorescently labeled plus-EB proteins in living neuronal cells (Jaworski et al., 2009; Morrison et al., 2002; Stepanova et al., 2003). In particular, it was

found that the microtubule plus-end signal of EB3-GFP in cultured neurons is brighter than that detected with the other plus-EB proteins (Stepanova et al., 2003). Thus, fluorescently labeled EB3 can be used as tools for visualizing the dynamic behavior of microtubules in developing and mature neurons.

This chapter describes detailed protocols for imaging microtubules and microtubule plus-EB proteins in primary hippocampal neurons in culture. We provide protocols detailed enough to set up the primary hippocampal culture system and discuss the important principles of visualizing microtubules and microtubule plus-ends in neurons by total internal reflection fluorescence microscopy (TIRFM) and spinning disk confocal microscopy. We will specify the reagents and equipment necessary to conduct each subprocedure. First, we will describe how to prepare hippocampal neurons in culture (Section III). Second, we will explain how to express fluorescently labeled tubulin and microtubule plus-EB proteins in cultured neurons using plasmid DNA transfection (Lipofectamine 2000) (Section IV) and Semliki Forest virus (SFV)- mediated gene delivery (Section V). Third, we will describe how to image dynamic microtubules in mature hippocampal neurons (Section VI). Finally, we will briefly discuss the data analysis (Section VII).

## II. RATIONALE

The brain is a network of electrically active neurons that communicate with each other through synapses. Chemical synapses are asymmetric contacts formed between axons of the presynaptic neuron and dendritic specializations of the postsynaptic cell. In excitatory synapses of the hippocampus, the presynaptic terminal typically releases the neurotransmitter glutamate, which diffuses across the synaptic cleft to bind to and activate glutamate receptors in the postsynaptic membrane on top of dendritic spines, small membrane protrusions on neuronal dendrites. In addition to glutamate receptors, dendritic spines contain the postsynaptic machinery, including postsynaptic density (PSD), actin cytoskeleton, and a wide variety of membrane-bound organelles, such as smooth endoplasmic reticulum, mitochondria, and endosomes (Sheng and Hoogenraad, 2007) (Figure 1). Live imaging studies showed that spines are remarkably dynamic, changing size and shape over timescales of seconds to minutes and of hours to days (Holtmaat and Svoboda, 2009). Such dynamic changes in spine morphology are closely linked to changes in strength of synaptic connections and believed to be associated with learning and memory formation in the brain (Yuste and Bonhoeffer, 2001). Furthermore, the loss of synaptic stability or alterations of spine morphology are linked to many psychiatric and neurological diseases, including addiction, mental retardation, such as Fragile X syndrome, autism spectrum disorders, and neurodegenerative diseases such as Alzheimer's disease (Kauer and Malenka, 2007; Selkoe, 2002; Sudhof, 2008). Therefore, knowledge about molecular mechanisms underlying spine morphology and synaptic stability in primary neurons in culture will be important for understanding the basic molecular mechanisms underlying learning and memory formation, as well as synaptic disorders and traumatic injury (Blanpied and Ehlers, 2004; Hoogenraad and Bradke, 2009). Recent work from our laboratory revealed an important contribution of dynamic microtubules to the morphology and maintenance of dendritic spines (Figure 1). These unexpected findings further increase the long list of important cellular functions mediated by dynamic microtubules and necessitate future studies that closely examine microtubule dynamics in hippocampal neurons. The required procedures are described in detail in this chapter.

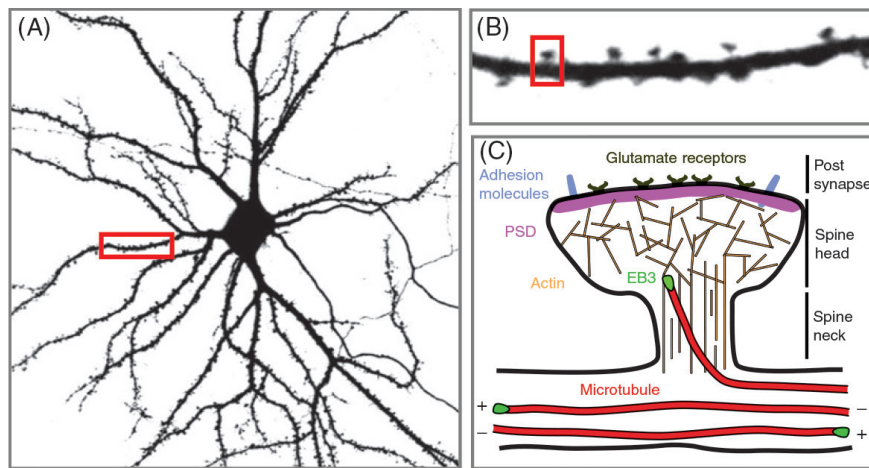


Figure 1. Microanatomy of Dendritic Spines

(A) Image of hippocampal neurons transfected at 13 days *in vitro* (DIV13) with green fluorescent protein (GFP) as a marker to visualize neuronal morphology. Two days after transfection, neurons were fixed for 10 min with 4% formaldehyde/4% sucrose in PBS. Confocal images were acquired using a LSM510 confocal microscope (Zeiss) with a 40x oil objective and sequential acquisition settings at the maximal resolution of the microscope (1024 x 1024 pixels). Each image was a z-series of 6–10 images each averaged two times. The resulting z-stack was “flattened” into a single image using maximum projection.

(B) Inset of the boxed area in (A) showing an enlarged dendritic segment containing several dendritic spines.

(C) Schematic diagram of mature mushroom-shaped spine, showing the actin (brown lines) and microtubule (red) cytoskeleton and the postsynaptic membrane containing the PSD, adhesion molecules, and glutamate receptors. The actin cytoskeleton is connected to the PSD and determines spine structure and motility. Microtubule plus-end binding protein EB3 is symbolized as a green oval. Microtubules depart from the dendritic shaft, curve, and transiently enter dendritic spines. Some microtubules move all the way up in the spine head and even appear to touch the synaptic membrane. (See Plate no. 1 in the Color Plate Section.)

### III. CULTURING PRIMARY HIPPOCAMPAL NEURONS

Over the last century, basic neuroscience research has taught us a great deal about the molecular and cellular mechanisms underlying neuronal development and plasticity. Pioneering work by the Banker lab using *in vitro* dissociated hippocampal neuron cultures provided an experimental system to study neuronal cell biology (Banker and Cowan, 1977). Using this culture method, hippocampal neurons from embryonic rats are cultured on glass coverslips in serum-free medium and then inverted and maintained above an astrocyte feeder layer (Kaech and Banker, 2006). The use of the neuron–glia cell coculture system allows hippocampal neurons to become appropriately polarized, develop extensive axonal and dendritic arbors, and form functional synaptic connections within a week after plating the cells (Dotti et al., 1988). However, for detailed analysis of synaptic plasticity mechanisms and dendritic spine morphology we prefer to use fully developed, mature hippocampal neurons, which are maintained for a longer time in culture (over > 2–3 weeks) (Figure 1). The major differences with the original Banker protocol is that we plate neurons at a medium density (375–500 cells/mm<sup>2</sup>), eliminate the need for astrocyte cocultures, and use serum-free Neurobasal medium supplemented with B27 (Brewer et al., 1993). For the last decade, the medium-density neuronal cultures without cocultured astrocytes have been used by many investigators to address fundamental questions in neuronal cell biology (Ehlers, 2003; Lise et al., 2006; Luscher et al., 1999; Sala et al., 2001; Shi et al., 2003), including the role of microtubules in spine morphology (Jaworski et al., 2009). In this section we will describe how to culture medium-density primary rat hippocampal neurons.

### A. Buffers, Solutions, and Equipment

The following materials are needed for medium-density serum-free cultures.

#### *Preparing Coverslips and Neurobasal/B27 Medium*

- Glass coverslips [VWR 406-0189-32 (19 mm), 406-0189-50 (24 mm); Gallard Schlesinger]
- Porcelain racks (85422-E40; Thomas Scientific)
- Oven gloves (32885-804; VWR)
- 1 l glass beakers, pack of 6 (13912-284; VWR)
- Nitric acid, 65% solution (84382; Sigma)
- 0.1 M borate buffer, pH 8.5 (500 ml): Dissolve 1.24 g boric acid (B-0252; Sigma), 1.90 g borax (B-9876; Sigma) in 500 ml H<sub>2</sub>O, and adjust pH to 8.5. Filter sterilize and store at 4°C.
- Poly-L-lysine (PLL) and laminin coating solution (40 ml): The PLL stock (P2636, solid powder; Sigma) is kept at 4°C. Dissolve 10 mg/ml PLL in H<sub>2</sub>O and store in 150 µl aliquots at –80°C. The laminin stock (1243217, 1 mg/ml solution; Roche) is kept in 150 µl aliquots at –20°C. Before making the coating solution, slowly thaw PLL and laminin aliquots on ice. Add 450 µl PLL and 300 µl laminin in 120 ml to 0.1 M borate buffer to make fresh coating solution.
- 12-well plates (353043; Falcon) and 6-well plates (3506; Corning Costar).
- Neurobasal/B27 medium (100 ml): 97.5 ml Neurobasal medium (21103-049; Invitrogen), 2 ml B27 supplement (17504-044; Invitrogen), 1 ml penicillin/streptomycin (15140-148; Invitrogen), 250 µl glutamine (200 mM stock) (25030-081; Invitrogen), and 125 µl glutamic acid (glutamate; 1.84 mg/ml stock) (RBI G-100). Note that for feeding cultured neurons, B27 medium is used without glutamic acid.
- Tissue culture incubator (37°C, 5% CO<sub>2</sub>).

#### *Hippocampal Dissection and Plating Cells*

- Timed pregnant Wistar rat (E19) with about 10–15 embryos (from Harlan Laboratories).
- 100% carbon dioxide (CO<sub>2</sub>) gas.
- Dissection tools: Medium forceps (11002-12; FST) and straight scissor (14001-12; FST) to dissect out embryos from pregnant rat. Two forceps #5 (11252-30; FST), two forceps, #4 (11242-40; FST), and small curved scissor (14061-09; FST) for brain and hippocampus dissection.
- Dissection M75 zoom stereomicroscope (Wild Heerbrugg).
- 0.3 M HEPES (100 ml): Dissolve 7.15 g HEPES (H-9136; Sigma) in 100 ml in H<sub>2</sub>O (pH to 7.3). Filter sterilize and store at 4°C.
- Hanks Balanced Salt Solution (HBSS) (500 ml): 50 ml 10x HBSS (14185-052; Invitrogen), 16.5 ml 0.3 M HEPES (pH 7.3), 5 ml Pen/Strep (15140-148; Invitrogen), and 435 ml H<sub>2</sub>O. Filter sterilize and store at 4°C.
- 100 ml glass beakers (13912-182; VWR).
- 10 cm dishes, TC dish 100 x 20 mm style TC-Treated BD Falcon (353003; VWR).
- 14 ml polypropylene round-bottom tube 17 x 100 mm style BD Falcon (352059; VWR).
- Trypsin (2.5%) (15090-046; Invitrogen). Aliquot in 200 µl and store at –20°C.

- Inverted phase contrast microscope (CKX31; Olympus) for cell counting and checking cell viability.
- Burkert bright-line counting chamber (0642030; Marienfeld-superior) for cell counting.
- Cell hand tally counter (23609-102; VWR).

### **B. Preparing Coverslips for Neuronal Cultures**

- Acid washing: Place coverslips (24 mm for live cell imaging and 19 mm for immunocytochemistry) in the porcelain racks and incubate in nitric acid for 2 days at room temperature.
- Water washing: Carefully transfer the racks into 1 l beakers (3 racks/beaker) containing about 600 ml of tap-distilled water. Allow the racks to sit undisturbed for 1 h at room temperature. Repeat washing for at least three more times for a total of 4 x 1 h of washing.
- Dry and bake coverslips: Remove racks from last wash and gently blot the base of each rack on a paper towel and allow the coverslips to air-dry on the bench for a while. Use vacuum suction to remove moisture caught between coverslips. Transfer the racks to a clean, dry beaker and cover the top with foil. If the coverslips are still wet, leave one edge of the foil slightly lifted. Bake coverslips overnight at 200°C.
- After baking, transfer the cooled coverslips to 12-well plates (19 mm) and 6-well plates (24 mm) in a sterile laminar flow hood. The coverslips can be directly used for coating or stored for later use.
- Coat coverslips overnight at room temperature (wrapped in aluminum foil in the tissue culture hood or in a drawer) with 1 ml per well of PLL and laminin-coating solution.
- Wash coated coverslips 4x with 2 ml per well of autoclaved MilliQ water. After the last wash, aspirate all the water and add 1 ml of Neurobasal/B27 medium to each well in a 12-well plate with 19 mm coverslips (2 ml of Neurobasal/B27 in a 6-well plate with 24 mm coverslips) and place in the incubator (37°C and 5% CO<sub>2</sub>) until needed. This step can be performed the day before the dissection.

### **C. Hippocampal Dissection**

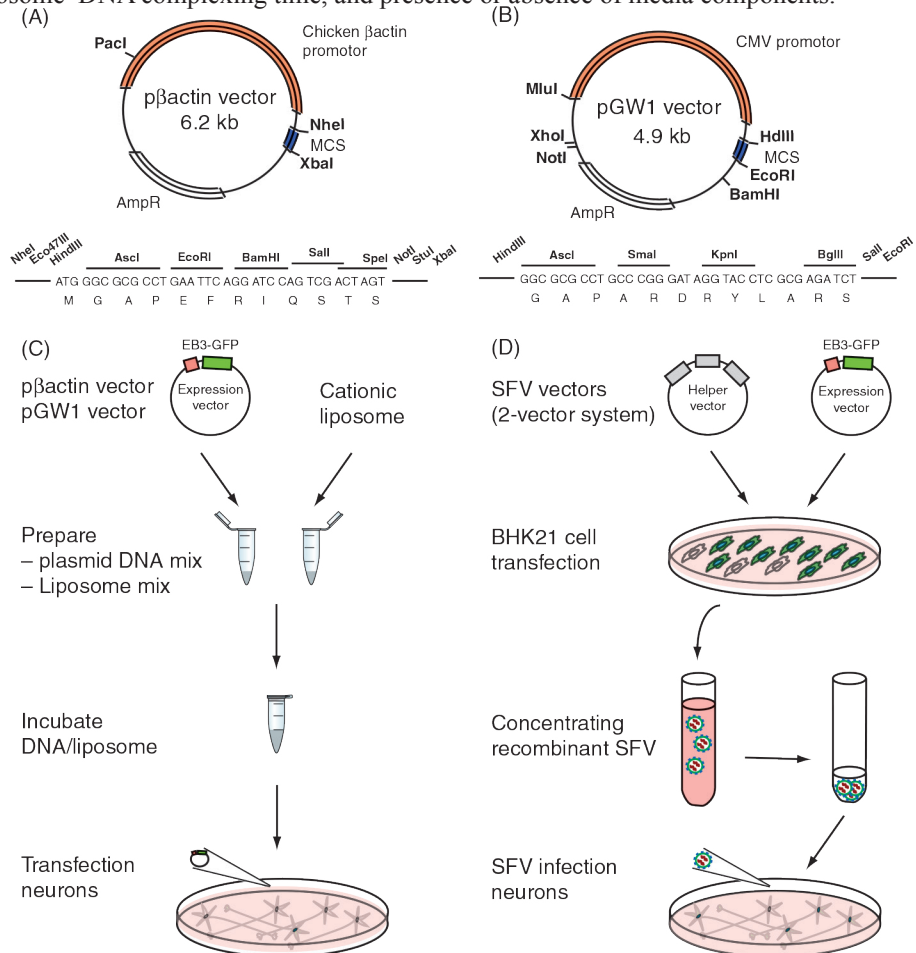
- Before starting the dissection: Sterilize the dissecting instruments (all medium and small forceps and scissors) dipping them in 70% alcohol and flaming them. When the flames go out the forceps are sterile. Put on ice 2 x 100 ml beakers with about 25 ml HBSS each with sterile petri dish covers, 1 x 14 ml Falcon snap-top with 10 ml of HBSS, 2 x 50 ml Falcon tubes with about 35 ml HBSS (place one on ice, the other in 37°C water bath), and 1x petri dishes with about 12 ml HBSS on ice.
- Anesthetize a time-pregnant rat (E19; Wistar) by CO<sub>2</sub> and kill it by cervical dislocation. In the flow hood spray the abdomen and instruments with 70% ethanol. To minimize contamination, cut first through the skin using medium forceps and scissor and lay it back away from the abdomen. Rinse again the instruments with 70% ethanol and then cut through the abdomen wall.
- Lift out the uterus and cut away the connection tissues. Remove embryos one at a time from the uterus and decapitate them, placing the heads immediately into the 100 ml beaker with 25 ml HBSS on ice.
- Take one embryo head and remove the skin covering the skull. Place forceps

- under the skull and peel it to the side. Scoop the embryo brain out into the second 100 ml beaker with 25 ml HBSS on ice. Repeat for all embryos.
- Transfer one embryo brain into the petri dishes with 12 ml HBSS and place on the dissection microscope. Turn the brain so that the bottom faces upward. Cut along the area marked out by the blood vessels to separate the hemispheres from the brainstem.
  - The hippocampus is located in the thicker end of the hemisphere. Place forceps in the narrow part of the hemisphere to hold it still and peel away the meninges from the medial part of the hemisphere. Usually it is possible to grasp the meninges and pull it away as a single sheet without tearing the underlying hippocampus.
  - The inner edge of the hippocampus is now free. Using scissors cut away the adjoining tissue from the outer edge and the ends of the hippocampus to remove it from the hemisphere.
  - Transfer the hippocampus into the 14 ml Falcon snap-top with 10 ml of HBSS on ice. Dissect out the hippocampi from the other hemisphere and repeat for all brains.
  - After collecting all hippocampi, gently wash five times with 10 ml ice-cold HBSS (from the 50 ml Falcon tube); wait for the tissue to sink to the bottom, then aspirate HBSS as much as possible without sucking up the cells. After the last wash, remove all but 4 ml of HBSS and add 10  $\mu$ l 2.5% trypsin/hippocampus (in general we add 200  $\mu$ l trypsin for ~10 brains).
  - Incubate for 15 min in the 37°C water bath and gently shake the tube every 5 min.
  - Gently wash five times with 10 ml HBSS (from the 50 ml Falcon tube in the 37°C water bath), wait for tissue to sink to the bottom, and then aspirate HBSS as much as possible without sucking up the cells.
  - After the last wash, remove all HBSS but leave 4 ml per ~12 brains and gently pipette the suspension up and down (about 10 times) with a 10 ml pipette to homogenize the tissue. This should result in virtually complete dissociation of the tissue into a homogenous single-cell suspension. If any debris is left, allow it to settle to the bottom of the tube and transfer the cell suspension to a new 14 ml Falcon tube.
  - Next count the number of viable cells under an inverted phase contrast microscope using a Burkner counting chamber (0.1 mm depth). Counting 16 small square zones will give the number of cells (c) per 0.1  $\mu$ l suspension. For plating 75,000 cells per 19 mm coverslip (375 cells per mm<sup>2</sup>), use the equation  $75,000 \text{ cells}/(c \times 10)$  to calculate the volume of cell suspension (in  $\mu$ l) to pipette into one well.
  - Incubate the cells in a 37°C and 5% CO<sub>2</sub> incubator for 2–3 weeks before DNA transfection or virus infection (Sections IV and V). Optional: after ~1 week in culture, exchange half of the medium with fresh Neurobasal/B27 medium. Never exchange all medium.

#### **IV. EXPRESSION OF EB3-GFP IN HIPPOCAMPAL NEURONS USING LIPOPHILIC TRANSFECTION**

Expression of specific genes in mature neurons in culture has become an invaluable approach to study the subcellular localization of neuronal proteins (e.g., by visualizing fluorescently

tagged recombinant proteins) and their functions (e.g., by introducing specific mutations, dominant-negative constructs, small hairpin RNA expression). Typically, the gene of interest is cloned into mammalian expression vectors and transfected into dissociated neurons in culture to obtain efficient neuronal expression. For optimal expression in mature hippocampal neurons in culture, we normally use either the cytomegalovirus-based pGW1-CMV expression vector for high-expression levels (Hoogenraad et al., 2005) or the chicken  $\beta$ -actin promoter vector p $\beta$ actin-16-pl for low expression of the transgene (Kaech et al., 1996) (Figure 2A, B). Several methods have been described to transfect hippocampal neurons in culture, including calcium phosphate transfection, microinjection, and electroporation (Jiang and Chen, 2006; Lappe-Siefke et al., 2008; Leclere et al., 2005), but we prefer to use Lipofectamine 2000 transfection (Dalby et al., 2004) (Figure 2C). Lipofectamine 2000 is a cationic liposome-based reagent that provides moderate transfection efficiency in primary cultured neurons (0.5–5%) using a relatively simple protocol. The positive surface charge on the liposome allows association of negatively charged groups such as DNA. The liposome–DNA complexes are subsequently carried through the positively charged and hydrophobic cell membrane into the cell, where it is released. Optimum transfection efficiency and subsequent neuronal viability depend on a number of experimental variables such as cell density, liposome and DNA concentrations, liposome–DNA complexing time, and presence or absence of media components.



The Lipofectamine 2000 transfection method is ideal for imaging subcellular structures in fully polarized neurons, so that axons and dendrites of a single neuron can be visualized and directionality of transport (anterograde vs retrograde) or microtubule orientations (plus-end movement outward vs plus-end movement inward) can be analyzed. We obtain optimal low expression of EB3-GFP and other +Tip markers in cultured neurons by using the p $\beta$ actin vector in combination with Lipofectamine 2000 transfection reagent.

### A. Buffers, Solutions, and Equipment

- Tissue culture incubator (37°C, 5% CO<sub>2</sub>)
- 1.5 ml Eppendorf tubes
- Tabletop microcentrifuge (5415D; Eppendorf)
- 50 ml tube (227261; Greiner)
- Lipofectamine 2000 (11668-027; Invitrogen)
- Neurobasal medium (21103-049; Invitrogen)
- 12-well plates (353043; Falcon) and 6-well plates (3506; Corning Costar)
- 250  $\mu$ l glutamine (200 mM stock) (25030-081; Invitrogen)
- Sterile forceps #5 (11252-30; FST)

### B. Transfection of Neurons Using Lipofectamine 2000

- Prepare the following before starting the transfection. (1) Plasmid DNA using Qiagen plasmid midi kit; (2) Incubation medium: for one 12-well plate containing 12 x 19 mm coverslips prepare 15 ml Neurobasal medium with 37.5  $\mu$ l glutamine and put in 37°C water bath; (3) Fill 50 ml tube with Neurobasal medium and put in 37°C water bath.
- Thaw plasmid DNA (in this case  $\beta$ actin -EB3-GFP or  $\beta$ actin -cherry- $\alpha$ -tubulin) and spin in microcentrifuge for 5 min at 13,000 rpm to remove any microaggregates. For each Lipofectamine 2000 (L2K) transfection start with two 1.5 ml Eppendorf tubes, one containing plasmid DNA (DNA mix) and one containing the Lipofectamine 2000 reagent (L2K mix). All the incubation steps can proceed at room temperature.
- Prepare DNA mix in the first 1.5 ml tube: 1.8  $\mu$ g plasmid DNA per 19 mm coverslip and add 100  $\mu$ l Neurobasal medium. Gently mix. Use 3.6  $\mu$ g plasmid DNA per 24 mm coverslip.
- Prepare L2K mix in the second 1.5 ml tube: 3.3  $\mu$ l Lipofectamine 2000 per 19 mm coverslip and add 100  $\mu$ l Neurobasal medium. Gently mix. Use 6.6  $\mu$ l Lipofectamine 2000 per 24 mm coverslip. To preserve the quality of the Lipofectamine 2000 stock reagent, it should be removed from the refrigerator for as short a time as possible and placed on ice when not in use.
- Add 100  $\mu$ l L2K mix to the DNA mixture and incubate for 30 min at room temperature.
- Note that no adjustments for cotransfections of two DNA constructs are required even though the Lipofectamine 2000 : DNA ratio will be halved in such cases. It is best to start testing 0.8  $\mu$ g for each plasmid DNA for optimal expression.

---

◀Figure 2. Expressing Microtubule Plus-End Tracking Proteins (+Tips) in Cultured Neurons (A–B) Mammalian expression vectors p $\beta$ actin (A) and pGW1 (B) are used for optimal expression in primary hippocampal neurons. The original p $\beta$ actin-16-pl vector was modified by inserting a multiple cloning site (NheI-Eco47III-HdIII-AscI-EcoRI-BamHI-SalI-SpeI-NotI-StuI-XbaI) and the pGW1-CMV vector contains the following multiple cloning site (HdIII-AscI-SmaI-KpnI-BglII-SalI-EcoRI). (C–D) Lipofectamine transfection procedure (C) and SFV flow diagram (D). See text for further details.

- Approximately 10 min before the end of the incubation time pipette 1 ml of conditioned medium from the culture plate to the new 12-well plate and add 1 ml incubation medium to the original plate. Do this per 4 wells at the time and repeat for the next 4 wells. For the 6-well plate pipette 2 ml. Store the plate with conditioned medium in the 37°C and 5% CO<sub>2</sub> incubator.
- Gently add dropwise 200 µl of DNA/L2K mix to each well and incubate for 45 min in the 37°C and 5% CO<sub>2</sub> incubator.
- Rinse the coverslips containing the neurons in fresh warm Neurobasal medium by dipping them in a full 50 ml tube. Return the coverslip to the plate containing conditioned medium.
- Incubate the transfected neurons in the incubator at 37°C and 5% CO<sub>2</sub>. Allow expression to proceed for the desired time before using them for immunocytochemistry or live cell imaging. We observed optimal microtubule labeling of cherry- $\alpha$ -tubulin and microtubule plus-end movement of EB3-GFP comets in cultured neurons in low-expressing neurons after 1–2 days after transfection by using the p $\beta$ actin-16-pl vector in combination with Lipofectamine 2000 transfection reagent.

### V. EXPRESSION OF EB3-GFP IN HIPPOCAMPAL NEURONS USING SFV

The SFV is an enveloped type alphavirus virus and has a single-stranded positive-sense RNA genome which functions directly as an mRNA after infection. Within host cells, translation can take place within a few hours after infection and thousands of exogenous protein copies can be made instantly. Compared to other viruses used to infect brain cells, SFVs exhibit a preference for neurons rather than glial cells (Ehrengruber, 2002). SFV vectors have been modified to be defective in their production of infectious viral particles (in this case pSFV2), and cotransfection with a packaging-deficient helper vector (in this case pSFV-Helper2) allows viral propagation (Figure 2D). By using this SFV vector system, SFV vector-mediated gene expression has been established in dissociated hippocampal neurons (de Hoop et al., 1994) and slice cultures (Ehrengruber et al., 1999). The advantages of SFV system is that it requires biosafety level 1, is relatively simple, and takes less than 2 days to make a high-titer virus. Moreover, cultured neurons can be infected with recombinant SFV with an efficiency of 60–80% within 3–4 h postinfection (de Hoop et al., 1994). On the other hand, SFV vector infections are cytotoxic which permits only short-term transgene expression (4–24 h). The SFV vector system we use to produce SFV EB3-GFP particles is previously described by the Ehrengruber laboratory (Ehrengruber and Lundstrom, 2007; Ehrengruber et al., 1999).

#### A. Buffers, Solutions, and Equipment

##### *Culturing BHK-21 cells*

- Baby hamster kidney-21 (BHK-21) cell line (c-13), American Type Culture Collection (ATCC; CCL-10)
- Glasgow MEM (G-MEM) BHK-21 (1x) liquid 500 ml (21710-025; Invitrogen)
- Streptomycin/penicillin (15140-114; Invitrogen)
- Phosphate-buffered saline (PBS) medium w/o Ca<sub>2</sub>/Mg<sub>2</sub><sup>+</sup> (14190-094; Invitrogen)
- Trypsin/EDTA (25300-054; Invitrogen)
- Fetal bovine serum (FBS) (PET10106169; Invitrogen)
- 5% FBS Media complete: 500 ml G-MEM, 5 ml streptomycin/penicillin, and

- 25 ml FBS
- 10 cm dishes, TC dish 100 x 20 mm style TC Treated BD Falcon (353003; VWR)
- 175 cm<sup>2</sup> flasks

### *Transfection BHK-21 cells*

- SFV plasmid system: pSFV2 and pSFV-Helper2
- 1.5 ml sterile and RNase-free Eppendorf tubes
- Phenol/chloroform/isoamylalcohol 25:24:1 (P-2069; Sigma)
- Roche Sp6 transcription kit containing Sp6 RNA polymerase and 10x transcription buffer, rNTP mix, 10–50 U/ $\mu$ l Rnase inhibitor (999644), 10 mM m<sup>7</sup>G (5' )ppp(5' )G (904988; Roche), 50 mM dithiothreitol (DTT) (197777; Roche)
- Opti-MEM I reduced serum medium (1x) with L-glutamine (31985047; Invitrogen)
- DMRIE-C reagent 2 mg/ml (10459-014; Invitrogen)
- 40–60 units  $\alpha$ -chymotrypsin (C4129; Sigma)
- 100 mg Aprotinin (4511388; Amersham Pharmacia Biotech)
- 0.22  $\mu$ m 33 mm Millipore filters (SLGSO 3355; Millipore)
- Ultracentrifuge with SW41Ti rotor and ultra clear SW41Ti centrifuge tubes 13.2 ml 14 x 89 mm (344059; Beckman Coulter)
- 40 mM HNE buffer (pH 7.4): 40 mM HEPES, 138.5 mM NaCl, 0.1 mM EGTA, and adjust pH with 4 M NaOH. Measure osmolarity (should be 300–310 mosm/l), autoclave, and store at 4°C

### **B. Preparation of Packaged SFV EB3-GFP Replicons in BHK-21 Cells**

- Clone the gene of interest into the multiple cloning site of the pSFV2 vector. In this case, the cDNA encoding for the microtubule plus-EB protein EB3 was fused to GFP (EB3-GFP) and subcloned in pSFV2.
- Digest ~10  $\mu$ g of recombinant pSFV2-EB3-GFP vector with NruI, and pSFV-Helper2 with SpeI to linearize plasmid DNA. Clean up linear DNA by phenol/chloroform extraction, precipitate, add 15  $\mu$ l RNase-free H<sub>2</sub>O, and use for *in vitro* transcription reaction.
- The Roche Sp6 transcription kit is used to synthesize single-stranded RNA for transfection in BHK-21 cells. The *in vitro* transcription mix contains 15  $\mu$ l linear DNA, 15  $\mu$ l 10x transcription buffer, 15  $\mu$ l 10 mM m<sup>7</sup>G(5' )ppp(5' )G, 15  $\mu$ l 50 mM DTT, 15  $\mu$ l rNTP mix, 9  $\mu$ l SP6 RNA polymerase, and 5.6  $\mu$ l 40 U/ $\mu$ l RNasin in a total volume of 150  $\mu$ l dH<sub>2</sub>O. Mix and incubate for 2 h at 37°C.
- Prepare BHK-21 cells. Grow BHK-21 stock cells in 10 cm<sup>2</sup> dishes with 5% FBS media complete in a tissue culture incubator (37°C + 5% CO<sub>2</sub>). When cells form a confluent monolayer, cells are split using 1 ml of prewarmed trypsin/EDTA. One or two weeks before the transfection, prepare BHK-21 cells in 175 cm<sup>2</sup> flasks.
- One day before transfection split a confluent 175 cm<sup>2</sup> flask of BHK-21 cells, seed 2.5 ml cells in a new 175 cm<sup>2</sup> flask (50 ml medium), and incubate cells overnight at 37°C in a 5% CO<sub>2</sub> incubator. Next day discard medium and wash cells two times with ~30 ml of prewarmed Opti-MEM I-reduced serum.
- Add in a sterile tube 17.5 ml Opti-MEM I, 175  $\mu$ l DMRIE-C, 450  $\mu$ l SFV-Helper2 RNA, 225  $\mu$ l SFV2-EB3-GFP RNA. Immediately add the transfection

- mix to the washed BHK-21 cells and mix gently. Incubate for 4 h at 37°C and 5% CO<sub>2</sub> in the incubator.
- Replace transfection media with 36 ml 10% FBS media complete and allow the BHK-21 cells to express and release virus particles into the media.
  - After 24 h, harvest 36 ml of medium and filter through a 0.22 μm sterile Millipore filter.
  - Virus was activated with 0.5 mg/ml α-chymotrypsin at room temperature for 30 min and aprotinin (900 μl, 250 μg/ml) added to stop protease activity.
  - Concentrate the virus by centrifugation of the activated viral stock in a SW41 rotor for 2.5 h at 35,000 rpm. Remove supernatant very carefully; the virus pellet is hardly visible and very small. Leave the last ~50 μl of the supernatant on the virus pellet. Dissolve the pellet by carefully pipetting up and down. Avoid air bubbles while dissolving the virus pellet.
  - At equal volume of 40 mM HNE buffer pH 7.4 (sterile) to the collected virus. Make 5–10 μl virus aliquots and store aliquots at –80°C. Aliquots can be used a few times but every freeze/thaw step will decrease the virus titer.
  - Determine the virus titer by infecting BHK-21 cells (in a dilution series) and count the number of infected cells per total number of cells. The virus titer should be 10<sup>7</sup>–10<sup>9</sup> replicons/ml after concentrating.
  - Primary hippocampal neurons at 14–21 days *in vitro* (DIV) were infected with (1–3 x 10<sup>3</sup>) SFV-EB3-GFP replicons. Expression of GFP-EB3 in neurons was visible after 4–6 h at 37°C and 5% CO<sub>2</sub>. Longer incubation times or higher virus titer results in high levels of fluorescence in the cytoplasm masking EB3-GFP signals at microtubule plus-ends.

## VI. IMAGING EB3-GFP BY TIRF AND SPINNING DISK MICROSCOPY

### A. Maintaining Neuronal Health

Observing and characterizing dynamic cellular processes, such as microtubule dynamics, often yields important information about cellular activity unavailable from static images. Although TIRF microscopy (Axelrod, 2008) and spinning disk confocal microscopy (Nakano, 2002) are now established tools to image living cells, experiments on living primary neurons pose some additional challenges. The most important challenge is to keep primary neurons alive under the microscope for a long time (hours to days).

Many high-resolution live cell experiments are typically performed using simple defined buffered solutions during imaging (e.g., Ringer's solution). Such defined solutions can be optimized to have minimal background fluorescence, are compatible with most chemical treatments, and do not require a special atmosphere for buffering (i.e., 5% CO<sub>2</sub>). However, because such simple solutions lack most components required for survival, they are not compatible with long-term imaging. Furthermore, even in short-term experiments, we frequently observed differences in organelle dynamics between buffered solutions and the full, conditioned medium used to promote neuron survival over several weeks (Section III A). We therefore routinely use full, conditioned medium as the standard medium for all our live cell-imaging experiments. This medium is bicarbonate buffered and, hence, requires the atmosphere surrounding cells on the microscope to comprise 5% CO<sub>2</sub>. In addition, for optimal survival, the temperature of the medium should be stable and uniform at 37° C. Finally, because the medium immersing the cells needs to be accessible for the CO<sub>2</sub>, the sample cannot be sealed and, hence, evaporation of the medium needs to be prevented by maintaining high humidity of the surrounding atmosphere.

To meet all these requirements, we use a small incubator system that fits our motorized stage insert space (Tokai Hit; INUG2-ZILCS-H2) and keeps the cells in a temperature, humidity, and CO<sub>2</sub> concentration-controlled environment. A 24 mm cover glass with cultured neurons are removed from the 6-well plate and mounted on a metal ring (Invitrogen, Attofluor cell chamber A-7816) that is placed in the incubator. Environmental control is achieved by heating several parts of the microscope and the incubator (objective heater, 37°C; incubator water bath, 38°C; stage heater, 37°C; and a transparent top heater at 40.5°C to prevent condensation of water on the lid) and by connecting to an automated digital gas mixer that mixes pure CO<sub>2</sub> and air. In addition, to compensate the evaporation from the water bath that occurs over tens of hours, we use an automatic water supply system (Tokai Hit, IMF-I-W). Altogether, the stage incubator conditions closely mimic those of a regular cell culture incubator and facilitate cell survival for many days.

The use of local heating and atmosphere control, rather than enclosing the whole microscope with an environment chamber, facilitates rapid and accurate equilibration of the chamber conditions. However, the focal drift induced by the temperature gradient in the objective renders this approach incompatible with long-term experiments on microscopes without focus feedback. We use Nikon's Perfect Focus System on both the TIRF and the spinning disk confocal microscopy systems.

### **B. Total Internal Reflection Fluorescence Microscopy**

Light traveling from one medium to another with different index of refraction ( $n_1$ ) will be refracted according to Snell's law. When traveling from glass ( $n_{11} = 1.5$ ) to water ( $n_{12} = 1.33$ ) the exit angle will exceed the entry angle, and a critical angle  $\theta_c$  exists above which light will not propagate through the water but instead be totally reflected on the internal surfaces of the interface (i.e.,  $\theta_c = \arcsin(n_{12}/n_{11}) \approx 62.5^\circ$ ). In this situation, a small exponentially decaying electromagnetic standing wave will emerge at the interface in the second medium. The penetration depth of this field depends on the wavelength and precise angle of incidence, but is of order 150 nm. This light can be used to selectively excite fluorophores present within this zone and therefore allows the specific high-contrast detection of a subset of fluorescent signals (down to single-molecule fluorescence) in situations where the overall particle density is high (Axelrod, 2008). For example, numerous studies have used TIRFM to detect single fluorophores in *in vitro* assays, while many others applied TIRFM to the study of living cells to examine the dynamics of structures close to the cell membrane, such as focal adhesions. When applying TIRFM to the study of cells, it should be noted that the precise properties of evanescent wave are hard to predict because cells do not have a uniform index of refraction. In general, cellular index of refraction is higher than that of water, necessitating a higher angle of incidence to achieve total internal reflection and affecting penetration depth. Furthermore, it is important to note that we and others frequently use the TIRFM setup in a semi-TIRF mode that allows excitation deeper into the sample, while still providing far better contrast than epiillumination (Nakata and Hirokawa, 2003). Since in this case there is no evanescent wave, this would be more appropriately called oblique illumination microscopy rather than TIRFM.

Our TIRF microscope is based on the inverted research microscope Nikon Eclipse TE2000E (Nikon). The microscope is equipped with the Perfect Focus System (Nikon, T-PFS) and a motorized stage (Prior, Proscan II). Metamorph 7.1 (Universal Imaging) is used to control all motorized parts and cameras. A HBO 103 W/2 Mercury Short Arc Lamp (Osram) is used for regular episcopic wide-field illumination, whereas evanescent wave excitation is achieved by a commercially obtained multicolor TIRF arm (Nikon). Lasers (113 mW 488 nm laser line of an argon laser (Spectra-Physics Lasers) and 11 mW 561 nm diode-pumped

solid-state laser (Melles Griot), mounted on a Nikon laser combiner (Nikon, C-LU3EX 3) are coupled into the TIRF arm using an optical fiber whose exit point can be shifted in a plane conjugate to the objective back focal plane. Shifting the fiber exit will thus shift its image (the focused laser) in the objective back focal plane and induce a tilt in the (near-parallel) laser beam that exits the objective. Precise focusing of the laser in the objective back focal plane can be obtained by axially sliding one of the lenses in the optical path between fiber entry and objective back pupil.

The maximal (theoretical) exit angle  $e$  that an objective can achieve is related to its numerical aperture (N.A.) by  $\text{N.A.} = n_{i1} \sin\theta$ . This means that  $\text{N.A.} > n_{i2}$  is the minimal requirement for objectives in order to achieve total internal reflection of the entering laser beam on the interface between cover glass and medium. In practice, N.A. should be at least 1.4 to achieve internal reflection of the whole, spatially extending, laser beam. In our setup, we use a CFI Apo TIRF 100x 1.49 N.A. oil objective (Nikon). Laser light enters the objective after being reflected on a dichroic mirror. Correct laser entry depends critically on the precise positioning of the dichroic mirror and laser alignment needs to be adjusted for each dichroic separately to prevent oblique laser entry. If only a single laser color is used, we use single-band dichroics (Chroma, T495lp for 488 nm and T570lp for 561 nm). However, for simultaneous dual-color TIRF microscopy a multispectral dichroic is required (Chroma, 59022 bs). These dichroics are mounted in metal filter cubes (Nikon, C-FL-HQ) that allow fine-tuning of their tilt and also contain single-band emission filters (Chroma, ET525/25 and ET620/60, respectively) or a double-band emission filter (Chroma, 59022 m).

Fluorescence emission can be detected using two different cameras mounted to different exit ports of the microscope. A Coolsnap HQ2 camera (Photometrics) is attached to a high-speed filter wheel (LB10-NWE, Sutter Instruments) that is mounted to the right exit port of the microscope. This camera has a large detection area (1392 x 1040 pixels) and small pixel size (6.45  $\mu\text{m}$ ) and we use it to image large field of views ( $\sim 90 \times 67 \mu\text{m}$  or  $224 \times 167 \mu\text{m}$  with 100x or 40x magnification, respectively) of reasonably bright samples. Near-simultaneous dual-color TIRFM is achieved by alternating the emission filters in the filter wheel mounted to the exit port (either ET525/25 or ET630/75) in combination with the corresponding excitation laser.

At the left port of the microscope, we use a QuantEM:512SC EMCCD (Electron Multiplying CCD technology) camera (Photometrics). This camera is perfectly suited for low-light level microscopy, because the back-illuminated CCD detector of this camera has a high-quantum efficiency (generated electrons per photon  $> 90\%$  at 575 nm wavelength) and features on-chip multiplication to minimize readout noise. In addition, the camera can achieve high acquisition rates by using frame transfer, which means that before readout the charge distribution accumulated during exposure is rapidly shifted to the unexposed part of the CCD chip and read out while the exposed part is acquiring again. The camera can thus be used for continuous (unshuttered) exposure, with the minimum exposure time of frames being limited by the readout time, which for the full chip at 10 MHz is about 35 ms ( $\sim 512 \times 512$  pixels  $\times 10^{-7}$  s). The QuantEM:512SC camera has an exposed CCD area of 512 x 512 pixels with a pixel size of 16  $\mu\text{m}$ . At 100x magnification this results in an effective pixel size of 160 nm and  $\sim 82 \times 82 \mu\text{m}$  field of view. However, to prevent undersampling of the point spread function (width  $\sim \lambda/(2\text{N.A.}) \sim 200$  nm, with emission wavelength,  $\lambda \sim 600$  nm) we typically use an additional 2.5x magnification lens (Nikon, VM Lens C-2.5x) to achieve effective pixel sizes similar to the Coolsnap camera (i.e., 64 nm at 100x). Finally, to achieve true simultaneous dual-color TIRFM we used a DualView (MAG Biosystems, DV2) with beam splitter (Chroma, 565DCXR) and additional emitter (Chroma, ET525/25) in the GFP light path. This optical device features two relay lenses to project the native image plane of

the microscope onto the displaced camera. In the infinity space between these two lenses, a dichroic mirror separates the emission from the two emitters (e.g., GFP and RFP) and adjustable mirrors redirect the two emission light paths onto the second relay lens at slightly different angles to create two spatially (and spectrally) separated images on the same CCD chip.

### C. Spinning Disk Confocal Microscopy

TIRF microscopy is an excellent tool to study processes that occur close to the surface of the cover glass. However, neurons do not entirely attach to the surface and large parts of dendrites and axons are therefore out of reach for the evanescent wave. Confocal microscopes, in contrast, can acquire high-contrast images throughout the sample. Excitation in confocal microscopy occurs through a focused laser that rapidly scans the image plane. The power of confocal microscopy lies in the pinhole that is used to exclude out-of-focal-plane fluorescence emission from the (biological) specimen, allowing the high-contrast imaging of an optically sectioned slice. In combination with z-scanning of the sample by use of a motorized stage or objective, this allows complete sectioning of the specimen to create a three-dimensional reconstruction. In conventional confocal laser scanning microscopes, scanning of the excitation lasers is achieved through mechanical movement of mirrors. This method is rather slow and requires seconds to scan just one plane of a specimen, which makes this approach incompatible with fast live cell microscopy. This disadvantage can be overcome by using spinning disk confocal microscopy. In this technique, scanning of confocal excitation light is achieved through two spinning disks in which one contains thousands of pinholes and the other contains an equal number of microlenses to focus the laser beam into the pinholes. This enables fast, multicolor, three-dimensional live cell imaging.

To perform live cell spinning disk confocal microscopy, we use a Nikon Eclipse-Ti (Nikon) microscope with a CFI Apo TIRF 100x 1.49 N.A. oil objective (Nikon). The microscope is equipped with a motorized stage (ASI, PZ-2000) and Perfect Focus System (Nikon) and uses MetaMorph 7.6.4 software (Molecular Devices) to control the cameras and all motorized parts. Confocal excitation and detection is achieved using a 50 mW 491 nm laser (Cobolt Calypso) and a Yokogawa spinning disk confocal scanning unit (CSU-X1-A1N-E, Roper Scientific) equipped with a triple-band dichroic mirror (z405/488/568trans-pc, Chroma) and a filter wheel (CSU- X1-FW-06P-01, Roper Scientific) containing a GFP emission filter (ET525/50m, Chroma). Confocal images were acquired with a QuantEM:512 SC EMCCD camera (Photometrics) at a final magnification of 64 nm/pixel, including the additional 2.5x magnification introduced by an additional lens mounted between scanning unit and camera (VM Lens C-2.5x, Nikon). The small incubator system (Tokai Hit; INUG2- ZILCS-H2) and Nikon's Perfect Focus System are also used on this system.

## VII. DATA ANALYSIS

Using TIRFM or spinning disk confocal microscopy, fluorescent EB3 comets high-lighting the growing microtubule plus tip can be readily imaged and followed over time. Speeds and directionality of microtubule growth can then be analyzed by manual or automatic tracking of comet trajectories. We recently became particularly interested in using SFV vector-mediated expression of EB3-GFP to identify potential events of microtubules growth into dendritic spines (Jaworski et al., 2009). To rapidly identify potential spine-entering events, we create maximum (Figure 3A) and average (Figure 3B) projections of entire time-lapse recordings. This results in a single image, in which each pixel value corresponds to the maximum or average value of that pixel position across the entire time series, respectively.

Because comets are short-lived and disappear when microtubules undergo catastrophe and start shrinking, the average projection is a close approximation to the distribution of the diffuse pool of nonmicrotubule-bound EB3-GFP. This provides a direct marker for neuron morphology, without requiring coexpression of another fluorescent protein (such as mRFP). In many cases, the maximum projection of the time series reveals locations of microtubule-associated comets and can be used to identify potential spine-entering events. In other cases, however, the large pool of diffuse EB3-GFP not associated with microtubules obscures the unambiguous identification of microtubule-bound EB3-GFP comets. We therefore generally subtract the average projection from each frame of the time series before creating a maximum projection (Figure 3C). This procedure dramatically enhances the appearance of EB3-GFP comets (Figure 3C) and also permits creating color-coded merges of background and comets (Figure 3D–E). If spine entry events are identified (marked by arrows in Figure 3C), kymography can be used to display comet dynamics along a line over time (Figure 3F).

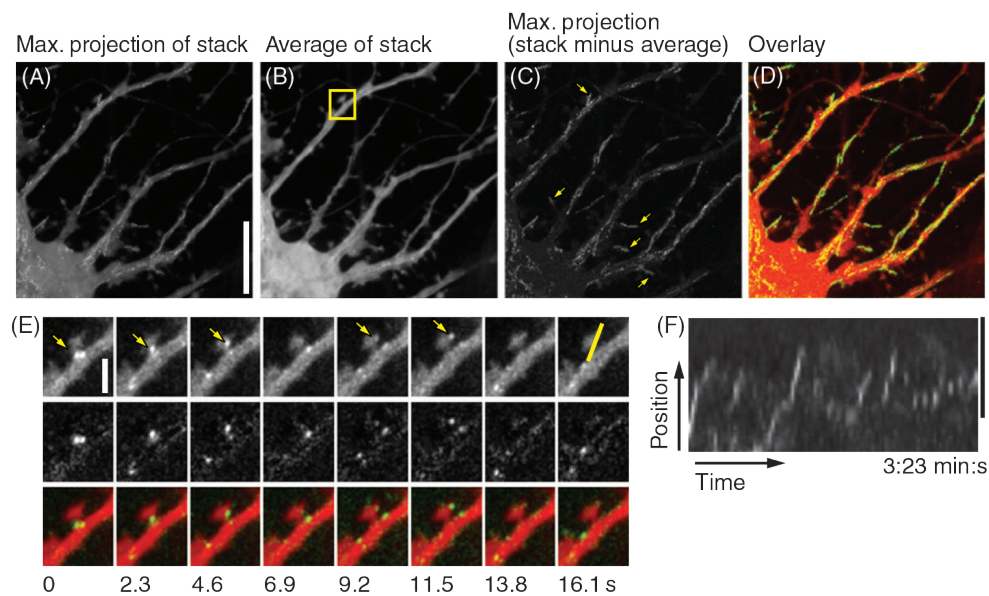


**Figure 3. EB3-GFP Imaging Using Spinning Disk and TIRF**

(A–D) DIV15 Hippocampal neurons infected by SFV and expressing EB3-GFP were imaged using a spinning disk confocal microscope (Nikon). Each 2.3 s a series of 11 z-slices (spaced 0.5  $\mu\text{m}$ ) was recorded and merged into a single image by maximum projection. The resulting time series was then low-pass filtered before subsequent operations to produce (A–D). Scale bar represents 10  $\mu\text{m}$ . (A) Maximum projection of the low-pass-filtered time-lapse recording. (B) Average projection of the time-lapse recording used to obtain an approximate background (noncomet) fluorescence image. Box indicates the region used in (E). (C) Maximum projection of the time series obtained by subtracting the average projection [shown in (B)] from the original, low-pass filtered, time series. EB3 comet spine entry events are now readily detectable. (D) Merge of (B) red) and (C) (green).

(E) Video frames of the region shown in (B). Upper row shows the original, low-pass filtered data. Second row displays frames obtained by subtracting the average fluorescence shown in (B). The third row shows the merge of average and average-subtracted stills. Arrows indicate comet entering spine. Yellow line marks region used for kymography in (F). Scale bar represents 2  $\mu\text{m}$ .

(F) Kymograph over the total time-lapse recording for the line shown in (E). Scale bar represents 2  $\mu\text{m}$ . (See Plate no. 2 in the Color Plate Section.)

We found that EB3 comet entry was often followed by an increase in spine size (Jaworski et al., 2009). To quantify spine size change upon EB3-GFP comet entry, we compare the spine area before the first recorded entry event to the area 5 min after the last entry event that occurred within a window of 3 min after the first event, provided no new entries occurred in those 5 min. To obtain spine area, image regions including head and neck, but not dendritic shaft, are first low-pass filtered, then binarized by thresholding at ~30% of maximum intensity above background, and finally closed by morphological filtering (dilation followed by erosion). Area is then measured as the number of nonzero pixels and multiplied by the calibration factor (1 pixel<sup>2</sup> = 642 nm<sup>2</sup>). To analyze control spine growth, spines that exist throughout the imaging but do not show EB3 entry events can be selected.

### VIII. CONCLUSION

Primary neuron cultures have become an important tool for addressing fundamental questions in molecular and cellular neurobiology, especially when combined with the ability to express specific genes and perform quantitative high-resolution live cell imaging experiments to address the subcellular localization and function of neuronal proteins in their native cellular context. Although the study of the neuronal cytoskeleton has a long and rich history that spans several decades, it seems that a new era has started now that state-of-the-art imaging techniques are readily available from commercial sources and can easily be combined with the rapidly expanding repertoire of techniques that allow expressing, tagging, or silencing of specific proteins and/or modulation of their functions using chemical biology toolboxes. We hope that the detailed protocols provided in this chapter will contribute to a better understanding of the dynamic cytoskeleton in neuronal cells.

### ACKNOWLEDGMENTS

We thank Samantha Spangler and Nanda Keijzer for preparing neuron cultures and establishing the dissection protocol. L.C.K. is supported by the Erasmus Medical Center (EMC fellowship) and the Netherlands Organization for Scientific Research (NWO-VENI). C.C.H. is supported by the Netherlands Organization for Scientific Research (NWO-ALW and NWO-CW), the Netherlands Organization for Health Research and Development (ZonMW-VIDI and ZonMW-TOP), the European Science Foundation (EURYI), EMBO Young Investigators Program (YIP), and the Human Frontier Science Program (HFSP-CDA).

### REFERENCES

- Axelrod, D. (2008). Chapter 7: Total internal reflection fluorescence microscopy. *Methods Cell Biol.* 89, 169–221.
- Baas, P. W., et al., (1988). Polarity orientation of microtubules in hippocampal neurons: Uniformity in the axon and nonuniformity in the dendrite. *Proc. Natl. Acad. Sci. U. S. A.* 85, 8335–8339.
- Baas, P. W., et al., (1989). Changes in microtubule polarity orientation during the development of hippocampal neurons in culture. *J. Cell Biol.* 109, 3085–3094.
- Banker, G. A., and Cowan, W. M. (1977). Rat hippocampal neurons in dispersed cell culture. *Brain Res.* 126,397–42.
- Blanpied, T. A., and Ehlers, M. D. (2004). Microanatomy of dendritic spines: Emerging principles of synaptic pathology in psychiatric and neurological disease. *Biol. Psychiatry* 55, 1121–1127.
- Bramham, C. R. (2008). Local protein synthesis, actin dynamics, and LTP consolidation. *Curr. Opin. Neurobiol.* 18, 524–531.
- Brewer, G. J., et al., (1993). Optimized survival of hippocampal neurons in B27-supplemented neurobasal, a new serum-free medium combination. *J. Neurosci. Res.* 35, 567–576.
- Cheeseman, I. M., and Desai, A. (2008). Molecular architecture of the kinetochore-microtubule interface. *Nat. Rev. Mol. Cell Biol.* 9, 33–46.
- Conde, C., and Caceres, A. (2009). Microtubule assembly, organization and dynamics in axons and dendrites. *Nat. Rev. Neurosci.* 10, 319–332.
- Dalby, B., et al., (2004). Advanced transfection with Lipofectamine 2000 reagent: primary neurons, siRNA, and

- high-throughput applications. *Methods* 33, 95–103.
- de Hoop, M. J., et al., (1994). Semliki forest virus as a tool for protein expression in cultured rat hippocampal neurons. *Gene Ther.* 1(Suppl 1), S28–S31.
- Dombeck, D. A., et al., (2003). Uniform polarity microtubule assemblies imaged in native brain tissue by second-harmonic generation microscopy. *Proc. Natl. Acad. Sci. U. S. A.* 100, 7081–7086.
- Dotti, C. G., et al., (1988). The establishment of polarity by hippocampal neurons in culture. *J. Neurosci.* 8, 1454–1468.
- Ehlers, M. D. (2003). Activity level controls postsynaptic composition and signaling via the ubiquitin- proteasome system. *Nat. Neurosci.* 6, 231–242.
- Ehrengruber, M. U., et al., (1999). Recombinant Semliki Forest virus and Sindbis virus efficiently infect neurons in hippocampal slice cultures. *Proc. Natl. Acad. Sci. U.S.A.* 96, 7041–7046.
- Ehrengruber, M. U. (2002). Alphaviral vectors for gene transfer into neurons. *Mol. Neurobiol.* 26, 183–201.
- Ehrengruber, M. U., and Lundstrom, K. (2007). Alphaviruses: Semliki Forest virus and Sindbis virus vectors for gene transfer into neurons. *Curr. Protoc. Neurosci.* Chapter 4, Unit 4 22.
- Gu, C., et al., (2006). The microtubule plus-end tracking protein EB1 is required for kv1 voltage-gated K<sup>+</sup>channel axonal targeting. *Neuron* 52, 803–816.
- Hirokawa, N., and Takemura, R. (2004). Molecular motors in neuronal development, intracellular transport and diseases. *Curr. Opin. Neurobiol.* 14, 564–573.
- Hirokawa, N., and Takemura, R. (2005). Molecular motors and mechanisms of directional transport in neurons. *Nat. Rev. Neurosci.* 6, 201–214.
- Holtmaat, A., and Svoboda, K. (2009). Experience-dependent structural synaptic plasticity in the mammalian brain. *Nat. Rev. Neurosci.* 10, 647–658.
- Hoogenraad, C. C., et al., (2005). GRIP1 controls dendrite morphogenesis by regulating EphB receptor trafficking. *Nat. Neurosci.* 8, 906–915.
- Hoogenraad, C. C., and Bradke, F. (2009). Control of neuronal polarity and plasticity—a renaissance for microtubules?. *Trends Cell Biol.* 19, 669–676.
- Howard, J., and Hyman, A. A. (2009). Growth, fluctuation and switching at microtubule plus ends. *Nat. Rev. Mol. Cell Biol.* 10, 569–574.
- Jaworski, J., et al., (2008). Microtubule plus-end tracking proteins in differentiated mammalian cells. *Int. J. Biochem. Cell Biol.* 40, 619–637.
- Jaworski, J., et al., (2009). Dynamic microtubules regulate dendritic spine morphology and synaptic plasticity. *Neuron* 61, 85–100.
- Jiang, M., and Chen, G. (2006). High ca<sup>2+</sup>-phosphate transfection efficiency in low-density neuronal cultures. *Nat. Protoc.* 1, 695–700.
- Kaech, S., et al., (1996). Cytoskeletal plasticity in cells expressing neuronal microtubule-associated proteins. *Neuron* 17, 1189–1199.
- Kaech, S., and Banker, G. (2006). Culturing hippocampal neurons. *Nat. Protoc.* 1, 2406–2415.
- Kapitein, L. C., et al., (2010). Mixed microtubules steer dynein-driven cargo transport into dendrites. *Curr Biol.* 20(4): 290–9.
- Kauer, J. A., and Malenka, R. C. (2007). Synaptic plasticity and addiction. *Nat. Rev. Neurosci.* 8, 844–858.
- Lappe-Siefke, C., et al., (2008). Microinjection into cultured hippocampal neurons: A straightforward approach for controlled cellular delivery of nucleic acids, peptides and antibodies. *J. Neurosci. Methods* 175, 88–95.
- Leclere, P. G., et al., (2005). Effective gene delivery to adult neurons by a modified form of electroporation. *J. Neurosci. Methods* 142, 137–143.
- Lee, H., et al., (2004). The microtubule plus end tracking protein orbit/MAST/CLASP acts downstream of the tyrosine kinase abl in mediating axon guidance. *Neuron* 42, 913–926.
- Lin, A. C., and Holt, C. E. (2008). Function and regulation of local axonal translation. *Curr. Opin. Neurobiol.* 18, 60–68.
- Lise, M. F., et al., (2006). Involvement of myosin Vb in glutamate receptor trafficking. *J. Biol. Chem.* 281, 3669–3678.
- Lowery, L. A., and Van Vactor, D. (2009). The trip of the tip: understanding the growth cone machinery. *Nat. Rev. Mol. Cell Biol.* 10, 332–343.
- Luscher, C., et al., (1999). Role of AMPA receptor cycling in synaptic transmission and plasticity. *Neuron* 24, 649–658.
- Martinez-Lopez, M. J., et al., (2005). Mouse neuron navigator 1, a novel microtubule-associated protein involved in neuronal migration. *Mol. Cell. Neurosci.* 28, 599–612.
- Morrison, E. E., et al., (2002). EB1 identifies sites of microtubule polymerisation during neurite development. *Brain Res. Mol. Brain Res.* 98, 145–152.
- Nakano, A. (2002). Spinning-disk confocal microscopy—a cutting-edge tool for imaging of membrane traffic. *Cell*

- Struct. Funct. 27, 349–355.
- Nakata, T., and Hirokawa, N. (2003). Microtubules provide directional cues for polarized axonal transport through interaction with kinesin motor head. *J. Cell Biol.* 162, 1045–1055.
- Newpher, T. M., and Ehlers, M. D. (2008). Glutamate receptor dynamics in dendritic microdomains. *Neuron* 58, 472–497.
- Sala, C., et al., (2001). Regulation of dendritic spine morphology and synaptic function by shank and homer. *Neuron* 31, 115–130.
- Selkoe, D. J. (2002). Alzheimer's disease is a synaptic failure. *Science* 298, 789–791.
- Sheng, M., and Hoogenraad, C. C. (2007). The postsynaptic architecture of excitatory synapses: A more quantitative view. *Annu. Rev. Biochem.* 76, 823–847.
- Shi, S. H., et al., (2003). Hippocampal neuronal polarity specified by spatially localized mPar3/mPar6 and PI3-kinase activity. *Cell* 112, 63–75.
- Steinmetz, M. O., and Akhmanova, A. (2008). Capturing protein tails by CAP-gly domains. *Trends Biochem. Sci.* 33, 535–545.
- Stepanova, T., et al., (2003). Visualization of microtubule growth in cultured neurons via the use of EB3- GFP (end-binding protein 3-green fluorescent protein). *J. Neurosci.* 23, 2655–2664.
- Sudhof, T. C. (2008). Neuroligins and neuroligins link synaptic function to cognitive disease. *Nature* 455, 903–911.
- Sudhof, T. C., and Rothman, J. E. (2009). Membrane fusion: Grappling with SNARE and SM proteins. *Science* 323, 474–477.
- Tsai, J. W., et al., (2005). LIS1 RNA interference blocks neural stem cell division, morphogenesis, and motility at multiple stages. *J. Cell Biol.* 170, 935–945.
- Yuste, R., and Bonhoeffer, T. (2001). Morphological changes in dendritic spines associated with long-term synaptic plasticity. *Annu. Rev. Neurosci.* 24, 1071–1089.
- Zhou, F. Q., et al., (2004). NGF-induced axon growth is mediated by localized inactivation of GSK-3beta and functions of the microtubule plus end binding protein APC. *Neuron* 42, 897–912.



## Chapter 3

# NMDA Receptor Activation Suppresses Microtubule Growth and Spine Entry

Lukas C. Kapitein,<sup>1,2</sup> Kah Wai Yau,<sup>1,2</sup> Susana Montenegro Gouveia,<sup>3</sup> Wouter A. van der Zwan,<sup>2</sup> Phebe S. Wulf,<sup>1,2</sup> Nanda Keijzer,<sup>2</sup> Jeroen Demmers,<sup>4</sup> Jacek Jaworski,<sup>2,5</sup> Anna Akhmanova,<sup>1,3</sup> and Casper C. Hoogenraad<sup>1,2</sup>

<sup>1</sup>Cell Biology, Faculty of Science, Utrecht University, 3584CH Utrecht, The Netherlands, Departments of <sup>2</sup>Neuroscience and <sup>3</sup>Cell Biology and Genetics, <sup>4</sup>Proteomics Center, Erasmus Medical Center, 3015CE Rotterdam, The Netherlands, and <sup>5</sup>International Institute of Molecular and Cell Biology, 02-109 Warsaw, Poland

### ABSTRACT

Dynamic microtubules are important to maintain neuronal morphology and function, but whether neuronal activity affects the organization of dynamic microtubules is unknown. Here, we show that a protocol to induce NMDA-dependent long-term depression (LTD) rapidly attenuates microtubule dynamics in primary rat hippocampal neurons, removing the microtubule-binding protein EB3 from the growing microtubule plus-ends in dendrites. This effect requires the entry of calcium and is mediated by activation of NR2B-containing NMDA-type glutamate receptor. The rapid NMDA effect is followed by a second, more prolonged response, during which EB3 accumulates along MAP2-positive microtubule bundles in the dendritic shaft. MAP2 is both required and sufficient for this activity-dependent redistribution of EB3. Importantly, NMDA receptor activation suppresses microtubule entry in dendritic spines, whereas overexpression of EB3-GFP prevents NMDA-induced spine shrinkage. These results suggest that short-lasting and long-lasting changes in dendritic microtubule dynamics are important determinants for NMDA-induced LTD.

*J Neurosci.* 2011 Jun 1;31(22):8194-209

### INTRODUCTION

Most excitatory glutamatergic synapses in the mammalian brain are formed at tiny dendritic protrusions, named dendritic spines (Bourne and Harris, 2008). Dendritic spines play critical roles in synaptic function and exhibit a striking degree of structural plasticity, which is closely linked to changes in strength of synaptic connections (Holtmaat and Svoboda, 2009). Several studies have reported that glutamate receptor activation changes spine morphology by modulating postsynaptic cargo trafficking and actin cytoskeleton dynamics (Hotulainen and Hoogenraad, 2010). For example, it has been shown that enhanced actin polymerization induces spine enlargement during long-term potentiation (LTP) (Matsuzaki et al., 2004; Okamoto et al., 2004), whereas long-term depression (LTD) involves spine shrinkage through actin depolymerization (Okamoto et al., 2004; Zhou et al., 2004). In contrast, the roles of microtubules and associated proteins in postsynaptic signaling mechanisms and their role in spine plasticity have remained mostly unexplored. Both stable and dynamic microtubules are abundantly present in mature neurons (Jaworski et al., 2008; Conde and Cáceres, 2009; Hoogenraad and Bradke, 2009). In dendrites, microtubule-associated protein 2 (MAP2) binds along the length of microtubules and its phosphorylation state is believed to regulate microtubule stability (Sánchez et al., 2000; Cassimeris and Spittle, 2001; Dehmelt and Halpain, 2005). Many reports have documented the close relationship between glutamate receptor activation and MAP2 alterations (Aoki and Siekevitz, 1985; Halpain and Greengard, 1990; Montoro et al., 1993; Quinlan and Halpain, 1996; Philpot et al., 1997). However, recent work has established an important role for dynamic microtubules in the maintenance of dendritic spines. Inhibition of microtubule growth or depletion of EB3, one of the major microtubule plus-end binding proteins in mature neurons, caused the specific loss of mushroom-headed spines and increased the percentage of filopodia (Jaworski et al., 2009). Live imaging revealed that dynamic microtubules regularly depart from the dendritic shaft and enter dendritic spines (Gu et al., 2006; Hu et al., 2008; Jaworski et al., 2009) to stimulate actin polymerization and induce transient morphological changes, such as the formation of spine head protrusions or spine growth (Jaworski et al., 2009). These observations support a model in which EB3 plus-end decorated microtubules control actin dynamics and regulate spine morphology and synaptic plasticity. Nevertheless, little is known about the effect of glutamate receptor activation on the microtubule network. Here, we show that transient NMDA receptor activation induces sustained alterations in the microtubule network in dendrites. A chemical LTD protocol affects EB3 localization in hippocampal neurons in two phases: a fast phase (>1 min) leading to the loss of EB3 comets and a slow phase (>10 min) where EB3 binds along MAP2-positive microtubule bundles. MAP2 directly interacts with EB3 and is essential for the spatial redistribution of EB3 along the dendritic microtubules. NMDA receptor activation also suppresses microtubule entry in dendritic spines, whereas overexpression of EB3-GFP prevents LTD-induced spine shrinkage. These results demonstrate that excitatory stimuli can alter the cytoskeletal organization in dendrite branches and spines by directly affecting microtubule dynamics.

### MATERIALS AND METHODS

#### Antibodies and reagents

The following primary and secondary antibodies were used in this study: rabbit anti-EB3 (02-1005-07) (Stepanova et al., 2003; Jaworski et al., 2009), mouse anti-MAP2 (AP14; AP118) (Kalcheva et al., 1994), mouse anti-tau, mouse anti- $\beta$ -actin (Millipore Bioscience Research Reagents), rabbit anti-GFP (Abcam; 1:1000), mouse anti-MAP2 (HM-2), mouse anti- $\alpha$ -tubulin, mouse anti-acetylated tubulin (Sigma-Aldrich), mouse anti-bassoon

(Nventa Biopharmaceuticals), rabbit anti- $\beta$ -galactosidase (MP Biomedicals), mouse anti- $\beta$ -galactosidase (Promega), rabbit anti-HA, mouse anti-Myc, rabbit anti-GFP (Medical and Biological Laboratories), mouse class III  $\beta$ -tubulin antibody (Tuji; Covance), mouse anti-GFP (Quantum), and Alexa 488-, Alexa 568-, and Alexa 630-conjugated secondary antibodies (Invitrogen).

Other reagents used in this study include nocodazole, DL-2-amino-5-phosphonopentanoic acid (APV), 6-cyano-7-nitroquinoxaline-2,3-dione (CNQX), glycine, NMDA, AMPA, tetrodotoxin (TTX), bicuculline, *a*-(4-hydroxyphenyl)- $\beta$ -methyl-4-benzyl-1-piperidineethanol (ifenprodil), *a*-(4-hydroxyphenyl)- $\beta$ -methyl-4-(phenylmethyl)-1-piperidinepropanol hydrochloride (Ro 25-6981), 1,2-bis(2-aminophenoxy)ethane-N, N,N',N'-tetraacetic acid tetrakis(acetoxymethyl ester) (BAPTA-AM), 1-amino-1,3-cyclopentanedicarboxylic acid (ACPD), 2-amino-4-phosphonobutyric acid (4-AP), okadaic acid and staurosporine (Sigma-Aldrich), and microtubule-associated protein fraction (Cytoskeleton).

### Expression constructs

The following mammalian expression plasmids have been described: pGW1-EB3-GFP (Jaworski et al., 2009), pGW1-GFP, p $\beta$ actin-HA- $\beta$ -galactosidase (Hoogenraad et al., 2005), pSuper vector (Brummelkamp et al., 2002), pSuper-EB3-shRNA (Jaworski et al., 2009), GFP-MAP2c (Farah et al., 2005), NR2B-shRNA and NR2A-shRNAs (Kim et al., 2005), mCherry- $\alpha$ -tubulin (Shaner et al., 2004), and GST-EB3 (Komarova et al., 2005). GFP-KIFC2 was generated by PCR cloning full-length rat KIFC2 cDNA into pEGFP-C1. The MAP2#1 shRNA sequence (cagggcac-ctattcagata) and MAP2#2 shRNA sequence (ttcgtgagccttagaca) targeting rat MAP2 mRNA was designed based on the experimentally verified sequences (Krichevsky and Kosik, 2002; Fontaine-Lenoir et al., 2006). The complementary oligonucleotides were annealed and inserted into pSuper vector.

### Primary hippocampal neuron cultures, transfection, infection, and immunohistochemistry

Primary hippocampal cultures were prepared from embryonic day 18 rat brains (Banker and Goslin, 1998; Kapitein et al., 2010). Cells were plated on coverslips coated with poly-L-lysine (30  $\mu$ g/ml) and laminin (2  $\mu$ g/ml) at a density of 75,000/well. Hippocampal cultures were grown in Neurobasal medium (NB) supplemented with B27, 0.5 mM glutamine, 12.5  $\mu$ M glutamate, and penicillin/streptomycin. Hippocampal neurons were transfected using Lipofectamine 2000 (Invitrogen). Briefly, DNA (3.6  $\mu$ g/well) was mixed with 3  $\mu$ l of Lipofectamine 2000 in 200  $\mu$ l of NB, incubated for 30 min, and then added to the neurons in NB at 37°C in 5% CO<sub>2</sub> for 45 min. Next, neurons were washed with NB and transferred in the original medium at 37°C in 5% CO<sub>2</sub> for 2–4 d.

To express EB3-GFP in cultured hippocampal neurons, we used Semliki Forest virus (SFV)-mediated gene delivery. The EB3-GFP construct was cloned into the pSFV2 vector and packaged into SFV replicons as described previously (Jaworski et al., 2009). In short, SFV-replicons were harvested 24 h after transfection of helper and pSFV2-EB3 vector RNA into baby hamster kidney-21 cells, filter-sterilized, activated with  $\alpha$ -chymotrypsin (Sigma-Aldrich), and concentrated by ultracentrifugation. Virus titer was determined by infection of BHK-21 cell with serial dilutions, followed by fluorescence examination at 18–24 h after infection. Cultured hippocampal neurons were infected at DIV21 by the addition of 1  $\mu$ l ( $\sim 10^7$  replicons/ml) of SFV infectious replicons to the cultures at least 4 h before live-cell imaging.

For immunohistochemistry, neurons were fixed for 5 min with ice-cold 100% methanol/1 mM EGTA at -20°C, followed by 5 min with 4% formaldehyde/4% sucrose in PBS at room temperature. After fixation, cells were washed two times in PBS for 30 min at room

temperature, and incubated with primary antibodies in GDB buffer (0.2% BSA, 0.8 M NaCl, 0.5% Triton X-100, 30 mM phosphate buffer, pH 7.4) overnight at 4°C. Neurons were then washed three times in PBS for 5 min at room temperature and incubated with Alexa-conjugated secondary antibodies in GDB for 2h at room temperature and washed three times in PBS for 5 min. Slides were mounted using Vectashield mounting medium (Vector Laboratories). Confocal images were acquired using a LSM510 confocal microscope (Zeiss) with a 40X or 63X oil objective.

### **GST pull-down assays**

GST fusions of EB3 expression and purification of the GST-tagged proteins from *Escherichia coli* and Western blotting was performed as described previously (Komarova et al., 2005). GFP-MAP2c and GFP-KIFC2 constructs were expressed in HEK293 cells for 24 h, lysates were prepared in a lysis buffer containing 20 mM Tris-HCl, pH 7.5, 100 mM NaCl, 1% Triton X-100, 1 mM DTT, and protease inhibitors (Complete; Roche), and mixed with GST-fusion proteins. Brains were obtained from adult female rats and homogenized in 10X volume/weight in the same lysis buffer. Brain lysates were centrifuged at 16,000 X g for 15 min at 4°C, and the supernatant was incubated with individual GST fusion proteins for 2 h at 4°C. Beads were washed four times with a buffer containing 20 mM Tris-HCl, pH 8, 150 mM NaCl, 0.05% Triton X-100, and 1 mM DTT. The proteins retained on the beads were analyzed by Western blotting (GFP expression constructs) or mass spectrometry (brain lysates).

### **Mass spectrometry analysis**

For mass spectrometry analysis, proteins bound to the beads were separated on a 3–8% NuPAGE Tris-acetate gel and stained with the Colloidal Blue staining kit (Invitrogen). Gel lanes were cut into 2 mm slices using an automatic gel slicer and subjected to in-gel reduction with dithiothreitol, alkylation with iodoacetamide, and digestion with trypsin (Promega; sequencing grade), essentially as described previously (Wilm et al., 1996). Nanoflow liquid chromatography (LC)/MS/MS was performed on an 1100 series capillary LC system (Agilent Technologies) coupled to a linear trap quadrupole linear ion trap mass spectrometer (Thermo Fisher Scientific) operating in positive mode and equipped with a nano-spray source. Peptide mixtures were trapped on a ReproSil C18 reversed-phase column (Dr. Maisch GmbH; column dimensions, 1.5 cm X 100 µm; packed in-house) at a flow rate of 8 µl/min. Peptide separation was performed on ReproSil C18 reversed-phase column (Dr. Maisch GmbH; column dimensions, 15 cm X 50 µm; packed in-house) using a linear gradient from 0 to 80% B [A, 0.1 M acetic acid; B, 80% (v/v) acetonitrile, 0.1 M acetic acid] in 70 min and at a constant flow rate of 200 nl/min using a splitter. The column eluent was directly sprayed into the electrospray ionization source of the mass spectrometer. Mass spectra were acquired in continuum mode; fragmentation of the four peptides was performed in data-dependent mode. Peak lists were automatically created from raw data files using the Mascot Distiller software (version 2.1; Matrix Science). The Mascot search algorithm (version 2.1; Matrix Science) was used for searching against the NCBI database (release NCBI\_nr\_20070217; taxonomy, *Rattus norvegicus*). The peptide tolerance was typically set to 2 Da and the fragment ion tolerance to 0.8 Da. A maximum number of two missed cleavages by trypsin was allowed, and carbamidomethylated cysteine and oxidized methionine were set as fixed and variable modifications, respectively. The Mascot score cutoff value for a positive protein hit was set to 60. Individual peptide MS/MS spectra with Mowse scores <40 were checked manually and either interpreted as valid identifications or discarded.

### **Total internal reflection fluorescence and spinning disk microscopy and image processing**

Total internal reflection fluorescence microscopy (TIRFM) was performed as described previously (Jaworski et al., 2009; Kapitein et al., 2010) on an inverted research microscope (Nikon Eclipse TE2000E; Nikon) with a CFI Apo TIRF 100X, 1.49 numerical aperture (NA), oil objective (Nikon), equipped with Coolsnap HQ CCD cameras (Photometrics).

To perform live-cell spinning disk confocal microscopy, we use a Nikon Eclipse-Ti (Nikon) microscope with a CFI Apo TIRF 100X, 1.49 NA, oil objective (Nikon). The microscope is equipped with a motorized stage (ASI; PZ-2000) and Perfect Focus System (Nikon) and uses MetaMorph 7.6.4 software (Molecular Devices) to control the cameras and all motorized parts. Confocal excitation and detection is achieved using a 50 mW 491 nm laser (Cobolt Calypso) and a Yokogawa spinning disk confocal scanning unit (CSU-X1-A1N-E; Roper Scientific) equipped with a triple-band dichroic mirror (z405/488/568transpc; Chroma) and a filter wheel (CSUX1-FW-06P-01; Roper Scientific) containing a GFP emission filter (ET525/50m; Chroma). Confocal images were acquired with a QuantEM:512 SC EMCCD camera (Photometrics) at a final magnification of 68 nm/pixel, including the additional 2.5X magnification introduced by an additional lens mounted between scanning unit and camera (VM Lens C-2.5X; Nikon). All imaging was performed in full conditioned medium and a small incubator system (Tokai Hit; INUG2-ZILCS-H2) is used on this system to maintain neuronal health (Kapitein et al., 2010).

For chemical LTD, NMDA was added to a final concentration of 50  $\mu$ M during the time-lapse recordings. In control experiments, 200  $\mu$ M APV was also present for at least 1 h before addition of NMDA. For glycine and KCl/chemical LTP treatments, neurons were transferred to HEPES-buffered extracellular solution (ECS) (10 mM HEPES, 150 mM NaCl, 5 mM KCl, 2 mM  $\text{CaCl}_2$ , 30 mM glucose, pH 7.4) containing 20  $\mu$ M bicuculline 10 min before imaging (Lu et al., 2001; Park et al., 2006). During imaging, KCl and glycine were added to final concentrations of 50 mM and 200  $\mu$ M, respectively, for 1 min and subsequently replaced with the original ECS. For local stimulation, a micropipette filled with 100  $\mu$ M NMDA and 10  $\mu$ M glycine (Rose et al., 2009) was positioned very close to the dendrite and a single 20 s pressure ejection of 30 psi was generated using a Femtojet express microinjector (Eppendorf).

Images of live cells were processed and analyzed using MetaMorph, Adobe Photoshop, or LabVIEW (National Instruments) software. To analyze comet numbers during chemical treatments, comet numbers were obtained from binarized images generated by thresholding images that were first convoluted with the Mexican hat-type kernel described by Mashanov and Molloy (2007) to enhance fluorescent particles and remove background fluorescence. Dendritic area was determined in MetaMorph by inclusive, binary, thresholding images down to 30%. Spine entry events were identified from maximum and average projections of entire time-lapse recordings, as shown in Figure 11 A–F.

### **Image analysis and quantification**

*Morphometric analyses of dendritic protrusions of fixed hippocampal neurons.* For the morphometric analysis of dendritic protrusions, we used  $\beta$ -gal, GFP, or mRFP as an unbiased cell fill. Because protrusions often crossed several z planes, we took series stacks from the bottom to the top of all dendrites and used the LSM software to generate image projections for quantitative analyses. Images were not further processed and were of similar high quality to the original single planes. The number of planes, typically six to eight, was chosen to cover the entire dendrite from top to bottom. All experiments were repeated at least three times with an  $n > 7$  for individual experiments were analyzed in a double-blind manner. Between 150 and 300 protrusions were scored for every neuron and expressed per 10  $\mu$ m length of dendrite. Discrimination was made between filopodia-like protrusions and mushroom-shaped spines; measurements of length and width of the protrusions were performed as described previously

(Jaworski et al., 2009) and were classified based on the ratio of spine head width to protrusion length according to the following ratios: the spine whose width was equal to or more than one-half the size of its length was judged as standard mushroom spine. The protrusion whose width was smaller than one-half the size of its length was judged as filopodia or thin spine (Jaworski et al., 2009). In those cases in which the total length of the spine could not be adequately seen or its length was  $>5 \mu\text{m}$ , protrusions were excluded from analysis.

*Quantification of EB3 distribution in dendrites and axons.* Measurements of endogenous EB3 and EB3-GFP localization in fixed neurons were performed as described previously (Jaworski et al., 2009). The number of EB3 comets per  $10 \mu\text{m}$  of axon/dendrite length, the length of the EB3 comets, and average fluorescent intensity of EB3 signals in the cell body, dendrites, and axons were measured using MetaMorph software. The dendrites and axons of GFP-expressing neurons were identified based on their morphology and by immunostaining for the dendritic marker MAP2 and axonal marker tau. Statistical analysis was performed with Student's t test assuming a two-tailed and unequal variation. N was defined as the number of transfected neurons.

## RESULTS

### Glutamate receptor activation affects EB3 distribution

To determine how glutamate stimulation affects microtubule organization in primary cultures of rat hippocampal neurons, we examined the distribution of dynamic microtubules using antibodies that recognize the microtubule plus-end binding protein EB3 (Stepanova et al., 2003; Jaworski et al., 2009). Without stimulation, EB3 in fully differentiated neurons ( $>14$  d in vitro; DIV14) was found in comet-like structures corresponding to growing microtubule plus tips throughout the cell body, axon, and dendritic shaft and occasionally in spines that colocalize with synaptic markers (Figure 1 A) (Jaworski et al., 2009). On average,  $6.6 \pm 0.5$  EB3 comets per  $10 \mu\text{m}$  primary dendrite were observed (Figure 1C). We next examined the localization of EB3 on bath application of  $50 \mu\text{M}$  glutamate to maximize the number of synapses undergoing plasticity. On treatment with  $50 \mu\text{M}$  glutamate for 5 min, the characteristic EB3 comet-like staining was strongly decreased and replaced by a diffuse cytoplasmic signal within the dendrites (Figure 1 B). Interestingly, the EB3 staining in tau-positive axons was unaffected (Figure 1 B, E).

Quantification of these observations for different time intervals of glutamate stimulation revealed that a striking decrease in the number of dendritic EB3-positive comets already occurred within 1–2 min after application of  $50 \mu\text{M}$  glutamate (Figure 1C,D). The maximal effect, a  $>20$ -fold decrease in the number of comets per  $10 \mu\text{m}$  primary dendrite, was observed after 5 min of exposure to glutamate (Figure 1 D). Dose–response experiments revealed that glutamate-induced comet removal was concentration dependent, with  $30 \mu\text{M}$  glutamate already removing 70% of the EB3 comets in dendrites. The glutamate-induced redistribution of EB3 was not associated with changes in the localization of presynaptic protein bassoon (Figure 1 A, B) and postsynaptic protein PSD-95 (data not shown) staining, indicating that glutamate caused a rapid redistribution of EB3 without affecting synaptic markers. Moreover, we never observed focal swellings along the dendrites, vacuole-like structures, or abnormal MAP2 distribution that emerge after excessive glutamate receptor stimulation (Figure 1 A, B) (Faddis et al., 1997; Hoskison et al., 2007), indicating that the EB3 redistribution is not attributable to excitotoxicity.

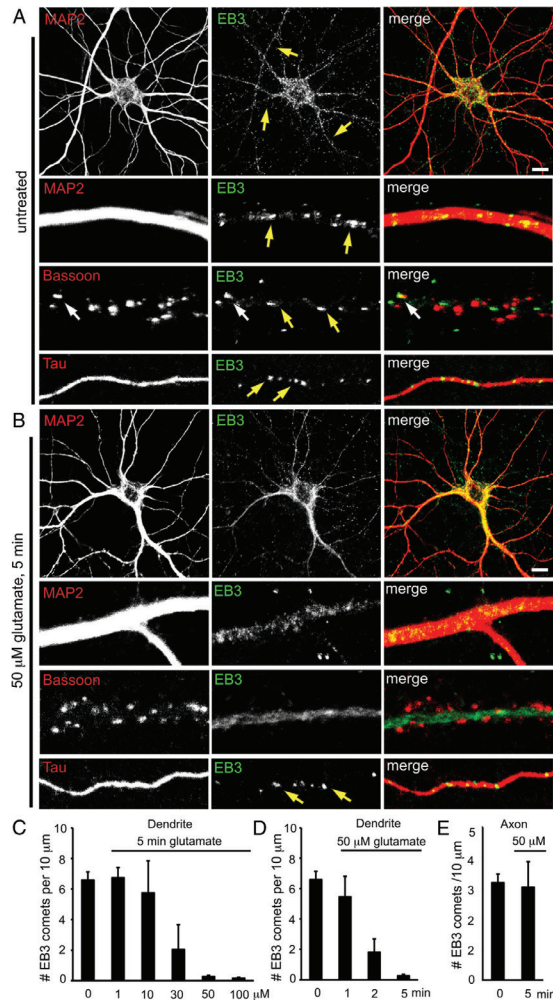


**Figure 1. Glutamate Receptor Activation Affect EB3 Localization**

(A, B) Representative images of rat hippocampal neurons (DIV17) untreated (A) or treated with 50 μM glutamate for 5 min (B) and double-labeled with rabbit anti-EB3 antibody (green) and mouse anti-MAP2 antibody (red). Only the merge is shown in color. Neuronal segments (bottom panels) are enlarged to show the localization of EB3 in dendrites (MAP2), axons (tau), and near synapses (bassoon). The yellow arrows indicate endogenous EB3 comet-like staining. After stimulation, EB3 comets are strongly decreased and replaced by a diffuse cytoplasmic signal within the dendrites. Scale bar, 10 μm.

(C, D) Quantification of the number of EB3 comets per 10 μm dendrite (mean ± SEM) of hippocampal neurons stimulated with various concentrations of glutamate for 5 min (C) or 50 μM glutamate for various time intervals (D). (E) Quantification of the number of EB3 comets per 10 μm axon (mean ± SEM) of hippocampal neurons untreated (0) or stimulated with 50 μM glutamate for 5 min.

### Glutamate induces EB3 translocation through Ca<sup>2+</sup> influx and NMDA receptors

Glutamate acts via ionotropic glutamate receptors that include the AMPA-type receptor, kainate (KA) receptor, and the NMDA-type receptor as well as mGluRs (Hollmann and Heinemann, 1994; Dingledine et al., 1999). To determine which glutamate receptor classes mediated the redistribution of EB3, we treated the cultures with a variety of subtype-selective glutamate receptor agonists and antagonists (Figure 2 A–F ). Blocking NMDA receptors with

the antagonists APV or MK-801 greatly reduced the EB3 redistribution on stimulation with 100  $\mu\text{M}$  glutamate (Figure 2 A, D) (data not shown). In contrast, blocking either AMPA/KA receptors (CNQX) or metabotropic glutamate receptors [AIDA (1-aminoindan-1,5-dicarboxylic acid)], or both together, did not inhibit the glutamate-induced EB3 relocation (Figure 2 A, D). The NMDA receptor specificity of this effect was confirmed by using a chemical LTD protocol (Kameyama et al., 1998; Lee et al., 1998; Beattie et al., 2000; Ehlers, 2000; Colledge et al., 2003), whereby cells were treated with NMDA itself. Bath application of 50  $\mu\text{M}$  NMDA for 5 min strongly decreased the number of dendritic EB3-positive comets in all cells examined (Figure 2 B, E), which could be blocked by APV and MK-801 (Figure 2C,F) (data not shown). Stimulating cells with the metabotropic glutamate receptor agonist ACPD or AMPA glutamate receptor agonist AMPA was ineffective (Figure 2 B, E). The decrease in the proportion of dendritic EB3-positive comets also occurred after shorter NMDA incubation times, within 1–2 min after NMDA application (Figure 3 A, C). Similar results were obtained with lower concentrations of NMDA and 10  $\mu\text{M}$  NMDA already removed most of the EB3 comets in dendrites (Figure 3 B, D). The disappearance of EB3-positive comets was not attributable to the degradation of the protein, because immunoblot analysis showed unchanged levels of total EB3 in NMDA-stimulated cultures, independent of concentration and time of the treatment (Figure 3 E, F). These results demonstrate that a classic chemical LTD protocol induces the redistribution of the microtubule plus-end binding protein EB3 after NMDA receptor activation.

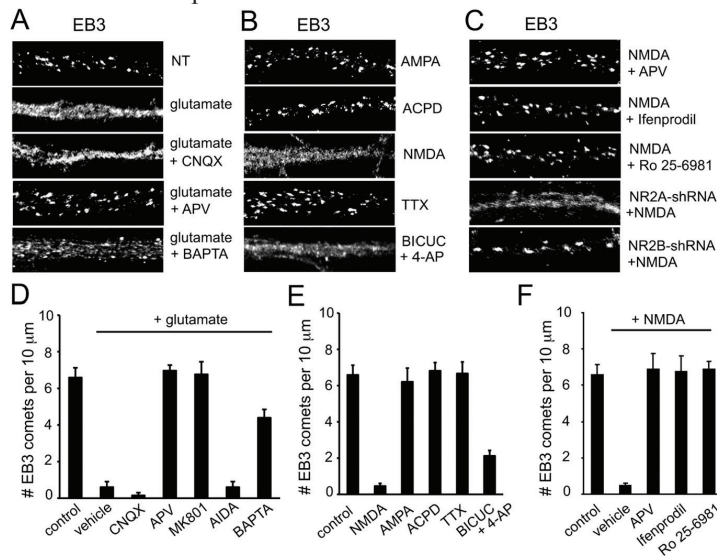


Figure 2. NMDA Stimulation Affects EB3 Distribution in Dendrites

(A) High-magnification images of dendrites of hippocampal neurons (DIV17) untreated (NT) or treated with 50 $\mu\text{M}$  glutamate for 5 min alone or in combination with 10  $\mu\text{M}$  CNQX, 100  $\mu\text{M}$  APV, or 50  $\mu\text{M}$  BAPTA-AM and labeled with rabbit anti-EB3 antibody.

(B) High-magnification images of dendrites of hippocampal neurons (DIV17) treated with 50  $\mu\text{M}$  AMPA, 10  $\mu\text{M}$  ACPD, or 50  $\mu\text{M}$  NMDA for 5 min or 2  $\mu\text{M}$  TTX or 50 $\mu\text{M}$  bicuculline/2.5 mM 4-AP for 24 h and labeled with rabbit anti-EB3 antibody.

(C) High-magnification images of dendrites of hippocampal neurons (DIV17) treated with 50 $\mu\text{M}$  NMDA in combination with 100  $\mu\text{M}$  APV, 5 $\mu\text{M}$  ifenprodil, or 5  $\mu\text{M}$  Ro 25-6981 for 5 min or transfected at DIV13 for 4 d with NR2A-shRNA or NR2B-shRNA constructs and treated with 50  $\mu\text{M}$  NMDA for 5 min and labeled with rabbit anti-EB3 antibody.

(D–F) Quantification of the number of EB3 comets per 10 $\mu\text{m}$  dendrite for hippocampal neurons stimulated as indicated. Histograms show mean  $\pm$  SEM.

Calcium influx into the postsynapse is considered a critical event in NMDA-dependent signaling in the hippocampus (Collingridge et al., 2004; Lau and Zukin, 2007). Indeed, the EB3 redistribution was dependent on calcium levels, as addition of the intracellular calcium chelator BAPTA-AM blocked the NMDA effect (Figure 2 A, D). To test whether EB3 redistributes in response to other NMDA/calcium-dependent signaling pathways, we used chemical LTP stimulation (glycine/KCl) (Lu et al., 2001; Park et al., 2004) and network disinhibition protocols (bicuculline/4-AP) (Tapia et al., 1999; Hardingham et al., 2002). Exposure of neurons to glycine/KCl or bicuculline/4-AP for short time periods, 5 or 15 min, respectively, did not cause any obvious changes in the distribution of endogenous EB3 (data not shown). However, after 24 h bicuculline/4-AP treatment, approximately one-half of the neurons showed significant loss of dendritic EB3 comets (Figure 2 B, E), an effect that was blocked by NMDA receptor antagonist APV. These data suggest that, in addition to chemical LTD, prolonged elevations in electrical activity can also affect EB3 localization.

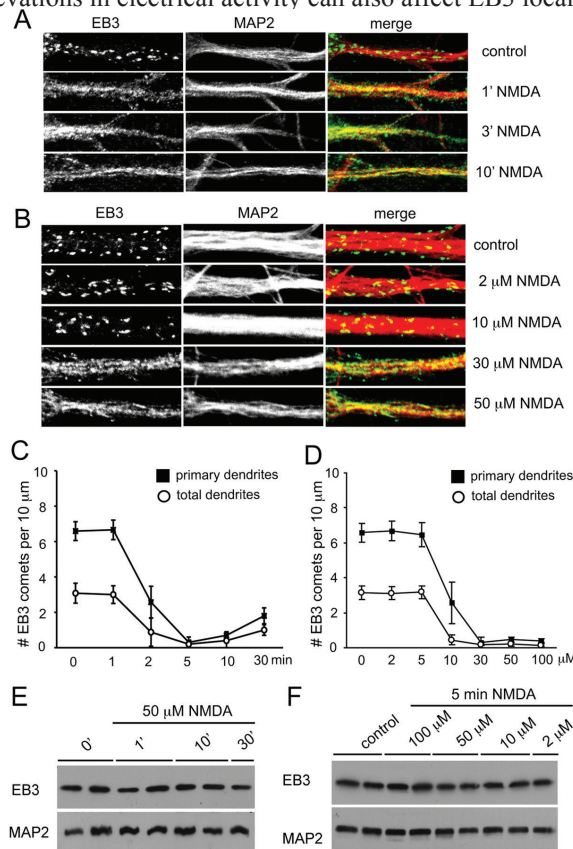


**Figure 3. Time- and Concentration-Dependent Effect of NMDA**

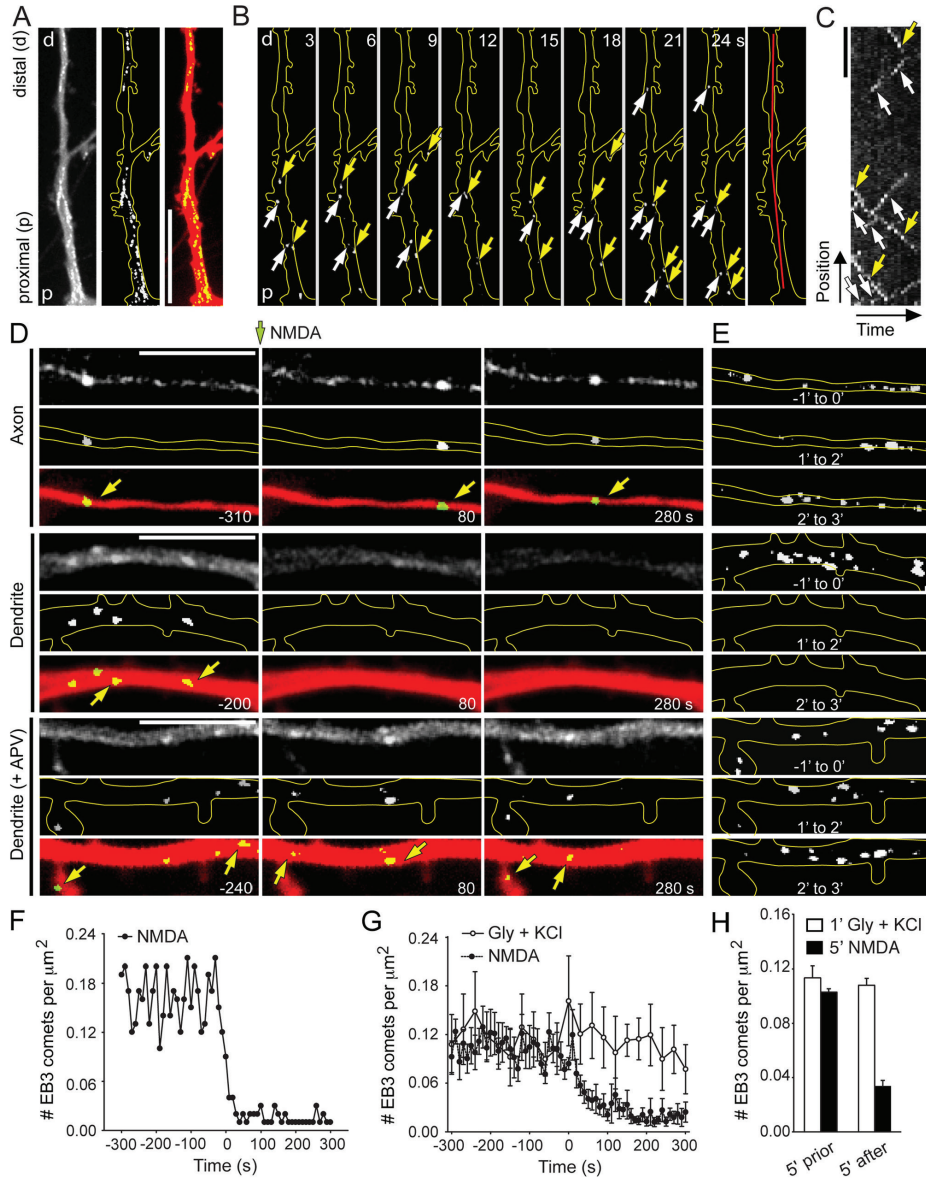
(A, B) High-magnification images of dendrites of hippocampal neurons (DIV17) untreated (control) or stimulated with 50 μM NMDA for various time intervals (A) or with various concentrations of NMDA for 5 min (B) and labeled with rabbit anti-EB3 antibody (green) and mouse anti-MAP2 (red).

(C, D) Quantification of the number of EB3 comets per 10 μm total or primary dendrite (mean ± SEM) of hippocampal neurons stimulated with 50 μM NMDA for various time intervals (C) or with various concentrations of NMDA for 5 min (D).

(E, F) Western blot analysis of extracts of hippocampal neurons either untreated or stimulated with 50 μM NMDA for various time intervals (E) or with various concentrations of NMDA for 5 min (F). Blots are probed for the indicated proteins. NMDA treatment did not affect total EB3 protein levels.

## Chapter 3

In mature hippocampal neuron cultures, calcium-dependent signalling through NMDA receptors mainly occurs through either NR2A- or NR2B-containing receptors (Cull-Candy et al., 2001; Lau and Zukin, 2007). RNA interference experiments using DNA (pSuper)-based constructs that reduce the expression of endogenous NR2A and/or NR2B (Kim et al., 2005) showed that knockdown of NR2B rather than NR2A blocked the glutamate-dependent EB3 redistribution (Figure 2C). Consistently, no effect on EB3 was found when selective NR2B-containing NMDA receptor blockers ifenprodil and Ro 25-6981 were used during the stimulation (Figure 2C,F). Together, these data demonstrate that NMDA stimulates EB3 translocation via calcium influx through NR2B-containing NMDA receptors.



### NMDA receptor activation attenuates microtubule growth

To investigate EB3 redistribution dynamics, we performed time-lapse imaging of GFP-tagged EB3, expressed using a SFV-based vector, in live hippocampal neurons. In dendrites, exogenous EB3-GFP labeled growing microtubule plus-ends and both retrograde and anterograde displacements of EB3-GFP comets were observed (Figure 4A–C). In addition, diffuse EB3-GFP signals with lower intensity were observed throughout the dendritic shaft. Although EB3-GFP comets were very dynamic, their overall distribution in unstimulated neurons was constant over time (Figure 4A, B), as previously published (Stepanova et al., 2003; Jaworski et al., 2009). We observed on average  $1.02 \pm 0.03$  comets per  $10 \mu\text{m}^2$ , which moved at an average growth velocity of  $0.12 \pm 0.03 \mu\text{m/s}$ . Consistent with the immunohistochemical data, NMDA stimulation induced a strong and rapid decrease in the number of EB3-GFP comets in dendrites, whereas in axons the number of EB3-GFP comets was unchanged (data not shown). This effect occurred within 1–2 min after NMDA stimulation and persisted after the washout of the drug (Figure 4D–F). In contrast, application of glycine/KCl for 1 min to induce chemical LTP (Lu et al., 2001; Park et al., 2004) had no significant effect on EB3 comet dynamics (Figure 4G,H).

Previous work has demonstrated that inhibition of microtubule dynamics redistributes the microtubule-binding protein EB3 from the growing microtubule plus-ends and decreases the number of EB3 comets in both fibroblasts and neuronal cells (Mimori-Kiyosue et al., 2000; Jaworski et al., 2009). To test whether the observed EB3 redistribution on NMDA receptor activation reflected a change in microtubule growth in dendrites, we expressed mCherry- $\alpha$ -tubulin in neurons and directly analyzed microtubule dynamics by using TIRF microscopy. In control neurons, or neurons imaged before addition of NMDA, individual microtubules could be observed in dendrites, which alternated between periods of growth and shrinkage. NMDA receptor activation dramatically suppressed microtubule growth, resulting in either the shrinkage or stalling of microtubule ends (Figure 5A–E).

#### ◀ Figure 4. NMDA Receptor Activation Suppresses EB3 Plus-End Tracking

(A) Dendritic region of a hippocampal neuron expressing EB3-GFP, shown as maximum intensity projection of a low-pass filtered sequence of 21 frames acquired using spinning disk confocal microscopy (left). The middle image shows the maximum projection with the average projection subtracted. The right image shows overlay of middle image and average projection. Scale bar,  $10 \mu\text{m}$ . “p” and “d” mark proximal and distal ends, respectively.

(B) Stills from the time-lapse recording corresponding with A. The white and yellow arrows indicate EB3 comets moving toward the distal or proximal end of the dendrite, respectively. The time-lapse recording was low-pass filtered and individual frames were average subtracted. The final image indicates region used for kymography in C.

(C) Kymograph corresponding to the recording shown in B. The white and yellow arrows indicate EB3 comets moving toward the distal or proximal end of the dendrite, respectively. Scale bar,  $5 \mu\text{m}$ . Total time, 1 min.

(D) Spinning disk confocal images of axon and dendritic segments of hippocampal neurons treated with  $50 \mu\text{M}$  NMDA for 5 min (axon and dendrite) or  $50 \mu\text{M}$  NMDA for 5 min in the presence of  $200 \mu\text{M}$  APV (dendrite plus APV). At each time point, the top, middle, and bottom panels show low-pass-filtered image, low-pass-filtered data with average subtracted, and merge of middle panel (green) and average image (red), respectively. Scale bar,  $5 \mu\text{m}$ . Also see videos 1 and 2 (see Notes).

(E) Maximum projection of time-lapse-filtered stacks shown in D for the indicated time intervals.

(F) Time trace of the number of EB3 comets per square micrometer from a single time-lapse recording. NMDA ( $50 \mu\text{M}$ ) is added at 0 s.

(G) Average time traces of the number of EB3 comets per square micrometer before and after application (at 0 s) of either  $200 \mu\text{M}$  glycine or  $50 \text{ mM}$  KCl for 1 min (open circles;  $N = 4$  neurons) or  $50 \mu\text{M}$  NMDA (closed circles;  $N = 8$  neurons). Error bars denote SEM.

(H) Average number of EB3 comets per square micrometer during the 5 min before and after chemical LTP (glycine plus KCl) or LTD (NMDA). Error bars are SEM.

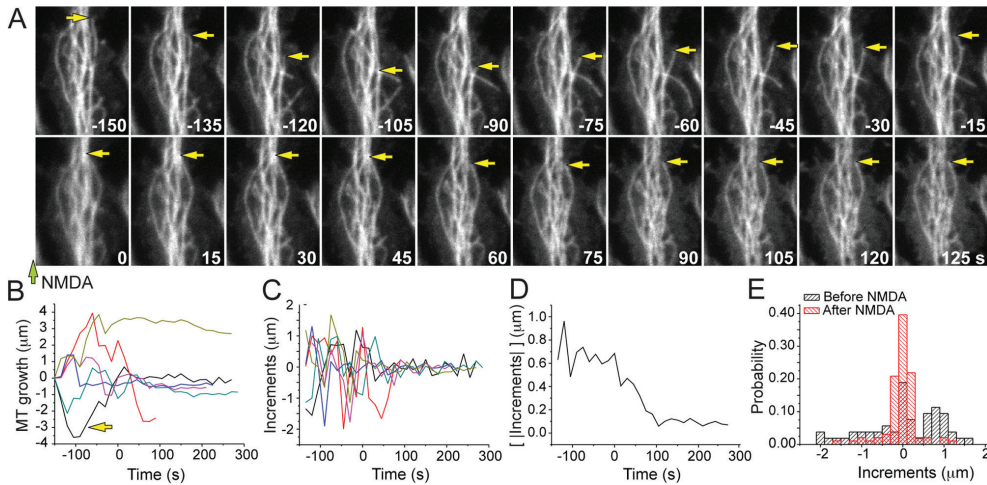


**Figure 5. NMDA Stimulation Suppresses Microtubule Growth**  
 (A) Stills from a TIRFM time-lapse recording of dendritic microtubules labeled using mCherry-tubulin, showing microtubule dynamics before and after addition of 100 $\mu$ M NMDA treatment at  $t = 0$ . The arrows highlight example microtubule whose dynamics are suppressed on NMDA addition. Also see video 3 (see Notes).  
 (B) Plot of microtubule tip position relative to  $t = -150$  s for six traceable microtubules.  
 (C) Plot of consecutive length increments for the traces shown in B. Negative values indicate shrinkage.  
 (D) Average of absolute increment values for the traces shown in B.  
 (E) Histogram of all increments before (black) and after (red) treatment with NMDA.

This rapid NMDA effect was specific for dynamic microtubules, since the overall microtubule organization was unaltered, as indicated by MAP2 and tubulin costaining (Figs. 1 A, B, 3 A, B) (data not shown). Moreover, total EB3 and MAP2 levels were unchanged (Figure 3E), and polymerized microtubule levels measured by tubulin preextraction (He et al., 2002) were not significantly affected (Figure 6 A, B). Similar to NMDA receptor activation, blocking microtubule dynamics directly by the addition of 200 nM nocodazole did not affect microtubule density (Figure 6 B) (Jaworski et al., 2009). These data indicate that chemical LTD suppresses microtubule growth, which results in a loss of EB3 comets and a more static microtubule network in dendrites.

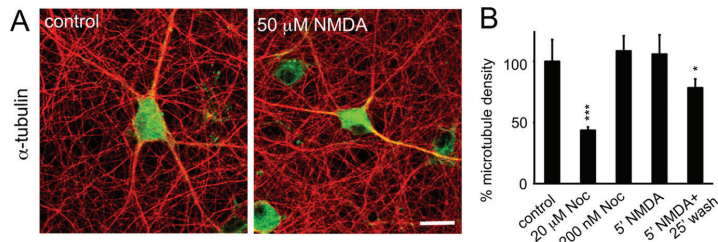


**Figure 6. NMDA-Dependent Effect on Microtubule Density**  
 (A) Measurement of polymerized microtubule levels by tubulin preextraction method. Hippocampal neurons were treated with vehicle (control) or 50 $\mu$ M NMDA, fixed and extracted at the same time to eliminate free tubulin monomers, and double-labelled with rabbit anti-EB3 antibody (green) and mouse anti- $\alpha$ -tubulin antibody (red). Polymerized microtubules are present in dendrites and axons in untreated neurons. Treatment of hippocampal neurons with 50 $\mu$ M NMDA for 5 min has no effect on microtubule density. Scale bar, 20 $\mu$ m.  
 (B) Quantification of relative microtubule density (compared with control neurons) in hippocampal neurons under indicated conditions. Error bars indicate SEM. \* $p < 0.05$ ; \*\*\* $p < 0.0005$ .

**Local NMDA stimulation affects microtubule dynamics**

We next tested whether more local NMDA receptor activation also induced EB3 comet redistribution in dendrites. During time-lapse imaging of EB3-GFP, hippocampal neurons were stimulated locally with a single 20 s puff of 100  $\mu$ M NMDA and 10  $\mu$ M glycine (Rose et al., 2009) delivered from a pipette placed near the dendrite. Consistent with bath application of NMDA, we observed that, within the stimulated portion of the dendrite, EB3-GFP comets disappeared on stimulation (Figure 7 A, B). The EB3 redistribution was confined to the stimulation site along the dendrite and was not observed in other dendrites from the same neurons or neighbouring neurons. The effect was quickly reversible, since 1 min after stimulation the displacement of EB3-GFP is back to control levels (Figure 7C). These results show that local NMDA receptor stimulation can induce a transient effect on microtubule dynamics.

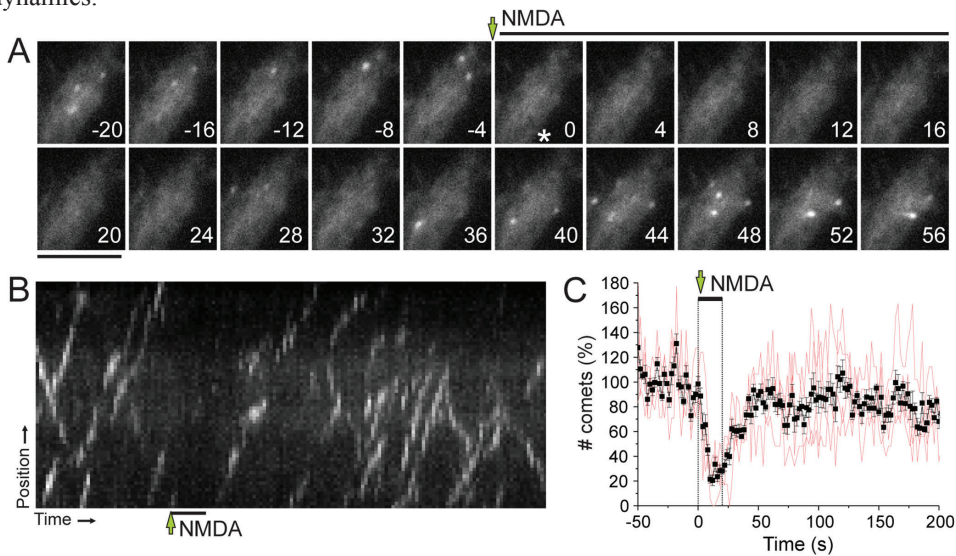


*Figure 7. Local NMDA Stimulation Transiently Affects Microtubule Dynamics*  
 (A) Stills from a TIRFM time-lapse recording of EB3-GFP at growing microtubule plus-ends, showing microtubule dynamics before and after a 20 s puff of 100 $\mu$ M NMDA and 10 $\mu$ M glycine at  $t = 0$ .  
 (B) Kymograph of the recording in A showing EB3-GFP comet dynamics before and after chemical stimulation.  
 (C) Individual (red) and average (black) time traces of the relative number of comets in a 10 $\mu$ m radius circle around the pipette outlet, measured in four different neurons. A 20 s puff of 100 $\mu$ M NMDA and 10 $\mu$ M glycine was applied at  $t = 0$ . Error bar represents SEM.

**EB3 localizes to MAP2-positive microtubule bundles on NMDA receptor activation**

To examine the persistence of EB3 redistribution after NMDA receptor activation, cultures were incubated with 50  $\mu$ M NMDA for 5 min, returned to their original medium, and subsequently fixed at different times points. Consistent with the above results, almost no endogenous EB3 comet-shaped staining was present in dendrites after 5 min of NMDA stimulation. Interestingly, 10 min after the washout, approximately one-third of the neurons instead showed an intense staining of endogenous EB3 along long and thick bundles in the dendritic shaft. In most neurons, the strongest effect was observed 25 min after washout (Figure 8 A–C). Quantification revealed that these EB3 accumulations are on average  $5.8 \pm 0.7 \mu$ m in length (EB3 comets in control cells are  $0.81 \pm 0.4 \mu$ m), but several longer stretches were found, extending for 20–30  $\mu$ m. NMDA receptors antagonists APV and MK-801 block this EB3 accumulation, as do exposure to BAPTA-AM and knockdown of NR2B (data not

shown). Consistent with these immunohistochemical data, live-cell imaging of EB3-GFP also revealed the gradual recruitment to these filamentous structures starting 10 min after NMDA treatment (Figure 8 D, E). These results indicate a second, more prolonged NMDA receptor-dependent effect on EB3 and the microtubule cytoskeleton.

Immunofluorescent analysis revealed that EB3 was not localized to the actin bundles that are often found in the dendritic shaft after glutamate treatment (Hering and Sheng, 2003) but was instead colocalized with a subset of microtubule structures, especially MAP2-positive microtubule bundles (Figure 8G). EB3 did not show a preference for other microtubule subtypes, such as  $\alpha$ -,  $\beta$ III-, and acetylated microtubules (data not shown). Moreover, in axons, the EB3 comet-like staining was still unaffected. No difference in total EB3 protein levels was found by Western blot analysis 25 min after washout (Figure 8 F). These results demonstrate that NMDA receptor activation affects EB3 localization in two phases; a rapid phase (>1 min), during which EB3 comets are lost, and a slow phase (>10 min), during which EB3 emerges along MAP2 microtubule bundles.

Glutamate stimulation has been shown to decrease MAP2 phosphorylation (Halpain and Greengard, 1990; Montoro et al., 1993; Quinlan and Halpain, 1996). Within 15 min after NMDA receptor activation, a 95% decrease in MAP2 phosphorylation was observed (Quinlan and Halpain, 1996). Because these MAP2-dephosphorylation events occur at a similar timescale as the EB3 recruitment along MAP2-positive microtubules (Figure 8G), we tested the correlation between the EB3 redistribution and phosphorylation state of MAP2 by using Ser-136 phosphoantibodies (AP-18) (Berling et al., 1994; Kalcheva et al., 1994). Indeed, NMDA treatment decreased overall MAP2 phosphorylation (Figure 8 F) and phospho-MAP2-Ser-136 was mostly absent from dendrites with intense filamentous staining of EB3 (Figure 8 H). The positive correlation between MAP2-dephosphorylation on Ser-136 and EB3 accumulation was maximal at 25 min after NMDA treatment (Figure 8 H). Together with the live-imaging data, these results suggest that NMDA-mediated dephosphorylation of MAP2 gradually recruit EB3 along dendritic microtubules.

**Figure 8. NMDA Induces EB3 Localization Along MAP2 Microtubules** ▶

(A) High-magnification images of dendrites of hippocampal neurons (DIV17) untreated (control) or treated with 50  $\mu$ M NMDA for 5 min with or without 25 min washout and double-labeled with rabbit anti-EB3 antibody (green) and mouse anti-MAP2 antibody (red). Only the merge is shown in color.

(B) Quantification of the number of EB3 comets per 10  $\mu$ m total or primary dendrites (mean  $\pm$  SEM) of hippocampal neurons stimulated as indicated in A.

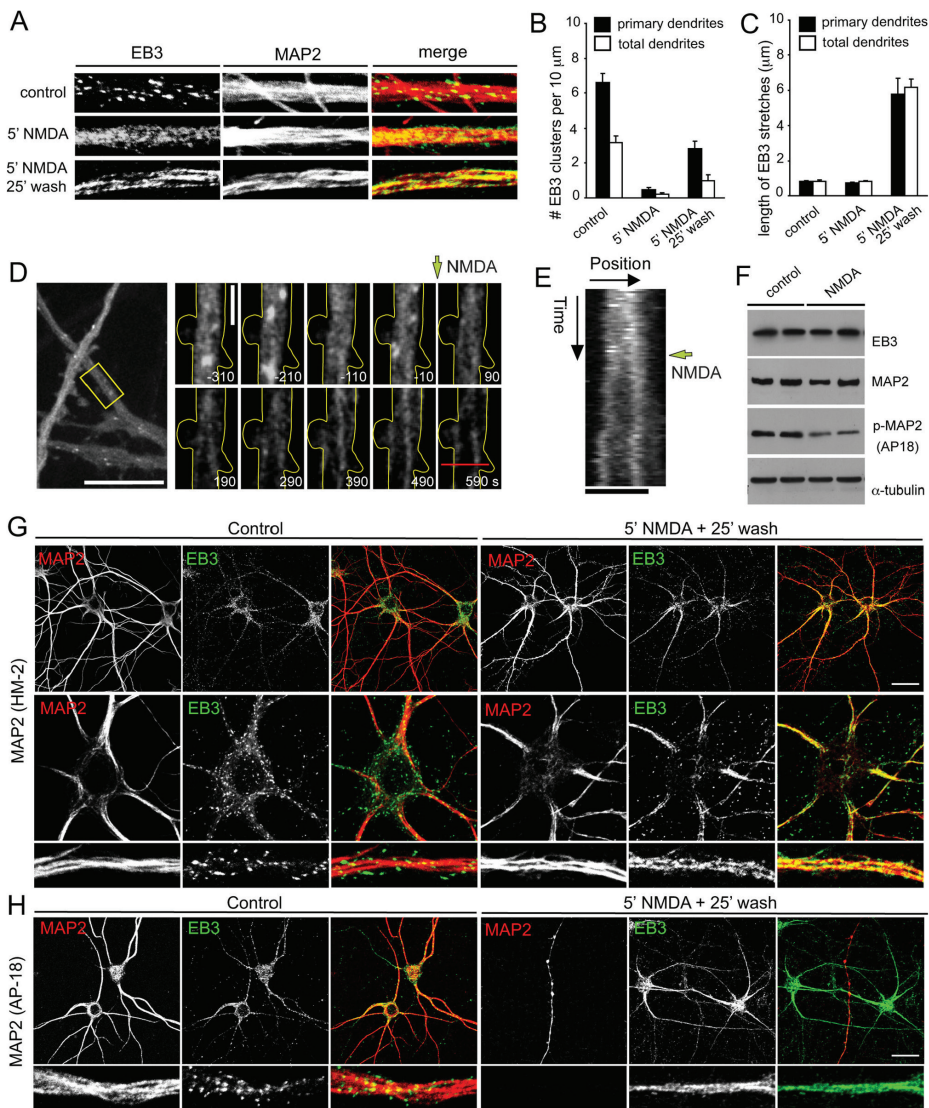
(C) Quantification of the length of the EB3 stretches (in micrometers) in total or primary dendrites (mean  $\pm$  SEM) of hippocampal neurons stimulated as indicated in A.

(D) Low-pass-filtered frame of a time-lapse recording of hippocampal neurons expressing EB3-GFP acquired with a spinning disk confocal microscope. The yellow box marks region used for zoomed still. Before addition of NMDA (marked by green arrow), EB3 comets are visible, whereas several minutes after NMDA treatment EB3 stretches appear. Scale bars: first image, 10  $\mu$ m; zooms, 2  $\mu$ m. Also see video 4 (see Notes).

(E) Kymograph of the red region indicated in D. Stable, bright EB3-positive bundles appear after NMDA application (green arrow). Scale bar, 2  $\mu$ m. Total time, 16:30 (min:sec).

(F) Western blot analysis of extracts of hippocampal neurons either untreated or treated for 5 min with 50  $\mu$ M NMDA. Blots are probed for the indicated proteins. Quantification of the signal intensities (mean  $\pm$  SD) of total MAP2 (HM-2 antibody) and phosphorylated MAP2 bands (AP-2 antibody) revealed that NMDA decreases MAP2 phosphorylation. HM-2 antibody (control, 71.97  $\pm$  5.76; NMDA, 61.20  $\pm$  12.58;  $p$  = 0.424) and AP-2 antibody (control, 61.36  $\pm$  1.44; NMDA, 31.14  $\pm$  3.12;  $p$  = 0.021).

(G,H) Representative images of rat hippocampal neurons (DIV17) untreated (left) or treated with 50  $\mu$ M glutamate for 5 min with 25 min washout (right) and double-labeled with rabbit anti-EB3 antibody (green) and mouse anti-MAP2 antibody (red) (G) or mouse anti-MAP2 Ser-136 phosphoantibody (AP-18; red) (H). Only the merge is shown in color. The cell body and dendrites (bottom panels) are enlarged to show the localization of EB3 before and after NMDA stimulation. Scale bar, 20  $\mu$ m.



### EB3 binds directly to MAP2

To further validate the association between MAP2 and EB3, we performed GST pull-down experiments using GST-EB3 and lysates of HEK293 cells expressing GFP-MAP2c. These experiments revealed a specific interaction between MAP2 and EB3 (Figure 9A–C), as GFP-MAP2c strongly associated with the GST-EB3 but not with GST alone. Mass spectrometry analysis of GST-EB3 pull-down experiments from rat brain extracts confirmed the interaction with endogenous MAP2, along with other known EB binding proteins (Table 1). The interaction between EB3 and MAP2 is direct because a purified MAP2 fraction from bovine brain interacts with GST-EB3 (Figure 9G). Interestingly, from the purified MAP2 fraction, MAP2c was most efficiently pulled down with GST-EB3, rather than the longer MAP2 isoforms (Figure 9G). Furthermore, treating GFP-MAP2c-expressing HEK293 cells with the general ATP-competitive protein kinases inhibitor staurosporine resulted in increased binding

of MAP2 to EB3 in pull-down experiments (Figure 9A–C), consistent with our observation that EB3 recruitment to MAP2 correlates with MAP2 dephosphorylation (Figure 8 F, H ). These data indicate that EB3 has a higher affinity for dephosphorylated MAP2.

**Table 1. Binding partners of GST-EB3 in rat brain extracts identified by mass spectrometry**

Identified protein	Molecular weight (Da)	% Cover	Peptides unique	Peptides total	NCBI GI number
CLIP-115	116,260	53.9	45	155	149063106
MAP2	202,744	38.3	49	177	547890
CLIP-170	148,800	29.5	31	57	8247352
CLASP2	141,463	44.3	44	172	16758540
p140Cap	138,559	3.2	4	4	9507127

The table shows proteins identified with a significant Mascot score in GST-EB3 pull downs from rat brain extracts. The list is corrected for background proteins that were identified in a control GST pull down. For each identified protein, the list is filtered for duplicates and shows only the hits with most identified peptides. Abbreviations used in the table to indicate the identified proteins are as follows: CLIP-115, cytoplasmic linker protein of 115 kDa (also known as CLIP2, CYLN2, WSCR4, WBSCR4); MAP2, microtubule-associated protein 2; CLASP2, cytoplasmic linker-associated protein 2 [also known as multiple asters (Mast)-like homolog 2]; CLIP-170, cytoplasmic linker protein of 170 kDa (also known as CLIP1, Restin); p140Cap, p130Cas-associated protein of 140 kDa [also known as SNIP (SNAP-25-interacting protein)].

GFP-MAP2c expression in heterologous cells causes a rearrangement of microtubules into bundles (Takemura et al., 1992; Kaech et al., 1996; Dehmelt et al., 2006). We next tested whether MAP2 in COS-7 cells is able to redistribute and recruit endogenous EB3 along these microtubule bundles. In control cells, EB3 was present as comet-shaped structures that labeled growing microtubule plus-ends (Figure 9D). However, in GFP-MAP2c-expressing cells, all endogenous EB3 is concentrated along the MAP2-induced microtubule bundles (Figure 9D), confirming the interaction between MAP2c and EB3. Endogenous EB3 was not relocalized to GFP-KIFC2-induced microtubule bundles (data not shown), indicating that EB3 specifically binds to MAP2 microtubules. MAP2 is a multidomain protein, with an N-terminal projection domain (Pro) and a C-terminal microtubule binding (MT) sites (Dehmelt and Halpain, 2005) (Figure 9I ), and by expressing GFP-fused deletion mutants of MAP2 in COS-7 cells, we mapped the EB3 binding region within the C-terminal microtubule-binding domain of MAP2 (Figure 9D). This was confirmed by GST pull-down assays using GST-EB3 and extracts from HEK293 cells expressing GFP-MAP2c-MT (Figure 9E).

**Figure 9. EB3 Binds to MAP2**

(A) Coomassie-stained gel of GST and GST-EB3 fusion proteins.

(B) GST pull-down assays with the GST alone and GST-EB3 fusion proteins and extracts of HEK293 cells overexpressing GFP-MAP2c and GFP-KIFC2. GFP fusions were detected by Western blotting with antibodies against GFP.

(C) GST pull-down assays with the GST alone and GST-EB3 fusion proteins and extracts of HEK293 cells overexpressing GFP-MAP2c and untreated or treated with okadaic acid (O.A.) (0.5 $\mu$ M for 60 min) or staurosporine (stauro) (1.0 $\mu$ M for 60 min). Quantification of the ratio of signal intensities (mean  $\pm$  SD) of GFP-MAP2 input and GST-EB3 pull down revealed that staurosporine treatment increased binding of MAP2. Control ratio is 0.74  $\pm$  0.15, O.A. ratio is 0.65  $\pm$  0.12 ( $p$  = 0.243), and stauro ratio is 1.27  $\pm$  0.18 ( $p$  = 0.016).

(D) COS-7 cells transfected with GFP-MAP2c, GFP-MAP2c-pro, or GFP-MAPc-MT (green) and stained for endogenous EB3 (red). The insets show enlargements of the boxed area. Scale bar, 10 $\mu$ m.

(E) GST pull-down assays with the GST alone and GST-EB3 fusion proteins and extracts of HEK293 cells overexpressing GFP-MAP2c-Pro and GFP-MAP2c-MT. GFP fusions were detected by Western blotting with antibodies against GFP. (Figure legend continues on the next page)

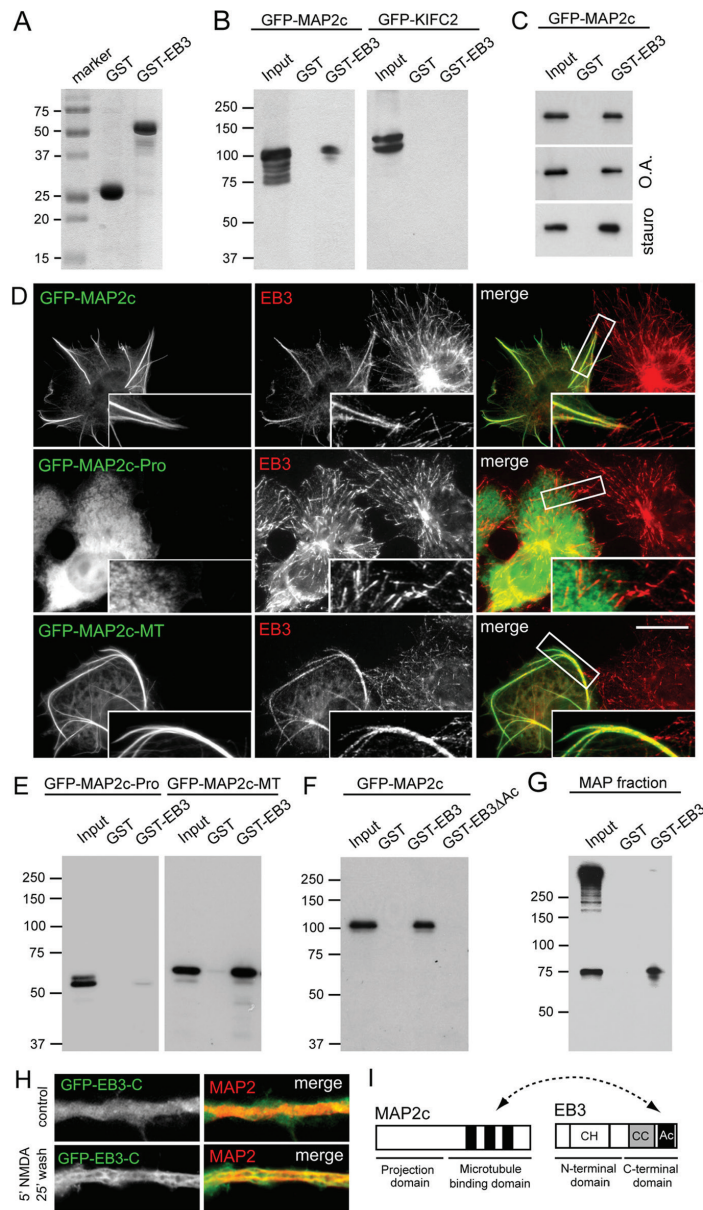


(Figure legend continued from previous page)

(F) GST pull-down assays with the GST alone, GST-EB3, and GST-EB3ΔAc fusion proteins and extracts of HEK293 cells overexpressing GFP-MAP2c. GFP fusions were detected by Western blotting with antibodies against GFP.

(G) GST pull-down assays with the GST alone and GST-EB3 fusion proteins and purified microtubule-associated protein (MAP) fraction from bovine brain.

(H) High-magnification images of dendrites of hippocampal neurons (DIV17) transfected with GFP-EB3-C untreated (control) or stimulated 5' (5 min) with 50μM NMDA followed by 25 min washout and labelled with mouse anti-MAP2 (red).

(I) Schematic representation of MAP2c and EB3 protein structure and deletion mutants used in this study. The arrow indicates the domains important for the interaction between EB3 and MAP2. CH, Calponin homology domain; CC, coiled coil; Ac, acidic tail.

EB proteins contain a N-terminal microtubule-binding calponin homology domain, responsible for the recognition of the polymerizing microtubule ends, and the C-terminal domain consisting of a dimeric coiled coil, which ends in a four-helix bundle and a C-terminal acidic tail, responsible for binding to partners (Akhmanova and Steinmetz, 2008; Hoogenraad and Akhmanova, 2010) (Figure 9I ). Since MAP2c-MT is rich in basic, serine, and proline residues (SxI/LP), we next investigated whether the acidic tail of EB3 is important for interaction between EB3 and MAP2. An EB3 mutant that lacks the acidic tail (GST-EB3dAc) does not bring down GFP-MAP2 in GST-pull down assays indicating that the acidic C-terminal tail of EB3 is important for the interaction with MAP2 (Figure 9F ). We also tested whether the C-terminal tail of EB3 (EB3-C), which lacks the N-terminal microtubule-binding domain, accumulates along MAP2-associated microtubule bundles after NMDA receptor activation. In nonstimulated neurons, GFP-EB3-C is diffusely present through the cytoplasm and does not interact with microtubules, as expected (Komarova et al., 2005), whereas 25 min after NMDA treatment GFP-EB3-C accumulates along MAP2 positive microtubules in the dendritic shaft (Figure 9H ). Thus, although the EB3-C constructs lacks the classic microtubule binding domain at the N terminus, the C-terminal region can associate with microtubules via MAP2. Together, these data demonstrate that the C-terminal domain of EB3 is both necessary and sufficient for MAP2 binding.

Because many other MAPs are present in dendrites of hippocampal neurons, we next used MAP2 knockdown experiment to examine whether MAP2 is necessary for EB3 recruitment after NMDA receptor activation. We found that NMDA treatment did not induce EB3 recruitment in cells transfected with MAP2-shRNA (Figure 10). Together, these results demonstrate MAP2 directly binds to EB3, and this interaction is both necessary and sufficient for the accumulation of EB3 along microtubules after NMDA treatment.

### **EB3 overexpression protects spines against LTD-induced spine shrinkage**

Whereas most dendritic EB3-GFP comets are found in the dendritic shaft, EB3-GFP comets can also enter dendritic spines and induce spine growth (Jaworski et al., 2009) (Figure 11 A–F ). In agreement with our previous findings (Jaworski et al., 2009), we observed an average of  $0.07 \pm 0.03$  EB3 comet entries per spine per frame in control neurons (Figure 11G). Since NMDA receptor activation attenuates microtubule growth, we tested whether microtubule entry in spines is also affected. Indeed, bath application of NMDA has a robust effect on persistent microtubule growth; most dendritic microtubules stopped growing and EB3-GFP entries into spines were almost completely abolished during the 5 min after NMDA addition (Figure 11G–I ).

It has been shown that neurons exposed to a chemical LTD protocol change spine morphology (Halpain et al., 1998; Horne and Dell'Acqua, 2007). Indeed, bath application of 50  $\mu$ M NMDA significantly decreased the number of spines, without affecting protrusion density (Figure 11 J–L). Intriguingly, EB3 knockdown (Figure 11 J–L) has similar effects on spine morphology as NMDA treatment, and we therefore investigated whether these effects are mutually occlusive. However, NMDA receptor activation did not further reduce the number of spines in neurons transfected with shRNA-EB3. To further establish the role of microtubules in LTD-induced spine morphology, we increased the number of microtubules in dendritic spines by overexpression of EB3-GFP (Jaworski et al., 2009). Our previous results have shown that overexpression of EB3-GFP transiently stabilizes microtubules in dendritic spines and increases the number of mushroom spines (Jaworski et al., 2009). In contrast to control neurons, where NMDA receptor activation reduced the number of spines, NMDA treatment hardly affected spine numbers in neurons expressing EB3-GFP (Figure 11 J–L), indicating that targeting of EB3-labeled microtubules to spines blocks LTD-induced

spine remodelling. No protective effect could be seen with expression of other microtubule-binding proteins, such as CLIP-115 and GFP-KIFC2 (data not shown). Together, these experiments demonstrate an intricate involvement of EB3-labeled microtubules in regulating spine morphology during LTD.

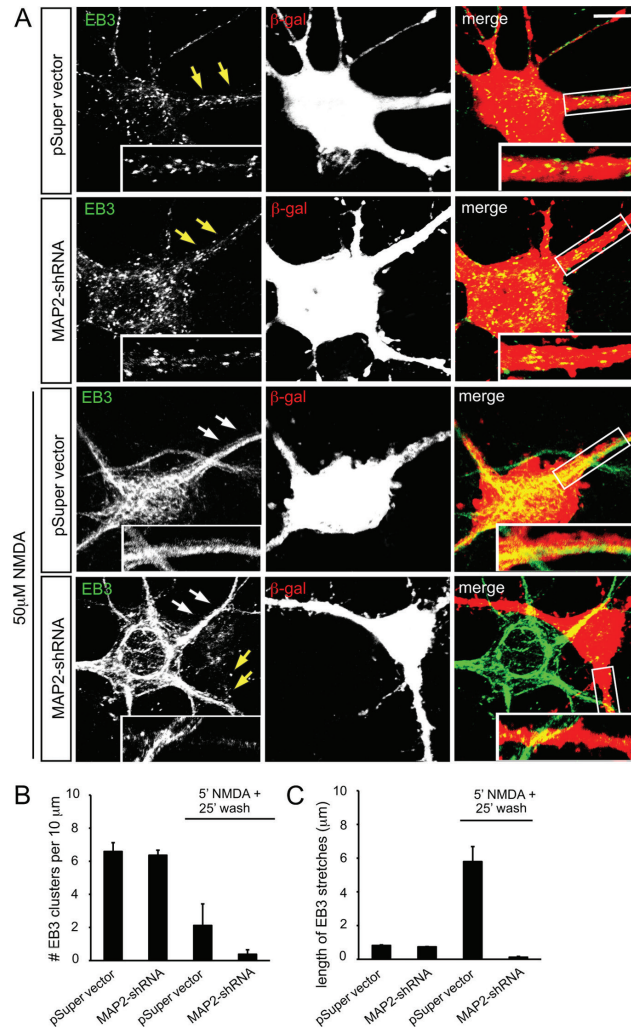


**Figure 10. MAP2 is Required For EB3 Relocalization**

(A) Representative images of hippocampal neurons cotransfected at DIV13 with  $\beta$ -galactosidase and control pSuper vector or pSuper-MAP2-shRNA#2 for 4 d, untreated or stimulated with 50 $\mu$ M NMDA for 5 and 25 min washout, fixed with methanol, and stained with rabbit EB3 antibody (red). Scale bar, 10 $\mu$ m.

(B, C) Quantification of the average number of EB3 dashes per 10 $\mu$ m dendrite (B) and the length of the EB3 stretches (in micrometers) in dendrites (C) in hippocampal neurons under indicated conditions. Graph shows mean  $\pm$  SEM.

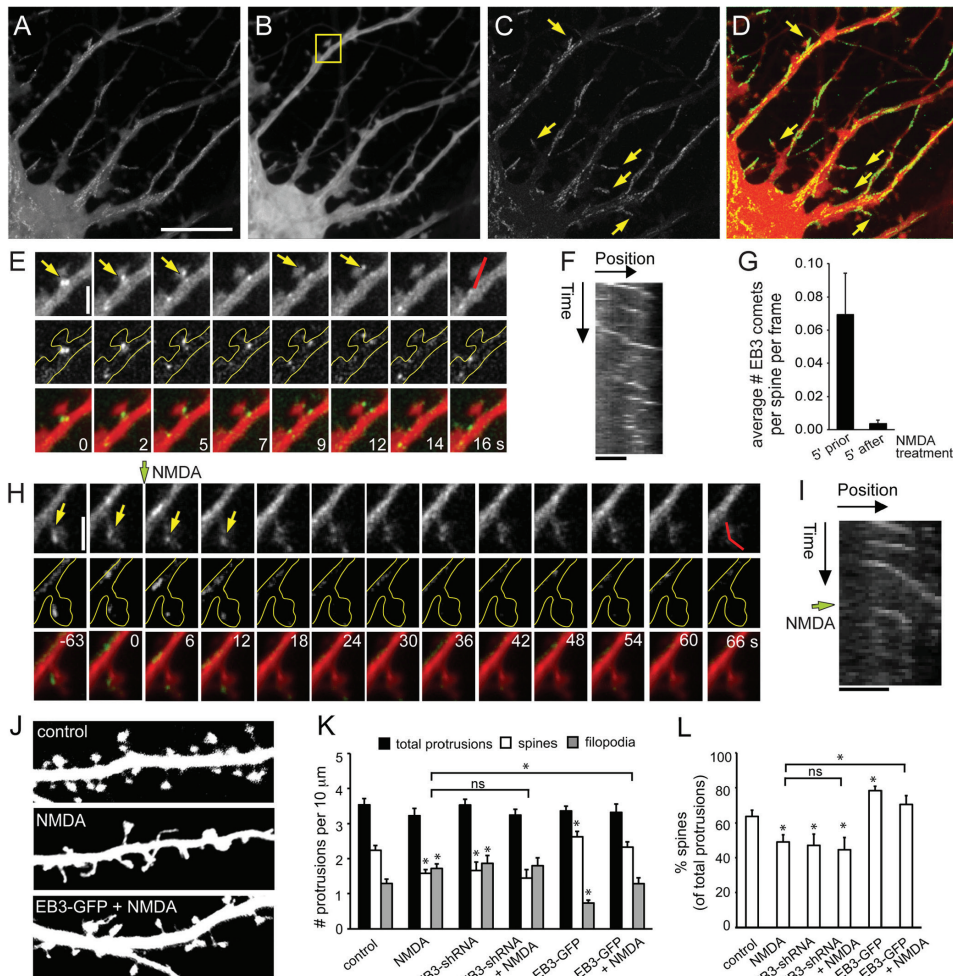


**Figure 11. NMDA Inhibits EB3 Entry in Dendritic Spines**  
 (A–D) Time series of hippocampal neurons expressing EB3-GFP acquired with a spinning disk confocal microscope. A, Maximum projection of the low-pass-filtered time-lapse recording. (B) Average projection of the time-lapse recording used to obtain an approximate background (noncomet) fluorescence image. (C) Maximum projection of the time series obtained by subtracting the average projection (shown in B) from the original, low-pass-filtered, time series. EB3 comet spine entry events are now readily detectable. (D) Merge of B (red) and C (green). Scale bar, 10 $\mu$ m. For more details, see Kapitein et al. (2010). (E) Sequential images of the dendritic region shown in B. The top row shows the original, low-pass-filtered data. The second row displays frames obtained by subtracting the average fluorescence shown in B. The third row shows the merge of average and average-subtracted stills. The yellow arrows indicate comets entering the spine. Scale bar, 2 $\mu$ m. (F) Kymograph over the total time-lapse 3:23 (min:sec) recording for the red line shown in E. Scale bar, 1 $\mu$ m. (G) Average number of EB3 comets per spine per frame during 5 min before and after addition of 50 $\mu$ M NMDA ( $N = 3$  different neurons). Error bars indicate SEM. (H) Sequential images of a EB3-GFP-expressing neuron before and after NMDA treatment. The top row shows frames of the low-pass-filtered time series. The second row displays frames obtained by subtracting the average projection from the low-pass-filtered time series. The third row represents the merge of the average projection and images of the second row. The green arrow indicates the time point at which 50 $\mu$ M NMDA is added ( $t = 0$  s). (Figure legend continues on the next page)

### DISCUSSION

The microtubule cytoskeleton plays a fundamental role in maintaining neuronal morphology and function and also contributes to the organization of dendritic spines and excitatory synapses (Hoogenraad and Bradke, 2009). We have shown here that transient NMDA receptor activation using a chemical LTD protocol suppresses dendritic microtubule dynamics and microtubule entry into dendritic spines. Our data suggest a model in which activity-dependent modulation of the neuronal microtubule cytoskeleton contributes to the local structural plasticity that facilitates neuronal circuitry remodelling.

### NMDA receptor activation suppresses microtubule growth in dendrites

One form of long-lasting synaptic modulation in the hippocampus is LTD, which is triggered by the synaptic activation of NMDA receptors (Bear and Abraham, 1996; Collingridge et al., 2004). Calcium influx through the NMDA receptor activates a number of signalling pathways that have been implicated in the regulation of AMPA receptor trafficking, translation of local mRNAs, and the induction of gene expression (Malinow and Malenka, 2002; Sheng and Kim, 2002; Kennedy et al., 2005; Shepherd and Huganir, 2007; Greer and Greengard, 2008). In addition, NMDA receptor activation also modulates the function of several cytoskeletal proteins and influences neuronal morphology (Halpain and Greengard, 1990; Wong and Ghosh, 2002; Hotulainen and Hoogenraad, 2010). Consistently, our work now demonstrates that transient NMDA receptor activation affects microtubule organization in dendrites in two phases; a fast phase (>1 min) that leads to reduced microtubule growth and the loss of EB3 comets at the microtubule plus-end and a slow phase (>10 min) during which EB3 binds along MAP2-positive microtubule bundles.

Previous work has revealed a close relationship between glutamate receptor activation and the modulation of MAP2 phosphorylation (Halpain and Greengard, 1990; Montoro et al., 1993; Quinlan and Halpain, 1996). NMDA-induced MAP2 dephosphorylation occurs gradually and takes several minutes to complete (Halpain and Greengard, 1990; Quinlan and Halpain, 1996), suggesting that the initial effects on EB3 and microtubule dynamics are independent of MAP2 modifications. Indeed, neurons lacking MAP2 show normal EB3 distributions and NMDA stimulation results in loss of EB3 comets similar to control neurons (Figure 10), indicating that MAP2 is not involved in the initial regulation of EB3 localization and suppression of microtubule growth. Instead, the initial disappearance of EB3 comets from microtubule plus-ends is most likely a consequence of the stalling of microtubule growth.

---

*(Figure legend continued from previous page)*

*(I) Kymograph over the total time-lapse recording 2:09 (min:sec) from the red region in H. After addition of NMDA (green arrow), spine entry of EB3 comets is no longer visible. Spines, 5' (5 min) NMDA and 25' washout.*

*(J) Representative high-magnification images of dendrites of hippocampal neurons cotransfected at DIV13 for 4 d with  $\beta$ -galactosidase (to mark dendrite and spine morphology) and either pSuper control vector; pSuper-EB3-shRNA, or EB3-GFP, and untreated or treated with 50 $\mu$ M NMDA for 5 min, returned to the original medium, and subsequently fixed after 25 min.*

*(K) Quantification of number of protrusions per 10 $\mu$ m dendrites in hippocampal neurons transfected and treated as indicated.*

*(L) Percentage of spines of hippocampal neurons transfected and treated as indicated. Error bars indicate SEM. \* $p < 0.05$ ; ns, not significant.*

How does NMDA receptor activation suppress microtubule growth? One possibility is that the initial phase of suppressed microtubule dynamics is a direct effect of the increased calcium concentration in the neurons. *In vitro* studies on MT assembly using purified tubulin have shown that calcium in the millimolar range directly affects microtubule polymerization (Olmsted and Borisy, 1975; Strömberg and Wallin, 1994). Studies in detergent-extracted cells showed that microtubules polymerize at low calcium concentrations, whereas increasing calcium concentrations to the micromolar range directly induced microtubule disassembly (Fuller and Brinkley, 1976; Schliwa, 1976). These effects have been hypothesized to be mediated by calcium-dependent regulators of microtubule assembly, such as the abundant neuronal protein calmodulin (Marcum et al., 1978; Schliwa et al., 1981; Lee and Wolff, 1982; Deery et al., 1984). A recent report furthermore suggests that posttranslational modifications that are associated with microtubule stability, such as glutamylation, are regulated by synaptic activity (Maas et al., 2009).

In our case, the results argue for a relative specific calcium-dependent mechanism, because redistribution of EB3 depends on calcium-dependent signalling pathways specifically through NR2B-containing NMDA receptors. The precise functional difference between the NR2A- and NR2B-NMDA receptor subtypes is mostly unknown. Differential and even opposing actions on NMDA receptor synaptic targeting (Tovar and Westbrook, 1999), AMPA receptor recycling (Kim et al., 2005), and synaptic plasticity (Liu et al., 2004) have been reported, but consensus is hitherto lacking (Lau and Zukin, 2007). It is, however, recognized that the divergent C-terminal tails of the NR2 subunits associate with distinct sets of signalling proteins and are crucial for activating different downstream signalling pathways (Ryan and Grant, 2009). Therefore, the different effects of NR2 subunits on microtubule dynamics in dendrites probably reflect the different local signaling pathways activated by these subunits (Sheng and Kim, 2002; Vanhoutte and Bading, 2003; Lau and Zukin, 2007). Additional studies are needed to determine which specific NR2B receptor-activated signaling complexes regulate microtubule dynamics in dendrites.

### **Stable MAP2-decorated microtubules trap EB3**

We have also shown that, several minutes after the loss of EB3 comets from microtubule plus-ends induced by NMDA receptor activation, EB3 accumulates along MAP2-positive microtubule bundles. Moreover, MAP2 directly interacts with EB3 and is required for the observed redistribution of EB3 along the dendritic microtubules. Although EB3 and MAP2 are both abundantly present in neuronal dendrites and also both interact with microtubules, they do not display significant colocalization in basal conditions (Figure 1) (Jaworski et al., 2009). Rather, they associate with two separate populations of microtubules. MAP2 localizes to stable microtubules and is believed to also contribute to microtubule stability, through microtubule binding and bundling. MAP2 is a substrate for many protein kinases and phosphatases, and various signaling mechanisms are known to influence MAP2 function (Sánchez et al., 2000; Cassimeris and Spittle, 2001; Dehmelt and Halpain, 2005). EB3, however, localizes to the growing plus-ends of microtubules and typically promotes persistent microtubule growth by suppressing microtubule catastrophes (Komarova et al., 2009). In addition, EB proteins are essential for the microtubule plus-end tracking of many other plus tips (Akhmanova and Steinmetz, 2008) and for the spatial regulation of certain immobile targets, such as p140Cap in spines (Jaworski et al., 2009).

The precise role of the remarkable EB3 redistribution to stable MAP2-decorated microtubules remains unresolved. It is tempting to speculate that recruitment of EB3 to MAP2-decorated microtubules partially depletes the soluble pool of EB3 available to decorate growing MT plus tips. In that case, MAP2 acts as a sink that traps EB3 along the microtubule

lattice and reduces the concentration of free EB3 available to promote growth of dynamic microtubules, required for spine maintenance. Alternatively, EB3 recruitment to MAP2-positive microtubules might serve to recruit some of the numerous EB3-interacting proteins and create specific signaling modules along the microtubule lattice. This would support the existing idea that MAP2-positive microtubules function as docking sites for neuronal signaling enzymes, such as PKA (protein kinase A) and phosphatase PP-1 (Illenberger et al., 1996; Lim and Halpain, 2000; Zhong et al., 2009). Our data also indicate that EB3 has a higher affinity for dephosphorylated MAP2. This is fully in line with the existing data on other known EB partners, such as APC (adenomatous polyposis coli protein), MCAK (mitotic centromere-associated kinesin), and CLASPs (cytoplasmic linker-associated proteins)—their phosphorylation inhibits binding to the C terminus of the EB proteins (Akhmanova and Steinmetz, 2008). Finally, changes in microtubule modifications and microtubule dynamics could also affect intracellular transport. It has been shown that molecular motor proteins are able to select subsets of microtubules and segregate membrane trafficking events between stable and dynamic microtubule populations (Cai et al., 2009). Eliminating dynamic microtubules and/or decorating MAP2 microtubules with EB3 proteins after NMDA receptor activation might therefore directly influence postsynaptic cargo trafficking.

### **The effect of cytoskeletal changes on spine morphology**

It is widely believed that changes in dendritic spine morphology are correlated with the strength of excitatory synaptic connections in the brain (Holtmaat and Svoboda, 2009; Yoshihara et al., 2009; Wang and Zhou, 2010). Such changes in the shape and size of dendritic spines depend on remodeling of its underlying actin cytoskeleton (Hotulainen and Hoogenraad, 2010). Indeed, many reports document the close relationship between NMDA receptor activation and the modulation of actin dynamics and actin-associated proteins in spines (Halpain et al., 1998; Nägerl et al., 2004; Zhou et al., 2004). Here, we show that transient NMDA receptor activation suppresses microtubule dynamics in dendrites and prevents microtubule entry into spines. Several studies have demonstrated that intracellular calcium concentration returns to baseline levels within minutes after washout of 50  $\sim\mu\text{M}$  NMDA (Randall and Thayer, 1992). The EB3 redistribution and sustained suppression of microtubule growth reported here greatly outlast the duration of NMDA receptor activation and subsequent increase in calcium levels as microtubule dynamics in dendritic shafts and spines were suppressed for at least 1 h after NMDA receptor activation (data not shown). This raises the intriguing possibility that dendritic microtubules directly function in long-term plasticity and contribute to the persistence of LTD.

In addition, we have shown that spine entry of EB3 labeled microtubule plus-ends protects spines against chemical LTD-induced spine shrinkage (Figure 11 J–L). This might indicate that initial LTD-inducing stimuli only affect spines devoid of microtubules. Because NMDA receptor activation affects microtubule growth inside the dendritic shaft, it could transiently decrease the microtubule content of neighboring spines and enhance their response to subsequent NMDA receptor stimulation. These mechanisms could contribute to so-called clustered plasticity, which means that similar long-term synaptic changes are more likely to occur at spines that are clustered on one dendritic branch (Govindarajan et al., 2006). Future experiments will be required to determine the *in vivo* importance of persistent suppression of microtubule dynamics and examine the duration of suppression required to influence long-term structural changes in the brain.

### **NOTES**

Supplemental material for this article is available at [www.cellbio.nl](http://www.cellbio.nl). See link to resources for

complementary videos 1–4. This material has not been peer reviewed.

### ACKNOWLEDGEMENTS

This work was supported by the Erasmus Medical Center (Erasmus Medical Center fellowship) and the Netherlands Organization for Scientific Research (NWO-VENI) (L.C.K.). J.J. is supported by a KNAL–Polish Academy of Sciences exchange fellowship and European Community FP7-HealthProt Grant 229676. S.M.G. is supported by Fundação para a Ciência e a Tecnologia fellowship. A.A. is supported by the Netherlands Organization for Scientific Research (NWO-ALW-VICI). C.C.H. is supported by the Netherlands Organization for Scientific Research (NWO-ALW-VICI and NWO-CW), the Netherlands Organization for Health Research and Development (ZonMW-VIDI and ZonMW-TOP), the European Science Foundation (European Young Investigator Award), European Molecular Biology Organization Young Investigators Program, and the Human Frontier Science Program (Human Frontier Science Program Career Development Award). We thank Dr. Roger Tsien for mCherry- $\alpha$ -tubulin, Dr. Morgan Sheng for NR2A/B shRNAs, Dr. Nicole Leclerc for MAP2c constructs, Dr. Lester Binder for monoclonal antibodies AP-14 and AP-18 to MAP2, and Karel Bezstarosti for help with mass spectrometry analyses.

### REFERENCES

- Akhmanova A, Steinmetz MO (2008) Tracking the ends: a dynamic protein network controls the fate of microtubule tips. *Nat Rev Mol Cell Biol* 9:309–322.
- Aoki C, Siekevitz P (1985) Ontogenetic changes in the cyclic adenosine 3',5'-monophosphate-stimulatable phosphorylation of cat visual cortex proteins, particularly of microtubule-associated protein 2 (MAP 2): effects of normal and dark rearing and of the exposure to light. *J Neurosci* 5:2465–2483.
- Banker G, Goslin K, eds (1998) *Culturing nerve cells*. Cambridge, MA: MIT. Bear MF, Abraham WC (1996) Long-term depression in hippocampus. *Annu Rev Neurosci* 19:437–462.
- Beattie EC, Carroll RC, Yu X, Morishita W, Yasuda H, von Zastrow M, Malenka RC (2000) Regulation of AMPA receptor endocytosis by a signaling mechanism shared with LTD. *Nat Neurosci* 3:1291–1300.
- Berling B, Wille H, Röhl B, Mandelkow EM, Garner C, Mandelkow E (1994) Phosphorylation of microtubule-associated proteins MAP2a,b and MAP2c at Ser136 by proline-directed kinases in vivo and in vitro. *Eur J Cell Biol* 64:120–130.
- Bourne JN, Harris KM (2008) Balancing structure and function at hippocampal dendritic spines. *Annu Rev Neurosci* 31:47–67.
- Brummelkamp TR, Bernards R, Agami R (2002) A system for stable expression of short interfering RNAs in mammalian cells. *Science* 296:550–553.
- Cai D, McEwen DP, Martens JR, Meyhofer E, Verhey KJ (2009) Single molecule imaging reveals differences in microtubule track selection between Kinesin motors. *PLoS Biol* 7:e1000216.
- Cassimeris L, Spittle C (2001) Regulation of microtubule-associated proteins. *Int Rev Cytol* 210:163–226.
- Colledge M, Snyder EM, Crozier RA, Soderling JA, Jin Y, Langeberg LK, Lu H, Bear MF, Scott JD (2003) Ubiquitination regulates PSD-95 degradation and AMPA receptor surface expression. *Neuron* 40:595–607.
- Collingridge GL, Isaac JT, Wang YT (2004) Receptor trafficking and synaptic plasticity. *Nat Rev Neurosci* 5:952–962.
- Conde C, Cáceres A (2009) Microtubule assembly, organization and dynamics in axons and dendrites. *Nat Rev Neurosci* 10:319–332.
- Cull-Candy S, Brickley S, Farrant M (2001) NMDA receptor subunits: diversity, development and disease. *Curr Opin Neurobiol* 11:327–335.
- Deery WJ, Means AR, Brinkley BR (1984) Calmodulin-microtubule association in cultured mammalian cells. *J Cell Biol* 98:904–910.
- Dehmelt L, Halpain S (2005) The MAP2/Tau family of microtubule-associated proteins. *Genome Biol* 6:204.
- Dehmelt L, Nalbant P, Steffen W, Halpain S (2006) A microtubule-based, dynein-dependent force induces local cell protrusions: implications for neurite initiation. *Brain Cell Biol* 35:39–56.
- Dingledine R, Borges K, Bowie D, Traynelis SF (1999) The glutamate receptor ion channels. *Pharmacol Rev* 51:7–61.
- Ehlers MD (2000) Reinsertion or degradation of AMPA receptors determined by activity-dependent endocytic

- sorting. *Neuron* 28:511–525.
- Faddis BT, Hasbani MJ, Goldberg MP (1997) Calpain activation contributes to dendritic remodeling after brief excitotoxic injury in vitro. *J Neurosci* 17:951–959.
- Farah CA, Liazoghli D, Perreault S, Desjardins M, Guimont A, Anton A, Lauzon M, Kreibich G, Paiement J, Leclerc N (2005) Interaction of microtubule-associated protein-2 and p63: a new link between microtubules and rough endoplasmic reticulum membranes in neurons. *J Biol Chem* 280:9439–9449.
- Fontaine-Lenoir V, Chambraud B, Fellous A, David S, Duchossoy Y, Baulieu EE, Robel P (2006) Microtubule-associated protein 2 (MAP2) is a neurosteroid receptor. *Proc Natl Acad Sci U S A* 103:4711–4716.
- Fuller GM, Brinkley BR (1976) Structure and control of assembly of cytoplasmic microtubules in normal and transformed cells. *J Supramol Struct* 5:497(349)–514(366).
- Govindarajan A, Kelleher RJ, Tonegawa S (2006) A clustered plasticity model of long-term memory engrams. *Nat Rev Neurosci* 7:575–583.
- Greer PL, Greenberg ME (2008) From synapse to nucleus: calcium-dependent gene transcription in the control of synapse development and function. *Neuron* 59:846–860.
- Gu C, Zhou W, Puthenveedu MA, Xu M, Jan YN, Jan LY (2006) The microtubule plus-end tracking protein EB1 is required for Kv1 voltage-gated K<sup>+</sup> channel axonal targeting. *Neuron* 52:803–816.
- Halpain S, Greengard P (1990) Activation of NMDA receptors induces rapid dephosphorylation of the cytoskeletal protein MAP2. *Neuron* 5:237–246.
- Halpain S, Hipolito A, Saffer L (1998) Regulation of F-actin stability in dendritic spines by glutamate receptors and calcineurin. *J Neurosci* 18:9835–9844.
- Hardingham GE, Fukunaga Y, Bading H (2002) Extrasynaptic NMDARs oppose synaptic NMDARs by triggering CREB shut-off and cell death pathways. *Nat Neurosci* 5:405–414.
- He Y, Yu W, Baas PW (2002) Microtubule reconfiguration during axonal retraction induced by nitric oxide. *J Neurosci* 22:5982–5991.
- Hering H, Sheng M (2003) Activity-dependent redistribution and essential role of cortactin in dendritic spine morphogenesis. *J Neurosci* 23:11759–11769.
- Hollmann M, Heinemann S (1994) Cloned glutamate receptors. *Annu Rev Neurosci* 17:31–108.
- Holtmaat A, Svoboda K (2009) Experience-dependent structural synaptic plasticity in the mammalian brain. *Nat Rev Neurosci* 10:647–658.
- Hoogenraad CC, Akhmanova A (2010) Dendritic spine plasticity: new regulatory roles of dynamic microtubules. *Neuroscientist* 16:650–661.
- Hoogenraad CC, Bradke F (2009) Control of neuronal polarity and plasticity—a renaissance for microtubules? *Trends Cell Biol* 19:669–676.
- Hoogenraad CC, Milstein AD, Ethell IM, Henkemeyer M, Sheng M (2005) GRIP1 controls dendrite morphogenesis by regulating EphB receptor trafficking. *Nat Neurosci* 8:906–915.
- Horne EA, Dell'Acqua ML (2007) Phospholipase C is required for changes in postsynaptic structure and function associated with NMDA receptor-dependent long-term depression. *J Neurosci* 27:3523–3534.
- Hoskison MM, Yanagawa Y, Obata K, Shuttleworth CW (2007) Calcium-dependent NMDA-induced dendritic injury and MAP2 loss in acute hippocampal slices. *Neuroscience* 145:66–79.
- Hotulainen P, Hoogenraad CC (2010) Actin in dendritic spines: connecting dynamics to function. *J Cell Biol* 189:619–629.
- Hu X, Viesselmann C, Nam S, Merriam E, Dent EW (2008) Activity-dependent dynamic microtubule invasion of dendritic spines. *J Neurosci* 28:13094–13105.
- Illenberger S, Drewes G, Trinczek B, Biernat J, Meyer HE, Olmsted JB, Mandelkow EM, Mandelkow E (1996) Phosphorylation of microtubule-associated proteins MAP2 and MAP4 by the protein kinase p110mark. Phosphorylation sites and regulation of microtubule dynamics. *J Biol Chem* 271:10834–10843.
- Jaworski J, Hoogenraad CC, Akhmanova A (2008) Microtubule plus-end tracking proteins in differentiated mammalian cells. *Int J Biochem Cell Biol* 40:619–637.
- Jaworski J, Kapitein LC, Gouveia SM, Dortland BR, Wulf PS, Grigoriev I, Camera P, Spangler SA, Di Stefano P, Demmers J, Krugers H, Defilippi P, Akhmanova A, Hoogenraad CC (2009) Dynamic microtubules regulate dendritic spine morphology and synaptic plasticity. *Neuron* 61:85–100.
- Kaech S, Ludin B, Matus A (1996) Cytoskeletal plasticity in cells expressing neuronal microtubule-associated proteins. *Neuron* 17:1189–1199.
- Kalcheva N, Albala JS, Binder LI, Shafit-Zagardo B (1994) Localization of specific epitopes on human microtubule-associated protein 2. *J Neurochem* 63:2336–2341.
- Kameyama K, Lee HK, Bear MF, Haganir RL (1998) Involvement of a post-synaptic protein kinase A substrate in the expression of homosynaptic long-term depression. *Neuron* 21:1163–1175.
- Kapitein LC, Yau KW, Hoogenraad CC (2010) Microtubule dynamics in dendritic spines. *Methods Cell Biol* 97:111–132.

## Chapter 3

---

- Kennedy MB, Beale HC, Carlisle HJ, Washburn LR (2005) Integration of biochemical signalling in spines. *Nat Rev Neurosci* 6:423–434.
- Kim MJ, Dunah AW, Wang YT, Sheng M (2005) Differential roles of NR2A- and NR2B-containing NMDA receptors in Ras-ERK signaling and AMPA receptor trafficking. *Neuron* 46:745–760.
- Komarova Y, Lansbergen G, Galjart N, Grosveld F, Borisov GG, Akhmanova A (2005) EB1 and EB3 control CLIP dissociation from the ends of growing microtubules. *Mol Biol Cell* 16:5334–5345.
- Komarova Y, De Groot CO, Grigoriev I, Gouveia SM, Munteanu EL, Schober JM, Honnappa S, Buey RM, Hoogenraad CC, Dogterom M, Borisov GG, Steinmetz MO, Akhmanova A (2009) Mammalian end binding proteins control persistent microtubule growth. *J Cell Biol* 184:691–706.
- Krichevsky AM, Kosik KS (2002) RNAi functions in cultured mammalian neurons. *Proc Natl Acad Sci U S A* 99:11926–11929.
- Lau CG, Zukin RS (2007) NMDA receptor trafficking in synaptic plasticity and neuropsychiatric disorders. *Nat Rev Neurosci* 8:413–426.
- Lee HK, Kameyama K, Haganir RL, Bear MF (1998) NMDA induces long-term synaptic depression and dephosphorylation of the GluR1 subunit of AMPA receptors in hippocampus. *Neuron* 21:1151–1162.
- Lee YC, Wolff J (1982) Two opposing effects of calmodulin on microtubule assembly depend on the presence of microtubule-associated proteins. *J Biol Chem* 257:6306–6310.
- Lim RW, Halpain S (2000) Regulated association of microtubule-associated protein 2 (MAP2) with Src and Grb2: evidence for MAP2 as a scaffolding protein. *J Biol Chem* 275:20578–20587.
- Liu L, Wong TP, Pozza MF, Lingenhoehl K, Wang Y, Sheng M, Auberson YP, Wang YT (2004) Role of NMDA receptor subtypes in governing the direction of hippocampal synaptic plasticity. *Science* 304:1021–1024.
- Lu W, Man H, Ju W, Trimble WS, MacDonald JF, Wang YT (2001) Activation of synaptic NMDA receptors induces membrane insertion of new AMPA receptors and LTP in cultured hippocampal neurons. *Neuron* 29:243–254.
- Maas C, Belgardt D, Lee HK, Heisler FF, Lappe-Siefke C, Magiera MM, van Dijk J, Hausrat TJ, Janke C, Kneussel M (2009) Synaptic activation modifies microtubules underlying transport of postsynaptic cargo. *Proc Natl Acad Sci U S A* 106:8731–8736.
- Malinow R, Malenka RC (2002) AMPA receptor trafficking and synaptic plasticity. *Annu Rev Neurosci* 25:103–126.
- Marcum JM, Dedman JR, Brinkley BR, Means AR (1978) Control of microtubule assembly-disassembly by calcium-dependent regulator protein. *Proc Natl Acad Sci U S A* 75:3771–3775.
- Mashanov GI, Molloy JE (2007) Automatic detection of single fluorophores in live cells. *Biophys J* 92:2199–2211.
- Matsuzaki M, Honkura N, Ellis-Davies GC, Kasai H (2004) Structural basis of long-term potentiation in single dendritic spines. *Nature* 429:761–766.
- Mimori-Kiyosue Y, Shiina N, Tsukita S (2000) The dynamic behavior of the APC-binding protein EB1 on the distal ends of microtubules. *Curr Biol* 10:865–868.
- Montoro RJ, Díaz-Nido J, Avila J, López-Barneo J (1993) N-Methyl-D-aspartate stimulates the dephosphorylation of the microtubule-associated protein 2 and potentiates excitatory synaptic pathways in the rat hippocampus. *Neuroscience* 54:859–871.
- Nägerl UV, Eberhorn N, Cambridge SB, Bonhoeffer T (2004) Bidirectional activity-dependent morphological plasticity in hippocampal neurons. *Neuron* 44:759–767.
- Okamoto K, Nagai T, Miyawaki A, Hayashi Y (2004) Rapid and persistent modulation of actin dynamics regulates postsynaptic reorganization underlying bidirectional plasticity. *Nat Neurosci* 7:1104–1112.
- Olmsted JB, Borisov GG (1975) Ionic and nucleotide requirements for microtubule polymerization in vitro. *Biochemistry* 14:2996–3005.
- Park M, Penick EC, Edwards JG, Kauer JA, Ehlers MD (2004) Recycling endosomes supply AMPA receptors for LTP. *Science* 305:1972–1975.
- Park M, Salgado JM, Ostroff L, Helton TD, Robinson CG, Harris KM, Ehlers MD (2006) Plasticity-induced growth of dendritic spines by exocytic trafficking from recycling endosomes. *Neuron* 52:817–830.
- Philpot BD, Lim JH, Halpain S, Brunjes PC (1997) Experience-dependent modifications in MAP2 phosphorylation in rat olfactory bulb. *J Neurosci* 17:9596–9604.
- Quinlan EM, Halpain S (1996) Postsynaptic mechanisms for bidirectional control of MAP2 phosphorylation by glutamate receptors. *Neuron* 16:357–368.
- Randall RD, Thayer SA (1992) Glutamate-induced calcium transient triggers delayed calcium overload and neurotoxicity in rat hippocampal neurons. *J Neurosci* 12:1882–1895.
- Rose J, Jin SX, Craig AM (2009) Heterosynaptic molecular dynamics: locally induced propagating synaptic accumulation of CaM kinase II. *Neuron* 61:351–358.
- Ryan TJ, Grant SG (2009) The origin and evolution of synapses. *Nat Rev Neurosci* 10:701–712.
- Sánchez C, Díaz-Nido J, Avila J (2000) Phosphorylation of microtubule-associated protein 2 (MAP2) and its relevance for the regulation of the neuronal cytoskeleton function. *Prog Neurobiol* 61:133–168.

## NMDA Receptor Activation and Microtubule Dynamics

---

- Schliwa M (1976) The role of divalent cations in the regulation of microtubule assembly. In vivo studies on microtubules of the heliozoan axopodium using the ionophore A23187. *J Cell Biol* 70:527–540.
- Schliwa M, Euteneuer U, Bulinski JC, Izant JG (1981) Calcium lability of cytoplasmic microtubules and its modulation by microtubule-associated proteins. *Proc Natl Acad Sci U S A* 78:1037–1041.
- Shaner NC, Campbell RE, Steinbach PA, Giepmans BN, Palmer AE, Tsien RY (2004) Improved monomeric red, orange and yellow fluorescent proteins derived from *Discosoma* sp. red fluorescent protein. *Nat Biotechnol* 22:1567–1572.
- Sheng M, Kim MJ (2002) Postsynaptic signaling and plasticity mechanisms. *Science* 298:776–780.
- Shepherd JD, Huganir RL (2007) The cell biology of synaptic plasticity: AMPA receptor trafficking. *Annu Rev Cell Dev Biol* 23:613–643.
- Stepanova T, Slemmer J, Hoogenraad CC, Lansbergen G, Dortland B, De Zeeuw CI, Grosveld F, van Cappellen G, Akhmanova A, Galjart N (2003) Visualization of microtubule growth in cultured neurons via the use of EB3-GFP (end-binding protein 3-green fluorescent protein). *J Neurosci* 23:2655–2664.
- Strömberg E, Wallin M (1994) Differences in the effect of Ca<sup>2+</sup> on isolated microtubules from cod and cow brain. *Cell Motil Cytoskeleton* 28:59–68.
- Takemura R, Okabe S, Umeyama T, Kanai Y, Cowan NJ, Hirokawa N (1992) Increased microtubule stability and alpha tubulin acetylation in cells transfected with microtubule-associated proteins MAP1B, MAP2 or tau. *J Cell Sci* 103:953–964.
- Tapia R, Medina-Ceja L, Peña F (1999) On the relationship between extracellular glutamate, hyperexcitation and neurodegeneration, in vivo. *Neurochem Int* 34:23–31.
- Tovar KR, Westbrook GL (1999) The incorporation of NMDA receptors with a distinct subunit composition at nascent hippocampal synapses in vitro. *J Neurosci* 19:4180–4188.
- Vanhoutte P, Bading H (2003) Opposing roles of synaptic and extrasynaptic NMDA receptors in neuronal calcium signalling and BDNF gene regulation. *Curr Opin Neurobiol* 13:366–371.
- Wang XB, Zhou Q (2010) Spine remodeling and synaptic modification. *Mol Neurobiol* 41:29–41.
- Wilm M, Shevchenko A, Houthaeve T, Breit S, Schweigerer L, Fotsis T, Mann M (1996) Femtomole sequencing of proteins from polyacrylamide gels by nano-electrospray mass spectrometry. *Nature* 379:466–469.
- Wong RO, Ghosh A (2002) Activity-dependent regulation of dendritic growth and patterning. *Nat Rev Neurosci* 3:803–812.
- Yoshihara Y, De Roo M, Muller D (2009) Dendritic spine formation and stabilization. *Curr Opin Neurobiol* 19:146–153.
- Zhong H, Sia GM, Sato TR, Gray NW, Mao T, Khuchua Z, Huganir RL, Svoboda K (2009) Subcellular dynamics of type II PKA in neurons. *Neuron* 62:363–374.
- Zhou Q, Homma KJ, Poo MM (2004) Shrinkage of dendritic spines associated with long-term depression of hippocampal synapses. *Neuron* 44:749–757.



## Chapter 4

# Microtubule Minus-End Stabilization by Polymerization-Driven CAMSAP Deposition

Kai Jiang,<sup>1</sup> Shasha Hua,<sup>1</sup> Renu Mohan,<sup>1</sup> Ilya Grigoriev,<sup>1</sup> Kah Wai Yau,<sup>1</sup> Qingyang Liu,<sup>1,2</sup> Eugene A. Katrukha,<sup>1</sup> A.F. Maarten Altelaar,<sup>2</sup> Albert J.R. Heck,<sup>2</sup> Casper C. Hoogenraad,<sup>1</sup> and Anna Akhmanova<sup>1</sup>

<sup>1</sup>Cell Biology, Faculty of Science, Utrecht University, 3584 Utrecht, the Netherlands

<sup>2</sup>Biomolecular Mass Spectrometry and Proteomics, Bijvoet Center for Biomolecular Research, Utrecht Institute for Pharmaceutical Sciences and The Netherlands Proteomics Centre, Utrecht University, 3584 Utrecht, the Netherlands

### ABSTRACT

Microtubules are cytoskeletal polymers with two structurally and functionally distinct ends, the plus- and the minus-end. Here, we focus on the mechanisms underlying the regulation of microtubule minus-ends by the CAMSAP/Nezha/Patronin protein family. We show that CAMSAP2 is required for the proper organization and stabilization of interphase microtubules and directional cell migration. By combining live-cell imaging and *in vitro* reconstitution of microtubule assembly from purified components with laser microsurgery, we demonstrate that CAMSAPs regulate microtubule minus-end growth and are specifically deposited on the lattice formed by microtubule minus-end polymerization. This process leads to the formation of CAMSAP-decorated microtubule stretches, which are stabilized from both ends and serve as sites of noncentrosomal microtubule outgrowth. The length of the stretches is regulated by the microtubule-severing protein katanin, which interacts with CAMSAPs. Our data thus indicate that microtubule minus-end assembly drives the stabilization of noncentrosomal microtubules and that katanin regulates this process.

*Dev Cell.* 2014 Feb 10;28(3):295-309

### INTRODUCTION

The microtubule (MT) cytoskeleton is essential for intracellular transport, cell division, and morphogenesis. MTs are asymmetric polymeric tubes built from dimers of  $\alpha$ - and  $\beta$ -tubulin that are arranged in a head-to-tail manner. In solutions of purified tubulin, MTs grow and shrink from their two ends, the rapidly growing plus-end where  $\beta$ -tubulin is exposed and the more slowly growing minus-end where  $\alpha$ -tubulin is exposed (Dammermann et al., 2003; Desai and Mitchison, 1997; Jiang and Akhmanova, 2011). In cells, MT growth occurs at the MT plus-ends, whereas the MT minus-ends are generally believed to be either stabilized or serve as sites of depolymerization (Dammermann et al., 2003; Howard and Hyman, 2003).

The MT plus-end is the major site where MT dynamics is controlled; therefore, it interacts with numerous regulatory factors. A large and diverse group of proteins collectively known as MT plus-end tracking proteins, or +TIPs, decorate growing MT plus-ends (Akhmanova and Steinmetz, 2008; Schuyler and Pellman, 2001). The core components of the +TIP complexes are the members of the End Binding protein (EB) family that recognize the stabilizing MT cap associated with MT polymerization (Maurer et al., 2012; Zanic et al., 2009). Crucial regulators of MT dynamics, such as the MT polymerase XMAP215/ch-TOG or MT depolymerases of the kinesin-13 or kinesin-8 families can target MT plus-ends independently of other +TIPs, but they can also associate with them to form a complex protein interaction network (Akhmanova and Steinmetz, 2008; Galjart, 2010; Howard and Hyman, 2007).

In contrast to the abundance of MT plus-end interacting proteins, only a limited number of factors are known to specifically localize to the MT minus-ends. These factors include the  $\gamma$ -tubulin ring complex, required for MT nucleation, and its interaction partners (Kollman et al., 2011). Many +TIPs, such as EBs, do not distinguish between growing MT plus- and minus-ends and thus accumulate at the polymerizing MT minus-ends *in vitro* (Bieling et al., 2007). Although MT minus-end growth accompanied by EB1 accumulation has been observed in cells (Goodwin and Vale, 2010), it is generally believed that *in vivo*, MT minus-ends usually do not to grow (Dammermann et al., 2003) and that +TIPs are thus confined to the MT plus-ends.

Recently, the members of the calmodulin-regulated spectrin-associated protein (CAMSAP)/Nezha/Patronin family were shown to specifically associate with the MT minus-ends. Three members of this family, CAMSAP1, CAMSAP2, and CAMSAP3/Nezha, exist in mammals (Baines et al., 2009). CAMSAP3/Nezha was initially characterized as a protein tethering MT minus-ends to adherens junctions (Meng et al., 2008). The *Drosophila* homolog of CAMSAP3, ssp4/Patronin, was discovered as a protein the depletion of which induces short spindles in mitosis and MT fragmentation in interphase (Goshima et al., 2007). A subsequent study demonstrated that Patronin stabilizes MT minus-ends against depolymerization by kinesin-13, and it was suggested that Patronin acts as an MT minus-end capping factor (Goodwin and Vale, 2010). Subsequent analysis in mammalian epithelial cells showed that CAMSAP2 and CAMSAP3 colocalize in clusters at the minus-ends of non-centrosomal MTs and cooperate in their organization (Nagae et al., 2013; Tanaka et al., 2012).

In spite of these significant advances, it remained unclear how CAMSAP clusters protecting the MT minus-ends are generated, and whether CAMSAPs cap the MT minus-ends in mammalian cells, as was proposed for Patronin in flies. Here, we have performed a systematic high-resolution analysis of the dynamics of individual free MT minus-ends in epithelial cells and found that they predominantly pause but can also undergo periods of slow growth. The depletion of CAMSAP2 abolished this behavior and strongly promoted MT minus-end shrinkage. Importantly, we found that CAMSAP2 is rapidly recruited to nascent MT minus-ends and decorates them in an MT minus-end growth-dependent manner, forming segments of stabilized MT lattice. These data indicate that CAMSAP2 stabilizes free growing

minus-ends of preexisting MTs.

We next reconstituted this behavior of CAMSAPs *in vitro* by using purified proteins. We used a microscopy-based MT polymerization assay to show that CAMSAP2 and CAMSAP3 are specifically deposited on the growing MT minus-ends and form stable MT stretches that can serve as “seeds” for repeated MT outgrowth. We identified the protein domains of mammalian CAMSAP family members important for the association with polymerizing MT minus-ends and stabilization of the CAMSAP- decorated MT lattices. Furthermore, we found that katanin, an MT-severing and -depolymerizing protein (Roll-Mecak and McNally, 2010; Sharp and Ross, 2012), binds to CAMSAPs and regulates the length of CAMSAP stretches. Functional analysis showed that CAMSAP2 is essential for sustaining non-centrosomal MTs, posttranslational modified stable MTs, cell polarization, and migration. Our data thus demonstrate that MT minus-end growth drives formation of stable noncentrosomal MTs and that katanin serves as one of the regulators of this process.

### RESULTS

#### **CAMSAP2 Forms Stretches at MT Minus-Ends in Interphase Cells**

We have investigated the expression of the three CAMSAP family members in HeLa and RPE cells and found that CAMSAP2 was strongly expressed along with CAMSAP1, whereas CAMSAP3 expression was weak (Figure S1A available online). In interphase cells, CAMSAP2 formed distinct stretches at MT ends (Figure 1A), with an average length of  $1.3 \pm 0.6 \mu\text{m}$  (mean  $\pm$  SD, 1,085 stretches measured in ten HeLa cells). Costaining with MT plus-end marker EB1 confirmed that CAMSAP2 stretches were confined to the MT minus-ends (Figure S1B). A similar localization was observed in other cell lines; in some fibroblast lines such as Chinese hamster ovary (CHO)-K1 and Swiss 3T3, CAMSAP2 labelling at the MT minus-ends appeared dot-like rather than stretch-like (Figure S1C). The stretch-like localization of CAMSAP2 could be recapitulated after expressing low levels of fluorescently tagged CAMSAP2 in different cell types, including MRC5 human lung fibroblasts, which have a very sparse MT system that facilitates MT end visualization (Figure 1B; Movie S1). The average length of GFP-CAMSAP2 stretches was similar to that of the endogenous CAMSAP2,  $1.0 \pm 0.7 \mu\text{m}$  (1,003 stretches measured in 27 cells). CAMSAP2 stretches were mobile and could repeatedly emanate growing MT plus-ends, suggesting that they are stabilized against disassembly not only from the minus-end but also from the plus-end (Figure 1B). A similar phenomenon was previously described for the much shorter CAMSAP2 and CAMSAP3 clusters in Caco2 cells (Tanaka et al., 2012). During mitotic entry, the CAMSAP2 pattern became diffuse: MT-associated stretches disappeared in prophase and reappeared during telophase, when they strongly accumulated at the peripheral ends of the central spindle (Figure S1D). The diffuse localization of CAMSAP2 during cell division correlated with a decreased electrophoretic mobility of CAMSAP2 (Figure S1E), which was likely caused by mitosis-specific protein phosphorylation. CAMSAP1 could not be detected by immunofluorescent staining, but the expression of fluorescently tagged CAMSAP1 showed that it was often concentrated as a small dot at the minus-ends of CAMSAP2 stretches (Figure S1F). We conclude that CAMSAP2 decorates extended segments of MT lattice at the MT minus-ends, whereas CAMSAP1 can concentrate at the outmost MT minus-ends.

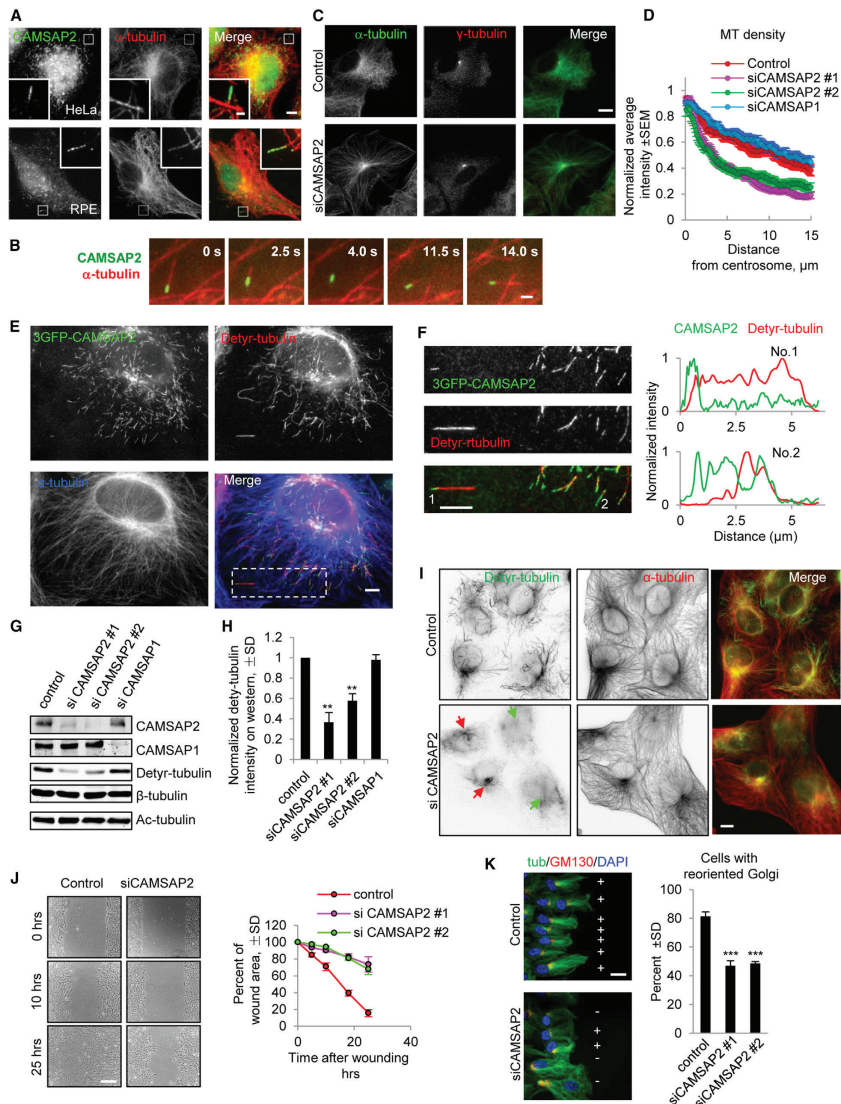


**Figure 1. CAMSAP2 Forms Stretches at MT Ends and Is Required for Interphase MT Organization, Cell Polarization, and Migration**

(A) Immunostaining of CAMSAP2 (green) and  $\alpha$ -tubulin (red) in HeLa and RPE cells. Scale bar represents 5  $\mu$ m. Enlarged portions of the boxed areas are shown in the insets. Scale bar represents 1  $\mu$ m.

(B) Time-lapse images of GFP-CAMSAP2 and mCherry- $\alpha$ -tubulin in MRC5 cells. Scale bar represents 2  $\mu$ m.

(C) Immunostaining of  $\alpha$ -tubulin (green) and  $\gamma$ -tubulin (red) in control and CAMSAP2-depleted RPE cells. Scale bar represents 10  $\mu$ m.

(D) Quantification of MT staining intensity along the cell radius in control and CAMSAP1- and CAMSAP2-depleted cells. Fluorescent staining intensity was measured within a 1- $\mu$ m wide stripe starting from the centrosome and positioned along the long axis of the lamella. Intensities were normalized to the maximal intensity per cell, and the average intensity from 20 cells per condition was plotted. Error bars represent SEM.

(E) Immunostaining of deetyrosinated-tubulin (red) and  $\alpha$ -tubulin (blue) in U2OS cells transfected with 3xGFP-CAMSAP2 (green). Scale bar represents 5  $\mu$ m.

(F) Enlargement of the area boxed in (E) and line scans along the MTs marked 1 and 2, showing partial colocalization of CAMSAP2 and deetyrosinated tubulin. (G) Western blots of extracts of U2OS cells cultured for 72 hr after the transfection with the indicated siRNA. Ac-tubulin, acetylated tubulin. (Figure legend continues on the next page)

### CAMSAP2 Plays a Role in Interphase MT Organization and Directional Cell Migration

Although the depletion of CAMSAP1 had no visible effect on the MT network (data not shown), knockdown of CAMSAP2 in HeLa cells led to altered MT organization and reduction of the density of MTs and EB1-positive MT ends (Figures S2A–S2E) that was similar to previous observations in Caco2 cells (Tanaka et al., 2012). In RPE cells, CAMSAP2 knockdown led to the transformation of the partially noncentrosomal MT array into a completely radial pattern where the majority of the MTs converged on the centrosome (Figure 1C). Analysis of the MT staining intensity along the cell radius showed that in control cells MT density was gradually reduced toward the cell periphery, but in CAMSAP2-depleted cells the density sharply decreased already at a short distance from the centrosome (Figure 1D). Theoretical analysis showed that this alteration in MT staining intensity was fully consistent with the acquisition of a radial MT pattern (see Experimental Procedures; Figure S2F). These data indicate that CAMSAP2 promotes homogeneous distribution of MTs in the cytoplasm.

Next, we tested whether CAMSAP2-dependent minus-end stabilization affects the abundance of long-lived, posttranslationally modified MTs as the MT plus-end stabilizers do. For this, we turned to U2OS cells, because unlike HeLa and RPE cells, they contain a significant number of stable, detyrosinated MTs distributed throughout the cytoplasm (Figure 1E). We found that detyrosinated MTs often terminated with a CAMSAP2 stretch (Figures 1E and 1F). Sometimes, we also observed a part of the CAMSAP2 stretch itself to be detyrosinated, suggesting that it might be long lived (Figure 1F). Both western blotting and immunofluorescent staining showed that CAMSAP2 depletion strongly reduced the abundance of detyrosinated, but not acetylated MTs in U2OS cells (Figure 1G–1I; data not shown), indicating that CAMSAP2 can control the formation of specific posttranslationally modified MT populations.

Next, we investigated the functional consequences of altered MT organization by testing cell migration in monolayer wound-healing assays. We found that the ability of RPE and U2OS cells to close the monolayer wound was significantly reduced, suggesting that CAMSAP2-dependent MT organization promotes directional cell migration (Figures 1J and S2G). CAMSAP2-depleted cells failed to polarize properly: in control cells the Golgi apparatus reoriented toward the wound in ~80% of the cells, but this happened in significantly fewer CAMSAP2-depleted cells (Figure 1K). Both the reduced ability of MTs to “populate” the cytoplasm in CAMSAP2-depleted cells and the alterations in posttranslational modifications could contribute to this defect. The changes in MT organization, cell polarization, and migration were similar for two different CAMSAP2 small interfering RNAs (siRNAs), supporting the specificity of the observed defects. In contrast, cell division in CAMSAP2-

(Figure legend continued from previous page)

(H) Quantification of the intensity of detyrosinated tubulin detected by western blotting. The intensity of detyrosinated tubulin was normalized by the intensity of  $\beta$ -tubulin probed on the same membrane. The plot is based on three independent experiments. Error bars represent SD.  $^{***}p < 0.01$ , *t* test.

(I) Immunostaining of detyrosinated tubulin (green) and  $\alpha$ -tubulin (red) in control and CAMSAP2-depleted U2OS cells. In some cells, detyrosinated tubulin is almost completely lost (green arrows), whereas in other cells some microtubule detyrosination is still observed in the pericentrosomal area (red arrows). Scale bar represents 10  $\mu$ m.

(J) Monolayer wound-healing assays in control and CAMSAP2-depleted RPE cells. Phase-contrast images at the indicated times are shown. Quantification was based on three independent experiments. Error bars represent SD. Scale bar represents 0.2 mm.

(K) Reorientation of the Golgi complex 7 hr after the monolayer wounding in control and CAMSAP2-depleted RPE cells. The images are overlays of the staining for  $\alpha$ -tubulin (green), the Golgi marker GM130 (red), and DNA (DAPI, blue). The Golgi complex was scored as reoriented (+) if it was positioned in the 90° sector facing the wound, and not reoriented (-) if it was localized outside this sector. The value for cells with randomly oriented Golgi is expected to be 25%. Approximately 290–460 cells from three independent experiments were analyzed for each condition. Error bars represent SD. Scale bar represents 20  $\mu$ m.  $^{***}p < 0.001$ , *t* test. See also Figures S1, S2, and Movie S1.

depleted cells proceeded without obvious deviations (data not shown), a finding that is in line with the loss of CAMSAP2 stretches during mitosis. Thus, CAMSAP2 is needed for the organization of interphase noncentrosomal MTs, which are required for cell polarization and migration, in agreement with a previous study (Abal et al., 2002).

### **CAMSAP2 Stabilizes Freshly Generated MT Minus-Ends**

Previous studies have not resolved whether CAMSAP clusters nucleate new MTs or stabilize the minus-ends of the pre-existing MTs (Meng et al., 2008; Tanaka et al., 2012). To address this question, we used a laser microsurgery-based assay (Botvinick et al., 2004; Colombelli et al., 2005; Khodjakov et al., 2004; Walker et al., 1989) in which an individual MT is severed by a focused laser beam. The behavior of the two nascent MT ends was observed using EB3-GFP as a marker; this marker strongly labels growing MT plus- and minus-ends and weakly labels the stable MT lattice (Figure 2A). By using this assay, we found that in RPE cells, newly generated MT plus-ends always depolymerize and can subsequently undergo rescue, whereas the minus-ends predominantly remain stable but can sometimes depolymerize (Figures 2A–2C). We have also observed episodes of MT minus-end growth; they could be distinguished from pausing by the enhanced accumulation of EB3-GFP at the MT minus-end and had an instantaneous rate of  $0.9 \pm 0.8 \mu\text{m}/\text{min}$  (16 MTs in 16 cells) (Figures 2B and S3A; Movie S2). While the depletion of CAMSAP1 had no effect on this MT behavior, the knockdown of CAMSAP2 abolished pausing and growth of MT minus-ends, and the observed minus-end depolymerization excursions became substantially longer, although the MT minus-end depolymerization velocity was not affected (Figures 2B and 2C; Movie S2). These results indicate that CAMSAP2 can stabilize free MT minus-ends that are not associated with MT nucleation sites.

### **CAMSAP1 and CAMSAP2 Associate with Growing MT Minus-Ends in Cells**

We next investigated whether CAMSAPs can bind to freshly severed MT minus-ends. Both CAMSAP1 and CAMSAP2 were indeed promptly recruited to the MT minus-ends after MTs were severed (Figures 3A, 3B, S3B, and S3C; Movie S3). Importantly, the photoablation procedure led to photobleaching of the part of the MT proximal to the photoablation site, and we could clearly observe the addition of fluorescent tubulin to the severed MT minus-end (Figures 3A, 3B, S3B, and S3C). The average minus-end polymerization rate measured in these conditions was somewhat slower than that observed with EB3-GFP,  $0.2 \pm 0.1 \mu\text{m}/\text{min}$  (31 MTs in 24 cells), likely because the accumulation of EB3 allows easier distinction between periods of growth and pausing. MT minus-end growth was accompanied by the elongation of the CAMSAP2 stretches (Figures 3A and 3B).

The ability of CAMSAP2 to decorate growing MT minus-ends could be selective for the ends generated by photoablation. To test whether this is the case, we photobleached intact CAMSAP2-decorated MT minus-end stretches and examined their recovery. Although only little recovery was observed along the length of the stretch, the appearance of a strong CAMSAP2 signal was often visible at the outmost tip of the MT minus-end (8 of 27 MTs in 23 cells; Figures 3C–3E). The appearance of CAMSAP2 signal correlated with the MT polymerization observed in the tubulin channel, whereas no signal recovery was observed at the plus-end side at the CAMSAP2 stretch (Figures 3C, 3D, S3D, and S3E), indicating that within the stretch CAMSAP2 is stably bound to the MT.

To gain further insight into the mechanism of formation of CAMSAP2 stretches, we treated cells with the MT-depolymerizing drug nocodazole and performed washout experiments. CAMSAP2 stretches were completely lost when MTs were depolymerized (Figures 3F and S3F). By using live-cell imaging, we observed that small dots of GFP-CAMSAP2 were

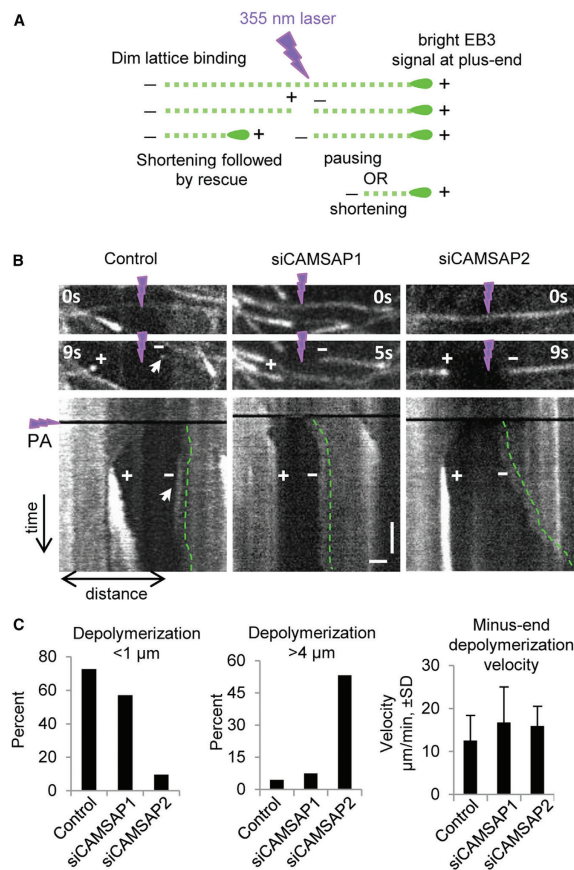


Figure 2. CAMSAP2 Protects MT Minus- Ends from Depolymerization

(A) Scheme of MT photoablation on a spinning disk microscope using EB3-GFP-expressing stable RPE cell line. MTs labeled by EB3-GFP were severed by the 355 nm pulsed laser: + and - indicate the MT plus- and minus-ends, respectively.

(B) Representative images of MTs before and after photoablation (PA, indicated by purple lightning bolts), and kymographs illustrating MT end behavior. MT minus-end polymerization manifested by the accumulation of EB3 is indicated by the white arrow. Green dashed lines trace the position of the MT minus-end in the kymograph. Scale bars, 1  $\mu\text{m}$  (horizontal), 5 s (vertical).

(C) Percentage of MT minus-end depolymerization events shorter than 1  $\mu\text{m}$  or longer than 4  $\mu\text{m}$  and quantification of the minus-end depolymerization velocities. Approximately 120–300 events in at least three experiments were analyzed for each condition. Error bars represent SD.

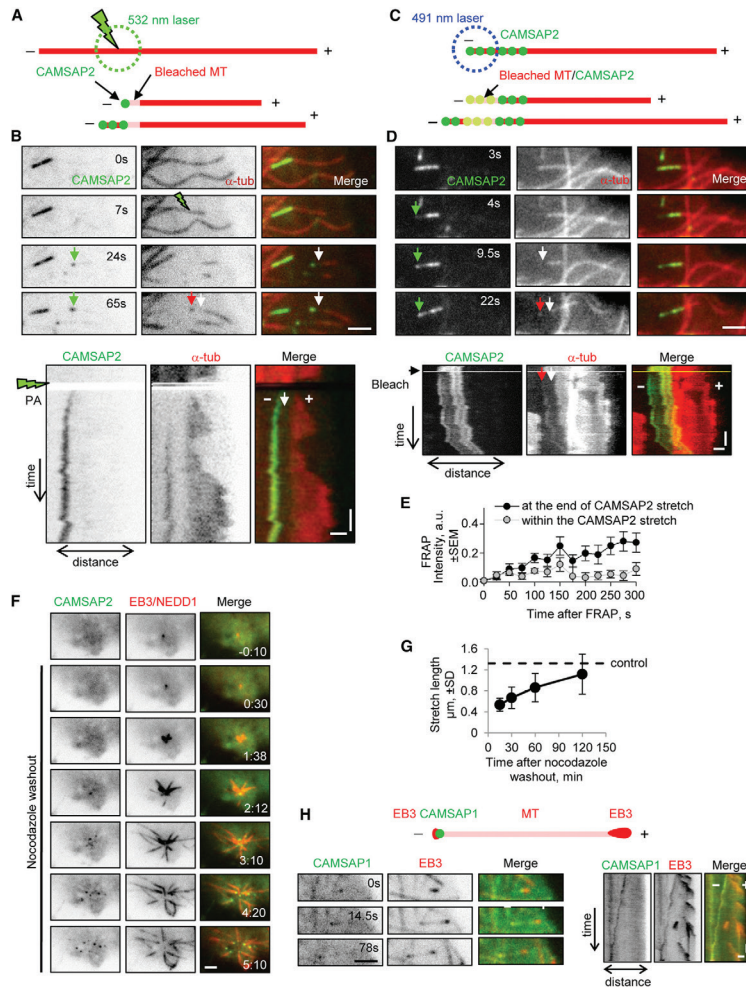
See also Movie S2.

recruited to the minus-ends of MTs released from centrosome within a few minutes after nocodazole washout (Figure 3F; Movie S4). This shows that CAMSAP2 is recruited to the free MT minus-ends that are generated by natural processes and not only by photoablation. By using immunofluorescent cell staining, we found that elongated stretches of endogenous CAMSAP2 became visible only 15 min after the drug washout, with the complete recovery taking more than an hour, although the MT network was completely restored within  $\sim 10$  min (Figures 3G and S3F). We conclude that CAMSAP2 foci form on free MT minus-ends and are transformed to extended CAMSAP2 stretches by decoration of MT minus-ends concomitantly with their slow polymerization.

CAMSAP1 also decorated growing MT minus-ends, but its localization was more dynamic: it tracked growing MT minus-ends without being deposited at the MT lattice (Figures 3H and S3G–S3I). When GFP-CAMSAP1 was mildly overexpressed, the average MT minus-end elongation rate after photoablation was higher than in GFP-CAMSAP2-expressing cells,  $0.4 \pm 0.2 \mu\text{m}/\text{min}$  (18 MTs in 15 cells), suggesting that CAMSAP proteins can regulate MT minus-end growth. Long processive events of MT minus-end growth were more frequent in the presence of CAMSAP1, and colocalization of CAMSAP1 and EB3, a marker of polymerizing MT ends, could be clearly seen (Figure 3H;MovieS5). Taken together, our data show that both CAMSAP1 and CAMSAP2 associate with growing MT minus-ends. However, CAMSAP1 does not remain bound to the MT lattice and thus behaves as a MT minus-end tracking protein, but CAMSAP2 forms stably decorated MT segments.

### CAMSAP Proteins Associate with Growing MT Minus- Ends In Vitro and Regulate Their Dynamics

To gain further insight into the mechanism of formation of the CAMSAP2-decorated MT stretches, we performed in vitro reconstitution experiments by using full-length CAMSAP proteins purified from HEK293T cells (Figure 4A). Mass spectrometry analysis showed



that these protein preparations contained some usual contaminants such as keratins and heat shock proteins, but no MT-binding factors (Table S1).

Previous studies showed that CAMSAP3 and its *Drosophila* homolog Patronin can specifically bind to the minus-ends of stabilized MTs, but their behavior on dynamic MTs has not been investigated (Goodwin and Vale, 2010; Meng et al., 2008). Here, we performed MT assembly assays in which MTs were grown by using porcine brain tubulin from GMPCPP-stabilized MT seeds attached to a functionalized glass surface and observed by total internal reflection fluorescence (TIRF) microscopy (Bieling et al., 2007; Montenegro Gouveia et al., 2010) (Figures 4B–4D). Purified GFP-CAMSAP1 bound only poorly to MT lattice but could specifically track growing MT minus-ends (Figure S4A–S4C; Movie S6), similarly to its behavior in cells (Figure 3H). CAMSAP2 tracked growing MT minus-ends and was also deposited on the MT lattice. This effect was more obvious at a higher concentration (50 nM) of CAMSAP2 (Figures 4D and 4E; Movie S6). CAMSAP3 strongly decorated MT stretches formed by MT minus-end polymerization even at low concentrations (10 nM) (Figures 4D and 4E; Movie S6). Both CAMSAP2 and CAMSAP3 showed very little binding to the MT seeds or the lattice generated by MT growth from the plus-end (Figures 4D and 4E), indicating that their MT association is strongly coupled to MT minus-end polymerization.

Both CAMSAP2 and CAMSAP3 altered MT minus-end dynamics by reducing MT minus-end growth rate, with CAMSAP3 being more potent (Figure 4F). In the standard conditions used (the assay buffer supplemented with 80 mM KCl and 20 mM tubulin), MT minus-end catastrophes were infrequent. However, in conditions when MT minus-end catastrophes were induced by either adding 20 nM mCherry-EB3 or by increasing ionic strength (110 mM KCl instead of 80 mM KCl added to the assay buffer) and reducing tubulin concentration from 20 to 15 mM, catastrophes were strongly suppressed by CAMSAP2 and especially CAMSAP3 (Figures 4G and 4H). These results demonstrate that CAMSAPs not only bind to MT minus-ends but also regulate their dynamics.

◀ **Figure 3. CAMSAPs Associate with Growing MT Minus-Ends in Cells**

(A) Scheme of photoablation in cells expressing GFP-CAMSAP2 and mCherry- $\alpha$ -tubulin on a TIRF microscope using a 532 nm pulsed laser: + and - indicate the MT plus- and minus-ends, respectively.

(B) Live images and a kymograph of GFP-CAMSAP2 and mCherry- $\alpha$ -tubulin before and after photoablation (PA, green lightning bolt). Arrows indicate the bleached MT lattice at the minus-end after photoablation (white), CAMSAP2 recruited to the nascent minus-end (green), and tubulin at the freshly polymerized minus-end (red). The signal is inverted. Scale bar represents 2  $\mu$ m. Scale bars in kymograph represent 1  $\mu$ m (horizontal), 10 s (vertical).  $\alpha$ -tub,  $\alpha$ -tubulin.

(C) Scheme of the FRAP experiments in cells expressing GFP-CAMSAP2 and mCherry- $\alpha$ -tubulin on a TIRF microscope using a 491 nm laser.

(D) Live images and a kymograph of GFP-CAMSAP2- and mCherry- $\alpha$ -tubulin-expressing cells at indicated time points. Arrows indicate the bleached part of the MT minus-end (white arrow), and CAMSAP2 (green) and tubulin (red) signal appearance at the distal tip of the minus-end. Scale bars are the same as in (B).  $\alpha$ -tub,  $\alpha$ -tubulin.

(E) Quantification of the recovery of CAMSAP2 stretches after FRAP. Fluorescence intensity in arbitrary units is shown, represented as mean  $\pm$  SEM. Fourteen CAMSAP2 stretches in 11 cells were analyzed. Error bars represent SEM.

(F) Live images of 3xGFP-CAMSAP2- and EB3-TagRFP-T-expressing cells at indicated time points after nocodazole washout. The cells were also cotransfected with mCherry-NEDD1 to locate the position of centrosome after drug treatment. Scale bar represents 2  $\mu$ m.

(G) Quantification of CAMSAP2 stretch length during recovery from nocodazole treatment. Even after 2 hr recovery, the average stretch length of CAMSAP2 was still shorter than that of in control ( $\sim$ 1,000 stretches in ten cells). Error bars represent SD.

(H) Scheme, live images, and a kymograph showing that GFP-CAMSAP1 colocalizes with EB3-TagRFP-T at a free MT minus-end in an RPE cell. The polarity of the MT was determined by the difference of the EB3 signal at the two MT ends. In this experiment, neither photoablation nor FRAP was performed. The signal is inverted. Scale bars are the same as in (B).

See also Figure S3 and Movies S3, S4, and S5.

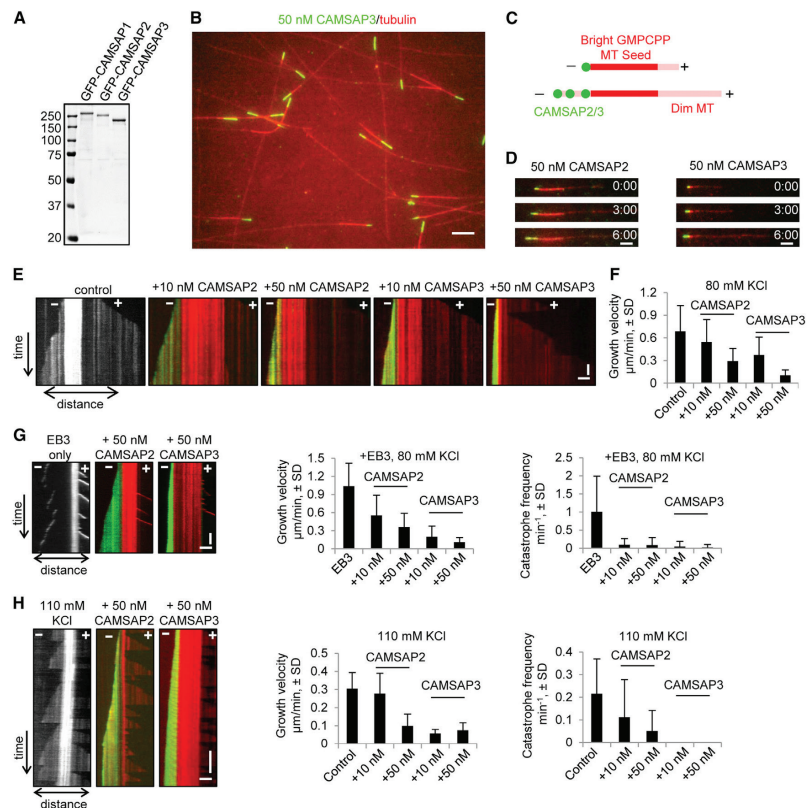


**Figure 4. Camsap2 and Camsap3 Decorate Growing MT Minus-Ends In Vitro and Regulate Their Dynamics**  
 (A) Coomassie Blue staining of a gel with GFP-CAMSAP proteins purified from HEK293T cells. Mass spectrometry analysis of purified proteins is shown in Table S1. (B) TIRF microscopy image showing Camsap3 decorating minus-end of MTs in vitro. The assay was performed with 20 μM unlabeled tubulin and 0.5 μM X-rhodamine-tubulin in MRB80 buffer supplemented with 80 mM KCl. Scale bar represents 5 μm.  
 (C) Scheme of the in vitro MT minus-end decoration assay. Camsap2 and Camsap3 specifically decorate the MT lattice polymerizing from minus-end (-) and not from the plus-end (+).  
 (D) Images of 50 nM GFP-Camsap2 and GFP-Camsap3 and X-rhodamine-labeled dynamic MTs at the indicated time points (minutes). MTs were polymerized in the same conditions as in (B). Scale bar represents 2 μm.  
 (E) Kymographs of MT dynamics in the presence of the indicated concentrations of Camsap2 and Camsap3 in the same conditions as in (B). Scale bars represent 2 μm (horizontal), 1 min (vertical).  
 (F) Quantification of minus-end growth velocities for conditions as in (B); ~40–190 MTs from at least two independent experiments were analyzed for each condition.  
 (G and H) Kymographs illustrating MT dynamics and quantification of MT minus-end growth velocities and catastrophe frequencies in the presence of 20 nM mCherry-EB3, 20 μM unlabeled tubulin in MRB80 buffer supplemented with 80 mM KCl (G) or of 15 μM unlabeled tubulin, 0.5 μM X-rhodamine-labeled tubulin in the assay buffer supplemented with 110 mM KCl (H), and the indicated concentrations of Camsap2 and Camsap3 proteins. Scale bars represent 2 μm (horizontal), 1 min (vertical). Approximately 40–80 MTs from at least two independent experiments were analyzed for each condition.  
 All error bars represent SD. See also Table S1 and Movie S6.

### CAMSAP2 and CAMSAP3 Stabilize MT Lattice against Spontaneous Depolymerization

One distinct feature of Camsap-decorated MT lattices in cells is the ability to block the MT plus-end depolymerization and thus function as “seeds” for MT outgrowth (Figure 1B). To test whether this is an autonomous property of Camsaps, we severed Camsap-decorated MTs to allow regrowth of a new plus-end from a fragment of Camsap-decorated MT (Figures 5A and 5B). These experiments showed that Camsap-decorated MT lattice displayed

altered stability: in control conditions, laser-severed MTs invariably depolymerized from the newly generated plus-end (Figures 5A, 5C, and 5F), as reported previously (Walker et al., 1989), but CAMSAP3-bound MTs displayed no visible depolymerization, and repeated MT outgrowth occurred from the same MT site (Figures 5B, 5E, and 5F; Movie S7). CAMSAP2 was also able to protect the MT plus-ends from persistent depolymerization, although this only occurred in conditions with a lower ionic strength (Figures 5B, 5D, and 5F; Movie S7), suggesting that CAMSAP2 might have a lower affinity for the MT than CAMSAP3. In the *in vitro* severing assays, the MT minus-ends were relatively stable, but they did undergo occasional shortening (Figure 5G). The extent of shortening of the nascent MT minus-end was reduced by CAMSAP2, and the shortening was completely blocked by CAMSAP3 (Figure 5G). These results show that CAMSAP-bound MT lattices are stabilized from both ends, explaining how they can function as “seeds” for MT outgrowth in cells.

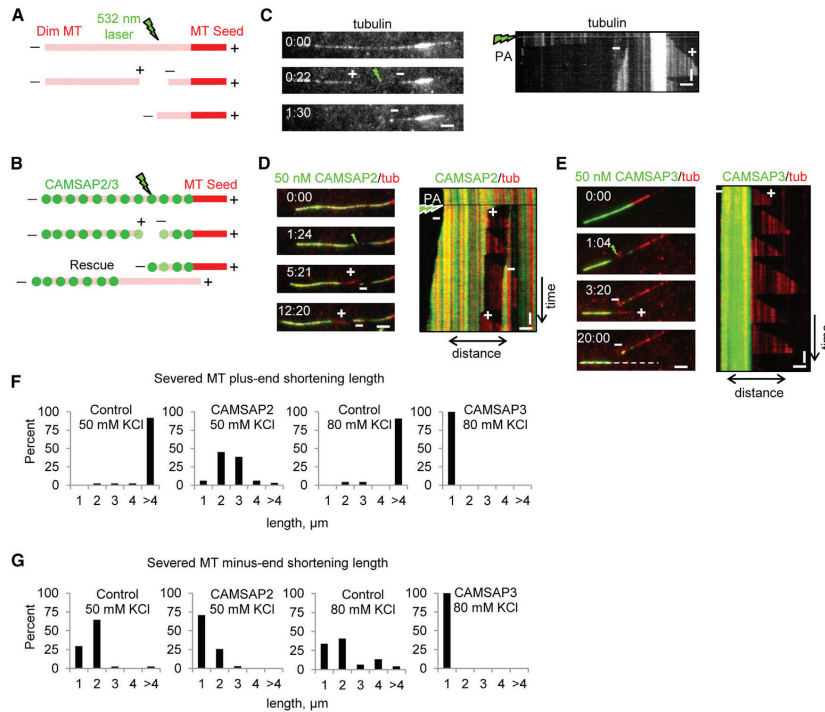


**Figure 5. CAMSAP2 and CAMSAP3 Regulate MT Lattice Stability**

(A and B) Schemes of MT photoablation *in vitro* in the absence (A) and presence (B) of CAMSAP proteins. (C–E) Images and kymographs of control (C), CAMSAP2 (D), or CAMSAP3 (E) decorated MTs after photoablation (PA) (green lightning bolt indicates the photoablation site, white dashed line indicates MT along which the kymograph was made). Time is indicated (minutes). PA was performed in the MRB80 buffer with 20 μM tubulin (tub), 0.5 μM X-rhodamine-tubulin supplemented with 50 or 80 mM KCl for CAMSAP2 or CAMSAP3, respectively. Scale bars represent 2 μm (horizontal), 1 min (vertical). The plus- (+) and minus-end (-) of each dynamic MT can be distinguished by the speed of MT polymerization, which is higher at the plus-end. Note that due to a relatively high catastrophe frequency and the absence of rescues, the length of the MT extension at the plus-end side of the seed is highly variable.

(F and G) Quantification of the MT plus-end (F) and minus-end (G) shortening length after photoablation; the concentration of KCl added to the assay buffer is indicated. Concentration of GFP-CAMSAP2 and GFP-CAMSAP3 was 50 nM. Approximately 20–40 MTs from two independent experiments were analyzed for each condition. Note that MT photoablation also leads to MT photobleaching. Because the regrowth of CAMSAP3-stabilized MTs occurs within the photobleached zone, the exact position of the rescue site is difficult to determine and the actual length of MT shortening is likely to be less than the indicated 1 μm. See also Movie S7.

### **CAMSAP Proteins Use Distinct Domains to Track and Decorate MT Minus-Ends**

To understand the molecular mechanisms underlying the MT minus-end tracking, decoration, and stabilization activities of the three mammalian CAMSAPs, we determined the functional domains that are responsible for these activities. All three CAMSAPs contain an N-terminal calponin homology (CH) domain, three predicted coiled-coil regions (CC1, CC2, and CC3) interspersed by linker sequences, a predicted helical domain, and a conserved C-terminal C terminus common to CAMSAPs (CKK) domain (Baines et al., 2009) (Figure 6A). We generated a collection of GFP-tagged CAMSAP1, CAMSAP2, and CAMSAP3 deletion mutants, purified them from HEK293T cells or *E. coli* (Figures S4D and S4E), and tested their ability to track or decorate the growing MT minus-ends and protect MT lattice against depolymerization after photoablation by using *in vitro* assays.

We found that a C-terminal fragment of CAMSAP1 that included a small part of the linker between CC2 and CC3 as well as the CC3 and CKK domains (amino acids 1227–1613) could robustly track MT minus-ends similarly to the full-length protein (Figures 6A, 6B, and S4C). The complementary deletion mutant (amino acids 1–1226) displayed no MT binding (data not shown). The CAMSAP1 CKK domain alone weakly decorated MT lattice (data not shown). However, in conditions with an increased ionic strength (110 mM KCl instead of 80 mM), MT lattice binding was suppressed and tracking of growing MT minus-ends could be clearly observed when the protein concentration was sufficiently high (~200 nM) (Figure 6B). The CKK domain was also sufficient to bind specifically to one end, presumably the minus-end, of GMPCPP-stabilized seeds (Figure 6C). Similar data were obtained with the CKK domains of CAMSAP2 and CAMSAP3 (Figures 6A–6E). Because the CKK domains used here were purified from bacteria, their behavior is unlikely to be mediated by some copurifying proteins. Our data suggest that the CKK domain represents the primary determinant of MT minus-end recognition by CAMSAPs.

For CAMSAP2, we found that the deletion mutant C1, which contained the complete linker region between CC2 and CC3, and the CC3 and CKK domains, could decorate growing MT minus-ends and stabilize them in MT-severing assays similarly to the full-length CAMSAP2 (Figures 6A, 6D, and 6F). In contrast, a CAMSAP2 mutant lacking the N-terminal portion of the linker region between CC2 and CC3 (CAMSAP2 fragment C2) tracked the growing MT minus-ends similarly to CAMSAP1 but failed to decorate them. This suggests that there is an additional functional domain responsible for the minus-end decoration and stabilization within the CC2-CC3 linker of CAMSAP2. Indeed, we found that the CAMSAP2 mutant encompassing this region, which we named the MT binding domain (MBD, amino acids 922–1,034) could selectively bind the GMPCPP-stabilized MT seeds but not the dynamic parts of the MT (Figures 6A, 6D, and S4F). This peculiar MT binding behavior suggested that MBD of CAMSAP2 can recognize some features of the MT lattice, which might contribute to the specific decoration of growing MT minus-ends by CAMSAP2.

Surprisingly, the deletion mapping of CAMSAP3 showed that the fragment sufficient for MT minus-end decoration and stabilization was substantially shorter than in the case of CAMSAP2: a C-terminal portion of CAMSAP3 containing only the  $\alpha$ -helical region and the CKK domain (CAMSAP3 fragment C3) could readily decorate and stabilize MT minus-ends (Figures 6A, 6E, 6F, and S4G). This protein fragment behaved very similarly when purified either from HEK293T cells or from bacteria, suggesting that its properties are not mediated by an additional protein copurified from mammalian cells (Figures 6E and S4G). Importantly, this fragment was unable to completely block the depolymerization of the severed plus-ends, as was observed for the full-length CAMSAP3 (cf. Figure 5E to Figure 6F). Such a strong MT lattice stabilization occurred only when the MBD of CAMSAP3 was also included (C1 mutant of CAMSAP3; Figures 6A and 6F). By itself, the MBD fragment of CAMSAP3

## Microtubule Minus-End Stabilization by CAMSAP

behaved similarly to the MBD of CAMSAP2: it specifically associated with the GMPCPP-stabilized seeds but not with the freshly polymerized MT lattices (Figures 6E and S4F).

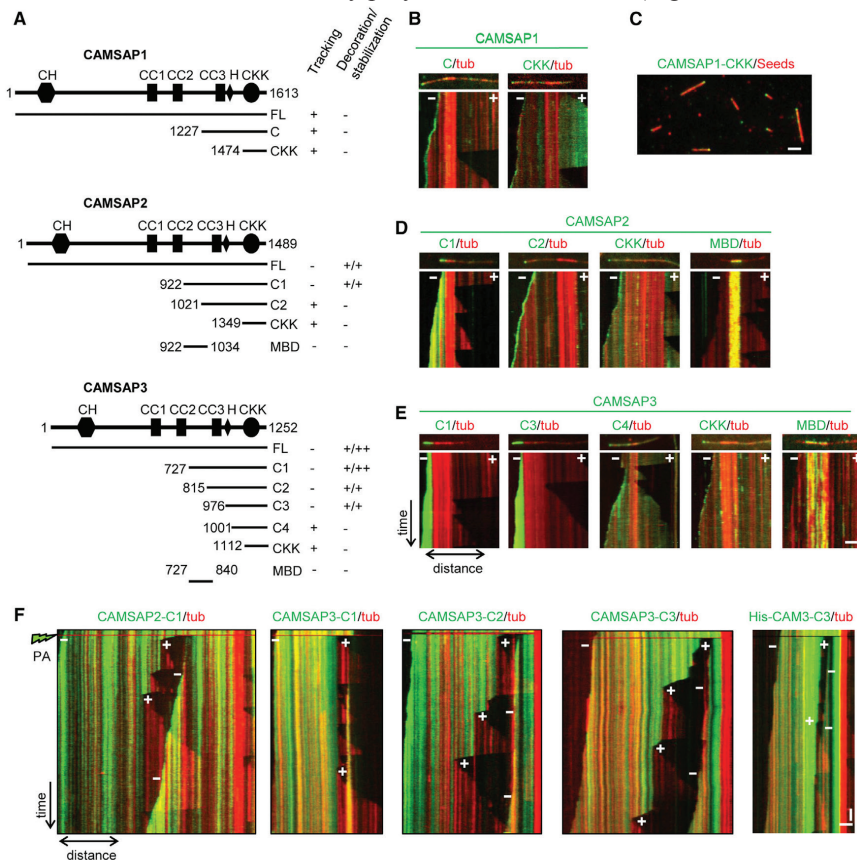


**Figure 6. CAMSAP Proteins Use Different Functional Domains to Track and Decorate MT Minus-Ends**  
**(A)** Schemes of domain organization of CAMSAPs and the deletion mutants used to map the domains responsible for MT minus-end tracking, MT lattice decoration, and stabilization. H,  $\alpha$ -helix.  
**(B)** Images and kymographs illustrating the behavior of CAMSAP1 deletion mutants on rhodamine-labeled dynamic MTs in vitro. For CAMSAP1-C, the assay was performed with 20  $\mu$ M unlabeled tubulin (tub) and 0.5  $\mu$ M rhodamine-tubulin in MRB80 buffer supplemented with 80 mM KCl and 50 nM CAMSAP1-C purified from HEK293T cells. In the case of CKK domain, 110 mM KCl and 200 nM protein purified from *E. coli* was used. Scale bars represent 2  $\mu$ m (horizontal), 1 min (vertical). The polarity of MTs is minus-end (-) on the left side and plus-end (+) on right side.  
**(C)** Image of the in vitro binding assay performed with 200 nM CAMSAP1 CKK and MT seeds in MRB80 buffer supplemented with 110 mM KCl. Scale bar represents 2  $\mu$ m.  
**(D and E)** Images and kymographs illustrating the behavior of different CAMSAP2 **(D)** and CAMSAP3 **(E)** deletion mutants on rhodamine-labeled dynamic MTs in vitro. The assay was performed with 20  $\mu$ M unlabeled tubulin (tub) and 0.5  $\mu$ M rhodamine-tubulin in MRB80 buffer supplemented with 80 mM KCl and 50 nM CAMSAP proteins purified from HEK293T cells except for the CKK domains. In the case of CKK domains, 110 mM KCl and 200 nM protein purified from *E. coli* was used. Scale bars represent 2  $\mu$ m (horizontal), 1 min (vertical). The polarity of MTs is minus-end (-) on the left side and plus-end (+) on right side.  
**(F)** Kymographs illustrating the behavior of MTs decorated by CAMSAP2 or CAMSAP3 deletion mutants after photoablation (PA, the green lightning bolt indicates the photoablation site). Photoablation was performed in the MRB80 buffer with 20  $\mu$ M tubulin and 0.5  $\mu$ M rhodamine-tubulin supplemented with 50 or 80 mM KCl for CAMSAP2 or CAMSAP3 deletion mutants, respectively. All protein fragments shown were purified from HEK293T cells with the exception of His-CAMSAP3-C3 (rightmost panel) that was purified from *E. coli*. Scale bars represent 2  $\mu$ m (horizontal), 1 min (vertical). See also Figure S4 and Table S1.

The distinct properties of the MBD domain of CAMSAP2 and CAMSAP3 and the  $\alpha$ -helical domain in CAMSAP3, which contribute to MT minus-end decoration and stabilization, are supported by the sequence comparison of the CAMSAP proteins. The MBD domain and especially its C-terminal portion are highly conserved in CAMSAP2 and CAMSAP3 but not in CAMSAP1, whereas the N-terminal part of the  $\alpha$ -helix is unique to CAMSAP3 (Figure S4H). In summary, the existence of three different protein domains (CKK, MBD, and the  $\alpha$ -helix) accounts for the distinct behavior of CAMSAP proteins at the MT minus-ends. CAMSAP1 can only track the minus-ends, an activity that is primarily dependent on the CKK domain and might be enhanced by the dimerization through the CC3 region. CAMSAP2 decorates and stabilizes the minus-ends through the combination of the CKK and MBD regions. CAMSAP3 possesses an additional MT-binding domain within the  $\alpha$ -helix, which promotes its capacity to strongly stabilize MTs.

### **Katanin Binds to CAMSAPs and Regulates the Length of CAMSAP-Decorated Stretches**

The ability of CAMSAP2 and CAMSAP3 to stabilize MT lattice suggests that in cells CAMSAP-decorated stretches would continuously elongate unless some mechanisms would counteract this process. To gain insight into such mechanisms, we searched for CAMSAP binding partners. Extracts of HEK293T cells expressing CAMSAP1, CAMSAP2, or CAMSAP3 tagged with a biotinylation (bio) and GFP tag together with the biotin ligase BirA were used for streptavidin pull-down assays, and the resulting proteins were analyzed by mass spectrometry. Two subunits of katanin, p60 and p80, were abundantly present in CAMSAP2 and CAMSAP3 but not CAMSAP1 pull downs, and this result was confirmed by western blotting (Figures 7A and 7B). By using deletion mutants of CAMSAP2, we found that the region between amino acids 477 and 574 in the N-terminal part of the molecule, but not the CKK domain, is required for the interaction with katanin (Figures 7C, 7D, and S4H). At low expression levels, the full-length CAMSAP2 and its deletion mutant DN1, which retained the capacity to bind to katanin, formed stretches with an average length of 1  $\mu\text{m}$  (Figures 7E and 7F); a shorter mutant, DN2, which could not bind to katanin, also formed stretches, but they were substantially longer ( $\sim 2.6 \mu\text{m}$ ), suggesting that binding to katanin restricts stretch elongation. To further substantiate this idea, we depleted the p60 subunit of katanin (Figure 7G). Although this treatment had no effect on the expression of CAMSAP2, the stretches decorated by this protein became 2-fold longer (Figures 7H and 7I). In contrast, the depletion of two abundantly expressed MT depolymerases of the kinesin-13 family, MCAK and KIF2A, had no strong effect on the length of CAMSAP2 stretches (data not shown). Taken together, these data indicate that katanin counteracts the formation of long CAMSAP-decorated MT lattices.

### **DISCUSSION**

In this study, we have used a combination of cellular and in vitro assays to investigate how the dynamics of free, noncentrosomal MT minus-ends is regulated. We found that, contrary to the previous reports, MT minus-ends do undergo polymerization in cells and that this process is required for the deposition of CAMSAP proteins on the MTs. As a result of this deposition, CAMSAPs form stretches of MT lattice that can resist depolymerization from both ends, and this leads to the formation of stable noncentrosomal MTs. By using in vitro assays, we found no evidence for a capping activity of MT minus-ends by CAMSAP proteins. Instead, we showed that all three mammalian CAMSAP family members recognize growing MT minus-ends and that CAMSAP2 and CAMSAP3 autonomously decorate and stabilize MT lattice formed by MT minus-end polymerization. The requirement for

the MT minus-end growth to generate CAMSAP stretches indicates that CAMSAPs act on free MT minus-ends that are not capped by MT-nucleating proteins or other factors.

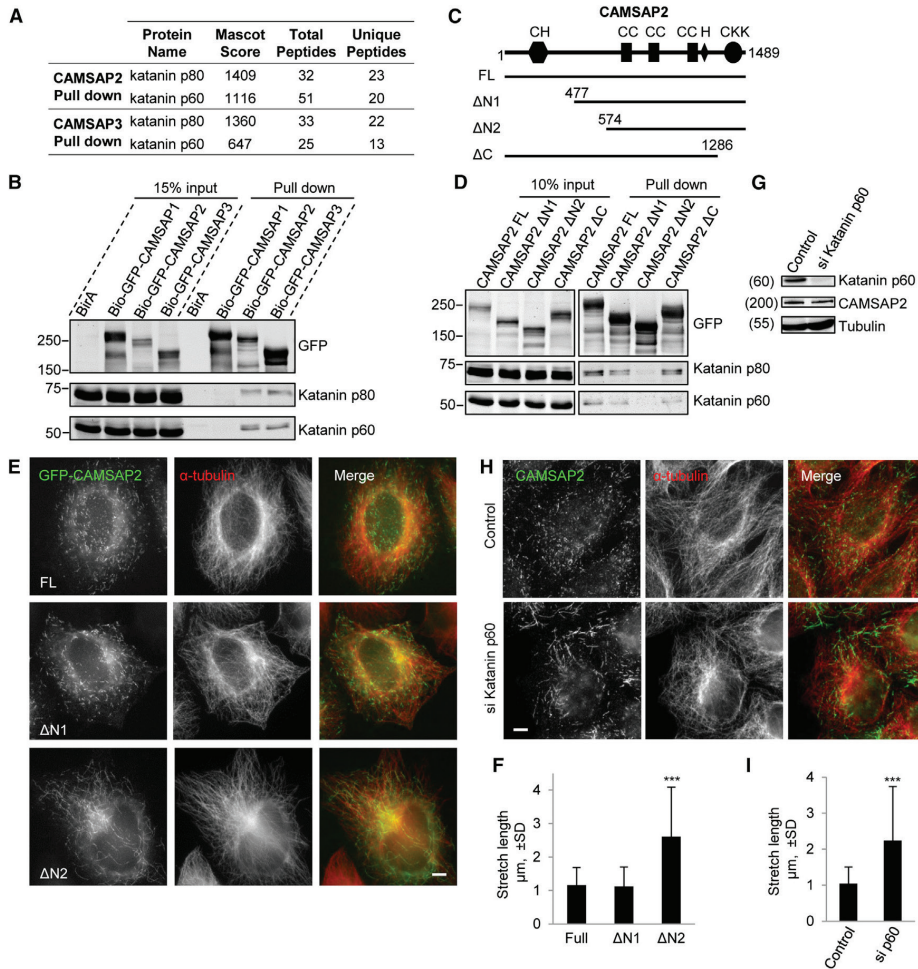


**Figure 7. Katanin Binds to CAMSAP2 and CAMSAP3 and Restricts the Length of CAMSAP Stretches**  
 (A) Identification of katanin p60 and p80 in streptavidin pull-down assays with biotinylated CAMSAP2 and CAMSAP3 by mass spectrometry.  
 (B) Streptavidin pull-down assays were performed with the extracts of HEK293T cells coexpressing bioGFP-tagged CAMSAP proteins and BirA and were analyzed by western blotting with the indicated antibodies.  
 (C) Scheme of domain organization of CAMSAP2 and the deletion mutants used to determine the interaction between CAMSAP2 and katanin p60/p80 complex. H,  $\alpha$ -helix.  
 (D) Mapping the interaction domain between CAMSAP2 and katanin p60 and p80 by streptavidin pull-down assays.  
 (E) HeLa cells were transfected with the indicated GFP constructs and stained for  $\alpha$ -tubulin. Scale bar represents 5  $\mu$ m.  
 (F) Quantification of GFP-CAMSAP2 stretch length for the experiments shown in (E). Approximately 1,000 stretches in ten cells were measured. (G) Western blots of extracts of HeLa cells cultured for 72 hr after the transfection with katanin p60 siRNA.  
 (H) Immunostaining for  $\alpha$ -tubulin (red) and CAMSAP2 (green) in control and katanin p60-depleted HeLa cells. Scale bar represents 5  $\mu$ m.  
 (I) Quantification of stretch length for the experiments shown in (H). Approximately 1,000 stretches in ten cells were measured. In (F) and (I), error bars represent SD, and values significantly different from control are indicated by asterisks ( $p < 0.001$ , Mann-Whitney U test).

Importantly, CAMSAPs not only protect MT minus-ends but also reduce the velocity of their polymerization. Because CAMSAPs rapidly associate with free MT minus-ends in cells, they can effectively slow down their growth; therefore, special approaches such as fluorescence recovery after photobleaching (FRAP) are needed to detect it. The observation of MT minus-end polymerization in cells is further strongly complicated by the fact that CAMSAP-decorated MT segments are quite mobile. A combination of slow growth and rapid motility likely explains why MT minus-end polymerization was overlooked in previous studies.

An important open question is how CAMSAP proteins recognize the MT minus-ends. Our results clearly show that CAMSAP deposition does not block tubulin dimer addition to the MT minus-ends, indicating that CAMSAPs do not occlude the longitudinal interface between  $\alpha$ - and  $\beta$ -tubulin. Because CAMSAPs exert a strong stabilizing effect on the MT lattice but can also recognize growing MT ends, they somewhat resemble doublecortin and EBs in their behavior and, similarly to these proteins, could potentially bind between the protofilaments (Bechstedt and Brouhard, 2012; Maurer et al., 2012; Moores et al., 2004). However, in contrast to EBs, which exchange rapidly on the binding sites at the MT ends (Bieling et al., 2007; Dragestein et al., 2008), CAMSAP2 and CAMSAP3 are stably deposited on the growing MT minus-ends. Interestingly, the third member of this protein family, CAMSAP1, dynamically tracks growing MT minus-ends. Until now, only proteins accumulating at both growing MT plus- and minus-ends (such as EBs and some of their partners), or proteins specific for the growing MT plus- ends (such as certain plus-end directed kinesins, including the fission yeast +TIP Tea2 [Bieling et al., 2007] and kinesin-8 family members [Su et al., 2012]), have been described. CAMSAP1 thus represents an interesting example of a specific “-TIP”.

Our deletion studies showed that the ability to track MT minus- ends and stabilize the MT lattice depend on separate domains of CAMSAP proteins. The conserved C-terminal CKK domain (Baines et al., 2009) appears to harbor the MT minus-end tracking activity, whereas the MT decoration and stabilization requires two additional protein regions: the MBD present in CAMSAP2 and CAMSAP3 and the predicted helical region, which increases the potency of MT stabilization by CAMSAP3. The invertebrate homolog of CAMSAPs, Patronin, seems to lack both the MBD domain and the  $\alpha$ -helix and might thus resemble CAMSAP1, acting as an MT minus-end tracker. However, it could also cap or decorate MT minus-ends in its own unique way.

The stable character of CAMSAP2 and CAMSAP3 stretches raises the question about how their length is controlled. We have identified katanin as one of the factors responsible for restricting CAMSAP stretch length. The interaction between CAMSAP and katanin, which is likely to be controlled by some additional factors, would allow fine-tuning the longevity of stable noncentrosomal MT “seeds.” Katanin can sever MTs but also depolymerize them from the ends (Díaz-Valencia et al., 2011; Zhang et al., 2011), and both activities could potentially contribute to the regulation of CAMSAP stretches.

In this study, we have shown that CAMSAP-dependent minus-end stabilization can generate specialized MTs in two different ways. Through minus-end growth-dependent deposition, CAMSAP2 and CAMSAP3 can directly stabilize stretches of MT lattice. An indirect consequence of the minus-end stabilization is the generation of long-lived MTs that can accumulate tubulin modifications that can specifically recruit certain motors or MT-associated proteins (Janke and Bulinski, 2011). Such indirect mechanisms are likely to be cell-type specific: for example, although we observed a strong loss of deetyrosinated MTs in CAMSAP2-depleted U2OS cells, an opposite effect was seen in Caco2 cells depleted of CAMSAP2 and CAMSAP3 (Tanaka et al., 2012).

Analysis of Patronin function in insect cells, as well as our data on MT photoablation in RPE cells, demonstrated that in the absence of the protective effect of CAMSAP/Patronin the dynamics of free MT minus-ends was strongly biased toward depolymerization, likely due to the activity of the MT depolymerases (Goodwin and Vale, 2010). In mammalian epithelial cells, loss of CAMSAP2 and CAMSAP3 function leads to the formation of centrosomally centered MT arrays (Nagae et al., 2013; Tanaka et al., 2012; this study), indicating that CAMSAP stretches are the major sites of stabilization of MT minus-ends that are not attached to the centrosome in interphase epithelial cells. Our data show that CAMSAP stretches form on free, polymerizing MT minus-ends. This suggests that, at least in epithelial cells, the  $\gamma$ -tubulin ring complex and other MT-interacting factors cannot efficiently promote MT minus-end stability when they are not embedded in the pericentrosomal matrix. This suggests that noncentrosomal MTs originate by MT breakage or MT release from the centrosome or other, possibly cytosolic or organelle-associated nucleation sites. These noncentrosomal MTs are important for the maintenance of organelle architecture (Nagae et al., 2013; Tanaka et al., 2012) and for the directional cell migration, possibly because they are necessary to create sufficient MT density throughout the cytoplasm or distinct MT modifications.

It is currently unclear whether CAMSAP family members play a role in mammalian mitosis. In flies, depletion of Patronin causes a short spindle phenotype, because Patronin counteracts the depolymerizing activity of the kinesin-13 Klp10A and decreases poleward flux (Goodwin and Vale, 2010; Goshima et al., 2007). Our data point to the inactivation of CAMSAP2-MT interaction during early mitotic stages, suggesting that in the cell types investigated here, CAMSAP2 function is mostly restricted to interphase. It is tempting to speculate that the loss of CAMSAP2 stretches contributes to the strong reorganization of the MT array to a much more centrosome centered configuration in G2 phase. CAMSAP2 stretches are restored in telophase and might contribute to the late stages of cell division.

CAMSAPs are not ubiquitous in the eukaryotic kingdom: yeasts and plants lack clear homologs of these proteins and generate noncentrosomal arrays by distinct combinations of MT nucleation, severing, and stabilization mechanisms (Janson et al., 2007; Wasteneys and Ambrose, 2009). However, CAMSAPs are likely to play an important role in organizing MTs in mammals. We found that CAMSAP2 is present at the MT minus-ends of different types, including not only epithelial cells but also fibroblasts, and is likely to participate in MT organization in all these cells, although its quantitative contribution might vary. For example, when present in a dot-like pattern (such as that found in CHO cells), CAMSAP2 might be less effective in protecting the MT minus-ends, and this would explain why free MT minus-ends are less stable in fibroblasts compared to epithelial cells (Rodionov et al., 1999). CAMSAPs are likely to be particularly important in cells where the noncentrosomal MTs constitute the major part of the MT system, such as differentiated epithelial, muscle, and neuronal cells (Bartolini and Gundersen, 2006). The control of MT minus-end growth by CAMSAPs and its spatiotemporal regulation during cell division and differentiation will thus need to be taken into account in future models of mammalian MT organization.

### EXPERIMENTAL PROCEDURES

The description of the details of the constructs, siRNAs, cell culture methods, microscopy equipment, and mass spectrometry analysis can be found in the Supplemental Experimental Procedures.

#### Antibodies and Immunofluorescent Cell Staining

We used rabbit polyclonal antibodies against CAMSAP1 (NBP1-26645, Novus), CAMSAP2 (NBP1-21402, Novus; 17880-1-AP, Proteintech), CAMSAP3 (AP18323a, Abgent), katanin

p60 and p80 (17560-1-AP and 14969-1-AP, Proteintech), and detyrosinated- $\alpha$ -tubulin (ab48389, Abcam); mouse monoclonal antibodies against GFP (11814460001, Roche), EB1 (610535, BD Biosciences), and acetylated  $\alpha$ -,  $\beta$ -, and  $\gamma$ -tubulin (T7451, T5201, and T6557, respectively, Sigma-Aldrich); and a rat monoclonal antibody against  $\alpha$ -tubulin YL1/2 (MA1-80017, Pierce).

To label EB1 and MTs, we fixed cells with  $-20^{\circ}$  C methanol for 10 min and postfixed them in 4% paraformaldehyde in PBS for 10 min at room temperature. To label other proteins, we fixed cells with  $-20^{\circ}$  C methanol for 5 min. Cells were rinsed with 0.15% Triton X-100 in PBS; subsequent washing and labeling steps were carried out in PBS supplemented with 2% bovine serum albumin and 0.05% Tween 20. At the end, slides were rinsed in 70% and 100% ethanol, air-dried, and mounted in Vectashield mounting medium (Vector Laboratories).

### Protein Purification

To purify GFP-CAMSAP full-length and deletion mutant proteins, we harvested HEK293T cells at 24–36 hr after transfection. The cells from one 10 cm dish were lysed in 400 ml of lysis buffer (50 mM HEPES, 300 mM NaCl, and 0.5% Triton X-100 [pH 7.4]) supplemented with protease inhibitors (Roche). Cell lysates were incubated with 50  $\mu$ l of streptavidin beads (Invitrogen) for 1 hr. Beads were washed five times with lysis buffer without protease inhibitors and twice with the TEV buffer (50 mM HEPES, 150 mM NaCl, 1 mM  $MgCl_2$ , 1 mM EGTA, 0.05% Triton X-100, and 1 mM dithiothreitol [DTT]). The proteins were eluted in 50  $\mu$ l of TEV buffer with 0.5  $\mu$ g of glutathione S-transferase-6x histidine Tobacco etch virus protease site (Sigma-Aldrich) for 1 hr at  $4^{\circ}$  C. Purified proteins were snap-frozen in liquid nitrogen and stored in  $-80^{\circ}$  C. To express GFP-CKK domain of CAMSAPs and GFP-CAMSAP3-C3 in *E. coli*, they were fused to an N-terminal 6x-histidine tag (His) in pET28a vector (Novagen). Proteins were purified by nickel-nitrilotriacetic acid agarose (QIAGEN). Bacterially expressed mCherry-EB3 (a gift of M. Steinmetz, Paul Sherrer Institut) was purified as described previously (Montenegro Gouveia et al., 2010).

### In Vitro Assays

To reconstitute MT minus-end decoration by CAMSAPs in vitro, we modified the conditions used to reconstitute MT plus-end tracking (Montenegro Gouveia et al., 2010). Double-cycled GMPCPP MT seeds (70% unlabeled tubulin, 17% biotin-tubulin, and 13% X-rhodamine-tubulin) were made as described previously (Gell et al., 2010). Flow chambers were assembled from plasma-cleaned glass coverslips and microscope slides. The surface of coverslip was functionalized by sequentially incubating it with 0.2 mg/ml PLL-PEG biotin (Susos AG) and 1 mg/ml NeutrAvidin (Invitrogen) in MRB80 buffer (80 mM piperazine-N,N[prime]-bis(2-ethanesulfonic acid), 4 mM  $MgCl_2$ , and 1 mM EGTA [pH 6.8]). MT seeds were attached to coverslips through biotin- NeutrAvidin interactions. Flow chambers were further blocked with 1 mg/ml  $\kappa$ -casein. The reaction mix with or without CAMSAPs (MRB80 buffer supplemented with 20  $\mu$ M porcine brain tubulin, 0.5  $\mu$ M X-rhodamine-tubulin, 80 mM KCl, 1 mM guanosine triphosphate, 0.2 mg/ml  $\kappa$ -casein, 0.1% methyl-cellulose, and oxygen scavenger mix [50 mM glucose, 400  $\mu$ g/ml glucose oxidase, 200  $\mu$ g/ml catalase, and 4 mM DTT]) was added to the flow chamber after centrifugation in an Airfuge for 5 min at 119,000 x g. For experiments in the presence of EB3, concentration of mCherry-EB3 was 20 nM and X-rhodamine-tubulin was omitted. To promote MT catastrophes without EB3, we used 15  $\mu$ M porcine brain tubulin and 110 mM KCl instead of 20  $\mu$ M porcine brain tubulin and 80 mM KCl. To enhance the binding between CAMSAP2 and MT in the photoablation experiments, we used 50 mM KCl instead of 80 mM KCl in the assay buffer. The flow chamber was sealed with vacuum grease, and dynamic MTs were imaged immediately at  $30^{\circ}$

C using a TIRF microscope. All tubulin products were from Cytoskeleton.

### Imaging and Image Analysis

Images of fixed cells were collected with an Eclipse 80i (Nikon) microscope equipped with a Plan Apo VC 100X 1.4 numerical aperture (N.A.), 60X 1.4 N.A., or Plan Fluor 40X 1.3 N.A. oil objective and a CoolSNAP HQ2 camera (Roper Scientific). TIRF microscopy was performed on an Eclipse Ti-E (Nikon) inverted research microscope with the perfect focus system, equipped with the CFI Apo TIRF 100X 1.49 N.A. oil objective (Nikon), Photometrics Evolve 512 EMCCD (Roper Scientific), and TIRF-E motorized TIRF illuminator modified by Roper Scientific France/PICT-IBiSA, Institut Curie, controlled with MetaMorph 7.7 software (Molecular Devices). Spinning disk microscopy was performed on a similar microscope equipped with CSU-X1-A1 spinning disc (Yokogawa). Both microscopes were equipped with an ILas system (Roper Scientific France/PICT-IBiSA) for FRAP and photoablation. The 532 nm Q-switched pulsed laser (Teem Photonics) was used for photoablation on the TIRF microscope, whereas a 355 nm passively Q-switched pulsed laser (Teem Photonics) was used for the photoablation together with the CFI S Fluor 100X 0.5–1.3 N.A. oil objective (Nikon) on the spinning disk microscope. Images were prepared for publication with MetaMorph and Photoshop (Adobe). All images were modified by adjustments of levels and contrast. Kymograph analysis and various quantifications were performed in MetaMorph. Statistical comparison between the data from the control and knockdown groups was performed in SigmaPlot (Systat Software) with the rank sum test function (Mann-Whitney U test) or the unpaired Student's t test.

### Theoretical Analysis of MT Staining Intensity along the Cell Radius in a Cell Where All MTs Are Attached to the Centrosome

We consider the case when MTs form a perfect radial array that emanates from a single centrosome with a radius  $r_0$  and ends at the cell boundary located at a distance  $R_c$ . If the total number of MTs is  $N$ , the number of microtubules  $N_{ds}^0$  located within a continuous segment  $dS$  of the perimeter of the circle  $r_0$  would be equal to

$$N_{ds}^0 = \frac{dS}{2\pi r_0} N$$

where  $2\pi r_0$  is the perimeter of circle. If the intensity of one microtubule is equal to  $I_{MT}$ , then the total intensity at  $r_0$  would be equal to  $I_0 = N_{ds}^0 I_{MT}$ . The number of microtubules intersecting the segment of the same length  $dS$  at some radius  $r$  is given by

$$N_r(r) = \frac{dS}{2\pi r} N = N_{ds}^0 \frac{r_0}{r}$$

and total intensity is

$$I(r) = I_{MT} N_r(r) = I_{MT} N_{ds}^0 \frac{r_0}{r} = I_0 \frac{r_0}{r}$$

Taking into account the background intensity  $I_B$ , the final expression for the change in intensity along the line for the radial array of microtubules would be

$$I(r) = I_0 \frac{r_0}{r} + I_B$$

Representative shape of this distribution is shown in Figure S2F.

### SUPPLEMENTAL INFORMATION

Supplemental Information includes Supplemental Experimental Procedures, four figures, one table, and seven movies and can be found with this article online at <http://dx.doi>.

org/10.1016/j.devcel.2014.01.001.

### ACKNOWLEDGMENTS

We thank M. Steinmetz for the gift of the purified mCherry-EB3 protein, J. Demmers and K. Bestarosti for the help with mass spectrometry experiments, Y. Mimori-Kiyosue for the gift of the EB3-TagRFP-T construct, A. Merdes for the gift of the GFP-NEDD1 construct, and L. Kapitein and M. Steinmetz for comments on the manuscript. This research was supported by the Netherlands Organization for Scientific Research NWO-ALW-VICI, ZonMw TOP, FOM Program, CW ECHO, and ALW Open program grants to A.A. and C.C.H. and a Marie-Curie International Incoming Fellowship to R.M.

### REFERENCES

- Abal, M., Piel, M., Bouckson-Castaing, V., Mogensen, M., Sibarita, J.B., and Bornens, M. (2002). Microtubule release from the centrosome in migrating cells. *J. Cell Biol.* 159, 731–737.
- Akhmanova, A., and Steinmetz, M.O. (2008). Tracking the ends: a dynamic protein network controls the fate of microtubule tips. *Nat. Rev. Mol. Cell Biol.* 9, 309–322.
- Baines, A.J., Bignone, P.A., King, M.D., Maggs, A.M., Bennett, P.M., Pinder, J.C., and Phillips, G.W. (2009). The CKK domain (DUF1781) binds microtubules and defines the CAMSAP/ssp4 family of animal proteins. *Mol. Biol. Evol.* 26, 2005–2014.
- Bartolini, F., and Gundersen, G.G. (2006). Generation of noncentrosomal microtubule arrays. *J. Cell Sci.* 119, 4155–4163.
- Bechstedt, S., and Brouhard, G.J. (2012). Doublecortin recognizes the 13-prot filament microtubule cooperatively and tracks microtubule ends. *Dev. Cell* 23, 181–192.
- Bieling, P., Laan, L., Schek, H., Munteanu, E.L., Sandblad, L., Dogterom, M., Brunner, D., and Surrey, T. (2007). Reconstitution of a microtubule plus-end tracking system in vitro. *Nature* 450, 1100–1105.
- Botvinick, E.L., Venugopalan, V., Shah, J.V., Liaw, L.H., and Berns, M.W. (2004). Controlled ablation of microtubules using a picosecond laser. *Biophys. J.* 87, 4203–4212.
- Colombelli, J., Reynaud, E.G., Rietdorf, J., Pepperkok, R., and Stelzer, E.H. (2005). In vivo selective cytoskeleton dynamics quantification in interphase cells induced by pulsed ultraviolet laser nanosurgery. *Traffic* 6, 1093–1102.
- Dammermann, A., Desai, A., and Oegema, K. (2003). The minus end in sight. *Curr. Biol.* 13, R614–R624.
- Desai, A., and Mitchison, T.J. (1997). Microtubule polymerization dynamics. *Annu. Rev. Cell Dev. Biol.* 13, 83–117.
- Díaz-Valencia, J.D., Morelli, M.M., Bailey, M., Zhang, D., Sharp, D.J., and Ross, J.L. (2011). *Drosophila* katanin-60 depolymerizes and severs at microtubule defects. *Biophys. J.* 100, 2440–2449.
- Dragestein, K.A., van Cappellen, W.A., van Haren, J., Tsibidis, G.D., Akhmanova, A., Knoch, T.A., Grosveld, F., and Galjart, N. (2008). Dynamic behavior of GFP-CLIP-170 reveals fast protein turnover on microtubule plus ends. *J. Cell Biol.* 180, 729–737.
- Galjart, N. (2010). Plus-end-tracking proteins and their interactions at microtubule ends. *Curr. Biol.* 20, R528–R537.
- Gell, C., Bormuth, V., Brouhard, G.J., Cohen, D.N., Diez, S., Friel, C.T., Helenius, J., Nitzsche, B., Petzold, H., Ribbe, J., et al. (2010). Microtubule dynamics reconstituted in vitro and imaged by single-molecule fluorescence microscopy. *Methods Cell Biol.* 95, 221–245.
- Goodwin, S.S., and Vale, R.D. (2010). Patronin regulates the microtubule network by protecting microtubule minus ends. *Cell* 143, 263–274.
- Goshima, G., Wollman, R., Goodwin, S.S., Zhang, N., Scholey, J.M., Vale, R.D., and Stuurman, N. (2007). Genes required for mitotic spindle assembly in *Drosophila* S2 cells. *Science* 316, 417–421.
- Howard, J., and Hyman, A.A. (2003). Dynamics and mechanics of the microtubule plus end. *Nature* 422, 753–758.
- Howard, J., and Hyman, A.A. (2007). Microtubule polymerases and depolymerases. *Curr. Opin. Cell Biol.* 19, 31–35.
- Janke, C., and Bulinski, J.C. (2011). Post-translational regulation of the microtubule cytoskeleton: mechanisms and functions. *Nat. Rev. Mol. Cell Biol.* 12, 773–786.
- Janson, M.E., Loughlin, R., Loiodice, I., Fu, C., Brunner, D., Nédélec, F.J., and Tran, P.T. (2007). Crosslinkers and motors organize dynamic microtubules to form stable bipolar arrays in fission yeast. *Cell* 128, 357–368.
- Jiang, K., and Akhmanova, A. (2011). Microtubule tip-interacting proteins: a view from both ends. *Curr. Opin. Cell Biol.* 23, 94–101.
- Khodjakov, A., La Terra, S., and Chang, F. (2004). Laser microsurgery in fission yeast; role of the mitotic spindle midzone in anaphase B. *Curr. Biol.* 14, 1330–1340.
- Kollman, J.M., Merdes, A., Mourey, L., and Agard, D.A. (2011). Microtubule nucleation by  $\gamma$ -tubulin complexes.

- Nat. Rev. Mol. Cell Biol. 12, 709–721.
- Maurer, S.P., Fourniol, F.J., Bohner, G., Moores, C.A., and Surrey, T. (2012). EBs recognize a nucleotide-dependent structural cap at growing microtubule ends. *Cell* 149, 371–382.
- Meng, W., Mushika, Y., Ichii, T., and Takeichi, M. (2008). Anchorage of microtubule minus ends to adherens junctions regulates epithelial cell-cell contacts. *Cell* 135, 948–959.
- Montenegro Gouveia, S., Leslie, K., Kapitein, L.C., Buey, R.M., Grigoriev, I., Wagenbach, M., Smal, I., Meijering, E., Hoogenraad, C.C., Wordeman, L., et al. (2010). In vitro reconstitution of the functional interplay between MCAK and EB3 at microtubule plus ends. *Curr. Biol.* 20, 1717–1722.
- Moores, C.A., Perderiset, M., Francis, F., Chelly, J., Houdusse, A., and Milligan, R.A. (2004). Mechanism of microtubule stabilization by doublecortin. *Mol. Cell* 14, 833–839.
- Nagae, S., Meng, W., and Takeichi, M. (2013). Non-centrosomal microtubules regulate F-actin organization through the suppression of GEF-H1 activity. *Genes Cells* 18, 387–396.
- Rodionov, V., Nadezhdina, E., and Borisy, G. (1999). Centrosomal control of microtubule dynamics. *Proc. Natl. Acad. Sci. USA* 96, 115–120.
- Roll-Mecak, A., and McNally, F.J. (2010). Microtubule-severing enzymes. *Curr. Opin. Cell Biol.* 22, 96–103.
- Schuyler, S.C., and Pellman, D. (2001). Microtubule “plus-end-tracking proteins”: The end is just the beginning. *Cell* 105, 421–424.
- Sharp, D.J., and Ross, J.L. (2012). Microtubule-severing enzymes at the cutting edge. *J. Cell Sci.* 125, 2561–2569.
- Su, X., Ohi, R., and Pellman, D. (2012). Move in for the kill: motile microtubule regulators. *Trends Cell Biol.* 22, 567–575.
- Tanaka, N., Meng, W., Nagae, S., and Takeichi, M. (2012). Nezha/CAMSAP3 and CAMSAP2 cooperate in epithelial-specific organization of noncentrosomal microtubules. *Proc. Natl. Acad. Sci. USA* 109, 20029–20034.
- Walker, R.A., Inoué, S., and Salmon, E.D. (1989). Asymmetric behavior of severed microtubule ends after ultraviolet-microbeam irradiation of individual microtubules in vitro. *J. Cell Biol.* 108, 931–937.
- Wasteneys, G.O., and Ambrose, J.C. (2009). Spatial organization of plant cortical microtubules: close encounters of the 2D kind. *Trends Cell Biol.* 19, 62–71.
- Zanic, M., Stear, J.H., Hyman, A.A., and Howard, J. (2009). EB1 recognizes the nucleotide state of tubulin in the microtubule lattice. *PLoS ONE* 4, e7585.
- Zhang, D., Grode, K.D., Stewman, S.F., Diaz-Valencia, J.D., Liebling, E., Rath, U., Riera, T., Currie, J.D., Buster, D.W., Asenjo, A.B., et al. (2011). *Drosophila* katanin is a microtubule depolymerase that regulates cortical-microtubule plus-end interactions and cell migration. *Nat. Cell Biol.* 13, 361–370.



## Chapter 5

# Microtubule Minus-End Binding Protein CAMSAP2 Controls Axon Specification and Dendrite Development

Kah Wai Yau,<sup>1,2</sup> Sam F.B. van Beuningen,<sup>1</sup> Inês Cunha-Ferreira,<sup>1</sup> Bas M.C. Cloin,<sup>1</sup> Eljo Y. van Battum,<sup>3</sup> Lena Will,<sup>1</sup> Philipp Schätzle,<sup>1</sup> Roderick P. Tas,<sup>1</sup> Jaap van Krugten,<sup>1</sup> Eugene A. Katrukha,<sup>1</sup> Kai Jiang,<sup>1</sup> Phebe S. Wulf,<sup>1</sup> Marina Mikhaylova,<sup>1</sup> Martin Harterink,<sup>1</sup> R. Jeroen Pasterkamp,<sup>3</sup> Anna Akhmanova,<sup>1</sup> Lukas C. Kapitein,<sup>1</sup> and Casper C. Hoogenraad<sup>1,2</sup>

<sup>1</sup>Cell Biology, Faculty of Science, Utrecht University, 3584 CH, Utrecht, The Netherlands

<sup>2</sup>Department of Neuroscience, Erasmus Medical Center, 3015 GE Rotterdam, The Netherlands

<sup>3</sup>Department of Translational Neuroscience, Brain Center Rudolf Magnus, University Medical Center Utrecht, 3584 CG, Utrecht, The Netherlands

### ABSTRACT

In neurons, most microtubules are not associated with a central microtubule-organizing center (MTOC), and therefore, both the minus and plus-ends of these noncentrosomal microtubules are found throughout the cell. Microtubule plus-ends are well established as dynamic regulatory sites in numerous processes, but the role of microtubule minus-ends has remained poorly understood. Using live-cell imaging, high-resolution microscopy, and laser-based microsurgery techniques, we show that the CAMSAP/Nezha/Patronin family protein CAMSAP2 specifically localizes to noncentrosomal microtubule minus-ends and is required for proper microtubule organization in neurons. CAMSAP2 stabilizes noncentrosomal microtubules and is required for neuronal polarity, axon specification, and dendritic branch formation *in vitro* and *in vivo*. Furthermore, we found that noncentrosomal microtubules in dendrites are largely generated by  $\gamma$ -Tubulin dependent nucleation. We propose a two-step model in which  $\gamma$ -Tubulin initiates the formation of noncentrosomal microtubules and CAMSAP2 stabilizes the free microtubule minus-ends in order to control neuronal polarity and development.

*Neuron*. 2014 Jun 4;82(5):1058-73

### INTRODUCTION

Neurons are polarized cells that critically depend on the microtubule (MT) cytoskeleton for their development and function. Mutations in different Tubulin genes cause a range of nervous system abnormalities and several neurological and neurodegenerative diseases have been linked to altered MT-based transport processes (Franker and Hoogenraad, 2013; Millecamps and Julien, 2013). MTs, which serve as tracks for long-distance transport to axons and dendrites, are polarized structures with two distinct ends, the plus and minus-ends (Conde and Cáceres, 2009). Most plus-ends are highly dynamic, whereas minus-ends are believed to be much more stable. Control of MT plus-end dynamics, often by plus-end-associated proteins, has recently been shown to play an important role in determining neuronal polarity and in regulating dendritic spine morphology and synaptic plasticity (Jaworski et al., 2009). In contrast, little is known about the functions of neuronal MT minus-ends and potential minus-end-associated proteins.

In many cell types, most MT minus-ends are anchored and stabilized at a MT-organizing center (MTOC), most often the centrosome (Bettencourt-Dias and Glover, 2007). However, neuronal cells do not rely entirely on centrosomal MT nucleation. *Drosophila* neurons lacking an active centrosomes display a normal MT network and have proper axon outgrowth and neuronal organization (Basto et al., 2006; Nguyen et al., 2011). In addition, electron microscopy studies in sympathetic rat neurons show that most neuronal MTs are not anchored by the centrosome and do not form large radial arrays (Baas and Lin, 2011). More recent experiments found that during neuronal development, the centrosome loses its function as an MTOC (Stiess et al., 2010). Noncentrosomal MTs can be generated by two distinct mechanisms: severing of preexisting MTs or local nucleation at noncentrosomal sites, such as cortical  $\gamma$ -Tubulin complexes (Bartolini and Gundersen, 2006; Kuijpers and Hoogenraad, 2011; Stiess and Bradke, 2011). Depletion of the MT severing enzymes katanin and spastin was found to alter axonal growth in young neurons (Yu et al., 2008). MT nucleation at noncentrosomal sites has been reported to occur on Golgi membranes (Efimov et al., 2007). Additionally, a recent study in *Drosophila* neurons reports that Golgi outposts in dendrites locally nucleate MTs and shape dendrite morphology (Ori- McKenney et al., 2012).

Regardless of the precise mechanisms of noncentrosomal MT formation, in a sequential step the newly generated MT minus- end must be stabilized in order to prevent depolymerization (Bartolini and Gundersen, 2006; Dammermann et al., 2003). Recently, a MT minus-end binding protein, called Patronin, was found to protect MT minus-ends in *Drosophila* cells from depolymerization (Goodwin and Vale, 2010). Three mammalian homologs of Patronin, calmodulin-regulated spectrin-associated protein 1–3 (CAMSAP1–3), have been identified (Baines et al., 2009). CAMSAP3/Nezha localizes at MT minus-ends close to adherent junctions in epithelial cells (Meng et al., 2008). Moreover, CAMSAP3/Nezha and CAMSAP2 cooperate in determining the overall growth pattern of MTs in epithelial cells (Tanaka et al., 2012), and recent *in vitro* experiments revealed that CAMSAP proteins associate with growing MT minus-ends and regulate their dynamics (Jiang et al., 2014). Nevertheless, whether these proteins also contribute to the establishment and maintenance of noncentrosomal MT arrays in developing and mature neurons has remained unresolved.

In this study, we use a combination of cell-biological approaches, quantitative/high-resolution microscopy, laser micro- surgery, *in utero* electroporation, and organotypic slice cultures to determine the role of CAMSAP2 during neuronal polarity and development. We show that CAMSAP2 localizes to the MT minus-ends in axon and dendrites, stabilizes noncentrosomal MTs, and is required for axon specification, dendritic branch formation, and brain-derived neurotrophic factor (BDNF)-induced dendritic outgrowth. Together, these results reveal a new mechanism for stabilizing neuronal MTs and reveal a critical role for

CAMSAP2 in axon specification and dendrite development.

### RESULTS

#### **Distinct CAMSAP2-Decorated Structures Are Present in Hippocampal Neurons**

Little is known about the expression and distribution of the CAMSAP minus-end binding protein family in neurons. According to the *in situ* hybridization data from the Allen Mouse Brain Atlas and proteomics data set from the Human Protein Atlas project, CAMSAP2 is the most abundant family member in the hippocampus. Consistent with these data, western blot analysis of the three CAMSAP family members in the developing and mature hippocampus revealed that CAMSAP2 is the most abundant family member, whereas CAMSAP1 and CAMSAP3 could not be detected (Figure 1A). The CAMSAP2 antibody is specific for CAMSAP2, as it does not recognize the other CAMSAP family members (Figure 1B). Immunocytochemistry of mature hippocampal neurons at *in vitro* day 21 (DIV 21) with CAMSAP2 antibodies revealed a variety of small clusters and distinct (punctated) stretches, scattered throughout the cell body, axon, and dendritic shaft as revealed by the axonal marker Tau and dendritic marker MAP2 (Figure 1C). Similar results were obtained by immunostaining with two other CAMSAP2 antibodies and by low-level expression of GFP-tagged CAMSAP2 in neurons (Figure 1D; Figure S1 available online). CAMSAP2 stretches were found within the soma, axon, and dendritic shaft (Figures 1C and S1). CAMSAP2 was absent from the actin-rich dendritic spines, showed minimal overlap with the synaptic marker Bassoon (Figures 1F and S1), and lacked a significant degree of colocalization with the diffuse  $\gamma$ -Tubulin protein (Figures 1E and S2A).

Next, we analyzed endogenous CAMSAP2 in different stages of developing hippocampal neurons (from DIV 0–14) by immunostaining. The centrosome of young neurons (DIV 0–1), detected by immunostaining for Centrin or  $\gamma$ -Tubulin, did not overlap with CAMSAP2 (Figure S2B). Interestingly, the size of the CAMSAP2-decorated structures changed during neuron development: CAMSAP2-positive puncta ( $\leq 1 \mu\text{m}$ ) and small clusters ( $>1 \mu\text{m}$  and  $<10 \mu\text{m}$ ) were clearly visible in young hippocampal neurons at  $< \text{DIV } 5$  but less in mature cells, whereas long CAMSAP2 stretches ( $\geq 10 \mu\text{m}$ ) were abundantly present in mature neurons at  $> \text{DIV } 14$  (Figures 1G and S2). The total CAMSAP2 expression levels were unchanged during neuronal development (Figure 1H). Thus, distinct CAMSAP2-decorated structures are present in hippocampal neurons, and the length of these structures changes during neuron development.

#### **CAMSAP2 Localizes to MT Minus-Ends in Hippocampal Neurons**

To further study the subcellular distribution of CAMSAP2, we performed *direct stochastic optical reconstruction microscopy* (dSTORM) imaging using neuron cultures stained for endogenous CAMSAP2 (Heilemann et al., 2008; Rust et al., 2006). In dSTORM reconstructions, CAMSAP2 stretches detected using conventional microscopy were often found composed of multiple shorter puncta or clusters of variable size (Figures 2A–2C). On average,  $1.1 \pm 0.3$  CAMSAP2 puncta per  $\mu\text{m}^2$  were observed in primary dendrites. To directly test whether CAMSAP2 localizes to MT ends in hippocampal neurons, we next optimized dSTORM imaging to resolve individual MTs within the crowded neuronal MT cytoskeleton. Whereas methanol fixation was required for immunolabeling of endogenous CAMSAP2, this was incompatible with sharp dSTORM imaging of MTs. In contrast, individual and continuous neuronal MTs, as well as many MT ends, could be clearly resolved using an optimized alternative fixation procedure that was compatible with GFP-based immunolabeling of GFP-CAMSAP2 (Figures 2D and 2E). Dual-color dSTORM imaging revealed that many individual MT ends were decorated with  $\sim 2\text{--}4$  GFP-CAMSAP2 puncta,

which appeared as stretches in diffraction-limited images (Figure 2F). Localization to MT ends was also observed with overexpressed GFP-CAMSAP3 in hippocampal neurons, except that the stretches were typically shorter and more continuous (Figure 2G). These data demonstrate that CAMSAP2 localizes to the ends of MTs in neurons.

To determine whether CAMSAP2 localizes to MT minus-ends, we expressed GFP-CAMSAP2 in COS7 cells together with mCherry- $\alpha$ -Tubulin and analyzed MT dynamics using TIRF microscopy. Consistent with previous observations (Tanaka et al., 2012), GFP-CAMSAP2 was specifically localized to one end of noncentrosomal MTs (Figure S3). The other end of these MTs alternated between rapid periods of growth and shrinkage, which is characteristic of MT plus-ends, suggesting that CAMSAP2 indeed enriches near the MT minus-end (Figure S3B; Movie S1). In addition, CAMSAP2 and the MT plus-end marker mCherry-MT+TIP were distributed differently along noncentrosomal MTs. The two proteins were localized at the opposite ends of the MT with the displacement of plus-end comets away from the GFP-CAMSAP2 signal (Figure S3C; Movie S2), demonstrating that CAMSAP2 localizes to MT minus-ends and allows MT extension and shortening by plus-end dynamics. Similar results were obtained in hippocampal neurons, where results demonstrate that CAMSAP2 labels the minus-ends of noncentrosomal MTs in neurons. GFP-CAMSAP2 specifically localizes to noncentrosomal MTs ends and MT plus-ends repeatedly emanated from stable CAMSAP2 stretches in the cell body (Figures 2H and 2I; Movie S3) and primary dendrites (Figures 2J and 2K; Movie S4). These results demonstrate that CAMSAP2 labels the minus-ends of noncentrosomal MTs in neurons.

---

**Figure 1. CAMSAP2 Distribution in Mature Hippocampal Neurons** ►

(A) Extracts of whole hippocampus and brain of E18 embryos and adult rats were analyzed by western blot with indicated antibodies. HeLa cell extracts were used as a positive control.

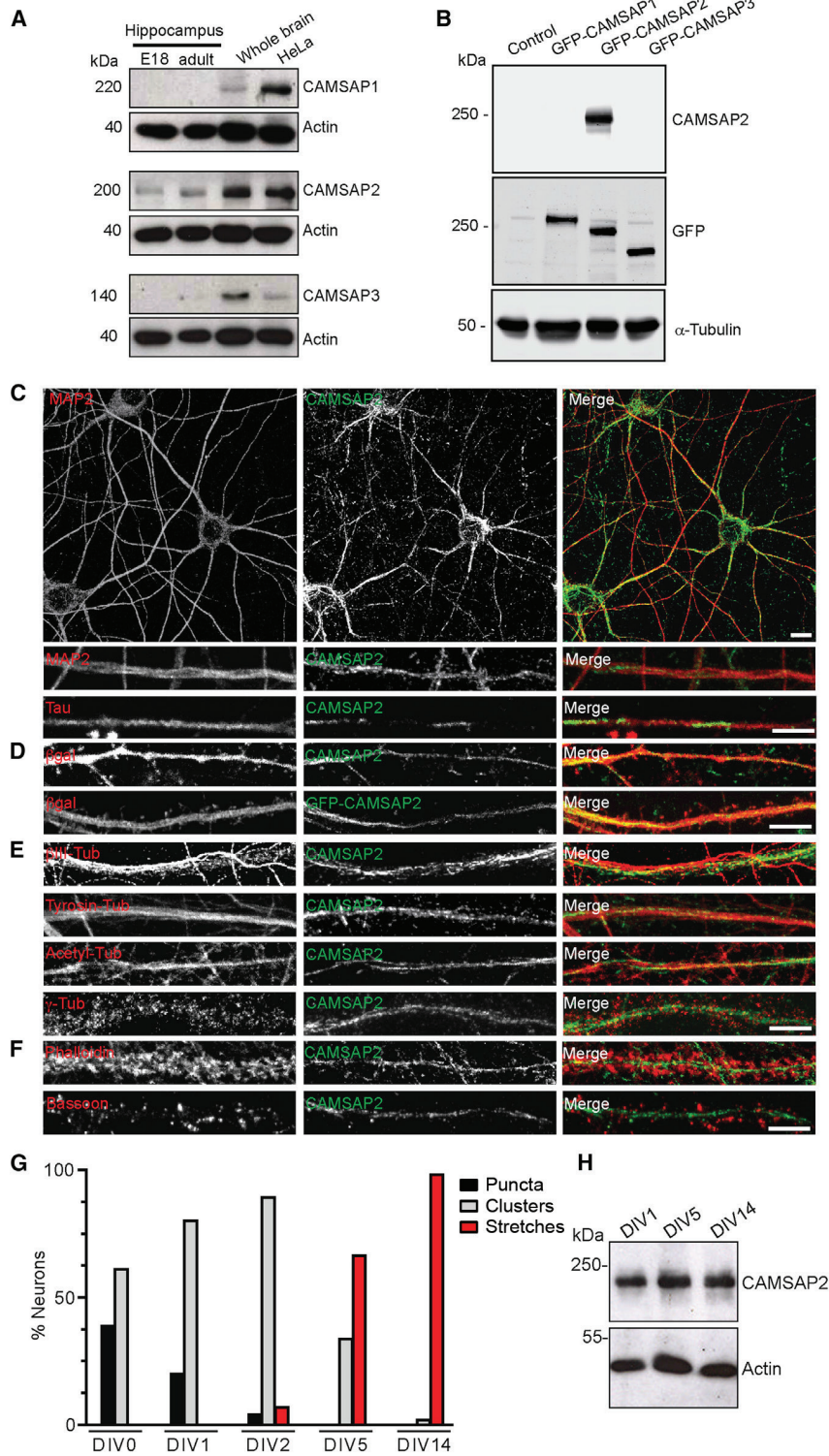
(B) HEK293 human cells transiently expressing indicated GFP-CAMSAP proteins were analyzed by western blot with CAMSAP2 and GFP anti-bodies.  $\alpha$ -Tubulin was used as a loading control. (C) Representative confocal images of hippocampal neurons (DIV 21) stained for both endogenous MAP2 (red) or Tau (red) and CAMSAP2 (green). Dendritic segment is shown enlarged in the bottom row.

(E and F) Double staining in hippocampal neurons (DIV21) for endogenous CAMSAP2 (green) with markers (red) for neuronal MTs ( $\beta$ III-Tubulin), MT modifications (acetylated-Tubulin and tyrosinated-Tubulin),  $\gamma$ -Tubulin (E), actin (Phalloidin), and synapses (Bassoon) (F).

(G) Quantification of CAMSAP2 stretches throughout neuronal development. CAMSAP2 structures were divided into three categories: (1) puncta (approximately  $\leq 1 \mu\text{m}$ ), (2) clusters (approximately  $> 1 \mu\text{m}$  and  $< 10 \mu\text{m}$ ), and (3) stretches (approximately  $\geq 10 \mu\text{m}$ ). At least 100 neurons were analyzed per developmental stage. (H) Extracts of hippocampal neurons were prepared at the indicated time points and probed by western blot for CAMSAP2 and actin antibodies. See also Figures S1 and S2.

(D) Representative images of dendritic segments of hippocampal neuron (DIV 21) expressing  $\beta$ -galactosidase (red) to highlight neuronal morphology and either stained for endogenous CAMSAP2 (green, top) or cotransfected with GFP-CAMSAP2 (green, bottom).

# CAMSAP2 Controls Neuronal Polarity and Development



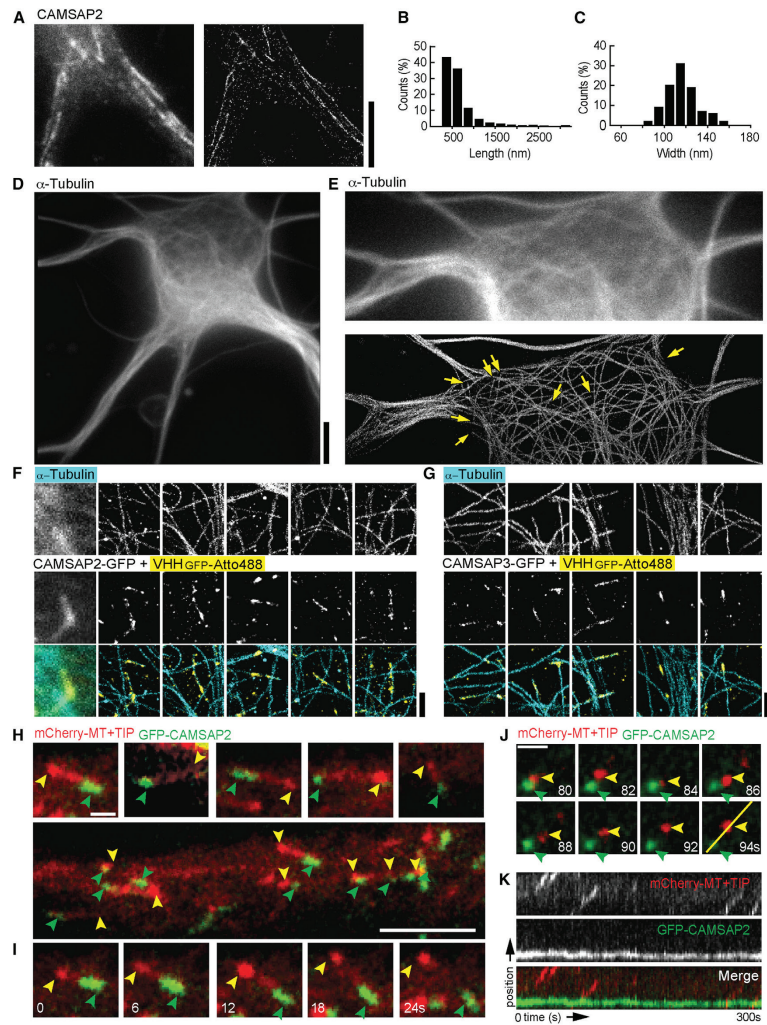


**Figure 2. CAMSAP2 Localizes to Microtubule Minus-Ends in Hippocampal Neurons**

(A) Conventional widefield image (left) and dSTORM reconstruction (right) of a methanol-fixed neuron stained for endogenous CAMSAP2 with Atto488. Scale bar is 5  $\mu$ m.

(B) Distribution of stretch lengths including 316 stretches from seven neurons.

(C) Distribution of stretch widths (FWHM) based on Gaussian fitting (88 stretches from seven neurons).

(D) Conventional widefield image of a DIV 5 neuron fixed using glutaraldehyde (GA) and paraformaldehyde (PFA) and stained with an AlexaFluor647-labeled antibody against  $\alpha$ -Tubulin.

(E) Zoom of (D) (top) and corresponding dSTORM reconstruction (bottom), where multiple MT ends can be clearly observed. The final dSTORM image is a stitch of four partially overlapping reconstructions.

(F and G) Zooms from different DIV 5 neurons overexpressing CAMSAP2-GFP (F) or CAMSAP3-GFP (G), fixed with GA and PFA, and stained with an AlexaFluor647-labeled  $\alpha$ -Tubulin antibody (top row) and a Atto488-labeled nanobody (VHH) against GFP (middle row). First two columns show conventional images and corresponding dSTORM reconstructions, followed by additional examples of CAMSAP2 decorated MT ends. Bottom row shows merge. Scale bars are 5  $\mu$ m, except (F) and (G), which are 1  $\mu$ m.

(H) Representative image of a dendritic segment from a hippocampal neuron (DIV 1) expressing mCherry-MT+TIP marker (red) and GFP-CAMSAP2 (green). Top row shows various examples. Yellow arrowheads indicate the MT plus-end; green arrowheads indicate the GFP-CAMSAP2-positive MT minus-end. Scale bars are 1 and 5  $\mu$ m.

(I and J) Stills from TIRFM time-lapse recording of DIV 1 (I) and DIV 5 (J) neuron similar to (H). Scale bar is 1  $\mu$ m.

(K) Kymograph of the yellow line (2.5  $\mu$ m) shown in (J).

### Small CAMSAP2 Clusters Are Transformed to Extended Stretches

To characterize the dynamics of CAMSAP2-positive structures in primary dendrites of mature neurons, we examined the fluorescence recovery after photobleaching (FRAP) of GFP-CAMSAP2 stretches. On average, GFP-CAMSAP2 fluorescence recovered to  $33\% \pm 1\%$  of prebleached intensity after  $\sim 10$  min with an average recovery half-time of  $206 \pm 20$  s (Figure 3A). This recovery of CAMSAP2 is remarkably slow and incomplete when compared to the MT-associated protein MAP2, which recovered to  $77\% \pm 1\%$  of prebleached intensity after  $\sim 10$  min with an average recovery half-time of  $106 \pm 6$  s. Interestingly, while a small recovery was observed along the length of the stretch, strong signals appear at the outmost edges of these structures (Figures 3B and 3C; Movie S5), suggesting that CAMSAP2 dynamics is increased at specific foci. To explore this phenomenon in more detail, GFP-CAMSAP2 recovery was monitored for extended periods ( $>30$  min) in several stretches along the dendrite (Figures 3D–3F; Movie S6). CAMSAP2 stretches are highly dynamic along the dendritic shaft and recover as small clusters that typically grow from one side toward either the proximal or distal site of the dendrite (Figures 3E and 3F). The elongating CAMSAP2 stretches occasionally pause or shrink before continuing growing into longer stretches (Figures 3E and 3F). These results demonstrate that small CAMSAP2 clusters are transformed to extended stretches. This data suggest that, in neurons, MT minus-ends can slowly grow and be stabilized by accumulation of CAMSAP2, explaining the existence of very long stretches in older neurons.

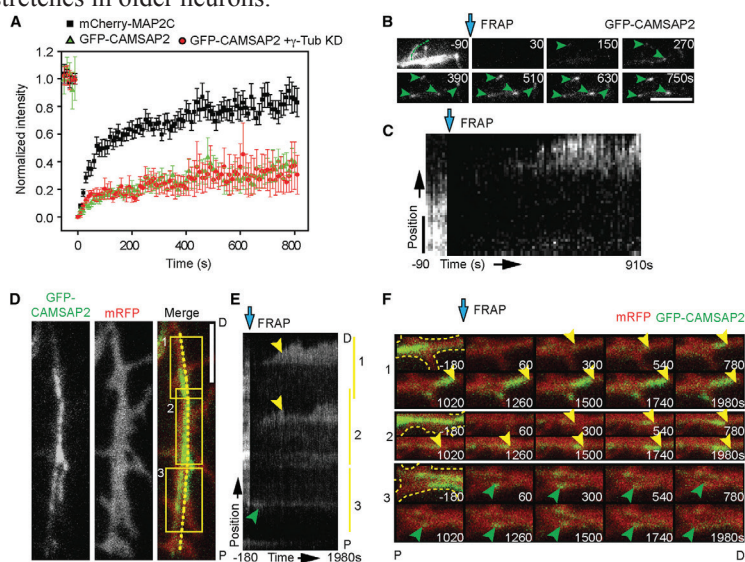


**Figure 3. Elongating CAMSAP2 Clusters Form Extended Stretches in Neurons**

(A) FRAP experiment intensity time traces of mCherry-MAP2C and pSuper ( $n = 12$ , black squares), GFP-CAMSAP2 and pSuper ( $n = 8$ , green triangles), or GFP-CAMSAP2 and  $\gamma$ -Tubulin shRNA ( $n = 5$ , red circles). FRAP was performed on GFP-CAMSAP2 stretches at  $t = 0$ . Error bars represent SEM.

(B) Stills from a TIRFM time-lapse recording of a neuron transfected with GFP-CAMSAP2. Green arrowheads point out recovery of specific points after photobleaching. Scale bar is  $5 \mu\text{m}$ .

(C) Kymograph of a TIRFM time-lapse recording corresponding to the dashed green line in (B). Blue arrows indicates the FRAP ( $t = 0$ ). Scale bar is  $1 \mu\text{m}$ .

(D) Still frame from TIRFM time-lapse recording of a DIV 24 hippocampal neuron expressing mRFP (red) and GFP-CAMSAP2 (green). D indicates the distal end and P indicates the proximal end of the dendrite.

(E) Kymograph from the TIRFM time-lapse recording in (D). Green arrow heads indicate GFP-CAMSAP2 elongating toward the cell body; yellow arrowheads indicate GFP-CAMSAP2 growing away from the cell body.

(F) Still frames corresponding to the boxed regions of the TIRFM time-lapse recording in (D). See also Movie S5 and S6.

### **CAMSAP2 Depletion Reduces MT Density in Neurons**

To examine the function of CAMSAP2 in neuronal cells, we next used RNAi to suppress endogenous CAMSAP2 in developing (DIV 5) and mature (DIV 21) hippocampal neurons and analyzed the MT cytoskeleton. The efficiency of CAMSAP2 protein depletion was tested by introducing two independent CAMSAP2 shRNAs into neuronal cultures by lentiviral transduction. Western blot analysis revealed that both CAMSAP2 shRNAs reduced the levels of CAMSAP2 by ~85% (Figure 4A). Immunostaining experiments confirmed that CAMSAP2 intensity was strongly decreased in neurons expressing CAMSAP2 shRNA (Figures 4B and S4A–S4D). The level of polymerized MTs in neurons was analyzed by Tubulin pre-extraction, followed by measurement of endogenous MAP2 fluorescent staining intensity in CAMSAP2 shRNA-expressing neurons compared to the nontransfected neurons in the same field of view (Figure 4C). In DIV 5 neurons expressing CAMSAP2 shRNA, the MAP2 staining was reduced by ~80% compared to control cells (Figure 4E). This reduction greatly exceeded the effect of the potent MT-depolymerizing drug nocodazole (40% reduction; Figure 4F), suggesting that in the latter case the remaining MT network was stabilized by CAMSAP2.

In addition, the number of growing MT plus-ends was analyzed by immunostaining for endogenous EB3 upon knock-down of CAMSAP2. All control and shRNA expressing neurons showed the characteristic comet-like MT plus-end patterns (Jaworski et al., 2009), but the number of comets was markedly decreased in cells depleted of CAMSAP2 (Figure 4D). In young neurons at DIV 5, a decrease of ~30% of EB3 comets in axons, dendrites, and soma was found in CAMSAP2 shRNA-expressing neurons compared to control cells (Figure 4G). In mature neurons at DIV 21, the number of EB3 comets in the soma was only reduced by ~20% in CAMSAP2 knockdown cells (Figure 4H), while the number of comets in the primary and secondary dendrites was decreased by ~70% (Figures 4I and 4J). Live-cell imaging of EB3-GFP-labeled growing MT plus-ends confirmed these results: the number of EB3-GFP comets was decreased in CAMSAP2 knockdown neurons, but other parameters, such as the average growth velocity and the direction of displacement (retrograde versus anterograde), were not affected (data not shown). These data demonstrate that CAMSAP2 is important to establish and maintain the MT network in developing and mature neurons.

### **CAMSAP2 and $\gamma$ -Tubulin Are Both Required for Noncentrosomal MTs**

Because both CAMSAP2 and  $\gamma$ -Tubulin associate with MT minus-ends, we next investigated the relationship between  $\gamma$ -Tubulin and CAMSAP2 in neurons. We used RNAi to suppress endogenous  $\gamma$ -Tubulin in hippocampal neurons and analyzed the subcellular distribution and dynamics of CAMSAP2. Immunostaining experiments confirmed that  $\gamma$ -Tubulin was strongly downregulated in the cytoplasm of shRNA-expressing neurons (Figures S4E and S4F). Similar to the knockdown of CAMSAP2, the intensity of MAP2 and EB3 in  $\gamma$ -Tubulin-depleted neurons was markedly decreased (Figures 4E–4J), which is consistent with a role for  $\gamma$ -Tubulin in the nucleation of noncentrosomal MTs (Stiess et al., 2010).  $\gamma$ -Tubulin knockdown also reduced the intensity of CAMSAP2 by ~70% compared to control cells (Figures S4G and S4H). A similar decrease in CAMSAP2 staining was obtained by depleting two other subunits within the  $\gamma$ -Tubulin ring complex ( $\gamma$ -TuRC),  $\gamma$ -Tubulin complex-associated proteins GCP2 and GCP6 (Figures S4G and S4H). Importantly, simultaneous depletion of  $\gamma$ -Tubulin and CAMSAP2 showed no additive effect in the reduction of MT density (Figures 4E–4J), suggesting that the two proteins mostly operate in the same pathway.

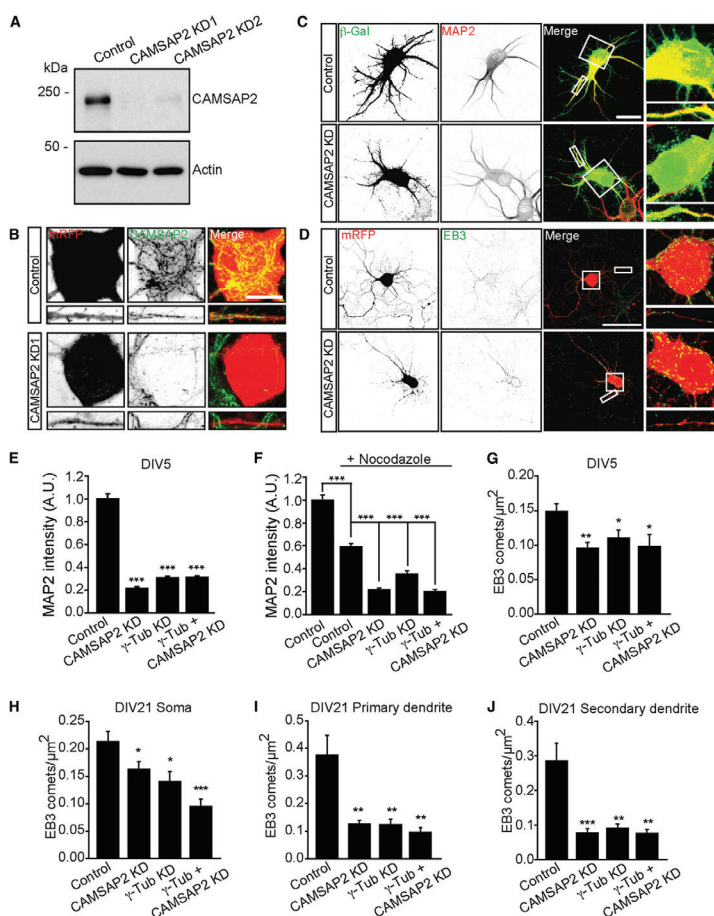


**Figure 4. CAMSAP2 Stabilizes Microtubules in Neurons**

(A) Extracts of DIV 25 hippocampal neurons sequentially infected at DIV 15 and DIV 20 with pSuper control, CAMSAP2-shRNA1 (KD1), and CAMSAP2-shRNA2 (KD2) lentivirus. Samples were analyzed by western blot with indicated antibodies.

(B) Representative images of hippocampal neurons transfected (DIV22) with mRFP (red) and pSuper (control) or CAMSAP2-shRNA1 (KD1) and stained for CAMSAP2 (green). Scale bar is 10  $\mu$ m.

(C) Hippocampal neurons transfected at DIV 1 with  $\beta$ -galactosidase (green) and pSuper or CAMSAP2-shRNA, pre-extracted, fixed, and stained for MAP2 (red) at DIV 5. Scale bar is 20  $\mu$ m.

(D) Hippocampal neurons at DIV 1 transfected with mRFP (red) and pSuper or CAMSAP2-shRNA, fixed, and stained for EB3 (green) at DIV 5. Scale bar is 50  $\mu$ m

(E) Diagram showing the normalized mean intensity of MAP2 in dendritic regions from DIV 5 neurons expressing control pSuper (n = 26), CAMSAP2-shRNA (n = 23),  $\gamma$ -Tubulin-shRNA (n = 20), or both CAMSAP2-shRNA and  $\gamma$ -Tubulin-shRNA (n = 20). AU, arbitrary unit.

(F) Diagram showing the normalized mean intensity of MAP2 in dendritic regions from neurons, which have been untreated (n = 26) or treated with 30  $\mu$ M nocodazole transfected as in (E) (n = 19, n = 15, n = 13, and n = 15, respectively). AU, arbitrary unit.

(G) Diagram showing the average number of EB3 comets/ $\mu$ m<sup>2</sup> in DIV 5 neurites transfected as in (E) at DIV 1 (n = 11, n = 11, n = 11, and n = 12, respectively). (H) Diagram showing the average number of EB3 comets/ $\mu$ m<sup>2</sup> in DIV 21 soma transfected as in (E) at DIV 17 (n = 16, n = 19, n = 10, and n = 12, respectively). (I) Diagram showing the average number of EB3 comets/ $\mu$ m<sup>2</sup> in DIV 21 primary dendrites transfected as in (E) at DIV 17 (n = 16, n = 19, n = 10, and n = 12, respectively).

(J) Diagram showing the average number of EB3 comets/ $\mu$ m<sup>2</sup> in DIV 21 secondary dendrites transfected as in (E) (n = 16, n = 19, n = 10, and n = 12, respectively).

Error bars represent SEM. \*p < 0.05; \*\*p < 0.01; \*\*\*p < 0.001 (t test). See also Figure S4.

To test whether GFP-CAMSAP2 localization to minus-ends directly depends on  $\gamma$ -Tubulin, we next used laser-based microsurgery to generate new MT ends (Figure 5A) and measure GFP-CAMSAP2 dynamics in control and  $\gamma$ -Tubulin-depleted cells. Upon laser-induced severing, GFP-CAMSAP2 was rapidly recruited to the newly generated MT minus-ends in both COS7 cells and neurons (Figures 5B–5G). Interestingly, repetitive MT plus-end growth and shrinkage was also observed from newly formed CAMSAP2 clusters (Figures 5B–5E; Movie S7), indicating that CAMSAP2 binding protects both sides of the decorated MT segments from depolymerization, consistent with *in vitro* observations (Jiang et al., 2014). The dynamics of GFP-CAMSAP2 accumulation upon laser-induced severing in  $\gamma$ -Tubulin knockdown neurons was indistinguishable from control cells (Figures 5F and 5G; Movie S8), indicating that CAMSAP2 can localize to MT minus-ends independent of  $\gamma$ -Tubulin. FRAP experiments with GFP-CAMSAP2 stretches in primary dendrites of  $\gamma$ -Tubulin knockdown neurons showed that although the number of events was reduced due to the decrease in overall MT density, the recovery rate and recovery levels were similar to the control cells (Figure 3A). The finding that  $\gamma$ -Tubulin depletion affects the number of CAMSAP2-decorated MT minus-ends but not the CAMSAP2 behavior is consistent with the *in vitro* data showing that CAMSAP family proteins accumulates on free, growing MT minus-ends, which are expected to lack  $\gamma$ -Tubulin (Goodwin and Vale, 2010; Jiang et al., 2014). Together, these data suggest that CAMSAP2 likely acts independently of  $\gamma$ -Tubulin at the molecular level but might act downstream after the generation of *de novo* noncentrosomal neuronal MT by  $\gamma$ -Tubulin.

### **CAMSAP2 Is Required for Dendrite Development and BDNF-Induced Dendritic Growth**

Stable MTs are important for both dendrite development and maintenance (Conde and Cáceres, 2009). To determine whether CAMSAP2 controls normal dendrite morphology, we examined the effect of CAMSAP2 knockdown on dendrites in developing (DIV 5) and mature (DIV 20) hippocampal neurons using the two CAMSAP2 shRNAs. In both cases, we observed a marked change in dendrite morphology (Figures 6A and 6B). Dendritic length was decreased by ~30% in CAMSAP2 knockdown DIV 5 neurons compared to the control (Figure 6C). Moreover, knockdown of CAMSAP2 decreased the number of dendritic branches and total dendritic complexity, whereas the number of primary dendrites was not significantly changed (Figures 6C and 6D). A similar morphological phenotype was observed in mature neurons (Figures 6B, 6F, and 6G), indicating that CAMSAP2 is important for both dendritic development and maintenance. To obtain further insight in how CAMSAP2 regulates dendrite development, we determined whether the minimal CAMSAP2 domain required for minus-end binding (CC2-CC3-CKK, Figure S5) is sufficient to rescue the dendritic phenotype. Neurons were co-transfected at DIV 17 with CAMSAP2- shRNA and full-length GFP-CAMSAP2 or GFP-CC2-CC3-CKK for 4 days. This experiment showed that GFP-CAMSAP2 can restore the knockdown phenotype, while GFP-CC2-CC3-CKK expression was unable to rescue the CAMSAP2 phenotype (Figures 6K and 6L). These findings show that the minimal CAMSAP2 minus-end binding domain is not sufficient to restore dendrite morphology, suggesting that additional domains of CAMSAP2 are critical for CAMSAP2 function.

To further examine the role of CAMSAP2 in dendrite development, we compared the effect of BDNF in control and CAMSAP2 knockdown cells. BDNF causes dendritic growth in hippocampal neurons (Cheung et al., 2007). The control DIV 22 neurons cultured in the presence of 50 ng/ml BDNF for 3 days acquired ~41% additional dendrites (Figures 6I and 6J). In contrast, BDNF-induced dendrite formation did not occur in neurons expressing CAMSAP2 shRNA (Figures 6I and 6J). Together, these data demonstrate that CAMSAP2 is

required for normal dendrite morphology and BDNF-induced dendritic growth.

Similar to knockdown of CAMSAP2,  $\gamma$ -Tubulin depletion also strongly reduced dendritic complexity in young and mature neurons (Figures 6E and 6H). Next, we tested whether CAMSAP2 acts upstream or downstream of  $\gamma$ -Tubulin in regulating dendrite morphology. While overexpression of GFP-CAMSAP2 partly restored the dendritic complexity in  $\gamma$ -Tubulin-depleted neurons (Figure 6N), GFP- $\gamma$ -Tubulin expression was unable to rescue the CAMSAP2 phenotype (Figure 6M). These data suggest that CAMSAP2 expression is to some extent able to stabilize dendritic MTs and reverse the effects of  $\gamma$ -Tubulin knock-down. Together, these results demonstrate that CAMSAP2 and  $\gamma$ -Tubulin are important to maintain noncentrosomal MT arrays and dendrite morphology and that these factors might act sequentially:  $\gamma$ -Tubulin initiates the formation of de novo noncentrosomal MTs while CAMSAP2 stabilizes them.

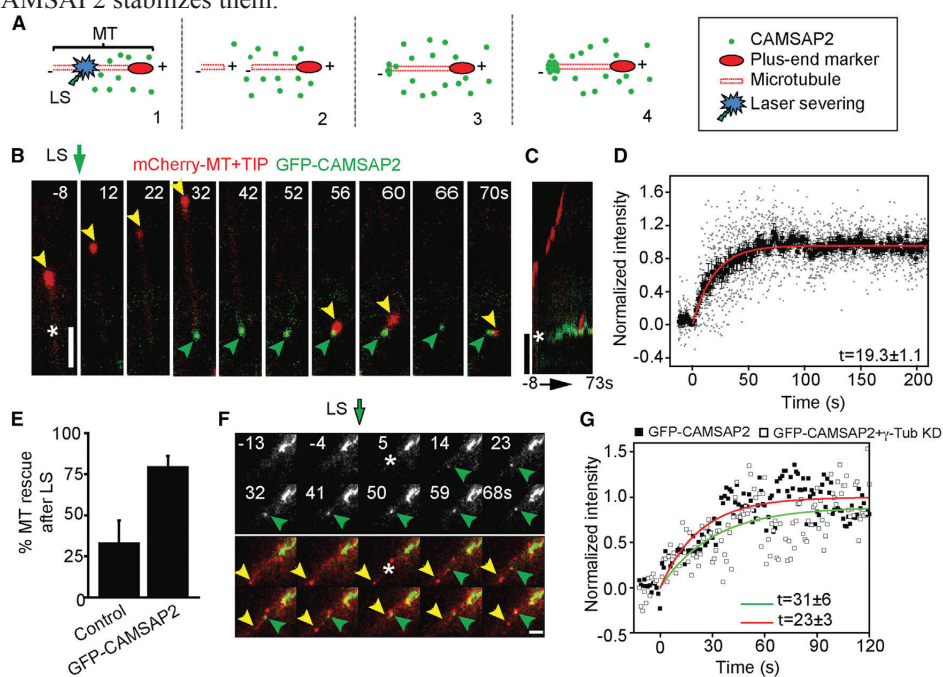


**Figure 5. CAMSAP2 Can Localize to Microtubule Minus-Ends Independent of  $\gamma$ -Tubulin**

(A) Schematic representation of MT laser-induced severing.

(B) Stills from a TIRFM time-lapse recording of a COS-7 cell expressing mCherry-MT+TIP (red) and GFP-CAMSAP2 (green). The yellow arrowheads indicate the MT plus-end marker. Green arrowheads indicate GFP-CAMSAP2 accumulating on MT minus-ends. Asterisk indicates the location of laser-induced severing at  $t = 0$ .

(C) Kymograph of the time-lapse recording shown in (B). Scale bars are  $2 \mu\text{m}$ .

(D) GFP-CAMSAP2 intensity time trace of individual MT minus-ends (gray squares) and average trace (black squares)  $n = 10$ . Single exponential fit of the data average points is shown in red.

(E) Quantification of the percentage of MTs that are rescued after laser-induced severing after expression of GFP-CAMSAP2 ( $n = 4-6$ ).

(F) Representative time-lapse recording of a hippocampal neuron (DIV 1) expressing GFP-CAMSAP2 (green) and mCherry-MT+TIP (red). Green arrowheads indicate GFP-CAMSAP2 accumulation, yellow arrowheads indicate MT plus-end, and the asterisk indicates the area of laser-induced severing. Scale bar is  $1 \mu\text{m}$ .

(G) GFP-CAMSAP2 intensity time trace (black squares) of a TIRFM time-lapse recording; single exponential fit of the data points is shown in red. The white squares correspond to the intensity time trace of neurons transfected with GFP-CAMSAP2 and  $\gamma$ -Tubulin shRNA; single exponential fit of the data points is shown in green. Error bars represent SEM.

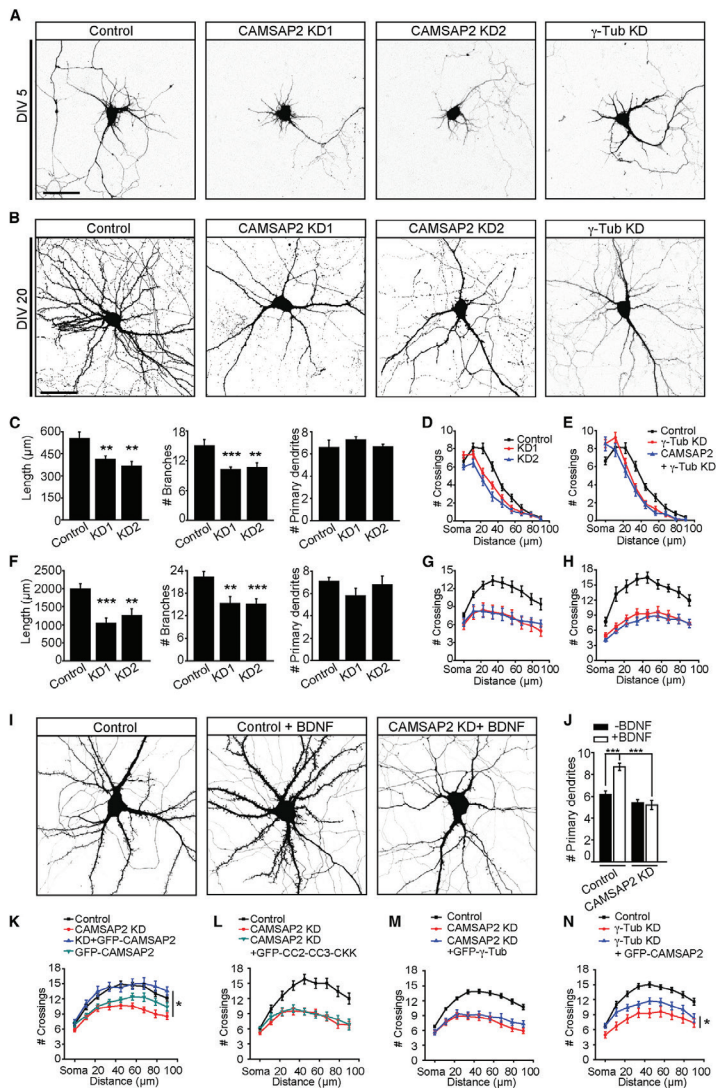


**Figure 6. CAMSAP2 Is Required for Dendrite Morphology**

(A) Representative images of DIV 5 hippocampal neurons transfected at DIV 1 with mRFP and control pSuper, CAMSAP2-shRNA1 (KD1), CAMSAP2-shRNA2 (KD2) or  $\gamma$ -Tubulin-shRNA.

(B) Representative images of DIV 20 hippocampal neurons transfected at DIV 16 with  $\beta$ -galactosidase alone or with CAMSAP2-shRNA1, CAMSAP2-shRNA2, or mRFP and  $\gamma$ -Tubulin-shRNA. Scale bars are 50  $\mu$ m.

(C) Quantification of dendrite morphology. Number of dendrites, branches, and total dendrite distance are determined from DIV 5 neurons transfected with control pSuper (n = 18), CAMSAP2-shRNA1 (n = 22) or CAMSAP2-shRNA2 (n = 17).

(D) Sholl analysis corresponding to the data used in (C).

(E) Sholl analysis of DIV 5 neurons transfected at DIV 1 with mRFP and control pSuper (n = 18),  $\gamma$ -Tubulin-shRNA (n = 22), or the combination of  $\gamma$ -Tubulin-shRNA and CAMSAP2-shRNA1 (n = 17).

(F) Quantification of the number of dendrites, branches, and total dendrite distance are determined from DIV 20 neurons transfected with control pSuper (n = 25), CAMSAP2-shRNA1 (n = 13), or CAMSAP2-shRNA2 (n = 13).

(G) Sholl analysis corresponding to the data in (F).

(H) Sholl analysis of DIV 22 neurons transfected at DIV 18 with mRFP and control pSuper (n = 11),  $\gamma$ -Tubulin-shRNA (n = 13), or the combination of  $\gamma$ -Tubulin-shRNA and CAMSAP2-shRNA1 (n = 15). (Figure legend continues on the next page)

### Neuronal Activity Activation Affects the Distribution of CAMSA2 in Dendrites

Previous studies have shown that neuronal activity modulates the stability of the MT arrays in dendrites (Halpain and Greengard, 1990). For instance, transient glutamate receptor activation suppresses MT growth and density (Kapitein et al., 2011). We next determined whether glutamate stimulation affects the distribution of CAMSA2-decorated MT minus-ends in dendrites. Upon treatment with 50  $\mu$ M glutamate for 5 min, the staining of CAMSA2 stretches was markedly decreased and replaced by a more diffuse cytoplasmic signal within the dendrites, which could be blocked by the NMDA receptors antagonist APV (Figures S6A and S6B). In contrast, blocking either AMPA-type and kainate receptors (CNQX) or metabotropic glutamate receptors (AIDA) did not prevent the decrease in CAMSA2 intensity at the dendrites (Figure S6B). We next determined whether a protocol to induce chemical LTD affects CAMSA2 localization. Bath application of 50  $\mu$ M NMDA for 5 min markedly decreased the intensity of the CAMSA2-positive stretches in dendrites (Figures S6A and S6C). In mature hippocampal neuronal cultures, signaling through NMDA receptors mainly occurs through either NR2A- or NR2B-containing receptors. Using shRNA constructs that reduce the expression of NR2A and/or NR2B, we found that the knockdown of NR2B rather than NR2A blocked the NMDA-dependent CAMSA2 redistribution (Figures S6A and S6C). Next we investigated GFP-CAMSA2 dynamics upon NMDA stimulation. Consistent with the immunohistochemical data, NMDA stimulation induced a strong and rapid decrease in the intensity of the CAMSA2-positive stretches in dendrites (Figure S6D). This effect started within the first minute after NMDA stimulation and persisted until GFP-CAMSA2 signals fully disappeared,  $\sim$ 10 min after treatment (Figure S6E). See also Figure S3 and Movies S1, S2, S3, and S4. Together, these data demonstrate that neuronal activity affects the distribution of CAMSA2 in dendrites, which could explain the observed decrease in MT density after NMDA receptor stimulation (Kapitein et al., 2011).

### CAMSA2 Is Required for MT Stabilization during Neuronal Polarization

It is well known that the MT cytoskeleton is also important during early neuronal development, and changes in MT stability markedly affect neuronal polarity (Witte and Bradke, 2008). To investigate whether CAMSA2 is directly involved in neuronal polarization, we first analyzed the distribution of endogenous CAMSA2 in hippocampal neurons at early stages of development. Upon plating, hippocampal neurons first form lamellipodia around the cell body (stage 1) followed by the formation of several processes about 6 hr later, the minor neurites (stage 2). After 20–48 hr in culture, one neurite starts to grow out quickly and becomes the axon (stage 3), which can initially be labeled with the axonal marker Tau

*(Figure legend continued from previous page)*

*(I) Representative images of DIV 22 neurons transfected with mRFP and pSuper control or CAMSA2-shRNA1 at DIV 18 and untreated or treated with 50 ng/ml BDNF for 3 days.*

*(J) Quantification of the number of primary dendrites untreated (n = 28) and treated with 50 ng/ml BDNF for 3 days and transfected control pSuper (n = 50) or CAMSA2-shRNA1 (n = 29-32 treated) at DIV 18. Neurons were fixed at DIV 22.*

*(K) Sholl analysis of DIV 21 neurons transfected at DIV 17 with pSuper (n = 40), CAMSA2-shRNA (n = 30), GFP-CAMSA2 (n = 21), or CAMSA2-shRNA and GFP-CAMSA2 (n = 16).*

*(L) Sholl analysis of DIV 21 neurons transfected at DIV17 with pSuper (n = 16), CAMSA2-shRNA (n = 15), CAMSA2-shRNA, and GFP-CC2-CC3-CKK (n = 15). (M) Sholl analysis of DIV 21 neurons transfected at DIV 17 with control pSuper (n = 48), CAMSA2-shRNA (n = 28), or CAMSA2-shRNA1 and GFP- $\gamma$ -Tubulin (n = 18).*

*(N) Sholl analysis of DIV 21 neurons transfected at DIV 17 with control pSuper (n = 34),  $\gamma$ -Tubulin-shRNA (n = 13), or  $\gamma$ -Tubulin-shRNA and GFP-CAMSA2 (n = 24). Error bars represent SEM. \*p < 0.05; \*\*p < 0.01; \*\*\*p < 0.001 (t test). See also Figures S5 and S6.*

and later on with axon initial segment (AIS) markers, such as Ankyrin G,  $\beta$ IV-Spectrin, and sodium channels (pan-Nav). As reported previously (Stiess et al., 2010), distinct centrosomal components disappeared from the MTOC during neuronal development and dispersed throughout the cytoplasm at later stages (Figure S7), consistent with a shift from centrosomal to noncentrosomal nucleation. Indeed, dSTORM imaging revealed that, whereas in DIV1 cells many MTs emanated radially from the centrosome, DIV5 neurons had a nonaxonal MT organization with many free CAMSAP-decorated minus ends (Figures 2 and S6).

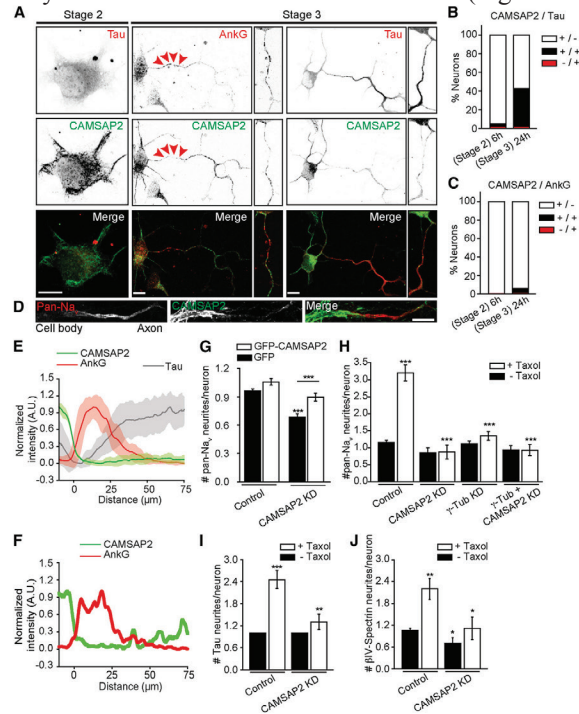


**Figure 7. CAMSAP2 Is Required for Axon Formation and Neuronal Polarization**

(A) Representative images of DIV 1 hippocampal neurons double stained for endogenous Tau (red) and CAMSAP2 or endogenous Ankyrin G (red) and CAMSAP2 (green). Scale bars are 10  $\mu$ m.

(B) Diagram showing the percentage of neurons at DIV 0.25 and DIV 1 with neurites positive for endogenous CAMSAP2+/Tau+, CAMSAP2+/Tau-, and CAMSAP2-/Tau+ (n = 150).

(C) Diagram showing the percentage of neurons at DIV 0.25 and DIV 1 with neurites positive for endogenous Ankyrin G+/Tau+, Ankyrin G+/Tau-, and Ankyrin G-/Tau+ (n = 150).

(D) Representative image of an axonal segment from DIV 21 neuron stained for CAMSAP2 and axon initial segment marker, pan-Nav. Scale bar is 10  $\mu$ m.

(E and F) Profiles of CAMSAP2 (green), Ankyrin G (red trace), and Tau (gray trace) fluorescence intensity in the axon of neurons at DIV 7. Examples of average intensity traces of at least 19 neurons for each dual staining (E) and representative single intensity traces (F). AU, arbitrary unit. Error bars represent SD.

(G) Diagram showing the number of pan-Nav- positive neurites per neuron in cortex neurons at DIV 4. Cells are electroporated before plating with pSuper control (n = 180), pSuper control and GFP-CAMSAP2 (n = 105), CAMSAP2-shRNA (n = 180), or CAMSAP2-shRNA and GFP-CAMSAP2 (n = 105) and stained for endogenous pan-Nav and CAMSAP2.

(H) Diagram showing the number of pan-Nav-positive neurites per neuron in hippocampal neurons at DIV 5; transfected at DIV 1 with mRFP and pSuper control (n = 35) or CAMSAP2-shRNA (n = 21 untreated, n = 16 treated),  $\gamma$ -Tubulin-shRNA (n = 17 untreated, n = 20 treated), CAMSAP2- shRNA, and  $\gamma$ -Tubulin-shRNA (n = 15 untreated, n = 14 treated); and untreated (n = 37) or treated with 10 nM Taxol for 48 hr.

(I and J) Diagram showing the number of Tau- or  $\beta$ IV-Spectrin-positive neurites per neuron in hippocampal neurons DIV 5, transfected with mRFP and pSuper control (n = 11) or CAMSAP2-shRNA (n = 10 untreated, n = 10 treated), and untreated (n = 17) or treated with 10nM Taxol for 48 hr. Error bars represent SEM. \*p < 0.05; \*\*p < 0.01; \*\*\*p < 0.001 (t test). See also Figures S7 and S8.

At 6 hr, all morphologically unpolarized neurons stained positively for endogenous CAMSAP2, showing puncta and small clusters in the soma and minor neurites (Figure 7A), and stained negatively for axonal marker Tau and the earliest AIS marker Ankyrin G (Figures 7B and 7C). Thus, CAMSAP2 is already expressed in stage 2 cells before the neurons form an axon and polarize. At 24 hr, polarized neurons maintained CAMSAP2 expression within the soma, neurites, and Tau-positive axon (Figures 7A–7C). Interestingly, CAMSAP2 was present at low levels at the AIS region but enriched in the proximal part of the soma to the axon (Figure 7A). Closer inspection indicated that CAMSAP2 was abundant in the soma and in the first part of the axons, but not in the AIS, and was also present as small clusters and distinct stretches in the proximal axonal compartment directly after the AIS (Figure 7D). The high levels of CAMSAP2 at proximal part of the axon, right before the start of the AIS, was consistent across the neuronal population and maintained throughout neuronal development (Figures 7E and 7F).

To determine whether CAMSAP2 is involved in neuronal polarization, we knocked down CAMSAP2 before polarization in stage 1–2 neurons. Directly after dissection, primary cortical neurons were electroporated to deliver CAMSAP2 shRNA. At DIV 4, we determined the number of polarized neurons using the AIS marker pan-Nav and found a reduced fraction of polarized cells compared to control cells (Figure 7G), indicating that CAMSAP2 contributes to neuronal polarization. To further test whether CAMSAP2 plays a role in MT stabilization during axon initiation and specification, we used the MT-stabilizing drug taxol to induce multiple axon formation (Witte et al., 2008). In the presence of low concentrations of taxol (10 nM) for 2 days, the number of pan-Nav positive processes per cell was increased more than 3-fold in control neurons (Figure 7H). However, such taxol-induced axonal processes did not emerge in neurons expressing CAMSAP2 shRNA. The same phenotype was also observed after  $\gamma$ -Tubulin depletion (Figure 7H). Similar results were obtained by analyzing the axon-specific marker Tau and AIS marker  $\beta$ IV-Spectrin (Figures 7I and 7J). These *in vitro* data suggest that CAMSAP2 is required for axon specification.

### **CAMSAP2 Is Required for Axon Formation and Neuronal Polarity In Vivo**

In the developing neocortex after terminal cell division, highly polarized neurons with a trailing process (future axon) and a unipolar leading process (future apical dendrite) are formed during neuronal migration (Barnes and Polleux, 2009). To investigate the effect of CAMSAP2 depletion in newborn neurons in the neocortex, we first performed *ex vivo* electroporation followed by organotypic slice cultures. E14.5 mouse embryos were subjected to intracranial electroporation to introduce GFP and CAMSAP2 shRNA plasmids selectively into neuronal precursors in the ventricular zone (VZ) (Figure 8A). Cortical slices were then prepared and cultured for 3 days to allow the labeled neurons to polarize and migrate to the cortical plate (CP) in a manner highly similar to that observed *in vivo*. Control GFP-positive neurons migrated to the CP (Figure 8B), while many CAMSAP2-depleted neurons accumulated in the (sub)ventricular zone (SVZ/VZ) and failed to migrate properly (Figure 8C), indicating that CAMSAP2 knockdown impairs neuronal migration in a cell-autonomous manner.

We next performed *in utero* electroporation for detailed analysis of neuronal morphogenesis. Following electroporation at E14.5, embryos were allowed to develop for 3 days (E17.5), at which point the morphology of GFP-positive migrating neurons was examined. In littermate controls, most GFP-positive migrating neurons possessed stereotypical bipolar morphologies consisting of a leading process and a long trailing edge axon (Figure 8D). In contrast, cells expressing GFP and CAMSAP2 shRNA failed to form a distinguishable axon and the leading edge process (Figure 8E). Moreover, whereas GFP-positive axons projecting through the

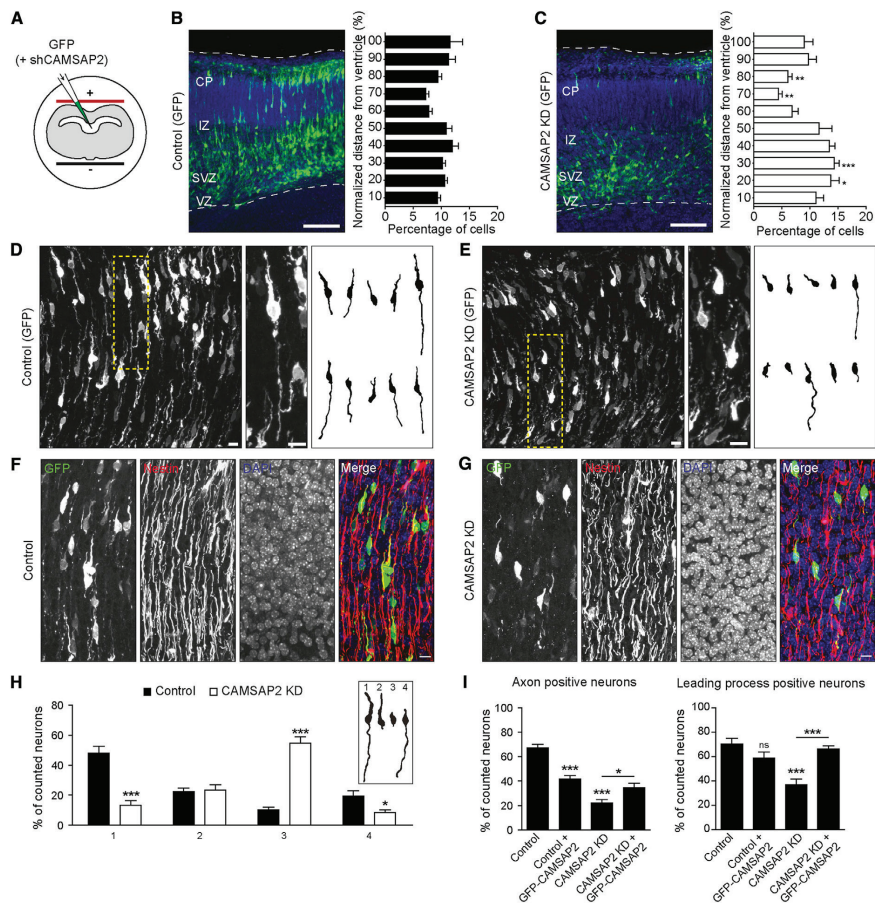


**Figure 8. CAMSAP2 Is Required for Axon Initiation and Neuronal Polarity In Vivo**

(A) Schematic cross section of the ex vivo electroporation procedure: E14.5 intact mouse embryo head were injected in the lateral ventricle with GFP alone or together with two CAMSAP2 shRNAs (shRNA1/2), electroporated, and followed by immediately slicing of the brains before subjecting them to organotypic slice culture for 4 days.

(B and C) Maximum intensity projection of ex vivo neuronal migration of GFP-positive neurons electroporated with either GFP only (B) or GFP and CAMSAP2 shRNAs (C). Bar diagram shows the normalized migration distribution along the radial axis from the ventricle. CP, cortical plate; IZ, intermediate zone; SVZ, subventricular zone; VZ, ventricular zone; scale bars, 100  $\mu$ m; \* $p$  < 0.05; \*\* $p$  < 0.01; \*\*\* $p$  < 0.001, comparing corresponding bins using a Mann-Whitney U Test.

(D and E) Neuron morphology (E17.5) of in utero electroporated (E14.5) mouse embryo brains. Morphology (maximum intensity projection) shown of neurons electroporated with either GFP only (D) or GFP and CAMSAP2 shRNAs (E). Middle panel contains a zoom of a typical neuron. Right panel contains individual traces of representative neurons found in the specific condition. Scale bars, 10  $\mu$ m.

(F and G) Maximum intensity projection of GFP and Nestin staining (E17.5) of in utero electroporated (E14.5) mouse embryo brains. Brains were electroporated with either GFP only (F) or GFP and CAMSAP2 shRNAs (G). Scale bars are 10  $\mu$ m.

(H) Quantification of the different (GFP-positive) neuronal cell morphologies found in the E17.5 brain after in utero electroporation (E14.5). \* $p$  < 0.05; \*\* $p$  < 0.01; \*\*\* $p$  < 0.001, comparing control versus shCAMSAP2 using a Mann-Whitney U Test.

(I) Quantification of the axon-positive and GFP-positive neurons (left graph), as well as the quantification of the leading-process-positive and GFP-positive neurons (right graph) found in the E17.5 brain after in utero electroporation (E14.5). Comparing control versus control and GFP-CAMSAP2, control versus shCAMSAP2, and shCAMSAP2 versus shCAMSAP2 and GFP-CAMSAP2 using a Mann-Whitney U Test. \* $p$  < 0.05; \*\* $p$  < 0.01; \*\*\* $p$  < 0.001.

intermediate zone (IZ) were observed in control animals, such structures were not seen in CAMSAP2 shRNA-expressing animals (Figures 8D and 8E). In contrast, the radial glial cell fibers, expressing nestin, were not affected by CAMSAP2 shRNA expression (Figures 8F and 8G). Quantification revealed that ~80% of control neurons possessed a morphologically discernible leading process compared to ~30% of CAMSAP2-depleted cells (Figures 8H and 8I). Moreover, whereas ~70% of control cells in the IZ possessed axons, only ~20% of CAMSAP2 knockdown cells had discernible axons (Figures 8H and 8I). Together, these findings demonstrate that CAMSAP2 is critical for axon formation and the establishment of neuronal polarity in the developing neocortex.

### DISCUSSION

Recent studies have identified different MT-mediated processes involved in regulating neuron polarization, development, and function (Conde and Cáceres, 2009; Hoogenraad and Bradke, 2009). MT minus-end dynamics has remained one of the least well-understood properties of the MT cytoskeleton in neurons. Especially, the mechanisms stabilizing the free noncentrosomal MT minus-ends have remained elusive. In this study, we demonstrate that by stabilizing minus-ends of noncentrosomal MTs, CAMSAP2 contributes to MT organization in developing and mature neurons, playing an important role in axon specification and dendritic branch formation *in vitro* and *in vivo*. In addition, similar to the widely used plus-end binding proteins to track growing MTs (Jaworski et al., 2009; Stepanova et al., 2003), the endogenous or fluorescently tagged CAMSAP2 provides a new molecular tool to identify noncentrosomal minus-ends and probe the MT organization in neuronal cells.

### CAMSAP2 Stabilizes Noncentrosomal Minus-Ends in Neurons

Neuronal development and differentiation require sophisticated architectural changes, which may be incompatible with a large MT network emanating from a single MTOC (Kuijpers and Hoogenraad, 2011; Stiess and Bradke, 2011). Indeed, it has been shown that the centrosome loses its function as an MTOC during early neuronal development and that noncentrosomal MT arrays within axonal and dendritic processes acquire distinct organization patterns at later developmental stages (Baas et al., 1989; Stiess et al., 2010). In this study, we show that CAMSAP2 accumulates at neuronal MT minus-ends and plays a key role in stabilizing noncentrosomal MT arrays in axons and dendrites. We also found that small CAMSAP2 structures can grow and transform into extended stretches. The dynamic behavior of CAMSAP2 in neurons is likely explained by our recent data showing that CAMSAP proteins decorate growing MT minus-ends (Jiang et al., 2014. See also Movie S7 and S8). Although it is generally believed that MT minus-ends do not to grow (Dammermann et al., 2003), the numerous elongating CAMSAP2 stretches in various parts of the dendrites instead suggest that MT minus-end growth events frequently occur in hippocampal neurons. Since the length of the CAMSAP2 structures markedly changes during neuron differentiation, this might indicate that MT minus-end growth is developmentally regulated. Moreover, the need for MT minus-end growth to generate long CAMSAP2 stretches implies that CAMSAP proteins likely act on free MT minus-ends that are not capped by  $\gamma$ -Tubulin or other factors. Indeed, we found that when already existing MTs are severed, CAMSAP2 is able to accumulate at the newly created MT minus-ends independently of  $\gamma$ -Tubulin.

CAMSAP2 is dynamic at the outmost edges of a bleached stretch, while CAMSAP2 is stably present along the length of the stretch. Once localized at the minus-ends, CAMSAP2 could act as a critical minus-end recognition signal involved in the recruitment and assembly of other factors to one specific MT end, similar to end-binding (EB) proteins at the plus-ends (Jiang et al., 2012). Our finding that the minimal CAMSAP2 minus-end binding domain

(CC2-CC3-CKK) is not sufficient to restore dendrite morphology suggests that other domains and potential binding partners are involved in CAMSAP2 functions in neurons. Additional studies are required to investigate such mechanisms and for the identification of CAMSAP2 binding partners.

### **CAMSAP2 Is Required for Axon Specification and Neuronal Polarization**

Axon formation during neuronal polarization is associated with increased MT stability (Hoogenraad and Bradke, 2009; Witte and Bradke, 2008). Here we show that neurons lacking CAMSAP2 fail to initiate axon formation and show impaired neuronal polarization during *in vitro* and *in vivo* development. The defects in neuronal migration upon CAMSAP2 depletion might be caused by the lack of polarization in the developing neocortex. Since CAMSAP2 stabilizes the neuronal MT arrays, these data suggest that noncentrosomal MT stabilization plays a critical role during the specification of axonal fate in early neuronal development. In addition, the complete block of taxol- induced axon formation in CAMSAP2-depleted neurons implies that unstable MTs and subsequent decreased MT density is sufficient to block axon specification. We found that CAMSAP2 was present in the soma and small processes of neurons at early stages of neuron development (stage 2), before neuronal polarization and axon formation. In polarizing stage 3 neurons, CAMSAP2 staining is reduced at the AIS but enriched in the soma and in the proximal part of the axon, suggesting that there are no MT minus-ends in the AIS and that most MTs are continuous throughout the AIS. High levels of CAMSAP2 at the first part of the axon may create a local pool of stabilized MT minus-ends and promote plus-end out-oriented MT growth in axons. Interestingly, the increase in CAMSAP2 at the first part of the axon is maintained throughout neuronal development. Local MT stability at the site of axon formation has been reported to cause polarized membrane flow (Bradke and Dotti, 1997). Consistently, MT-based motor proteins such as kinesin-1/KIF5 show a higher affinity for stabilized MTs and have been found to transport several vesicular carriers into the axon (Kapitein and Hoogenraad, 2011). Future work will be needed to resolve the molecular interplay between CAMSAP2 and axonal transport during neuronal polarization. In addition, signaling molecules involved in the regulation of MT dynamics in axon formation and polarity processes should be reassessed for their potential role in regulating CAMSAP2 activity (Arimura and Kaibuchi, 2007).

### **CAMSAP2 and $\gamma$ -Tubulin Are Required for Dendrite Development**

We further demonstrated that CAMSAP2 stabilizes noncentrosomal MTs in dendrites. Since dendritic outgrowth occurs after the centrosome loses its function as an MTOC (Stiess et al., 2010), noncentrosomal MT assembly and stabilization is most likely an essential process during later stages of neuronal development. Indeed, both stable MAP2-positive and dynamic EB3-positive MTs were reduced upon CAMSAP2 knockdown. CAMSAP2-decorated MTs were enriched in primary dendrites, consistent with the large fraction of minus-end-out MTs in this part of the dendrite (Baas et al., 1989; Stepanova et al., 2003). In the absence of CAMSAP2, dendritic branching was reduced and BDNF-induced dendrite development was inhibited. Similar to mechanisms governing neuronal polarization, we propose that dendritic branches are formed and maintained by noncentrosomal MTs that are stabilized by CAMSAP2. Our finding that  $\gamma$ -Tubulin knockdown also strongly reduces the MT population in dendrites suggests that many noncentrosomal MTs are generated by local nucleation. A distinct mechanism to generate noncentrosomal MTs is by severing of preexisting MTs (Bartolini and Gundersen, 2006; Kuijpers and Hoogenraad, 2011; Stiess and Bradke, 2011). Depletion of katanin and spastin has been shown to modulate axon growth in young neurons (Yu et al., 2008), but changes in dendrite outgrowth and morphology have so far not been

reported. Moreover, in *Drosophila* class IV dendritic arborization neurons, mutations in the two major MT-severing proteins spastin and katanin do not induce noticeable dendrite phenotypes (Lee et al., 2009). In contrast, the complexity of the dendritic arbor in these neurons depends on the presence of Golgi outposts, which were shown to behave as MTOCs (Ori- McKenney et al., 2012). The fact that we observed a decrease in  $\gamma$ -Tubulin at the centrosome at early stages of development without an overall change in total protein levels suggests that similar to other systems  $\gamma$ -Tubulin regulates local MT nucleation throughout the neuron in a centrosome-independent manner. Therefore, we hypothesize that  $\gamma$ -Tubulin-dependent MT nucleation and CAMSAP2-dependent stabilization are two key features of MT organization during dendritic development. We propose a two-step model in which  $\gamma$ -Tubulin initiates the formation of noncentrosomal MTs and CAMSAP2 subsequently stabilizes the newly formed free MT minus-ends.

In summary, we demonstrate that the CAMSAP/Nezha/Patronin family protein CAMSAP2 specifically stabilizes noncentrosomal MT minus-ends and plays an important role in the development and maintenance of neuronal structure. As changes in MT organization are important for many neuronal functions, including plasticity and regeneration, we anticipate that more neuronal processes that involve CAMSAP2 will be revealed in the future.

### EXPERIMENTAL PROCEDURES

#### Antibodies and Reagents

The following antibodies were used in this study: rabbit anti-EB3 (02-1005-07) (Stepanova et al., 2003), mouse anti- $\gamma$ -Tubulin (T6557, Sigma), rabbit anti- CAMSAP1 (Novus Biologicals, NBP1-26645), rabbit anti-CAMSAP2 (17880- 1-AP, Proteintech; NBP1-21402, Novus Biologicals; HPA0273, Sigma), and rabbit anti-CAMSAP3 (Abgent, AP18323a). Details of other antibodies and reagents are in the Supplemental Experimental Procedures.

#### DNA Constructs

The CAMSAP2 expression constructs and their deletion mutants were generated by a PCR-based strategy using the human CAMSAP2 cDNA (IMAGE clone 40124603). The mCherry-MT+TIP construct contains the general MT + tip localization signal (SxIP motif) of human MACF2 (E5455-R5497; NP\_899236) recognized by MT EB proteins. The following shRNAs were created and used in this study:  $\gamma$ -Tubulin-shRNA (50 -GGAGGACATCTCAAGGAC), CAMSAP2-shRNA1, (KD1, 50 -TTGCATGTGCTCAACAGTA), and CAMSAP2-shRNA2 (KD2, 50 -ATTCCAGAAGAATCGGGTG). For details see Supplemental Experimental Procedures.

#### Primary Hippocampal Neuron Cultures, Transfection, and Nucleofection

Primary hippocampal and cortical cultures were prepared from embryonic day 18 (E18) rat brains and transfected using Lipofectamine 2000 (Invitrogen) or the Amaxa Rat Neuron Nucleofector kit (Lonza), respectively.

#### Live-Cell Imaging and Laser-Induced Severing

Simultaneous dual color time-lapse live cell imaging and TIRFM was performed on a Nikon Eclipse TE2000E microscope with Coolsnap and QuantEM cameras (Roper Scientific). Neurons were maintained at 37° C with 5% CO<sub>2</sub> (Tokai Hit). ATeem Photonics 532 nm Q-switched pulsed laser is used for laser-induced severing. The FRAP experiments were performed on a TIRF microscope system using the ILas2 system (Roper Scientific). For details see Supplemental Experimental Procedures.

### Ethics Statement

All animal experiments were performed in compliance with the guidelines for the welfare of experimental animals issued by the Government of The Netherlands. All animal experiments were approved by the Animal Ethical Review Committee (DEC) of the Erasmus Medical Center and Utrecht University.

### SUPPLEMENTAL INFORMATION

Supplemental Information includes eight figures, eight movies, and Supplemental Experimental Procedures and can be found with this article online at <http://dx.doi.org/10.1016/j.neuron.2014.04.019>.

### ACKNOWLEDGMENTS

We thank Dr. Rasband for sharing  $\beta$ IV-Spectrin antibodies; N.T. Keijzer for cloning shRNA-constructs; Dr. F. Polleux and Dr. J. Courchet for sharing the cortical migration excel macro; and A.M.A. Chiotto for assisting with imaging and analyzing EB3 antibody stainings. This work was supported by the Netherlands Organization for Scientific Research (NWO-ALW-VICI to C.C.H. and A.A.; NWO-ALW-VIDI to L.C.K.; NWO-ALW-VENI to M.H.); the Foundation for Fundamental Research on Matter (FOM to C.C.H., L.C.K., and A.A.), which is part of the NWO; the Netherlands Organization for Health Research and Development (ZonMW-TOP to C.C.H.); the European Science Foundation (ESF-EURYI to C.C.H.); Swiss National Science Foundation (SNSF to P.S.); and European Molecular Biology Organization - Young Investigators Program (EMBO-YIP to C.C.H.).

### REFERENCES

- Arimura, N., and Kaibuchi, K. (2007). Neuronal polarity: from extracellular signals to intracellular mechanisms. *Nat. Rev. Neurosci.* 8, 194–205.
- Baas, P.W., and Lin, S. (2011). Hooks and comets: The story of microtubule polarity orientation in the neuron. *Dev. Neurobiol.* 71, 403–418.
- Baas, P.W., Black, M.M., and Banker, G.A. (1989). Changes in microtubule polarity orientation during the development of hippocampal neurons in culture. *J. Cell Biol.* 109, 3085–3094.
- Baines, A.J., Bignone, P.A., King, M.D., Maggs, A.M., Bennett, P.M., Pinder, J.C., and Phillips, G.W. (2009). The CKK domain (DUF1781) binds microtubules and defines the CAMSAP/ssp4 family of animal proteins. *Mol. Biol. Evol.* 26, 2005–2014.
- Barnes, A.P., and Polleux, F. (2009). Establishment of axon-dendrite polarity in developing neurons. *Annu. Rev. Neurosci.* 32, 347–381.
- Bartolini, F., and Gundersen, G.G. (2006). Generation of noncentrosomal microtubule arrays. *J. Cell Sci.* 119, 4155–4163.
- Basto, R., Lau, J., Vinogradova, T., Gardiol, A., Woods, C.G., Khodjakov, A., and Raff, J.W. (2006). Flies without centrioles. *Cell* 125, 1375–1386.
- Bettencourt-Dias, M., and Glover, D.M. (2007). Centrosome biogenesis and function: centrosomes brings new understanding. *Nat. Rev. Mol. Cell Biol.* 8, 451–463.
- Bradke, F., and Dotti, C.G. (1997). Neuronal polarity: vectorial cytoplasmic flow precedes axon formation. *Neuron* 19, 1175–1186.
- Cheung, Z.H., Chin, W.H., Chen, Y., Ng, Y.P., and Ip, N.Y. (2007). Cdk5 is involved in BDNF-stimulated dendritic growth in hippocampal neurons. *PLoS Biol.* 5, e63.
- Conde, C., and Cáceres, A. (2009). Microtubule assembly, organization and dynamics in axons and dendrites. *Nat. Rev. Neurosci.* 10, 319–332.
- Dammermann, A., Desai, A., and Oegema, K. (2003). The minus end in sight. *Curr. Biol.* 13, R614–R624.
- Efimov, A., Kharitonov, A., Efimova, N., Loncarek, J., Miller, P.M., Andreyeva, N., Gleeson, P., Galjart, N., Maia, A.R., McLeod, I.X., et al. (2007). Asymmetric CLASP-dependent nucleation of noncentrosomal microtubules at the trans-Golgi network. *Dev. Cell* 12, 917–930.
- Franker, M.A., and Hoogenraad, C.C. (2013). Microtubule-based transport - basic mechanisms, traffic rules and role in neurological pathogenesis. *J. Cell Sci.* 126, 2319–2329.
- Goodwin, S.S., and Vale, R.D. (2010). Patronin regulates the microtubule network by protecting microtubule minus

- ends. *Cell* 143, 263–274.
- Halpain, S., and Greengard, P. (1990). Activation of NMDA receptors induces rapid dephosphorylation of the cytoskeletal protein MAP2. *Neuron* 5, 237–246.
- Heilemann, M., van de Linde, S., Schüttelpelz, M., Kasper, R., Seefeldt, B., Mukherjee, A., Tinnefeld, P., and Sauer, M. (2008). Subdiffraction-resolution fluorescence imaging with conventional fluorescent probes. *Angew. Chem. Int. Ed. Engl.* 47, 6172–6176.
- Hoogenraad, C.C., and Bradke, F. (2009). Control of neuronal polarity and plasticity—a renaissance for microtubules? *Trends Cell Biol.* 19, 669–676.
- Jaworski, J., Kapitein, L.C., Gouveia, S.M., Dortland, B.R., Wulf, P.S., Grigoriev, I., Camera, P., Spangler, S.A., Di Stefano, P., Demmers, J., et al. (2009). Dynamic microtubules regulate dendritic spine morphology and synaptic plasticity. *Neuron* 61, 85–100.
- Jiang, K., Toedt, G., Montenegro Gouveia, S., Davey, N.E., Hua, S., van der Vaart, B., Grigoriev, I., Larsen, J., Pedersen, L.B., Bezstarosti, K., et al. (2012). A Proteome-wide screen for mammalian SxIP motif-containing micro-tubule plus-end tracking proteins. *Curr. Biol.* 22, 1800–1807.
- Jiang, K., Hua, S., Mohan, R., Grigoriev, I., Yau, K.W., Liu, Q., Katrukha, E.A., Altelaar, A.F.M., Heck, A.J.R., Hoogenraad, C.C., and Akhmanova, A. (2014). Microtubule minus-end stabilization by polymerization-driven CAMSAP deposition. *Dev. Cell* 28, 295–309.
- Kapitein, L.C., and Hoogenraad, C.C. (2011). Which way to go? Cytoskeletal organization and polarized transport in neurons. *Mol. Cell. Neurosci.* 46, 9–20.
- Kapitein, L.C., Yau, K.W., Gouveia, S.M., van der Zwan, W.A., Wulf, P.S., Keijzer, N., Demmers, J., Jaworski, J., Akhmanova, A., and Hoogenraad, C.C. (2011). NMDA receptor activation suppresses microtubule growth and spine entry. *J. Neurosci.* 31, 8194–8209.
- Kuijpers, M., and Hoogenraad, C.C. (2011). Centrosomes, microtubules and neuronal development. *Mol. Cell. Neurosci.* 48, 349–358.
- Lee, H.H., Jan, L.Y., and Jan, Y.N. (2009). Drosophila IKK-related kinase Ik2 and Katanin p60-like 1 regulate dendrite pruning of sensory neuron during metamorphosis. *Proc. Natl. Acad. Sci. USA* 106, 6363–6368.
- Meng, W., Mushika, Y., Ichii, T., and Takeichi, M. (2008). Anchorage of micro-tubule minus ends to adherens junctions regulates epithelial cell-cell contacts. *Cell* 135, 948–959.
- Millecamps, S., and Julien, J.P. (2013). Axonal transport deficits and neurodegenerative diseases. *Nat. Rev. Neurosci.* 14, 161–176.
- Nguyen, M.M., Stone, M.C., and Rolls, M.M. (2011). Microtubules are organized independently of the centrosome in Drosophila neurons. *Neural Dev.* 6, 38.
- Ori-McKenney, K.M., Jan, L.Y., and Jan, Y.N. (2012). Golgi outposts shape dendrite morphology by functioning as sites of acentrosomal microtubule nucleation in neurons. *Neuron* 76, 921–930.
- Rust, M.J., Bates, M., and Zhuang, X. (2006). Sub-diffraction-limit imaging by stochastic optical reconstruction microscopy (STORM). *Nat. Methods* 3, 793–795.
- Stepanova, T., Slemmer, J., Hoogenraad, C.C., Lansbergen, G., Dortland, B., De Zeeuw, C.I., Grosveld, F., van Cappellen, G., Akhmanova, A., and Galjart, N. (2003). Visualization of microtubule growth in cultured neurons via the use of EB3-GFP (end-binding protein 3-green fluorescent protein). *J. Neurosci.* 23, 2655–2664.
- Stiess, M., and Bradke, F. (2011). Neuronal polarization: the cytoskeleton leads the way. *Dev. Neurobiol.* 71, 430–444.
- Stiess, M., Maghelli, N., Kapitein, L.C., Gomis-Rüth, S., Wilsch-Bräuninger, M., Hoogenraad, C.C., Tolić-Nunrelykke, I.M., and Bradke, F. (2010). Axon extension occurs independently of centrosomal microtubule nucleation. *Science* 327, 704–707.
- Tanaka, N., Meng, W., Nagae, S., and Takeichi, M. (2012). Nezha/CAMSAP3 and CAMSAP2 cooperate in epithelial-specific organization of noncentrosomal microtubules. *Proc. Natl. Acad. Sci. USA* 109, 20029–20034.
- Witte, H., and Bradke, F. (2008). The role of the cytoskeleton during neuronal polarization. *Curr. Opin. Neurobiol.* 18, 479–487.
- Witte, H., Neukirchen, D., and Bradke, F. (2008). Microtubule stabilization specifies initial neuronal polarization. *J. Cell Biol.* 180, 619–632.
- Yu, W., Qiang, L., Solowska, J.M., Karabay, A., Korulu, S., and Baas, P.W. (2008). The microtubule-severing proteins spastin and katanin participate differently in the formation of axonal branches. *Mol. Biol. Cell* 19, 1485–1498.

## Chapter 5

---

Supplemental Information Microtubule Minus-End Binding Protein CAMSAP2 Controls Axon Specification and Dendrite Development

### LEGENDS TO SUPPLEMENTARY MOVIES

Movie S1. GFP-CAMSAP2 localizes to MT minus-ends in COS-7 cells

This video corresponds to Figure S3B. COS-7 cells were transfected with GFP-CAMSAP2 (green) and mCherry- $\alpha$ -Tubulin (red). Series of growth and shrinkage of the MT can be seen in respect to the GFP-CAMSAP2 stretch. Total time is 1 minute and 19 seconds. 1 second per frame. Movie is speeded up 15 times. (AVI, 0.318 MB).

Movie S2. GFP-CAMSAP2 localizes to MT minus-ends in COS-7 cells

This video corresponds to Figure S3C. COS-7 cells were transfected with GFP-CAMSAP2 (green) and mCherry-MT+TIP (red). Repetitive growth of the comet from the GFP-CAMSAP2 stretch is clearly observed. Total time is 1 minute. 2 seconds per frame. Movie is speeded up 15 times. (AVI, 0.207 MB)

Movie S3. GFP-CAMSAP2 localizes to MT minus-ends in neurons

This video corresponds to Figure 2H. Rat hippocampal neurons were transfected with GFP-CAMSAP2 (green) and mCherry-MT+TIP (red). This movie shows several individual MTs that have GFP-CAMSAP2 localized to the MT minus-end. Total time is 5 minutes. 1 second per frame. Movie is speeded up 30 times. (AVI, 2.372 MB)

Movie S4. MT plus-end marker originates from CAMSAP2 in neurons

This video corresponds to Figure 2J. Rat hippocampal neurons were transfected with GFP-CAMSAP2 (green) and mCherry-MT+TIP (red). MT plus-end marker mCherry-MT+TIP originates from CAMSAP2. Total time is 44 seconds. 2 seconds per frame. Movie is speeded up 30 times. (AVI, 0.059 MB)

Movie S5. GFP-CAMSAP2 recovers at one end of CAMSAP2 stretches in neurons

This video corresponds to Figure 3B. Rat hippocampal neurons were transfected with GFP-CAMSAP2. FRAP was performed at time point  $t=1:30$  (m:s). GFP-CAMSAP2 recovers specifically on MT minus-ends. Total time is 15 minutes. 10 seconds per frame. Movie is speeded up 150 times. (AVI, 0.209 MB)

Movie S6. CAMSAP2 clusters grow into extended stretches in neurons

This video corresponds to Figure 3F, which is related to Figure 1G-I. Rat hippocampal neurons were transfected with GFP-CAMSAP2 (green) and mRFP (red). FRAP was performed at time point  $t=3:00$ (m:s). GFP-CAMSAP2 specifically recovers at the MT minus-end. Multiple recoveries can be observed which reveal that CAMSAP2 stretches in dendrites enlarge towards both the proximal and distal regions. Total time is 40 minutes. 20 second per frame. Movie is speeded up 600 times. (AVI, 1.269 MB)

Movie S7. GFP-CAMSAP2 accumulates on newly formed MT minus-ends

This video corresponds to Figure 5B. COS-7 cells were transfected with GFP-CAMSAP2 (green) and mCherry-MT+TIP (red). MT was laser-induced severed at time point  $t=44$ s, the asterisk points the area of laser-induced severing. GFP-CAMSAP2 accumulates onto the newly formed MT minus-end over time and the MT continues to be dynamic. Total time is 1 minute and 55 seconds. 1 second per frame. Movie is speeded up 15 times. (AVI, 0.621 MB)

Movie S8. GFP-CAMSAP2 accumulates on newly formed MT minus-ends in neurons

This video corresponds to Figure 5F. Rat hippocampal neurons were transfected with GFP-CAMSAP2 (green) and mCherry-MT+TIP (red). MT was laser-induced severed at time point  $t=13$ s, the asterisk points the area of laser-induced severing. GFP-CAMSAP2 accumulates onto the newly formed MT minus-end over time and the MT continues to be dynamic. Total time is 1 minute and 33 seconds. 1 second per frame. Movie is speeded up 30 times. (AVI, 0.791 MB)

## SUPPLEMENTARY FIGURE LEGENDS

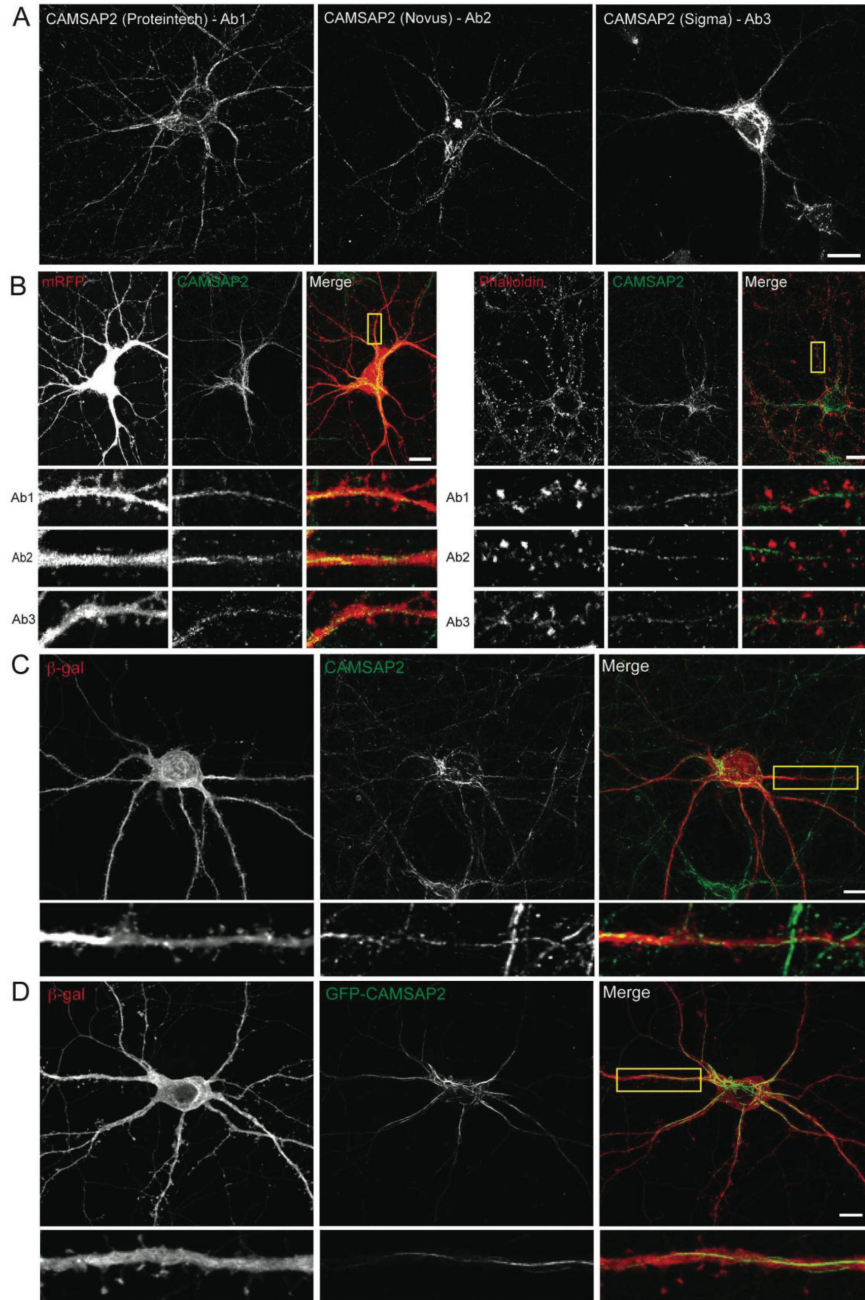


Figure S1, related to Figure 1C-F. Three independent CAMSAP2 antibodies label small clusters and distinct stretches in hippocampal neurons

(A) DIV 21 neurons immunostained with CAMSAP2 antibodies from three different companies. CAMSAP2 antibodies are purchased from Proteintech (Bioconnect) (CAMSAP2 antibody 1), Novus Biologicals (CAMSAP2 antibody 2) and Sigma (CAMSAP2 antibody 3). CAMSAP2 antibody 1 is the most used in this study and labels small clusters and distinct stretches throughout the neurons. This signal was strongly decreased after

## CAMSAP2 Controls Neuronal Polarity and Development

---

*knockdown of CAMSAP2 with two CAMSAP2 shRNAs. In addition to typical CAMSAP2 clusters and stretches, CAMSAP2 antibody 2 labels the nucleolus and CAMSAP2 antibody 3 labels the Golgi apparatus in hippocampal neurons. Antibodies 2 and 3 probably cross react, since CAMSAP2 depletion did not decrease the nucleolus and Golgi staining, respectively.*

*(B) Left panel shows neurons that are transfected at DIV 19 with mRFP fixed at DIV 21 and stained for CAMSAP2 with 3 different antibodies as described in (A). Right panel shows neurons fixed at DIV 21, double stained for 3 different CAMSAP2 antibodies with phalloidin. (C) Neurons are transfected with  $\beta$ -Galactosidase (red), fixed at DIV 22 and stained for endogenous CAMSAP2 (green).*

*(D) Neurons are transfected with  $\beta$ -Galactosidase (red) and GFP-CAMSAP2 (green) and fixed at DIV 22. Scale bars are 10  $\mu$ m.*

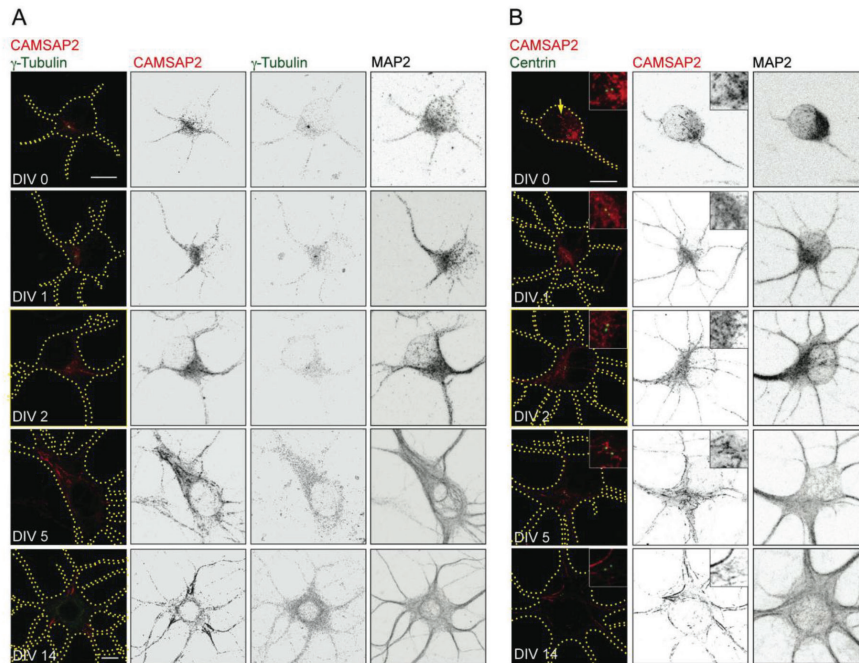


Figure S2, related to Figure 1C-H. Endogenous CAMSAP2 expression and distribution in hippocampal neurons throughout development

(A) Maximum intensity confocal projections representing the distribution and dynamics of CAMSAP2 and  $\gamma$ -Tubulin throughout development. Hippocampal neurons were fixed at the indicated time points and immunostained for CAMSAP2 (red),  $\gamma$ -Tubulin (green) and MAP2. All images were acquired with the same light intensity and exposure time. Individual neurons are outlined by dashed lines that represent the cell outline as judged by CAMSAP2,  $\gamma$ -Tubulin and MAP2 signals. Scale bar is 10  $\mu$ m.

(B) Maximum intensity confocal projections representing the distribution and dynamics of CAMSAP2 around the centrioles throughout development. Hippocampal neurons were fixed at the indicated time points and immunostained for CAMSAP2 (red), Centrin (green) and MAP2. All images were acquired with the same light intensity and exposure time. Insets depict the indicated centriole areas (2,5x magnification). Individual neurons are outlined by dashed lines that represent the cell outline as judged by CAMSAP2 and MAP2 signals. Scale bar is 10  $\mu$ m. Note that CAMSAP2 stretches are present in areas devoid of the centrosome already from DIV0 (marked with an arrow).

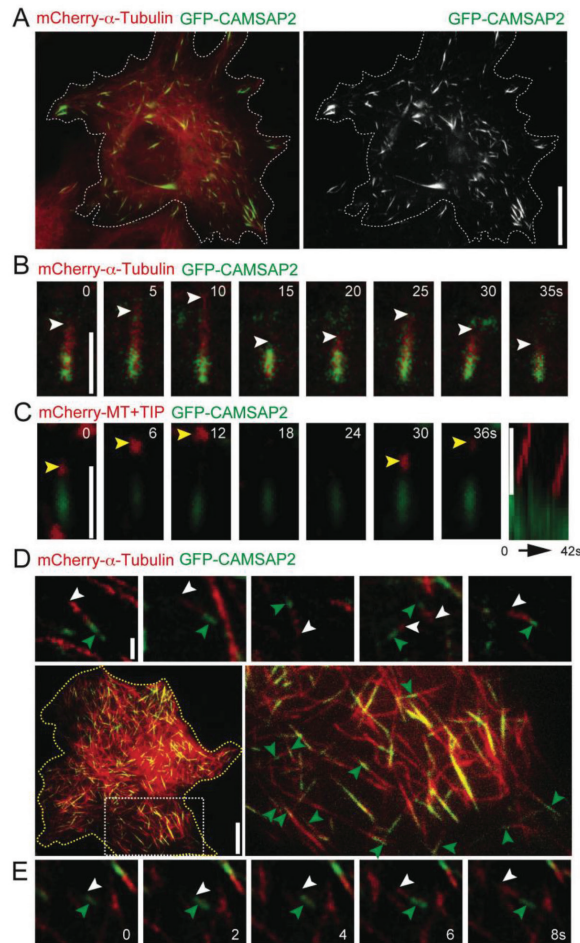


Figure S3, related to Figure 2H-K. CAMSAP2 localizes to microtubule minus-ends in COS7 cells  
 (A) An example of a COS7 cell transfected with mCherry- $\alpha$ -Tubulin (red) and GFP- CAMSAP2 (green). Scale bar is 10  $\mu$ m.  
 (B) Stills from TIRFM time-lapse recordings of a COS7 cell expressing mCherry- $\alpha$ -Tubulin (red) and GFP- CAMSAP2 (green). The white arrowheads indicate the growing MT plus-end. Scale bar is 2  $\mu$ m.  
 (C) Stills from TIRFM time-lapse recordings of a COS7 cell expressing mCherry-MT+TIP (red) and GFP- CAMSAP2 (green). The yellow arrowheads indicate the MT plus-end marker. The kymograph corresponds to the time-lapse recording. Scale bar is 2  $\mu$ m.  
 (D) An example of a COS7 cells are transfected with mCherry- $\alpha$ -Tubulin (red) and GFP- CAMSAP2 (green). Top row shows stills (low-pass filtered) from a TIRFM time-lapse recording of the COS7 cell shown in the bottom row. The white arrowheads indicate the fast growing MT plus-ends, green arrow heads indicate the MT minus-ends positive for GFP- CAMSAP2. The middle row shows a COS7 cell outlined with a dashed yellow line. Scale bars are 1 and 10  $\mu$ m.  
 (E) TIRFM time-lapse recording stills (low-pass filtered) from an area in the inset shown in (D). See also Movie S1 and S2.

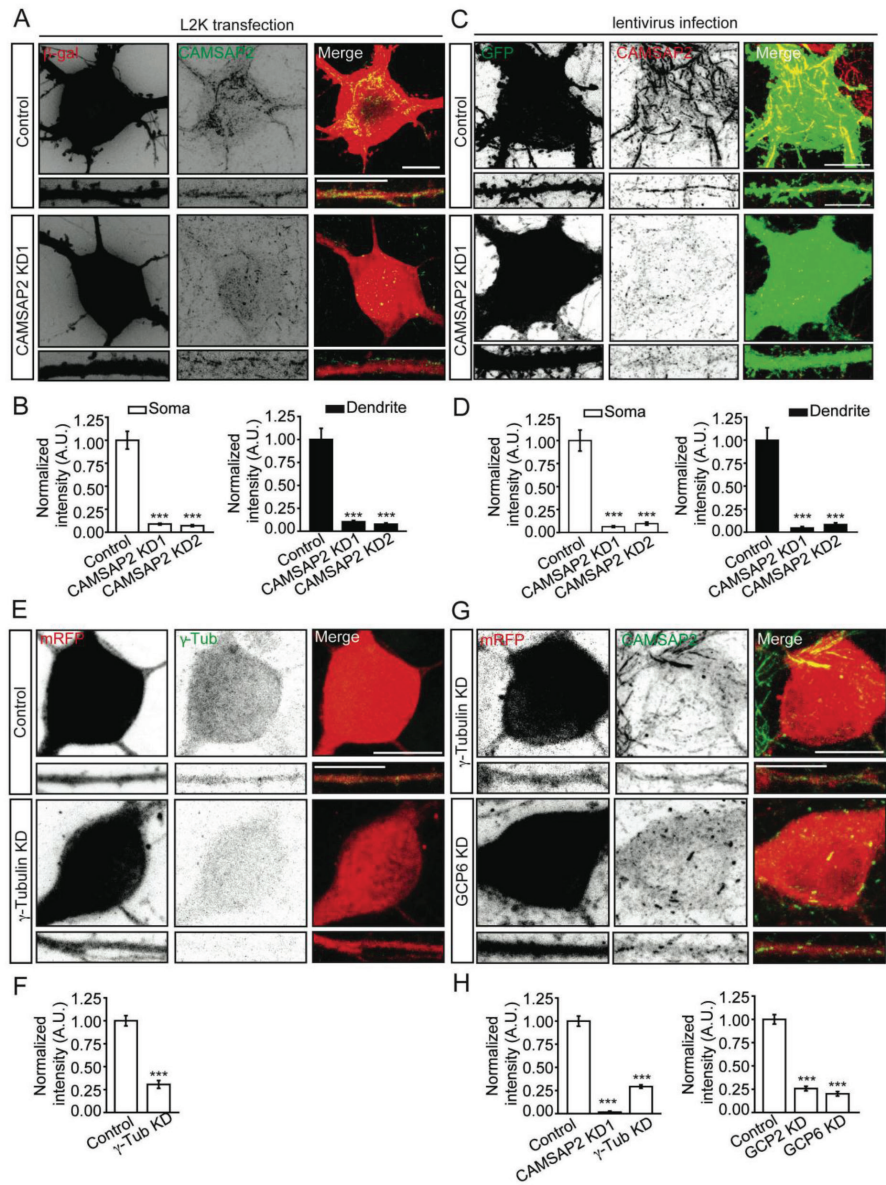


Figure S4, related to Figure 4A,B. Knockdown efficiency of CAMSAP2- and  $\gamma$ -Tubulin- shRNAs  
 (A) Representative images of hippocampal neurons transfected with fill  $\beta$ -Galactosidase (red) and control or CAMSAP2-shRNA1 (KD1) using Lipofectamine 2000 (L2K). Representative examples of the soma and dendrite are shown. Neurons are transfected at DIV 16 and fixed at DIV 20.  
 (B) Normalized intensities of CAMSAP2 for control neurons ( $n=14$ ) or neurons transfected with either of the two different CAMSAP2 shRNAs ( $n=18$  for CAMSAP2-shRNA1 (KD1),  $n=6$  for CAMSAP2-shRNA2 (KD2)) at DIV16 for 4 days. AU, arbitrary units.  
 (C) Representative images of hippocampal neurons (DIV21) infected with lentivirus expressing MARCKS-GFP (green) and control or CAMSAP2-shRNA1 (KD1). Neurons are stained for endogenous CAMSAP2.  
 (D) Normalized intensities of CAMSAP2 for control neurons ( $n=19$ ) and neurons infected with control, CAMSAP2-shRNA1 ( $n=23$ ) or GFP-CAMSAP2-shRNA2 ( $n=16$ ). AU, arbitrary units.  
 (E) Confocal maximum intensity projection images of the fill mRFP (red) and endogenous  $\gamma$ -Tubulin (green).

## CAMSAP2 Controls Neuronal Polarity and Development

---

*Representative examples of the soma and dendrite are shown. Neurons are transfected at DIV 16 and fixed at DIV 20.*

*(F) Normalized intensities of  $\gamma$ -Tubulin for control neurons (n=18) or neurons transfected with  $\gamma$ -Tubulin shRNAs (n=9) at DIV17 and fixed at DIV21. AU, arbitrary units.*

*(G) Confocal maximum intensity projection images of the full mRFP (red) and endogenous CAMSAP2 (green), where representative examples of the soma and dendrite are shown. Neurons are transfected at DIV 16 and fixed at DIV 20.*

*(H) Normalized intensities of CAMSAP2 for control neurons (n=11) or neurons transfected with  $\gamma$ -Tubulin shRNAs (n=11), GCP2 shRNA (n=11) or GCP6 shRNA (n=11) at DIV17 for 4 days. AU, arbitrary units. Error bars represent SEM. \*\*\*P<0.001. Scale bars are 10  $\mu$ m.*

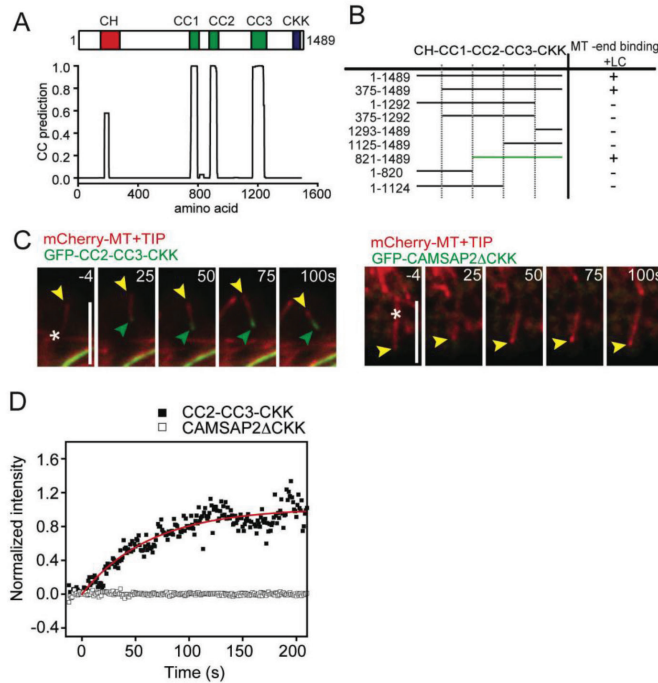


Figure S5, related to Figure 6K. CAMSAP2 mutants accumulate on new microtubule minus-ends

(A) Coiled coil prediction diagram of CAMSAP2 protein. N-terminal CH domain is indicated in red, the central coiled coil domains are indicated in green and the C-terminal CKK domain is indicated in blue.

(B) Mapping of the minimal MT minus-end binding domain of CAMSAP2. The mutant indicated with a green line consists of the minimal domains required for MT minus-end binding after laser-induced severing of the MT.

(C) Left row shows merge stills from a TIRFM time-lapse recording where a COS-7 cell is transfected with mCherry-MT+TIP (red) and GFP-CC2-CC3-CKK (green), CAMSAP2 mutant (821-1489). Yellow arrow heads indicate the MT plus-end marker. Green arrow heads indicate GFP-CC2-CC3-CKK accumulation on the MT minus-end after laser-induced severing. Right row shows merge stills from a TIRFM time-lapse recording where a COS-7 cell is transfected with mCherry-MT+TIP (red) and GFP-CAMSAP2ΔCKK (green), CAMSAP2 mutant (1-1292). Yellow arrow heads indicate the MT plus-end marker. Asterisk indicates the area of laser-induced severing. MT is laser-induced severed at  $t=0$ . Both time-lapse recordings are low-pass filtered. Scale bars are  $5\ \mu\text{m}$ .

(D) Intensity time traces corresponding to the stills in (C). The black squares represent the intensity time trace of the left row in (C). The white squares represent the intensity time trace from the bottom right in (C). Single exponential fit of the black squares is shown in red.

## CAMSAP2 Controls Neuronal Polarity and Development

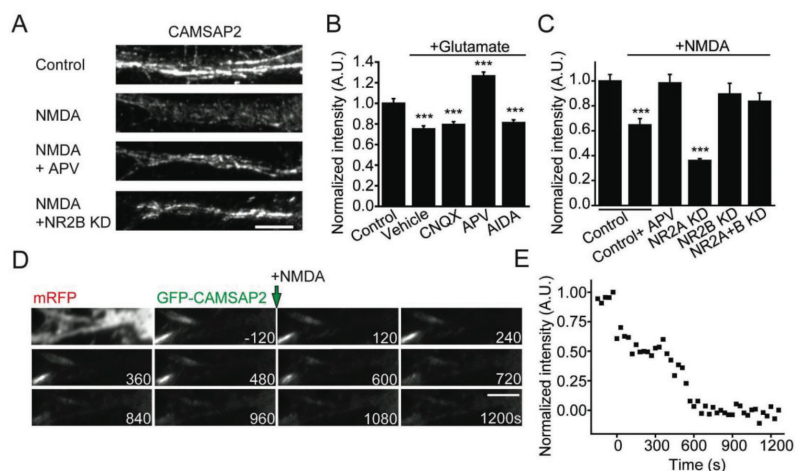


Figure S6, related to Figure 6. Neuronal activity affects the distribution of CAMSAP2 in dendrites

(A) Dendritic regions of hippocampal neurons at DIV 22 with endogenous CAMSAP2 staining treated with 50  $\mu$ M NMDA for 5 min and recovered for 25 min. From top to bottom representative control, NMDA treatment, APV and NMDA treatment and NR2B KD and NMDA treatment are shown. Scale bars are 5  $\mu$ m.

(B) Diagram showing the normalized mean intensity of CAMSAP2 in dendritic regions from neurons, which have been untreated ( $n=20$ ), treated with 50 $\mu$ M glutamate for 5 min (and recovered for 25min) alone ( $n=16$ ) or combined with either 10 $\mu$ M CNQX ( $n=19$ ), 100 $\mu$ M APV ( $n=19$ ) or 50 $\mu$ M AIDA ( $n=19$ ). AU, arbitrary unit. \*\*\* $P<0.001$  (T-test).

(C) Diagram showing the normalized mean intensity of CAMSAP2 in dendritic regions from neurons, which have been untreated ( $n=11$ ), treated with 50 $\mu$ M NMDA for 5 min (and recovered for 25min) alone ( $n=9$ ) or combined with either 100 $\mu$ M APV ( $n=12$ ), NR2A shRNA ( $n=13$ ), NR2B shRNA ( $n=7$ ) or NR2A/B shRNAs ( $n=9$ ). AU, arbitrary unit. \*\*\* $P<0.001$  (T-test).

(D) Stills from TIRFM time-lapse recordings of a dendritic segment of a hippocampal neuron (DIV 15) expressing GFP-CAMSAP2 and mRFP to highlight the morphology. The first image is an average projection from the mRFP channel showing the dendritic region. At  $t=0$  neurons are treated with 50 $\mu$ M NMDA bath application. Scale bar is 5  $\mu$ m. (E) Intensity time trace of GFP-CAMSAP2 corresponding to the time-lapse recording in (D).

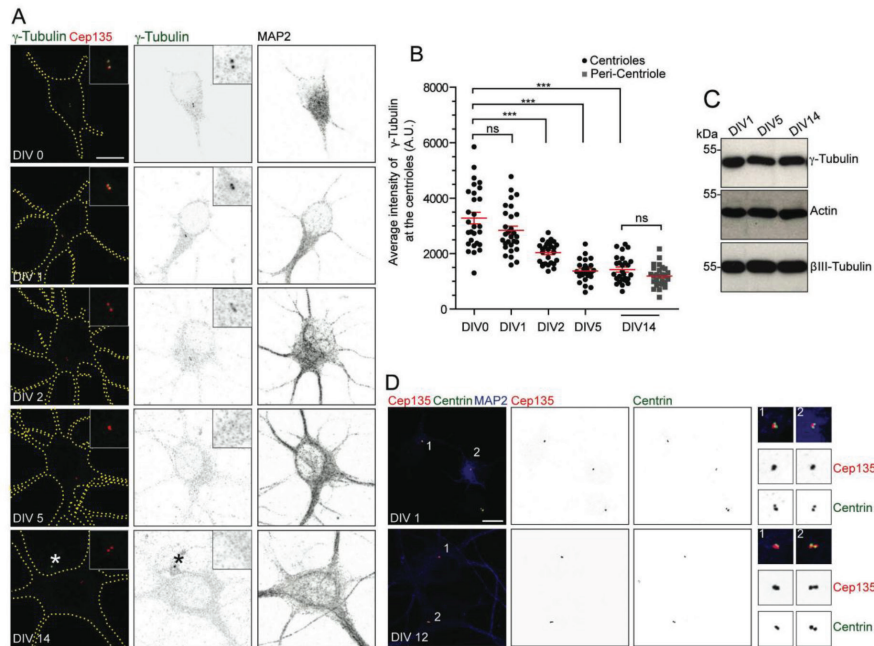


Figure S7, related to Figure 7A. Endogenous  $\gamma$ -Tubulin expression and distribution in hippocampal neurons throughout differentiation

(A) Maximum intensity confocal projections representing the distribution and dynamics of  $\gamma$ -Tubulin at centrioles throughout differentiation. Hippocampal neurons were fixed at the indicated time points and immunostained for  $\gamma$ -Tubulin (green), Cep135 (centriole marker, in red) and MAP2. All images were acquired with the same light intensity and exposure time. Insets depict the indicated centriole areas (2.5x magnification). Individual neurons are outlined by dashed lines that represent the cell outline as judged by  $\gamma$ -Tubulin and MAP2 signals. Scale bar is 10  $\mu$ m. Note that although  $\gamma$ -Tubulin is absent from centrioles in DIV 14, it is detected at centrioles of the surrounding glia cells (marked with an asterisk).

(B) Quantification of endogenous  $\gamma$ -Tubulin levels at both centrioles throughout hippocampal neuron differentiation. Centriolar  $\gamma$ -Tubulin was measured at the indicated time points. At least 26 hippocampal neurons were analyzed per developmental time point (DIV 0-14). Represented is the average intensity of  $\gamma$ -Tubulin at the centrioles. The average intensity of  $\gamma$ -Tubulin in the peri-centriolar area is also represented for DIV 14. Note that the total levels of  $\gamma$ -Tubulin at DIV5 and DIV14 at the centriole do not differ from the ones measured at the peri-centriolar area. The statistical difference between sample distribution of DIV0 and the other stages was evaluated with a Mann-Whitney test (\*\*\*,  $p < 0,001$ ; ns, not statistically significant).

(C)  $\gamma$ -Tubulin protein is expressed at constant levels throughout neuron differentiation. Extracts of hippocampal neurons were prepared at the indicated time points and probed by Western blot for  $\gamma$ -Tubulin, actin (loading control) and  $\beta$ III-Tubulin (loading control) antibodies.

(D) Cep135, used in (A) is a bona-fide centriolar marker in hippocampal neurons. Maximum intensity confocal projections representing the localization of Cep135 at both centrioles in hippocampal neurons throughout differentiation. Hippocampal neurons were fixed at the indicated time points and immunostained for Cep135 (red), Centrin (centriole marker, in green) and MAP2. Insets depict the indicated centriole areas (3x magnification). Scale bar is 10  $\mu$ m.

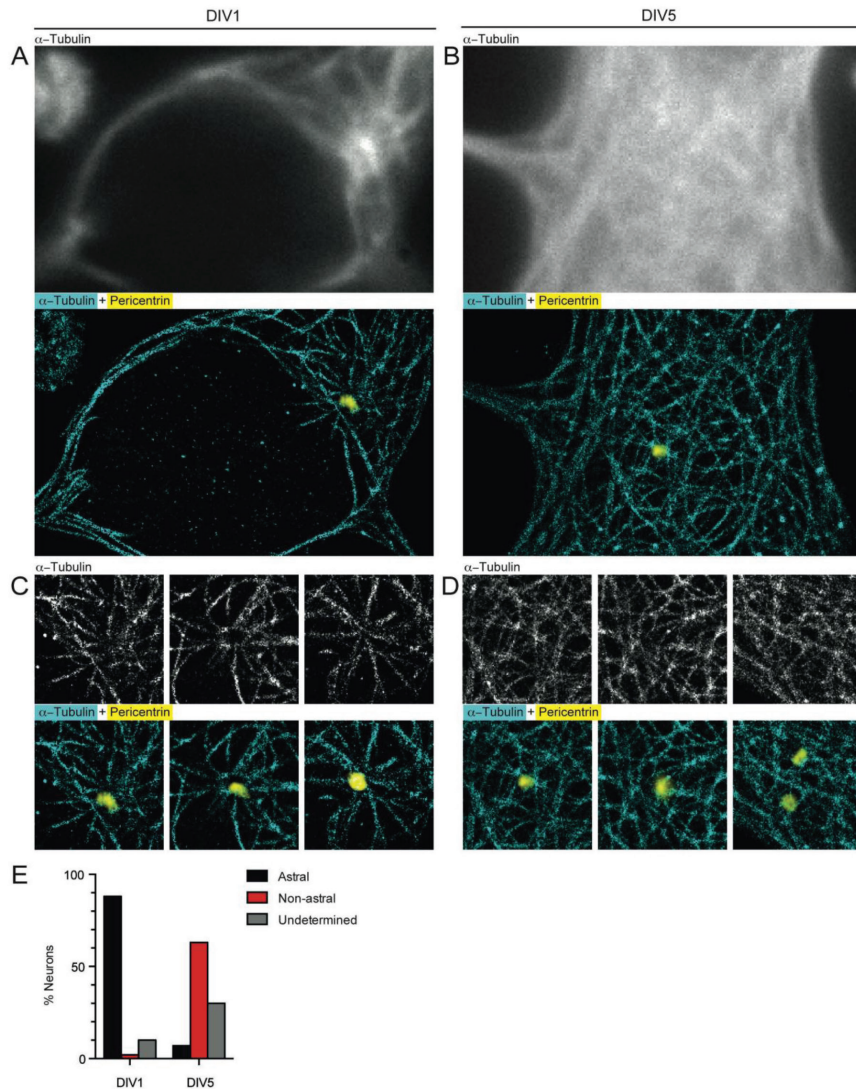


Figure S8, related to Figure 7A. dSTORM analysis of microtubule organization in DIV1 and DIV5 neurons (A,B) Conventional widefield Image (top) and corresponding dSTORM reconstruction (bottom) of a neuron at DIV1 (A) and DIV5 (B), labeled with primary antibodies against  $\alpha$ -tubulin and AlexaFluor647-labeled secondary antibodies. dSTORM image is overlaid with the conventional widefield image of Pericentrin staining to locate the centrosome (visualized using an AlexaFluor488-labeled secondary antibody). Scale bars, 2  $\mu$ m.

(C,D) Top: Three zooms of microtubule organization around the centrosome for three neurons at DIV1 (C) and DIV5 (D), including the neurons shown in A,B. Bottom: Overlay of dSTORM microtubule image with conventional widefield image of pericentrin. Scale bars, 2  $\mu$ m. (E) Occurrence of astral and non-astral microtubule organization for neurons at DIV1 (N=50 neurons) or DIV5 (N=43 neurons).

### SUPPLEMENTARY MATERIALS AND METHODS

#### Antibodies and reagents

The following primary and secondary antibodies were used in this study: rabbit anti-EB3 (02-1005-07), mouse anti-MAP2 (HM-2, M 9942, Sigma), chicken polyclonal anti-MAP2 (Abcam), mouse anti-acetylated-Tubulin (6-11B-1, T7451, Sigma), rat anti-tyrosinated-Tubulin (YL1/2, ab6160, Abcam), rabbit anti-GFP (598, MBL), mouse anti-Nestin (611658, BD Transduction Laboratories), mouse anti-Tau (PC1C6, MAB3420, Chemicon), mouse anti-Bassoon (SAP7F407, VAM-PS003, Stressgen), mouse anti- $\gamma$ -Tubulin (T6557, Sigma), mouse anti-Centrin (20H5, Milipore), rabbit polyclonal anti-Cep135 (Sigma), rabbit anti-CAMSAP1 (Novus Biologicals, NBP1-26645), rabbit anti-CAMSAP2 (17880-1-AP, Proteintech; NBP1-21402, Novus Biologicals; HPA0273, Sigma), rabbit anti-CAMSAP3 (Abgent, AP18323a), mouse anti-AFP (3E6, AFP5002), chicken anti- $\beta$ -Galactosidase (BGL-1040, Aveslab), rabbit anti-EB3 (Stepanova et al., 2003), mouse anti-Ankyrin G (N106/36, NeuroMab, clone 4G3F8, Life Technologies), mouse anti-pan-Nav (S8809, Sigma), rabbit anti- $\beta$ IV-Spectrin (gift from Dr. Rasband, (Ogawa et al., 2006)), Alexa-350-, Alexa 488-, Alexa 568- and Alexa 594- conjugated secondary antibodies (Invitrogen). Other reagents used in this study include: Nocodazole (M1404, Sigma), Taxol (T7402, Sigma), brain derived neurotrophic factor (rhBDNF G1491, Promega), DL-2-amino-5-phosphonopentanoic acid (APV), 6-cyano-7-nitroquinoxaline-2,3-dione (CNQX), N-methyl-D-aspartic acid (NMDA), 1-aminoinidan-1,5-dicarboxylic acid (AIDA). A recombinant single chain antibody against GFP, bio-VHGF, was derived from VVHGF4 (Caussin et al. 2011), subcloned into pMXB10-bio, and purified from bacteria using the intein system (IMPACT Kit, NEB).

#### DNA and shRNA constructs

The following mammalian expression plasmids have been described: pGW2-mRFP, pGW1-GFP, p $\beta$ actin-HA- $\beta$ -Galactosidase (Kapitein et al., 2010), pSuper vector (Brummelkamp et al., 2002), pCDNA3.1-mCherry- $\alpha$ -Tubulin (Shaner et al., 2004). All other constructs were created using PCR based strategy. For CAMSAP2 the human CAMSAP2 cDNA (IMAGE clone 40124603) was used to create CAMSAP2 fusion construct in pGW1-GFP. This construct was used to create all other CAMSAP2-mutant constructs and cloned into pGW1 GFP. For CAMSAP1 the human CAMSAP1 cDNA (IMAGE clone 40146611) was used to generate pGW1-GFP-CAMSAP1. For CAMSAP3 the mouse CAMSAP3 cDNA (IMAGE clone 6489361) was used to generate pGW1-GFP-CAMSAP3. The mCherry-MT+TIP construct contains the general microtubule tip localization signal, SxIP motif recognized by microtubule plus-end binding (EB) proteins (Honnappa et al., 2009) and was generated as follows. The two-stranded leucine zipper coiled-coil sequence corresponding to GCN4-p1 (RMKQLEDKVEELLSKNYHLENEVARLKKLVGER) was fused to N-terminal 43 amino acid peptide (ETVPQTHRPTPRAGSRPSTAKPSKIPTPQRKSPASKLDRKSSKR) of human MACF2 (E5455-R5497; NP\_899236) by PCR based strategy (Honnappa et al., 2009) A glycine rich-linker sequence (GAGG) was inserted between GCN4-p1 and MACF43 and subcloned in p $\beta$ actin-16-pl expression vectors (Kapitein et al., 2010) to generate p $\beta$ actin-mCherry-GCN4-MACF43. Since we use mCherry-GCN4-MACF43 as a general marker to analyze the dynamics of microtubule growing plus-ends, we named this construct mCherry- MT+TIP. The following shRNAs were created and used in this study:  $\gamma$ -Tubulin-shRNA (5'- ggaggacatctcaaggac) (Alvarado-Kristensson et al., 2009), GCP2-shRNA (5'- ttgcccttgctactgatta), GCP6-shRNA (5'-gaccatcaacctactgaag) CAMSAP2-shRNA1, (5'- ttgatgtgctcaacagt), CAMSAP2-shRNA2 (5'-attccagaagaatcggtg) and an additional mouse CAMSAP2-shRNA (5'-acacataatacagaatgct) used for *in utero* electroporation.

### **Lentivirus generation and transduction of neuron cultures**

RNAi expression cassettes (H1 promotor + shRNA) from pSuper constructs were excised via BamHI and ClaI sites and inserted in pLVTHM-GFP lentivirus vector backbone (Addgene 12247) (Wiznerowicz and Trono, 2003). Lentiviral particles were produced in HEK293T cells by polyethylenimine (PEI) transfection of 100µg pLVTHM-GFP plasmid, 35 µg env plasmid (pMD2.G) and 65µg packaging plasmid (pCMVΔR8.2) in a 500 cm<sup>2</sup> dish. Cell culture medium was exchanged to Opti-MEM medium after 6h and viral particles were harvested 48 h after transfection. Virus containing supernatant was cleared from debris (centrifugation 4000g, 30 min) and reduced from 100ml to 300µl by tangential flow filtration (Amicon Ultra-15 100K). Concentrated virus solution was diluted 1:1 in PBS, snap frozen in liquid nitrogen, and stored at -80°C until further usage. For CAMSAP2 knockdown experiments, 20µl of virus stock was applied at DIV 15 and DIV 20.

### **Primary hippocampal neuron cultures, transfection and immunohistochemistry**

Primary hippocampal cultures were prepared from embryonic day 18 rat brains. Cells were plated on coverslips coated with poly-L-lysine (30µg/ml) and laminin (2µg/ml) at a density of 75,000/well. Hippocampal cultures were grown in Neurobasal medium (NB) supplemented with B27, 0.5 µM glutamine, 12.5 µM glutamate and penicillin/streptomycin. Hippocampal neurons were transfected using Lipofectamine 2000 (Invitrogen). Briefly, DNA (1.8 µg/well, for a 12 wells plate) was mixed with 3.3 µl of Lipofectamine 2000 in 200µl NB, incubated for 30 min, and then added to the neurons in NB at 37°C in 5% CO<sub>2</sub> for 45 min. Next, neurons were washed with NB and transferred in their original medium at 37°C in 5% CO<sub>2</sub> for 2-4 days. For BDNF-induced dendritic growth experiments, mature neurons were treated with 50 ng/ml BDNF for 3 days (Cheung et al., 2007). For Taxol experiments, 10 nM Taxol was added to culture medium 1 day after plating and cells were further incubated for 48 hours at 37°C in the presence of the drug (Witte et al., 2008).

For general immunohistochemistry, neurons were fixed for 10 min with 4% paraformaldehyde (PFA)/4% sucrose in PBS at room temperature or 10 min with ice-cold methanol 100% containing 1mM EGTA at -20°C. For detection of CAMSAP2,  $\gamma$ -Tubulin, Cep135, and Centrin neurons were fixed in ice-cold methanol for 10 minutes at 100% containing 1 mM EGTA at -20°C. Fixing neurons to stain for EB3 comets required 2 min with ice-cold methanol 100% with 1mM EGTA at -20°C and subsequently 8 min with 4% paraformaldehyde/4% sucrose in PBS. After fixation cells were washed 3 times for 5 min in PBS at room temperature and incubated with the primary-antibody mix in GDB buffer (0.2% BSA, 0.8M NaCl, 0.5% Triton X-100, 30mM phosphate buffer, pH 7.4) overnight at 4°C. Next the neurons were washed 3 times for 5 min in PBS at room temperature and incubated with the secondary-antibody mix in GDB buffer for at most 1 hour at room temperature. Neurons were then washed 3 times for 5 min in PBS at room temperature and subsequently mounted on slides in Vectashield mounting medium (Vector Laboratories). To extract soluble cytoplasmic proteins before staining, neurons were fixed and extracted (Zhou et al., 2004). Confocal images were acquired using AR1-A1 confocal (Nikon), LSM510 (Zeiss), LSM 5 Pascal, or LSM 700 with a 20x (dry), 40x (oil), 63x (oil), or 100x (oil) objective. A total thickness of 10µm was scanned for each position and imaging settings were kept the same when pictures were compared for fluorescence intensity.

### **Primary cortical neuron cultures and nucleofection**

Primary cortical neurons were isolated from E18 rat brain. Cells ( $1 \times 10^6$ ) were transfected using the Amaxa Rat Neuron Nucleofector kit (Lonza) with 3µg of plasmid DNA and

plated on coverslips coated with poly-L-lysine (37.5µg/ml) and laminin (5µg/ml) in 12-wells plates ( $2-6 \times 10^4$  cells/well) containing DMEM supplemented with 10% FBS (Kaech and Banker, 2006). Cells were allowed to recover and adhere to the surface at 37°C in 5% CO<sub>2</sub>, after 4 hours the medium was replaced with Neurobasal medium supplemented with 2% B27, 0.5mM glutamine, 15.6µM glutamate, and 1% penicillin/streptomycin. Cells were grown for 4 days at 37°C in 5% CO<sub>2</sub> prior to fixation.

### **Cell culture heterologous cells**

African Green Monkey SV40-transformed kidney fibroblast cells (COS7) and Human Embryonic Kidney 293 cells (HEK293) cells were cultured in DMEM/Ham's F10 (50%/50%) containing 10% Fetal Calf Serum (FCS) and 1% penicillin/streptomycin at 37°C and 5% CO<sub>2</sub>. Prior to transfection, COS-7 cells were plated on 24mm glass coverslips for at least 2 days. COS-7 cells were transfected with Fugene6 (Roche) according to manufacturer's protocol, and incubated overnight. HEK293 cells were transfected for 48 hours with GFP-CAMSAP1, GFP-CAMSAP2 and GFP-CAMSAP3 constructs with polyethylenimine (PEI, Polysciences).

### **Cell extracts and Western blot**

HEK293 whole cell lysates were prepared by resuspending cells in equal amounts of lysis buffer containing 25mM Tris-HCl pH 8.0, 50mM NaCl, 0.5% Triton X-100 supplemented with 1x protease inhibitors cocktail (Roche). The soluble fraction was separated by centrifugation at 14000 RPM for 10 minutes and supplemented with sample buffer 4x (8% SDS, 25% glycerol, 0.05M Tris pH 6.8, 400mM DTT and 40mg/l bromophenol blue). Hippocampal homogenates of embryonic (E18) and adult (7 weeks) rats were prepared in ice cold extraction buffer containing 20mM Tris, pH 8.0, 150mM NaCl, 1% Triton-X100 and protease inhibitors cocktail (Roche) in a ratio of tissue and buffer 1:10. Rat primary hippocampal neurons (E18) were plated at a density of 20000 cells/cm<sup>2</sup> in 6-well dishes. After 1, 5 and 14 days in vitro (DIV), cells were lysed in hot denaturing sample buffer. Lysates prepared from 6 individual wells were pooled together. Single wells with lentiviral transduced hippocampal cultures were lysed by the same method. Equal protein concentrations were adjusted before supplementing with 4x sample buffer. Samples were boiled at 99° C for 5 minutes and centrifuged at 16000 g before being analysed by SDS-PAGE. Proteins were transferred on PVDF membranes (Millipore) using a wet blotting system (Bio-Rad). Membranes were blocked and incubated with primary antibodies (overnight at 4°C) in PBST (0.1% Triton X-100, 2% BSA). Peroxidase-coupled secondary antibodies were applied for 1 hour. Following primary CAMSAP antibodies have been used for detection: CAMSAP1 rabbit antibody (Novus, NBP1-26645 at 1:500), CAMSAP2 (Proteintech/NBP1-21402 at 1:500 for endogenous or 1:50000 for overexpression) and CAMSAP3 rabbit antibody (Abgent, RB24779 at 1:250). For quantifying CAMSAP2 depletion, the relative intensities of CAMSAP2 for each sample were obtained by normalization to the actin loading control. The percentage of depletion for each CAMSAP KD sample was obtained by normalization of the relative intensities with the relative intensity of the control (KD1 92%, KD2 81%). Quantifications were performed with Image J.

### **Live-cell imaging and laser-induced severing**

Total internal reflection fluorescence microscopy (TIRFM) was performed on an inverted microscope (Nikon Eclipse Ti with Perfect Focus System) with a CFI Apo TIRF 100x objective, 1.49 numerical aperture (NA), oil objective (Nikon) with an Evolve 512 EMCCD camera (Photometrics) and CoolSNAP HQ2 CCD (Photometrics). MetaMorph software

is used to control the camera and all motorized parts. The microscope is further outfitted with an ASI motorized stage MS-2000-XY, Optosplit III, ILas2 system (Roper Scientific), Shutter LB10-3. For fluorescence excitation a Calypso 491 nm, 100mW laser and Jive 561, 100mW laser (Cobolt). A Teem Photonics 532 nm Q-switched pulsed laser is used for laser-induced severing (Botvinick et al., 2004; Colombelli et al., 2005). ET-GFP/mCherry dichroic (59022 Chroma) and ET-mCherry (49008 Chroma) are used for wavelength selection. In order to perform laser-induced severing using the 532 nm Q-switched pulsed laser during simultaneous dual-color imaging, the filter cube containing mCherry dichroic was switched with ET-mCherry and switched back after laser-induced severing was successful. Frames recorded in the switched period were not taken into account for analysis of the intensity traces of CAMSAP2. No signs of toxicity or blebbing of cells was observed during laser-induced severing. All imaging was performed in full conditioned medium (for neurons) or Ringer's buffer (for COS-7 cells, 10mM Hepes, 155mM NaCl, 1mM CaCl<sub>2</sub>, 1mM MgCl<sub>2</sub>, 2mM NaH<sub>2</sub>PO<sub>4</sub>, 10mM glucose, pH 7.4). A Tokai Hit Stage Top Incubator (INUBG2E-ZILCS) was used to maintain an optimal environment for the cells. The FRAP experiments were performed on TIRF microscope system using the ILas2 system (Roper Scientific).

### **Ex vivo electroporation and organotypic slice cultures.**

Pregnant C57Bl/6 mice were sacrificed by cervical dislocation and E14.5 embryos were rapidly removed and decapitated. CAMSAP2 shRNA1/2 (0.6µg/µl) and/or a GFP vector (0.4 or 1µg/µl) dissolved in 0,05% Fast Green was injected in the lateral ventricles using glass micropipettes (Harvard Apparatus). Heads were electroporated using an ECM 830 Electro-Square-Porator (Harvard Apparatus) set to three unipolar pulses at 30V (100ms interval and pulse length) and using gold-plated Genepaddles (Fisher Scientific). Brains were then isolated, collected in ice-cold cHBSS, embedded in 3% LMP-agarose (Fisher Scientific) in cHBSS and sectioned coronally into 350µm thick slices using a vibratome (Leica). Sections were collected on poly-D-lysine-laminin-coated culture membrane inserts (Falcon), placed on top of slice culture medium (70% v/v Basal Eagle Medium, 26% v/v cHBSS, 2% Horse Serum, 20mM D-glucose, 1mM L-glutamine, penicillin/streptomycin) and cultured for 3 days prior to fixation in 4% paraformaldehyde in PBS. Fixed slices were blocked and permeabilized in 3% BSA + 0.1% Triton X-100 in PBS followed by a primary antibody staining against GFP (rabbit, MBL international Cat. 598) and secondary antibody labeled with Alexa488 (Life Technologies). Slices were mounted in Vectashield containing DAPI (Vector Laboratories Cat. H-1200). Z-stack acquisitions were taken using conventional confocal microscopy using a LSM700 (Zeiss). The degree of neuronal migration was quantified as described previously (Hand et al., 2005).

### **In utero electroporation**

Pregnant C57Bl/6 mice at E14.5 were deeply anaesthetized by Ketamin (75mg/kg)-Medetomidin (1.0mg/kg)-Atropin (0.04mg/kg)-injection and the abdominal cavity was opened. The uterus containing embryos was carefully exposed and the lateral ventricles of the embryo's were injected with GFP (1µg/µl), GFP (0,4µg/µl) + CAMSAP2 shRNA1/2 (0.6µg/µl), GFP (0,5µg/µl) + GFP-CAMSAP2 (0,5µg/µl), or GFP (0,2µg/µl) + CAMSAP2 shRNA1/2 (0.6µg/µl) + GFP-CAMSAP2 (0,2µg/µl) dissolved in 0,05% Fast Green was injected in the lateral ventricles using glass micropipettes (Harvard Apparatus). Brains were electroporated using an ECM 830 Electro-Square-Porator (Harvard Apparatus) set to three unipolar pulses at 30V (100ms interval and pulse length) and using gold-plated Genepaddles (Fisher Scientific). Embryos were placed back into the abdomen, abdominal muscles and skin were sutured separately and mother mice were injected with 0.05mg/kg

Buprenorphinehydrochloride and awakened by injection of 1 mg/kg antipamezole. Embryo's were collected at E17.5 and heads were fixed in 4% Paraformaldehyde in PBS and submerged in 30% Sucrose. 12 $\mu$ m cryosections were made and sections were blocked and permeabilized in 10% Normal Horse Serum + 0.2% Triton X-100 in PBS followed by a primary antibody staining against GFP (rabbit, MBL international Cat. 598). Secondary antibodies labeled with Alexa488 or Alexa568 (Life Technologies) were used following the primary antibodies. Sections were mounted in Vectashield containing DAPI (Vector Laboratories, H-1200). Z- stack acquisitions were taken using conventional confocal microscopy using a LSM700 (Zeiss).

### **Image analysis and quantification**

Image processing was performed in ImageJ, MetaMorph, MatLab, Origin and or LabVIEW. Confocal images were projected using maximum projection. For all of the analysis background subtraction of the image was applied. As indicated in the figure legends, some images were processed by low pass filtering with a 3x3 kernel.

*Analysis of laser-induced severing experiments.* To determine the intensity of GFP-CAMSAP2 before and after laser-induced severing, a 10x10 pixel region was selected at the site of laser cutting and a second region of the same size was used to subtract the background. The intensity trace was then plotted in origin and fitted with a single exponent:  $I(t)=A(1-e^{-\lambda t})$ . I, is the intensity (a.u.), A, is the amplitude,  $\lambda$ , is the time constant. The amplitude of the exponent was used to normalize the intensity trace.

*Analysis of FRAP experiments.* To analyze the recovery of fluorescence, 10x10 pixel regions including the bleached CAMSAP2 area were selected and background subtracted frame-by- frame by subtracting the average intensity of an empty, non-bleached area. Recovery R was then calculated as  $R = (I(t)-I(\text{directly after bleaching}))/I(\text{before bleaching})-I(\text{directly after bleaching})$ , with I denoting total dendrite intensity. After normalization, the final recovery R<sub>final</sub> for each individual trace was determined as the level at the end of the recording (800 s after bleaching). The immobile fraction was then calculated as 1-R<sub>final</sub>. The values obtained were similar to the values obtained by fitting an exponential recovery ( $R = R_{\text{final}}(1-\exp(-t/\tau))$ ), to the trace obtained by averaging all individual traces.

*Quantification of endogenous antibody staining in neurons.* To determine intensities from endogenous staining in an image (acquired with LSM700 40x objective and 63x objective), ImageJ is used to manually draw regions of interest (ROI) around the soma and primary dendrites. From the ROI the mean intensity was measured. To avoid measuring staining intensity from surrounding and overlapping neurons, smaller regions of 20x20 pixels were used for analysis of staining intensities. This method has been used for measuring the protein depletion in CAMSAP2 and  $\gamma$ -Tubulin shRNA expressing neurons. Measurements of endogenous EB3 localization in fixed neurons were performed as described previously (Jaworski et al., 2009; Kapitein et al., 2011). The number of EB3 comets per 10  $\mu$ m of soma or dendrite length was measured using MetaMorph software. The dendrites and axons of mRFP-expressing neurons were identified based on their morphology and by immunostaining for the dendritic marker MAP2. Statistical analysis was performed with Student's t-test assuming a two-tailed and unequal variation. N was defined as the number of neurons analyzed.

*Quantification of  $\gamma$ -Tubulin at the centrioles.* Confocal images of the Cep135 (centriolar marker) were thresholded and converted in binary images using ImageJ. Regions of interest (ROI) representing the location of each individual centriole were generated by applying the "Analyse particles" function. These ROIs were subsequently applied to the corresponding  $\gamma$ - Tubulin images and mean pixel intensities were quantified. Peri-

centrosomal signals were determined by measuring the mean pixel intensity within a 3 pixel radius encircling the ROI.

*Quantification of number of positive axons per neuron.* The Olympus BX53 upright microscope was used to quantify the number of axons per single neuron (stage 2 or stage 3 neurons), by counting the number of neurites positive for the axon specific marker tau, or axon initial segment markers pan-Nav or  $\beta$ IV-Spectrin. The counting was performed on neurons untreated and treated with 10 nM Taxol for 48 hours. The results of statistical analyses are performed using a Student's t-test assuming a two-tailed distribution and unequal variation. N was defined as the number of neurons analyzed

*Analysis of dendrite morphology.* For the morphometric analysis of dendrite morphology, we used  $\beta$ -Galactosidase, GFP, or mRFP as an unbiased cell fill. Images for dendritic morphology were performed with a 40x objective on the LSM510 and LSM5 Pascal. Morphometric analysis for dendrites was performed in MetaMorph. Quantification of the number of dendritic branches, primary dendrites, total dendrite length and Sholl analysis was done with the acquired images. For dendrite length all dendrites of a single neuron were traced in MetaMorph and the number of pixels was automatically converted to  $\mu\text{m}$ . For Sholl analysis concentric circles with 20  $\mu\text{m}$  differences in diameter were drawn around the cell body, and the number of dendrites crossing each circle was manually counted. The results of statistical analyses are performed using a Student's t-test assuming a two-tailed distribution and unequal variation. N was defined as the number of neurons analyzed

*Intensity profile analysis.* Characterization of fluorescence intensity profile in initial segment was performed similar to (Grubb and Burrone, 2011). For each neuron image, the intensity profile was traced along the axon in ImageJ using curves of appropriate thickness ( $\sim 0.5 \mu\text{m}$ ). This produced an array of intensities  $I(rk)$  at discrete distances  $rk$  from the initial point along the curve  $k \in \{1, 2, \dots, N\}$ . Further the smoothening of the profile was performed using moving average filter with the window equal to  $\sim 3 \mu\text{m}$ , giving profile  $\tilde{I}(r_k)$ . It was normalized with respect to its minimum and maximum values:

$$\hat{I}(r_k) = \frac{\tilde{I}(r_k) - \tilde{I}_{\min}}{\tilde{I}_{\max} - \tilde{I}_{\min}}$$

The result was used to locate points describing the shape of profile: maximum, minimum, "beginning" and "end". Position of the "beginning" reference point  $r_{\text{beg}}$  corresponded to the normalized intensity value of 0.33 while moving in the direction to the cell body from the maximum. Position of the "end"  $r_{\text{end}}$  used the same threshold intensity value, but moving in the direction away from cell body.

*Relative average alignment.* Intensity profiles were traced along the same line in two-channel image of double labeled neurons, where one channel corresponded to the CAMSAP2 staining and the other one to the protein of interest. Each profile was characterized as described above. As a common reference point we chose the "end" point of CAMSAP2, since its intensity distribution represents monotonically decreasing function. To perform the averaging between different neurons, we aligned all profiles in such a way that the position of the CAMSAP2 "end" point for each staining became the origin of  $r$  axis. To overcome different sampling of fluorescent intensity along the curve we performed linear interpolation of discrete profile:

$$\hat{I}(r) = \hat{I}(r) = \sum_{k=1}^{N-1} \hat{I}_k(r)$$

$$\text{Where } \hat{I}_k(r) = \begin{cases} \hat{I}(r_k) + \frac{\hat{I}(r_{k+1}) - \hat{I}(r_k)}{r_{k+1} - r_k} (r - r_k), & r \in [r_k, r_{k+1}] \\ 0, & r \notin [r_k, r_{k+1}] \end{cases}$$

We used these linear interpolations to equidistantly sample each profile with the step of 0.1  $\mu\text{m}$ . This allowed us to average normalized fluorescent intensity values from different neurons at the same points of  $r$  axis. All analysis routines were written using MATLAB software and are available at <https://github.com/ekatruxha/AIS>.

#### *dSTORM imaging*

dSTORM microscopy (Heilemann et al., 2008; Rust et al., 2006) was performed on a Nikon Ti microscope equipped with a 100x Apo TIRF objective (NA. 1.49), a Perfect Focus System and an additional 2.5x Optovar to achieve an effective pixel size of 64 nm. Evanescent or oblique laser illumination was achieved using a custom illumination pathway with a 15 mW 405 nm diode laser (Power Technology), a 50 mW 491 nm DPSS laser (Cobolt Calypso), and a 40 mW 640 nm diode laser (Power Technology). Fluorescence was detected using an Andor DU-897D EMCCD camera. To facilitate multicolor imaging, an image splitting device (Optosplit III, Cairn research) with ET series GFP, RFP, Cy5 filters (Chroma Technology) was placed between microscope and camera. All components were controlled by Micromanager software (Edelstein et al., 2010)

For dSTORM imaging of Alexa Fluor 647 and Atto 488, the sample was continuously illuminated with 640 nm and 491 nm light, respectively. In addition, the sample was illuminated with 405 nm light at increasing intensity to keep the number of fluorophores in the fluorescent state constant. Between 8000 and 13000 frames were recorded per acquisition with exposure times of 25-40 ms. For multi-color images, Alexa Fluor 647 was imaged before Atto 488.

Immunolabeling of endogenous CAMSAP2 required fixation using methanol, as no staining was observed after fixation with PFA, most likely due to epitope blocking. Unfortunately, whereas microtubules appeared normal using conventional microscopy after treatment with methanol, dSTORM imaging was unable to resolve individual neuronal microtubules in these conditions (as opposed to PFA fixation, see Figure 2D,E). To simultaneously resolve microtubule ends and CAMSAP2, we therefore overexpressed CAMSAP2-GFP, which could be immunolabeled using a single chain antibody against GFP (VHHGFP) upon PFA fixation.

For optimal microtubule imaging, cells were first extracted with 0.3% glutaraldehyde (GA) in extraction buffer (0.3% Triton-X + 5mM MgCl<sub>2</sub> + 150mM NaCl + 5 mM glucose in PEM80-buffer (80 mM PIPES, 1 mM EGTA, 4 mM MgCl<sub>2</sub>, pH 6.9) for one minute. After extraction, fixation was performed in 4% PFA for 10 minutes. After fixation, cells were washed 2 times 5 minutes in PBS and cells were further permeabilized 10 minutes in PBS +0.2% Triton-X. Cells were then washed 3 times 5 minutes in PBS and incubated for 45 minutes in blocking solution (2% w/v BSA, 0.2% w/v gelatin, 10 mM glycine, 50 mM NH<sub>4</sub>Cl in PBS, pH 7.4). Primary antibodies were incubated overnight at 4°C or 1.5 hours at RT and washed with PBS. Cells were post-fixed in 2% PFA for 10 minutes or stored at 4 C. Primary antibodies were  $\alpha$ -Tubulin (Sigma) conjugated to Alexa647 and VHHGFP coupled to atto488, both diluted 1:100.

For Alexa647 only, imaging was performed using 50-100mM MEA, 5% w/v glucose, 560  $\mu\text{g/ml}$  glucose oxidase, 40  $\mu\text{g/ml}$  catalase in PBS. For Atto488 alone or together

with Alexa Fluor 647, imaging was performed using 200mM MEA in 10mM Tris buffer (pH 10).

### *dSTORM Localization and Rendering Algorithms*

Single-molecule localization software was written in Java as an ImageJ plugin. Each image in an acquired stack was convoluted with the two dimensional mexican hat kernel matching the microscope's point spread function (PSF) size. The intensity histogram of the convolved image was fitted to a Gaussian distribution and used to calculate the threshold intensity value (mean value of the fit plus three standard deviations). The maximum intensity values within individual spots were chosen as initial positions for the peaks' fitting performed on the original image. We used unweighted nonlinear least squares fitting with Levenberg- Marquardt algorithm to the assumed asymmetric two-dimensional Gaussian PSF. Only fits with a calculated width within  $\pm 30\%$  of the measured PSF's standard deviation were accepted. Localizations within one pixel distance in a number of successive frames were considered to arise from the same molecule. In this case the weighted mean was calculated for each coordinate, where weights were equal to inverse squared localization errors. The resulting table with molecule coordinates and errors was used to render the final localization image with 10 or 20 nm pixel size. Each molecule was plotted as a 2D Gaussian of the integrated intensity equal to one and with standard deviations of 32 nm.

For two color imaging, chromatic corrections obtained from scanning multichromatic beads were applied to the Alexa647 dataset. In cases where sample drift was observed during acquisition, a correction algorithm was applied (Mlodzianoski et al., 2011). In short, a set of localization images was built from consecutive subsets of frames corresponding to different times. Drift was determined by maximizing the spatial normalized cross-correlation between these intermediate reconstructions.

### *Stretch Analysis*

Super-resolution images were thresholded at two standard deviations above the average pixel intensity and stretches and their length were detected using a custom ImageJ routine, with a threshold minimal stretch length of 250 nm. The width of a stretch was determined by fitting the intensity profile perpendicular to the length of the stretch with a Gaussian. The Full Width at Half Maximum (FWHM) of a stretch was determined from the standard deviation  $\sigma$  of the Gaussian fit.

## REFERENCES

- Alvarado-Kristensson, M., Rodriguez, M.J., Silio, V., Valpuesta, J.M., and Carrera, A.C. (2009). SADB phosphorylation of gamma-tubulin regulates centrosome duplication. *Nature cell biology* *11*, 1081-1092.
- Botvinick, E.L., Venugopalan, V., Shah, J.V., Liaw, L.H., and Berns, M.W. (2004). Controlled ablation of microtubules using a picosecond laser. *Biophysical journal* *87*, 4203-4212.
- Brummelkamp, T.R., Bernards, R., and Agami, R. (2002). A system for stable expression of short interfering RNAs in mammalian cells. *Science* *296*, 550-553.
- Caussinus, E., Kanca, O., and Affolter, M. (2011). Fluorescent fusion protein knockout mediated by anti-GFP nanobody. *Nature structural & molecular biology* *19*, 117-121.
- Cheung, Z.H., Chin, W.H., Chen, Y., Ng, Y.P., and Ip, N.Y. (2007). Cdk5 is involved in BDNF-stimulated dendritic growth in hippocampal neurons. *PLoS biology* *5*, e63.
- Colombelli, J., Reynaud, E.G., Rietdorf, J., Pepperkok, R., and Stelzer, E.H. (2005). In vivo selective cytoskeleton dynamics quantification in interphase cells induced by pulsed ultraviolet laser nanosurgery. *Traffic (Copenhagen, Denmark)* *6*, 1093-1102.
- Edelstein, A., Amodaj, N., Hoover, K., Vale, R., and Stuurman, N. (2010). Computer control of microscopes using microManager. *Current protocols in molecular biology* / edited by Frederick M. Ausubel ... [et al.] *Chapter 14*, Unit14 20.
- Grubb, M.S., and Burrone, J. (2011) Activity-dependent relocation of the axon initial segment fine-tunes neuronal excitability. *Nature* *465*, 1070-1074.
- Hand, R., Bortone, D., Mattar, P., Nguyen, L., Heng, J.I., Guerrier, S., Boutt, E., Peters, E., Barnes, A.P., Parras,

- C., et al. (2005). Phosphorylation of Neurogenin2 specifies the migration properties and the dendritic morphology of pyramidal neurons in the neocortex. *Neuron* *48*, 45-62.
- Heilemann, M., van de Linde, S., Schuttelz, M., Kasper, R., Seefeldt, B., Mukherjee, A., Tinnefeld, P., and Sauer, M. (2008). Subdiffraction-resolution fluorescence imaging with conventional fluorescent probes. *Angewandte Chemie (International ed)* *47*, 6172-6176.
- Honnappa, S., Gouveia, S.M., Weisbrich, A., Damberger, F.F., Bhavesh, N.S., Jawhari, H., Grigoriev, I., van Rijssel, F.J., Buey, R.M., Lawera, A., et al. (2009). An EB1-binding motif acts as a microtubule tip localization signal. *Cell* *138*, 366-376.
- Jaworski, J., Kapitein, L.C., Gouveia, S.M., Dortland, B.R., Wulf, P.S., Grigoriev, I., Camera, P., Spangler, S.A., Di Stefano, P., Demmers, J., et al. (2009). Dynamic microtubules regulate dendritic spine morphology and synaptic plasticity. *Neuron* *61*, 85-100.
- Kaech, S., and Banker, G. (2006). Culturing hippocampal neurons. *Nature protocols* *1*, 2406-2415.
- Kapitein, L.C., Yau, K.W., Gouveia, S.M., van der Zwan, W.A., Wulf, P.S., Keijzer, N., Demmers, J., Jaworski, J., Akhmanova, A., and Hoogenraad, C.C. (2011). NMDA receptor activation suppresses microtubule growth and spine entry. *The Journal of neuroscience : the official journal of the Society for Neuroscience* *31*, 8194-8209.
- Kapitein, L.C., Yau, K.W., and Hoogenraad, C.C. (2010). Microtubule dynamics in dendritic spines. *Methods in cell biology* *97*, 111-132.
- Mlodzianoski, M.J., Schreiner, J.M., Callahan, S.P., Smolkova, K., Dlaskova, A., Santorova, J., Jezek, P., and Bewersdorf, J. (2011). Sample drift correction in 3D fluorescence photoactivation localization microscopy. *Optics express* *19*, 15009-15019.
- Ogawa, Y., Schafer, D.P., Horresh, I., Bar, V., Hales, K., Yang, Y., Susuki, K., Peles, E., Stankewich, M.C., and Rasband, M.N. (2006). Spectrins and ankyrinB constitute a specialized paranodal cytoskeleton. *The Journal of neuroscience : the official journal of the Society for Neuroscience* *26*, 5230-5239.
- Rust, M.J., Bates, M., and Zhuang, X. (2006). Sub-diffraction-limit imaging by stochastic optical reconstruction microscopy (STORM). *Nature methods* *3*, 793-795.
- Shaner, N.C., Campbell, R.E., Steinbach, P.A., Giepmans, B.N., Palmer, A.E., and Tsien, R.Y. (2004). Improved monomeric red, orange and yellow fluorescent proteins derived from *Discosoma* sp. red fluorescent protein. *Nature biotechnology* *22*, 1567-1572.
- Stepanova, T., Slemmer, J., Hoogenraad, C.C., Lansbergen, G., Dortland, B., De Zeeuw, C.I., Grosveld, F., van Cappellen, G., Akhmanova, A., and Galjart, N. (2003). Visualization of microtubule growth in cultured neurons via the use of EB3-GFP (end-binding protein 3-green fluorescent protein). *The Journal of neuroscience : the official journal of the Society for Neuroscience* *23*, 2655-2664.
- Witte, H., Neukirchen, D., and Bradke, F. (2008). Microtubule stabilization specifies initial neuronal polarization. *The Journal of cell biology* *180*, 619-632.
- Wiznerowicz, M., and Trono, D. (2003). Conditional suppression of cellular genes: lentivirus vector-mediated drug-inducible RNA interference. *Journal of virology* *77*, 8957-8961.
- Zhou, F.Q., Zhou, J., Dedhar, S., Wu, Y.H., and Snider, W.D. (2004). NGF-induced axon growth is mediated by localized inactivation of GSK-3beta and functions of the microtubule plus end binding protein APC. *Neuron* *42*, 897-912.

## Chapter 6

# Dendrites In Vitro and In Vivo Contain Microtubules of Opposite Polarity and Axon Formation Correlates with Uniform Plus-End-Out Microtubule Orientation

Kah Wai Yau,<sup>1\*</sup> Philipp Schätzle,<sup>1\*</sup> Elena Tortosa,<sup>1</sup> Stéphane Pagès,<sup>2</sup> Anthony Holtmaat,<sup>2</sup> Lukas C. Kapitein,<sup>1</sup> and Casper C. Hoogenraad<sup>1</sup>

<sup>1</sup>Cell Biology, Faculty of Science, Utrecht University, 3584 CH, Utrecht, The Netherlands, and <sup>2</sup>Department of Basic Neurosciences, Faculty of Medicine and the Center for Neuroscience, University of Geneva, 1211 Geneva, Switzerland

\*K.W.Y. and P.S. contributed equally to this work.

### ABSTRACT

In cultured vertebrate neurons, axons have a uniform arrangement of microtubules with plus-ends distal to the cell body (plus-end-out), whereas dendrites contain mixed polarity orientations with both plus-end-out and minus-end-out oriented microtubules. Rather than non-uniform microtubules, uniparallel minus-end-out microtubules are the signature of dendrites in *Drosophila* and *Caenorhabditis elegans* neurons. To determine whether mixed microtubule organization is a conserved feature of vertebrate dendrites, we used live-cell imaging to systematically analyze microtubule plus-end orientations in primary cultures of rat hippocampal and cortical neurons, dentate granule cells in mouse organotypic slices, and layer 2/3 pyramidal neurons in the somatosensory cortex of living mice. In vitro and in vivo, all microtubules had a plus-end-out orientation in axons, whereas microtubules in dendrites had mixed orientations. When dendritic microtubules were severed by laser-based microsurgery, we detected equal numbers of plus- and minus-end-out microtubule orientations throughout the dendritic processes. In dendrites, the minus-end-out microtubules were generally more stable and comparable with plus-end-out microtubules in axons. Interestingly, at early stages of neuronal development in nonpolarized cells, newly formed neurites already contained microtubules of opposite polarity, suggesting that the establishment of uniform plus-end-out microtubules occurs during axon formation. We propose a model in which the selective formation of uniform plus-end-out microtubules in the axon is a critical process underlying neuronal polarization.

*J Neurosci.* 2016 Jan 27;36(4):1071-85

### INTRODUCTION

Neurons are polarized cells that have a long axonal process and several branched dendrites and strongly depend on the microtubule cytoskeleton for their integrity and organelle transport (Conde and Cáceres, 2009; Kapitein and Hoogenraad, 2015). Microtubule-based motor proteins recognize the intrinsic asymmetry of the microtubule lattice and drive transport to either the microtubule plus end or minus end (Hirokawa et al., 2010; Maday et al., 2014). In various model systems, it has been shown that microtubule arrays within axon and dendrites are highly organized with respect to their intrinsic polarity, and this specific microtubule organization is essential to direct polarized cargo transport (Kapitein and Hoogenraad, 2011; Rolls, 2011). For instance, studies in primary hippocampal neurons have demonstrated that microtubule plus-end-directed motor kinesin-1 selectively transports cargoes into the axon along plus-end-out microtubules (Nakata and Hirokawa, 2003; Hammond et al., 2010; Kapitein et al., 2010a; Nakata et al., 2011; Huang and Banker, 2012). In addition, the selective presence of minus-end-out oriented microtubules in dendrites enables the minus-end-directed motor dynein to selectively transport cargoes into dendrites (Kapitein et al., 2010b). Although the importance of the microtubule cytoskeleton for proper intracellular trafficking and cargo sorting is unambiguous, how the microtubules in axon and dendrites are organized in developing and mature neurons is essentially unknown.

The hook-decoration technique was used originally to determine the orientation of microtubules in axons and dendrites by electron microscopy (EM; Baas and Lin, 2011). Using this approach, uniformly plus-end-out microtubule polarity orientations were observed in axons of various types of cultured vertebrate neurons (Baas et al., 1987; Baas et al., 1988). In contrast, proximal dendrites contained non-uniformly oriented microtubules that were found to be approximately half plus-end-out and half minus-end-out (Baas et al., 1988; Burton, 1988). In olfactory bulb mitral cells, the mixed population of microtubules remained constant throughout the dendritic processes, although microtubules in distal dendritic segments in hippocampal neurons appeared primarily oriented plus-end-out (Baas et al., 1988; Burton, 1988). The different microtubule polarity orientations in axons and dendrites were confirmed using fluorescently labeled microtubule plus-end binding proteins in living hippocampal and Purkinje cell cultures (Stepanova et al., 2003). Nevertheless, the fraction of inward-growing comets is typically twofold lower than outward-growing comets. In addition, some evidence for mixed microtubule arrays in mouse brain tissue have been presented by both second-harmonic generation microscopy and live-cell imaging of microtubule growth (Kwan et al., 2008; Kleele et al., 2014). In invertebrate neurons, microtubules in axons are also arranged with their plus ends distal to the cell body, whereas in dendrites most microtubules are arranged with their minus ends distal to the cell body, although mixed orientation microtubules have also been observed (Stone et al., 2008; Goodwin et al., 2012; Maniar et al., 2012). These results suggest that the presence of minus-end-out oriented microtubules is a unique property of dendrites.

In this study, we use a combination of cell-biological approaches, quantitative microscopy, laser microsurgery, organotypic slice cultures, and *in vivo* imaging in living mice to determine microtubule orientations in axons and dendrites. In mature neurons, non-uniformly oriented microtubules are present in dendrite *in vitro*, *ex vivo*, and *in vivo*. Equal numbers of plus- and minus-end-out microtubule orientations are present throughout mature dendritic processes. During early stages of neuronal development, minus-end-out microtubules were already detected in growing neurites before neuronal polarization. These data suggest that mixed microtubule polarity is established before axon formation and neuronal polarization.

### MATERIALS AND METHODS

#### Animals

All experiments with animals were performed in compliance with the guidelines for the welfare of experimental animals issued by the government of The Netherlands or the Swiss Federal Act on Animal Protection and were approved by the Animal Ethical Review Committee of Utrecht University or the University of Geneva and the Geneva Cantonal Veterinary Office.

#### DNA constructs

CAMSAP2–shRNA (ttgcatgtgctcaacagt) has been described previously (Yau et al., 2014). The GFP–MT+TIP construct contains the general microtubule plus-tip localization signal (SxIP motif) of human MACF2, which is recognized by the end binding (EB) protein. It was generated by fusing the two-stranded leucine zipper coiled-coil sequence corresponding to GCN4-p1 (RMKQLEDKVEELLSKNYHLENEVARLKKLVGER) to N-terminal 18 aa peptide of human MACF2 (Gly5468-Lys5485; NP\_899236) by PCR-based strategy (Honnappa et al., 2009). A glycine rich-linker sequence (GAGG) was inserted between GCN4 pl and MACF18 and subcloned into p $\beta$ actin-16 pl expression vector to generate p $\beta$ actin–GFP–GCN4–MACF18. For stage 2–3 neurons, we used MACF43 that is identical to MACF18 except for the 43 N-terminal amino acids of human MACF2 (Glu5455–Arg5497). Because we used GFP–GCN4–MACF18/43 as a general marker to analyze the dynamics of microtubule growing plus ends, we named this construct GFP–MT+TIP. p $\beta$ actin–GFP and p $\beta$ actin–mRFP have been described previously (Kapitein et al., 2010a). The volume marker MARCKS–TagRFP-T was adapted from MARCKS–GFP (De Paola et al., 2003). The first 41 aa of MARCKS (MGCQFSKTAACKGEAAAERPGEAAVASSPSKANGQENGHVKV) containing an Ala-Cys mutation were fused to TagRFP-T spaced by a GS-linker (PCR). MARCKS–TagRFP-T was cloned upstream and GFP–GCN4–MACF18 downstream of an attenuated ECMV internal ribosome entry site (pIRES), resulting in high expression of the volume marker and low expression of GFP–MT+TIP. The bicistronic construct was either subcloned into pCAGGS vector for single-cell electroporation or into the lentivirus vector pSIN–TRE–mSEAP–hPGK–rtTA2sM2 (kind gift from Dr. Didier Trono, Ecole Polytechnique Fédérale de Lausanne, Lausanne, Switzerland). The human PGK promoter was replaced for a short rat synapsin (0.5 kb) promoter to restrict the expression primarily to neurons. Lentiviral particles were generated as described previously (Yau et al., 2014).

#### Primary cortical and hippocampal neuron cultures, transfection, and infections

Primary cortical and hippocampal cultures were prepared from embryonic day 18 rat brains (of either sex). Cells were plated on coverslips coated with poly-L-lysine (37.5  $\mu$ g/ml) and laminin (1.25  $\mu$ g/ml) at a density of 75,000/well. Dissociated neurons were cultured in Neurobasal medium (NB) supplemented with 2% B27 (Gibco), 0.5 mM glutamine (Gibco), 15.6  $\mu$ M glutamate (Sigma), and 1% penicillin/streptomycin (Gibco).

*Transfections.* Hippocampal neurons were transfected using Lipofectamine 2000 (Invitrogen). Briefly, DNA (1.8  $\mu$ g/well, for a 12-wells plate) was mixed with 3.3  $\mu$ l of Lipofectamine 2000 in 200  $\mu$ l of NB, incubated for 30 min, and then added to the neurons in NB at 37°C in 5% CO<sub>2</sub> for 45 min. Next, neurons were washed with NB and transferred to their original medium at 37°C in 5% CO<sub>2</sub> for 2–4 d.

*Nucleofections.* Primary cortical neurons (1.3 X 10<sup>6</sup> cells) were nucleofected with 0.5  $\mu$ g of GFP–MACF43 or GFP plasmid and 2.5  $\mu$ g of empty plasmid or shRNA using the Amaxa Rat Neuron Nucleofector kit (Lonza) according to the instructions of the manufacturer. Cells were grown for 18–24 h at 37°C in 5% CO<sub>2</sub> before imaging.

*Lentivirus infections.* Hippocampal neurons were transduced with lentivirus 7–10 d

before experiments. The tetracycline-dependent expression was induced 2 d before imaging by supplementing the medium with 500 ng/ml doxycycline.

### **Organotypic slice cultures and lentivirus infections**

Mouse hippocampal slices (350  $\mu\text{m}$ ) were prepared from postnatal day 5–6 pups (of either sex). Slices were transferred on small patches of FHLIC membrane (0.45  $\mu\text{m}$ ; Millipore) positioned on Millicell culture inserts (Millipore). Hippocampal slices were transduced with lentivirus directly after plating by pouring a drop of concentrated virus solution over the culture. Medium exchange and maintenance of the cultures followed the method described previously (Stoppini et al., 1991). Experiments were performed after 14–21 d in vitro (DIV). Slice culture medium was supplemented with doxycycline (500 ng/ml) at least 5 d before imaging.

### **In vivo single-cell electroporation**

In vivo single-cell DNA electroporation was performed as described previously (Page's et al., 2015). Briefly, young male mice (4–6 weeks old) were anesthetized with an intraperitoneal injection of MMF [a mixture of medetomidin (Dorbene, 0.2 mg/kg), midazolam (Dormicum, 5 mg/kg), and fentanyl (Duragesic, 0.05 mg/kg) in saline]. A craniotomy was performed above the somatosensory cortex. A 15–20 Mil glass pipette (GC150F-7.5; Harvard Apparatus) was filled with internal solution [in mM: 266 KMeSO<sub>4</sub>, 14 KCl, 20 Na-HEPES, 4 MgATP, 4 Na<sub>2</sub>ATP, 1 Na<sub>2</sub>GFP, and 0.1 EGTA, pH 7.2 (280–290 mOsm)], containing 30 ng/ $\mu\text{l}$  plasmid DNA and Alexa Fluor 488 hydrazide (50  $\mu\text{M}$ ; Life Technologies). Under visual guidance, cortical layer 2/3 (L2/3) pyramidal cells were targeted and electroporated (10 pulses, -12 V, 500  $\mu\text{s}$ , 50 Hz) using a head stage (AP-1AX1MU) attached to an Axoprotector 800A (Molecular Devices). Successful electroporations resulted in fast filling of cell bodies by Alexa. Finally, the pipette was withdrawn gently, and a glass coverslip (3  $\mu\text{m}$  diameter) was implanted to cover the craniotomy. Imaging was started after 1 week of recovery.

### **Live-cell confocal imaging and laser-induced severing**

Spinning-disk confocal microscopy was performed on an inverted microscope (Nikon Eclipse Ti with Perfect Focus System) with a Plan Apo VC 100X, 1.4 numerical aperture (NA) oil-immersion objective or an SFluor 100X, 0.5–1.3 NA oil-immersion objective (Nikon) for laser-induced severing (LS) experiments. MetaMorph software was used to control the Evolve 512 EMCCD camera (Photometrics) and all motorized parts. The microscope has been further outfitted with an ASI motorized stage MS-2000-XYZ with piezo top plate, ILas system (Roper Scientific France/PICT-IBiSA, Curie Institute), and Shutter LB10-3. For fluorescence excitation, a Calypso 491 nm, 100 mW laser and Jive 561, 100 mW laser (Cobolt) were used. A Teem Photonics 355 nm Q-switched pulsed laser was used for LS (Botvinick et al., 2004; Colombelli et al., 2005). ET-GFP/mCherry dichroic (59022; Chroma Technology) or sequential ET-GFP (49002; Chroma Technology) and ET-mCherry (49008; Chroma Technology) were used for wavelength selection. All imaging was performed in full conditioned medium for hippocampal neuron cultures. A Tokai Hit Stage Top Incubator (INUBG2E-ZILCS) was used to maintain neurons at 37°C with 5% CO<sub>2</sub>.

*Imaging stage 1–2 neurons.* Time-lapse acquisition was performed for 6 min (without LS) or for 1 min before LS and 5 min after, with a time interval of 1 s. LS was performed at 10  $\mu\text{m}$  from the soma. Regions of 10  $\mu\text{m}$  before and behind the position of LS were used for the quantifications. In neurites shorter than 20  $\mu\text{m}$ , LS was performed in the neurite midpoint.

*Imaging stage 3–5 neurons.* Microtubule plus-tip imaging in neuron cultures was performed with 6 X 0.5  $\mu\text{m}$  steps and sequential channel recordings. Time-lapse recordings

were performed in a single plane when LS was conducted sequentially.

*Imaging taxol-treated neurons.* Hippocampal neurons were incubated with DMSO or 10 nM taxol at DIV1 for 72 h. For microtubule LS experiments, control and taxol-treated neurons were transfected at DIV3 with GFP–MT+TIP using Lipofectamine 2000 (Invitrogen). At DIV4, neurons were fixed for immunostaining or imaged for live-cell experiments.

*Imaging organotypic slices.* Slice cultures were imaged in ACSF [126 mM NaCl, 3 mM KCl, 2.5 mM CaCl<sub>2</sub>, 1.3 mM MgCl<sub>2</sub>, 1.25 mM Na<sub>2</sub>HPO<sub>4</sub>, 26 mM NaHCO<sub>3</sub>, 20 mM glucose, and 1 mM Trolox (bubbled with 95% O<sub>2</sub>, 5% CO<sub>2</sub>)]. Dendrites were imaged with z-stacks of 6–8 X 0.5 μm steps, unless for LS experiments (single plane). Imaging positions along the dendrites were defined as follows: proximal <25%; middle between 25 and 60%; distal >60% of total dendritic length.

### **In vivo two-photon laser scanning microscopy**

Imaging was performed using a custom-built two-photon laser-scanning microscope (<https://openwiki.janelia.org/wiki/display/shareddesigns/Shared+Two-photon+Microscope+Designs>) and data acquisition software Scanimage (<https://openwiki.janelia.org/wiki/display/ephus/ScanImage>). Anesthetized mice (with MMF; see above) were head fixed under the microscope, and their temperature was kept constant by a feedback-controlled heating pad. Fluorophores were excited using a titanium:sapphire laser (Chameleon Ultra II; Coherent) tuned at 950 nm. Emitted fluorescence was collected using a 16X multiphoton objective (0.8 NA, N16XLWD-PF; Nikon), spectrally separated using two bandpass filters (HC530/55, HC607/70, BrightLine; Semrock) and detected using two photomultiplier tubes (10770PB-40 for green, and R3896 for red; Hamamatsu). Images were recorded at 0.2 Hz (512 X 512 pixels, 2 ms/line, 5 s interimage interval). Typical fields of view spanned from 30–50 μm square. The average excitation power was kept below 50 mW as measured under the objective.

### **Immunofluorescence staining**

Neurons were fixed in ice-cold 100% methanol/1 mM EGTA for 10 min at -20°C. After fixation, cells were washed three times for 5 min in PBS and incubated with the primary antibody in GDB buffer (0.2% BSA, 0.8 M NaCl, 0.5% Triton X-100, and 30 mM phosphate buffer, pH 7.4) overnight at 4°C. After extensive washing with PBS, neurons were incubated with secondary antibodies in GDB buffer for 1 h at room temperature and then washed again. Coverslips were mounted in Vectashield (Vector Laboratories) and sealed with nail polish. The following primary and secondary antibodies were used: rabbit anti-CAMSAP2 (17880-1-AP; Proteintech), mouse anti- $\alpha$ -tubulin (B-5-1-2; Sigma), mouse anti-Tau (MAB3420; Millipore Bioscience Research Reagents), ( $\beta$ III tubulin (PRB-435P; Covance), mouse anti-GFP (1814460; Roche), and Alexa Fluor 488- and Alexa Fluor 568-conjugated secondary antibodies (Invitrogen).

### **Image processing and quantifications**

Image analysis was performed using FIJI, and data processing and statistical analysis were done in Excel and GraphPad Prism (GraphPad Software).

*MT+TIP analysis.* Time-lapse recordings were low-pass filtered and subtracted with an average projection of the complete time lapse (Kapitein et al., 2010b). Kymography was performed on the filtered images using the FIJI “KymoResliceWide” plugin. Starting and end positions of the traces were marked by the “Cell Counter” plugin, and coordinates were exported for additional analysis. The number of microtubule plus-tip comets, comet growth speed, and distances to the cutting position were calculated from the starting and end

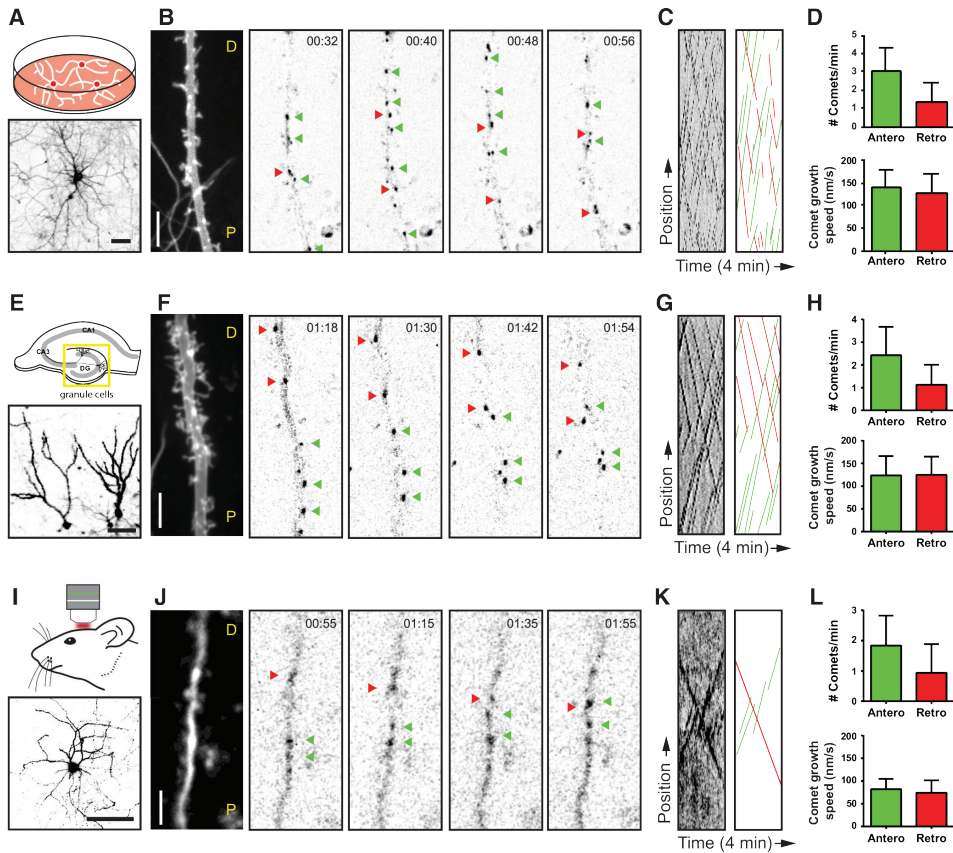
coordinates of the microtubule traces. To produce comparable data of microtubule plus-tip dynamics between the different model systems, we quantified comets that were detectable over 1 min within 20  $\mu\text{m}$  of axonal or dendritic segment (if not indicated differently). In LS experiments, the place of cutting was positioned in the center of this observation area.

*MT stability analysis.* Similar imaging and analysis was performed as described above. The starting points of comets relative to the site of LS within a time window of 1 min (before or after LS) were put into bins of 2  $\mu\text{m}$  and averaged with each DIV15 dendrite or axon. Multiple minutes were averaged for each dendrite and axon after LS. The median indicates 50% of the data points.

*Analysis of CAMSAP2 distribution.* Images from a wide-field fluorescence microscope (Eclipse 80i; Nikon) were used to quantify CAMSAP2 distribution. Localization of CAMSAP2 only at the tip of the neurite was classified as “tip,” homogenous distribution along the neurite as “equal,” and scattered accumulations along the neurite as “random.”

*Analysis of CAMSAP2 staining.* Cortical neurons were nucleofected with GFP and either pSuper control or CAMSAP2 shRNA before plating. Neurons were fixed 72 h after transfection and stained for CAMSAP2. Confocal images were taken with a Zeiss LSM 700. Mean intensities of CAMSAP2 signals were quantified in neurites of control and CAMSAP2 depleted neurons at 15  $\mu\text{m}$  distance from the soma using FIJI software.

**RESULTS**



**Mixed microtubule organization in dendrites in vitro and in vivo**

To determine the microtubule organization in vertebrate dendrites in vitro and in vivo, we systematically analyzed microtubule plus-end dynamics and orientations in primary cultures of rat hippocampal neurons, dentate granule cells in mouse organo-typic slices, and L2/3 pyramidal neuron in somatosensory cortex of living mice. We first performed two-color live-cell imaging in differentiated (DIV18) hippocampal neurons in culture. We generated a bicistronic construct expressing the microtubule plus-end marker GFP–MT+TIP (Yau et al., 2014) and MARCKS–TagRFP to highlight neuronal morphology and used lentivirus to transduce the dissociated cultures. In cases when the expression level was low, we observed unidirectional displacement of GFP–MT+TIP comets in axons, whereas in dendrites the movements were bidirectional, reflecting the different MT organization in axons and dendrites (Stepanova et al., 2003; Jaworski et al., 2009). Consistent with previous reports using EB3–GFP as +TIP marker (Jaworski et al., 2009; Kapitein et al., 2011), the total number of comets in DIV18 cultured hippocampal neurons was  $4.4 \pm 1.6$  comets/min/20  $\mu\text{m}$  (mean  $\pm$  SD;  $n = 32$  dendrites), and the average velocity of comet movements was  $132 \pm 53$  nm/s (mean  $\pm$  SD;  $n > 600$  comets). Next, we analyzed in detail the direction of GFP–MT+TIP comets that were recorded in middle segments of primary dendrites, calculated as the half-length of the total dendrite measured from the cell body to the dendritic tip (Figure 1A–C; Movie 1). We found on average 31% of labeled plus ends moving retrogradely toward the cell body, whereas the comet growth speed did not significantly differ between both directions (Figure 1D). These results indicate that one-third of the dynamic microtubules in dendrites of cultured hippocampal neurons are oriented with the plus end inward.

◀ *Figure 1. Mixed Dendritic Microtubule Organization In Vitro, Ex Vivo, and In Vivo*

- (A) Schematic drawing of dissociated neuron cultures (top) and a representative example expressing a volume marker (bottom). Neurons have been transduced with lentivirus expressing a bicistronic cassette of GFP–MT+TIP and the volume marker MARCKS–TagRFP.
- (B) Time-lapse acquisitions from a DIV18 neuron. The first frame shows an average projection of the volume marker. Dendrite orientation is indicated by P (proximal) and D (distal). All the following represent selected frames from the GFP–MT+TIP time-lapse. Green arrowheads point to individual anterograde moving GFP–MT+TIP comets, and red arrowheads point to retrograde moving comets.
- (C) Kymographs made from the complete time-lapse recording shown in B. The left shows the original kymograph, and the right shows an illustration of the manually traced comets displacements for better visualization.
- (D) Quantification of microtubule properties in dissociated cultures. The top diagram shows the number of GFP–MT+TIP comets within a defined observation window of 1 min and 20  $\mu\text{m}$  ( $n = 32$  dendrites). The bottom diagram displays the average speeds of anterograde and retrograde moving comets ( $n > 500$  comets).
- (E) Schematic drawing of a hippocampal slice (top) and two representative granule cells (bottom) imaged in organotypic slice cultures. The yellow box indicates the dentate gyrus region that has been analyzed exclusively in this study. Slices have been transduced with the same lentivirus used for dissociated neurons. (Figure legend continues on the next page)
- (F) Recordings from a granule cell dendrite at 18 d in culture. The first frame displays the dendritic profile labeled by the volume marker. Subsequent frames show the GFP–MT+TIP channel acquired from the same dendrite.
- (G) Original and illustrated kymographs of the time-lapse recording shown in F.
- (H) Quantification of the average comet number (top diagram;  $n = 38$  dendrites) and growth speed (bottom diagram;  $n > 300$  comets) in organotypic slice cultures. The method of quantification was identical to the data on dissociated cultures.
- (I) Schematic illustration of the in vivo imaging through a cranial window (top) and a representative example of a neuron at low magnification expressing the volume marker (bottom). Neurons were transfected by single-cell electroporation using the same bicistronic expression construct on which the lentivirus was based on.
- (J) In vivo two-photon time-lapse imaging of an L2/3 pyramidal neuron. The dendritic dimensions were visualized by an average projection of the GFP–MT+TIP channel (first frame), and the following frames represent selected time points of the same channel. Bidirectional microtubule displacements are indicated by colored arrowheads.
- (K) Original and illustrated kymographs of the time-lapse recording shown in J.
- (L) Quantification of the average comet number (top diagram;  $n = 12$  dendrites) and growth speed (bottom diagram;  $n > 100$  comets) of the observed in vivo microtubule dynamics. Scale bars: A, E, I, 50  $\mu\text{m}$ ; B, F, J, 5  $\mu\text{m}$ . Error bars indicate SD. See also Movie 1.

Next, we determined microtubule dynamics and growth direction in mouse organotypic hippocampal slice cultures. Using the same live-cell imaging approach, we then focused primarily on the dendrites of the granule cells, the principal neurons of the dentate gyrus (Figure 1E–G; Movie 1). Similar to the dissociated hippocampal neurons, middle segments of granule cell dendrites have on average 32% of the GFP–MT+TIP comets moving retrogradely toward the cell body (Figure 1H). In slice cultures, both the total number of comets and the comet growth speed were slightly reduced in both directions (Figure 1H).

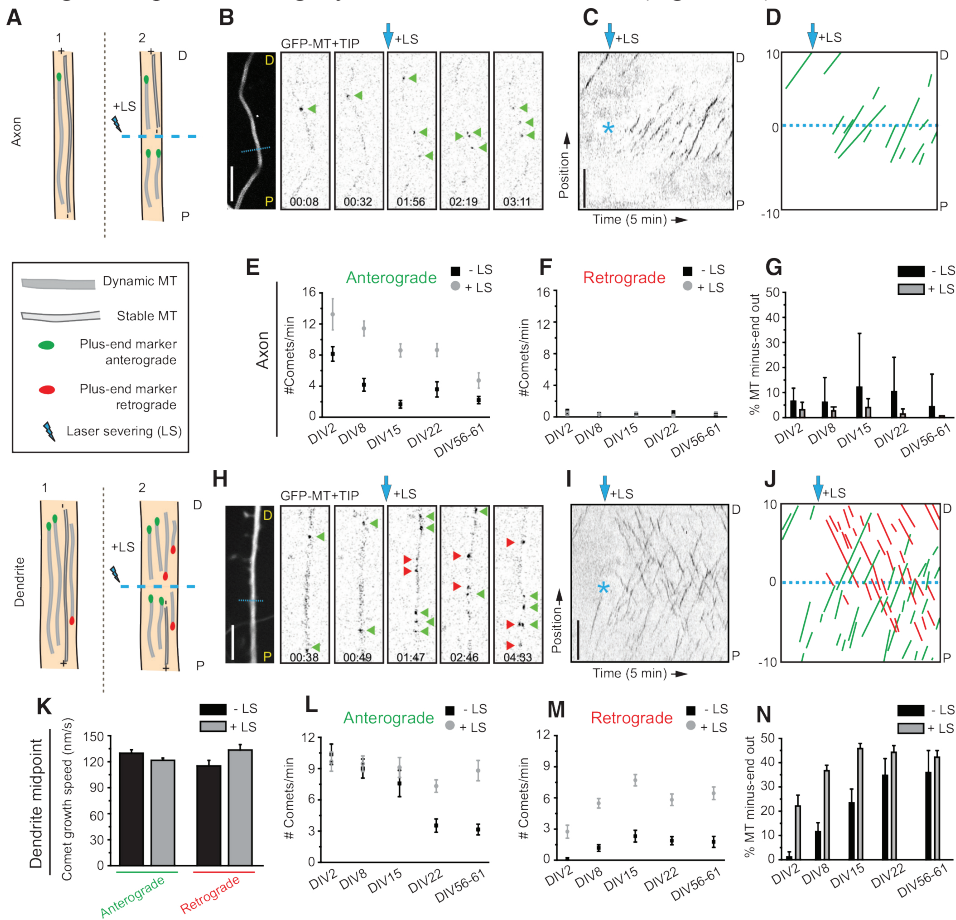


**Figure 2. Differential Microtubule Organization During Neuronal Development**

(A) Schematic representation of microtubule LS in axon (top) and dendrite (bottom). P indicates the proximal region and D the distal region.

(B) Stills from a spinning-disk time-lapse recording of an axon (DIV15) transfected with mRFP and GFP–MT+TIP at DIV13. The first still on the left is an average projection of the axon in which the dashed cyan line is the region of LS. Green arrowheads indicate GFP–MT+TIP comets pointing in an anterograde direction during the time-lapse recording. Cyan arrow indicates when LS is performed. The time-lapse recording is low-pass filtered and background subtracted.

(C) Kymograph of the time-lapse recording shown in B. Asterisk indicates time and location of LS.

(D) Schematic representation of the kymograph shown in C. Dashed cyan line separates the regions 10 μm before and 10 μm after LS. Green lines represent comets pointing in the anterograde direction.

(E, F) Quantification of the number of comets per minute pointing in the anterograde (E) or retrograde (F) direction, 10 μm before and after the position of LS. Black square data points are before LS, and the gray circles are after LS; n = 13 axons. (Figure legend continues on the next page)

Finally, we recorded microtubule dynamics and orientation in dendrites of L2/3 pyramidal cells in the somatosensory cortex of living mice (Figure 1I–K; Movie 1). The bicistronic construct expressing GFP–MT+TIP and MARCKS–TagRFP was delivered by single-cell electroporation into the neocortex of 6-week-old mice and in vivo two-photon laser scanning microscopy (2PLSM) imaging was performed through a cranial window (Cane et al., 2014; Page et al., 2015). Transfected neurons that were sufficiently bright in both channels were selected for imaging at high magnification. In dendrites, we observed clear displacements of GFP–MT+TIP comets in both anterograde and retrograde directions. Similar to the culture systems, pyramidal cell dendrites had on average 34% of the GFP–MT+TIP comets moving retrogradely toward the cell body (Figure 1L). The total number of comets and the comet growth speed were further reduced in dendrites in vivo compared with in vitro systems (Figure 1L). Together, these data demonstrate that a mixed microtubule organization is present in mature dendrites from different neuron types, both in vitro and in vivo. Although the number of dynamic microtubules and growth speed is markedly decreased in vivo, the ratio of dynamic plus-end-in (1:3) and plus-end-out (2:3) microtubules in dendrites is a constant parameter in all analyzed model systems.

### Gradual increase in minus-end-out microtubules during dendrite development

Imaging of plus-tip markers provides information about the dynamic ends of microtubules but not about the length of the remaining portion behind the plus end. Therefore, the fraction of comets moving in a specific direction does not directly reflect the fraction of corresponding microtubule orientations in a certain section, because microtubules of different orientations could have different lengths (Figure 2A). To elucidate in more detail the orientations within a bundle of microtubules, we used live-cell imaging in combination with laser-based microsurgery (Yau et al., 2014). Cutting a microtubule bundle with a short-pulsed laser creates new microtubule ends and allows analysis of the newly generated growing microtubule plus ends (Figure 2A). By observing the growth direction of GFP–MT+TIP comets before and after LS, this assay permits a direct readout of the orientations of microtubules within specific cellular regions, regardless of length or plus-end dynamicity (Figure 2B–D, H–J). An increased fraction of comets moving in one direction indicates that the microtubules with corresponding orientations are on average longer or nondynamic, both suggesting increased stability. Analyzing the growth direction of GFP–MT+TIP comets before and after LS in axons at different developmental stages (from DIV2 until DIV61) revealed that, in all

(Figure legend continued from previous page)

(G) Percentage of microtubules with their minus ends pointed out in axons before (black columns) and after (gray columns) LS.

(H) Stills from a spinning-disk time-lapse recording of a dendrite middle region (DIV15) transfected with mRFP and GFP–MT+TIP at DIV13. The first still on the left is an average projection of the axon in which the dashed cyan line is the region of LS. Green and red arrowheads indicate comets moving in anterograde or retrograde direction. The cyan arrow indicates when LS is performed. The time-lapse recording is low-pass filtered and background subtracted.

(I) Kymograph of the time-lapse recording shown in H. Asterisk indicates time and location of LS.

(J) Schematic representation of the kymograph shown in I. Dashed cyan line separates the regions 10 μm before and 10 μm after LS. Green and red lines represent comets pointing in the anterograde or retrograde direction, respectively.

(K) Growth speed of comets extending in anterograde or retrograde direction along the dendrite. Black bars are before LS and gray bars are after; n = 163, n = 475, n = 41, n = 335 number of comets.

(L, M) Quantification of the number of comets per minute pointing in the anterograde (L) or retrograde (M) direction, 10 μm before and after the position of LS. Black square data points are before LS, and the gray circles are after LS.

(N) Percentage of microtubules with their minus ends pointed out in dendrites before (black columns) and after (gray columns) LS; DIV2, n = 7 axons and 8 dendrites; DIV8, n = 11 axons and 17 dendrites; DIV15, n = 13 axons and 16 dendrites; DIV22, n = 12 axons and 17 dendrites; DIV56–DIV61, n = 10 axons and 13 dendrites. Scale bars, 5 μm. Error bars indicate SEM.

cases, the majority of the GFP–MT+TIP comets (>95%) showed anterograde displacement (Figure 2G). We also found that the total number of comets was decreased in more mature axons both before and after LS (Figure 2 E, F ). The observed decrease in axonal plus ends suggests the following: (1) the total number of microtubules in the axon shaft decreases during differentiation; or (2) the total number of axonal microtubules remains constant, and shorter microtubules are gradually replaced by longer ones.

Next, we analyzed the growth direction and speed of GFP–MT+TIP comets in middle segments of primary dendrites and found both anterograde and retrograde moving comets at all developmental stages (DIV2–DIV61; Figure 2H–K ). The ratio plus-end-in and plus-end-out microtubules changes markedly during early dendrite development (DIV2–DIV15) but remains constant in more mature dendrites (older than DIV22; Figure 2N ). In young dendrites (DIV2), the majority of the GFP–MT+TIP comets show predominantly anterograde displacement, whereas additional retrograde comets were observed after LS (Figure 2 M, N), demonstrating that stable (long or nondynamic) minus-end-out microtubules are present in dendrites at these early developmental stages. In more differentiated dendrites at later stages of development (DIV2–DIV15), the relative fraction of plus-end-in comets increased during LS, suggesting again that minus-end-out microtubules are on average more stable (i.e., longer or nondynamic; Figure 2 L, M ). At later stages (older than DIV22), the fraction of plus-end-in comets before LS increased because the number of plus-end-out comets decreased, indicating that, in mature dendrites, microtubules of both orientations are more stable (i.e., longer or nondynamics; Figure 2 L, M ). These results indicate that mature dendrites contain equal numbers of plus- and minus-end-out microtubule orientations.

### **Mixed microtubule orientations are present throughout the dendrites**

Previous EM studies suggested differences in microtubule orientation between distinct dendritic regions, with a gradual increase in plus-end-out microtubules in the more distal parts of the dendrites (Baas et al., 1989). Because all analysis was done on the middle segments of primary dendrites, we extended our live-cell imaging and LS study to proximal and distal regions of the dendrite (Figure 3A). In dendrites of DIV15 neurons, we observed mixed microtubule orientation in all dendritic regions with constant ratios of ~20% minus-end-out for dynamic microtubules (Figure 3B–D). During LS, the fraction of minus-end microtubule increased twofold, suggesting that minus-end-out microtubules are more stable (i.e., longer or nondynamic), whereas plus-end-out microtubules are dynamic throughout the whole dendrite. Similarly, LS in mature neurons (DIV55–DIV61) revealed that 40% of microtubules are oriented minus-end-out (Figure 3F–I ). Next, we analyzed microtubule dynamics in proximal, middle, and distal regions of granule cells in organotypic hippocampal slice cultures (Figure 4A–C). Dynamic minus-end-out microtubules were present in different numbers in all three dendritic segments (Figure 4D; Movie 2). In agreement with our data on mature dissociated cultures, we found an increased ratio of dynamic minus-end-out microtubules in the middle segment compared with other regions (Figure 4E). Because the analyzed granule cells varied in the length of their dendritic trees, we tested for potential position effects. Within the middle segments, defined as 25–60% of total dendritic length, we found no indication for differential microtubule organization with regard to absolute or relative dendritic length (Figure 4F ). This suggests a continuous microtubule organization within the middle segments of dendrites. LS in the same region confirmed that the majority of minus-end-out microtubules are also stable in slice cultures (Figure 4 H, I ). These results show that microtubule orientations are mixed throughout the dendrites and confirm the previous findings on differential stability of anterograde and retrograde microtubules in dendrites.

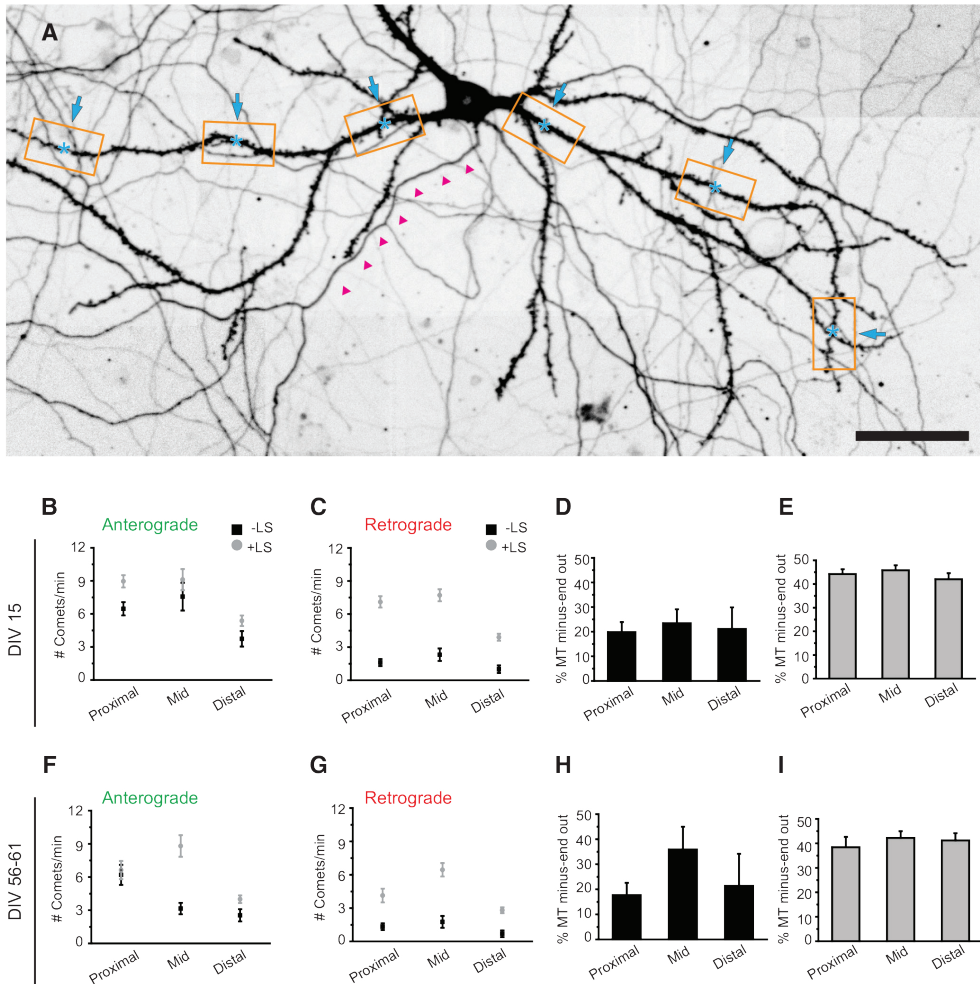


**Figure 3. Microtubule Organization is Maintained Throughout Dendritic Regions**

(A) Hippocampal neuron at DIV18 (stitched image of 20X recordings). The axon is highlighted by magenta arrowheads. Orange boxes show examples of proximal, middle, and distal regions along the dendrites. Laser-induced severing of microtubules was performed in proximal regions with a distance of 20  $\mu\text{m}$  to the soma and in distal regions with 20  $\mu\text{m}$  to the end of the dendrite (cyan asterisk).

(B, C) DIV15 quantification of the number of comets per minute pointing in the anterograde (B) and retrograde (C) direction, 10  $\mu\text{m}$  before and after the position of LS. Black square data points are before LS, and the gray circles are after LS.

(D, E) Percentage of microtubules with their minus ends pointed out in dendrites before (black columns; D) and after (gray columns; E) LS; DIV15, proximal dendrite  $n = 30$ , middle dendrite  $n = 16$ , distal dendrite  $n = 19$ .

(F, G) DIV56–DIV61 quantification of the number of comets per minute pointing in the anterograde (F) and retrograde (G) direction, 10  $\mu\text{m}$  before and after the position of LS. Black square data points are before LS, and the gray circles are after LS.

(H, I) Percentage of microtubules with their minus ends pointed out in dendrites before (black columns; H) and after (gray columns; I) LS; DIV56–DIV61, proximal dendrite  $n = 15$ , middle dendrite  $n = 13$ , distal dendrite  $n = 13$ ,  $n = 10$  axons. Scale bar, 50  $\mu\text{m}$ . Error bars indicate SEM.

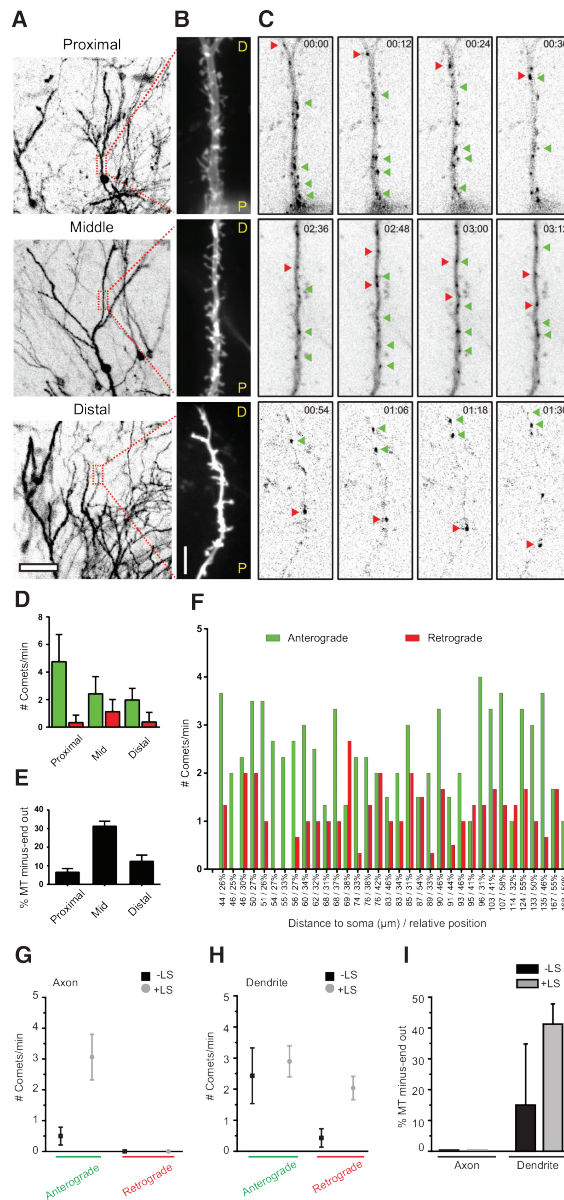


**Figure 4. Hippocampal Slice Cultures Exhibit Similar Microtubule Organization as Mature Dissociated Cultures**  
 (A) Lentivirus transduced hippocampal slice cultures expressing GFP–MT+TIP and a volume marker. Low-magnification overview images show dendritic tree recorded with the volume marker. Boxes label regions that were used for high-resolution imaging and localize at proximal, medial, or distal regions as indicated.  
 (B) Average projection of volume channels recorded sequentially to GFP–MT+TIP time-lapse imaging.  
 (C) Single still frames of a GFP–MT+TIP time-lapse recording acquired from the adjacent dendrite shown in B. Arrowheads point on individual comets moving in anterograde (green) or retrograde (red) direction. Recordings were performed at 6 s intervals. See also Movie 2.  
 (D) Quantification of microtubule plus tips moving in anterograde or retrograde direction analyzed for indicated dendritic regions (counted within a time window of 1 min and 20  $\mu\text{m}$  dendrite length); proximal dendrite  $n = 14$ , middle dendrite  $n = 34$ , distal dendrite  $n = 21$ . (Figure legend continues on the next page)

### Stable minus-end-out microtubules in dendrites

The increased fraction of plus-end-in comets during LS suggested that minus-end-out microtubules are either longer or less dynamic, both suggesting increased stability. To verify in more detail the difference in stability between plus- and minus-end-out microtubules, we analyzed the precise position of the new plus-end microtubules generated after LS. Cutting microtubules induces a quick depolymerization, followed by a rescue event and the formation of a new microtubule plus end from which we determine microtubule orientations. The positions from which new comets appear are a relative measurement of microtubule depolymerization before rescue and also reveal the resistance of a microtubule to depolymerization, allowing us to report on microtubule stability in different neuronal compartments. As stated above, using LS we cannot discriminate between different stable microtubule populations, such as nondynamic microtubules and long microtubules with a dynamic plus end. As expected, before LS, the GFP–MT+TIP comets are distributed randomly throughout the axon and dendrites in cultured hippocampal neurons at DIV15 (Figure 5A–C). The newly formed comets after cutting axonal microtubules start at 0–10  $\mu\text{m}$  proximal to the cut site, with a median at 5.7  $\mu\text{m}$  (Figure 5D). Similar to stable axonal microtubules, newly formed retrograde comets in dendrites are concentrated in close proximity to the LS position (median at 5.7  $\mu\text{m}$ ; Figure 5F). However, the newly formed anterograde comets in dendrites start at a greater distance from the cut site (median at 7.9  $\mu\text{m}$ ; Figure 5E), which is indicative of increased microtubule depolymerization caused by less stable anterograde microtubules in dendrites. These results suggest that the minus-end-out microtubules in dendrites exhibit similar stability as axonal microtubules and the plus-end-out microtubules in dendrites are relatively less stable.

### Minus-end-out microtubules are present in neurites before neuronal polarization

Previous EM studies have suggested that the mixed microtubule organization in dendrites appears after axon initiation and neuronal polarization (Baas et al., 1989). Because we found minus-end-out microtubules in DIV2 neurons (Figure 2 M, N), we next studied at which neurodevelopmental stage mixed microtubule polarity is established. Therefore, we extended our study to stage 2 (nonpolarized cells with only neurites) and stage 3 (neurons with an extended axon and minor neurites, which later will differentiate into dendrites; Dotti et al., 1988). Cortical neurons were nucleofected directly after dissociation with GFP–MT+TIP, and microtubule growth dynamics was imaged 18–24 h after transfection before and after LS (Figure 6A–E). Analysis of the growth direction of GFP–MT+TIP comets revealed that mixed polarity microtubules are already present in neurites before neuronal polarization. Although most comets moved outward, we observed  $\sim 10\%$  of dynamic minus-end-out microtubules in the neurites of stage 2 neurons, which increased approximately two-fold after LS (Figure 6G,H). Similar dynamic effects were found in minor neurites of stage 3 neurons (Figure 6G,H). However, the  $\sim 10\%$  minus-end-out microtubules in axons were unaffected by LS,

*(Figure legend continued from previous page)*

*(E) Percentage of microtubules with minus-end-out orientation in proximal, middle, and distal dendrites.*

*(F) Quantification of comets direction in middle regions of individual dendrites ( $n = 34$ ). Numbers on the x-axis show the distance of the imaging position center to the soma and the relative distance compared with the total dendritic length in percentage. The average number of comets/min/20  $\mu\text{m}$  moving anterograde (green) and retrograde (red) are presented for each dendrite.*

*(G, H) Quantification of GFP–MT+TIP moving anterograde or retrograde in axons and dendrites of hippocampal slice cultures. Black square data points are before LS, and gray circle data points are after LS; axon,  $n = 7$ ; dendrite,  $n = 8$ .*

*(I) Percentage of microtubules with their minus ends pointed outward in axons and dendrites before (black columns) and after (gray columns) LS. Scale bars: A, 50  $\mu\text{m}$ ; B, 5  $\mu\text{m}$ . Error bars indicate SD (D) and SEM (E, G, H, I).*

demonstrating that all axonal minus-end-out microtubules are dynamic in stage 3 neurons. These results suggest that the stable minus-end-out microtubule population, present in the neurites in nonpolarized cells, is lost from the axon directly after neuronal polarization.

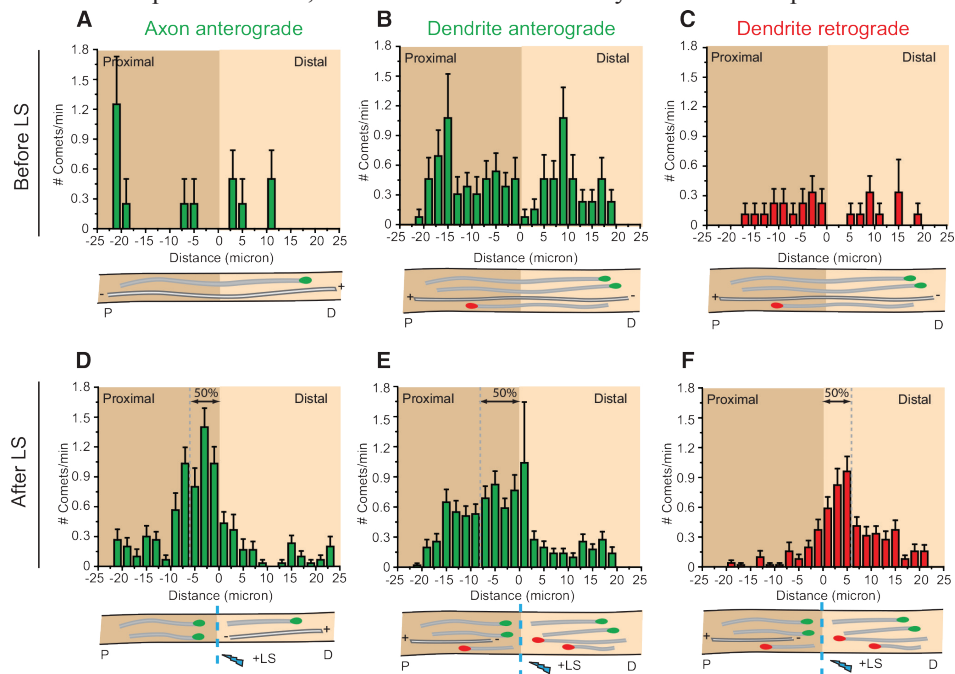


**Figure 5. Dendrites Contain Stable Minus-End-Out Microtubules.**

(A–C) Histograms of anterograde comet starting positions in axons (A) and dendritic middle region (B) before LS in green and retrograde comet starting positions in red (C). D–F, Histograms of anterograde comet starting positions in axons (D) and dendritic middle region (E) after LS in green and retrograde comet starting positions in red (F). Below the histograms are schematic representations of comets going anterograde (green) and retrograde (red). Error bars indicate SEM.

Because CAMSAP2 binds and stabilizes minus ends of non-centrosomal microtubules and is essential for neuronal polarization (Yau et al., 2014), we next determined the precise localization of CAMSAP2 in neurons before and after axon outgrowth (Figure 6I). A variety of small CAMSAP2 clusters and distinct (punctated) stretches were scattered throughout the neurites in developing neurons (Figure 6I–M). Knocking down of CAMSAP2 using previously published shRNAs (Yau et al., 2014) strongly decreased the antibody signal in stage 2 neurons (Figure 6J, K), confirming the specificity of the CAMSAP2 staining in neurites. Interestingly, in nonpolarized neurons, we observed that CAMSAP2 stretches were enriched at some of the neurite tips (Figure 6I–M), suggesting that CAMSAP2 may be involved in setting up minus-end-out microtubules in neurites. At later stages of development, CAMSAP2 was found along the axon and minor neurites (Figure 6I–O). Together, our results demonstrate that the mixed microtubule organizations are present in neurites of nonpolarized cells and that stable uniform plus-end-out microtubules are formed during the early steps of axon polarization.

### Taxol-induced axonal processes contain uniform plus-end-out microtubules

Our data suggest that the selective formation of uniform plus-end-out microtubules occurs during axon polarization. To further evaluate microtubule changes during neuronal

polarization, we used the microtubule-stabilizing drug taxol to induce the formation of multiple axons in cultured neurons (Witte et al., 2008) and analyzed the orientation of microtubules in newly formed axonal processes. In the presence of low concentrations of taxol (10 nM) for 3 d, the number of Tau- positive processes per cell was increased more than fourfold compared with control neurons (Figure 7A–D). Next, neurons were treated with taxol at DIV1 and transfected with GFP–MT+TIP at DIV3, and microtubule growth was analyzed before and after LS at DIV4 (Figure 7D–F). Consistent with our analysis in DIV2 and DIV8 neurons (Figure 2E–G, L, M), in nontreated cultures, GFP–MT+TIP comets in dendrites showed both anterograde and retrograde displacements, whereas in axons mainly anterograde moving comets were observed (Figure 7D–I). In the axon-like processes after taxol treatment, the majority of GFP–MT+TIP comets showed anterograde displacement and almost no retrograde comets were observed, both before and after LS (Figure 7G,H). Quantification revealed that only a few microtubules remain oriented minus-end-out in taxol-treated neurons, whereas the large majority of microtubules stay plus-end-out (Figure 7I), very similar to what we found in axons of control cells at the various developmental stages (Figure 2E–G). These data show that taxol nearly completely abolishes retrograde microtubules in the newly induced axonal processes. Thus, in addition to microtubule stabilization (Witte et al., 2008), the axon-inducing effect of taxol appears to be linked to the selective formation of uniform plus-end-out microtubules.

### DISCUSSION

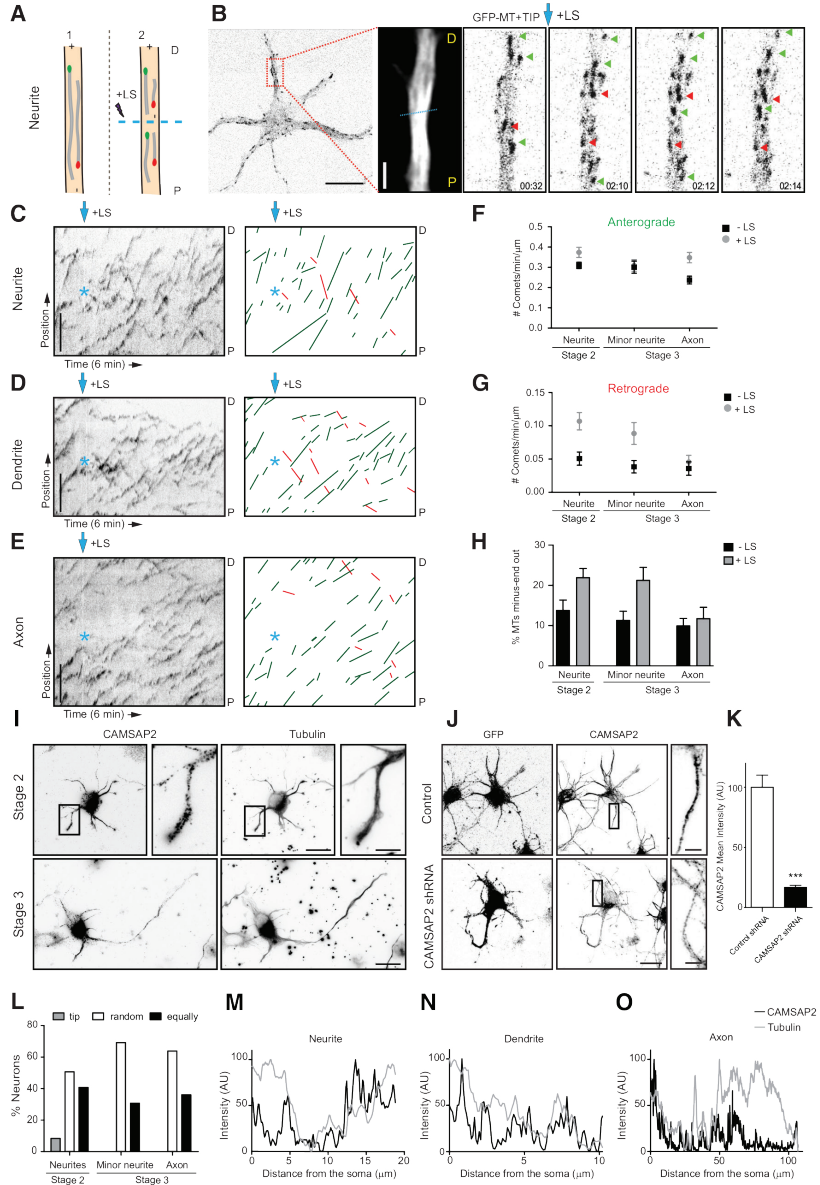
It is well known that the microtubule organization is different in axons and dendrites and has direct implications for neuronal cargo transport (Kapitein and Hoogenraad, 2011; Rolls, 2011). In axons, microtubules are typically arranged with their plus ends outward, whereas in dendrites, a mixed microtubule polarity is observed in mammalian neurons (Baas and Lin, 2011). Previous studies have reported unipolar microtubule arrays in apical dendrites from acute hippocampal slices using second-harmonic generation microscopy (Dombeck et al., 2003; Kwan et al., 2008) and demonstrated a predominantly microtubule minus-end-out orientation in dendrites of invertebrate neurons (Stone et al., 2008; Goodwin et al., 2012; Maniar et al., 2012). These findings motivated us to systematically analyze and compare neuronal microtubule dynamics in various mouse and rat model systems.

#### **Microtubule orientations are approximately equally mixed throughout the dendrites**

So far, most studies on neuronal microtubule organization focused on primary cultured neurons. Here, we presented a comprehensive study on mammalian in vitro, ex vivo, and in vivo model systems that was based on fluorescent microscopic imaging of the growing microtubule plus ends. We found that dendrites in organotypic slice cultures and in the cortex of living mice possess a slight decrease in the number of dynamic microtubule plus ends and growth speed compared with neuron cultures. However, the ratio of dynamic plus-end-out microtubules (2:3) and plus-end-in microtubules (1:3) in dendrites is a constant factor in various model systems. After LS of microtubules, we found an approximately equal ratio (1:1) of plus-end-out and plus-end-in microtubule organization in dendrites. Our findings are in agreement with early EM data obtained by the hook-decoration technique of olfactory bulb mitral cells, in which the mixed microtubule pattern remained constant throughout the entire dendrite (Burton, 1988). However, our data are inconsistent with early EM results in dendrites of hippocampal neurons, which were reported to contain uniform plus-end-out microtubule arrays in distal dendritic parts (Baas et al., 1988, 1989). Importantly, we did observe a great variation in microtubule orientations in some of the dendrites (Figure 4F). Therefore, it is possible that, because of the low number of dendrites ( $n = 3$  for the position

## Chapter 6

dependent orientations) used in the original EM analysis (Baas et al., 1988, 1989), a sampling bias may have occurred and that the reported dendrites are not representative of the general population. Alternatively, because the distal regions of dendrites are similar in size and diameter to axons (Baas et al., 1988, 1989), identification of distal dendrites in EM samples on size measurements only is challenging and may not be a reliable method.



Although mature *Drosophila* neurons have dendrites that contain minus-end-out microtubules, it is also important to note that developing *Drosophila* dendrites initially contain mixed microtubule polarity (Hill et al., 2012). Over a period of several days, this mixed microtubule array gradually matures to a minus-end-out array. In this study, we show in different neuronal cell types from distinct mammalian model systems that microtubules in mature dendrites remain in an antiparallel organization. Thus, it is now clear that dendrites of *Drosophila* and *Caenorhabditis elegans* neurons have a different organization of microtubules. Why mature mammalian dendrites still have plus-end-out microtubules and do not completely switch to minus-end-out polarity, like in *Drosophila* dendrites, remains an open question. Having opposite polarity microtubules in dendrites may increase the efficiency of polarized transport by coordinating the activity of both dynein and specific kinesin family members.

### Differential stabilities of specific microtubule orientations in axons and dendrites

Our results demonstrate that the majority of axonal microtubules are stable and orientated with their plus-end-out during different stages of neuronal development, which is consistent with previous reports (Baas et al., 1991; Kollins et al., 2009). The data also show a marked difference in the stability of anterograde and retrograde directed microtubules in dendrites. Our approach of combining live imaging with LS of microtubules allowed us to quantitatively discriminate between stable and dynamic microtubules. Based on these data, we can distinguish at least three stages of microtubule organization in dendrites. (1) Growing dendrites in young neurons (DIV2) have a 1:4 ratio of plus-end- in/out microtubule orientations, with stable minus-end-out microtubules and dynamic microtubules plus-end-out. (2) Although there are more dynamic plus-end-out microtubules, overall dendrites in developing neurons (DIV8 – DIV15) have an almost 1:1 ratio of microtubule orientations. (3) Dendrites in mature neurons (DIV22–DIV61 and slice cultures) contain slightly more stable plus-end-out microtubules, but the equal ratio of mixed microtubule orientations is unaffected. Microtubule stability in neurons is related to many different parameters (Kapitein and Hoogenraad, 2015) and most likely depends on the combined action of many microtubule regulatory proteins, such as

◀ *Figure 6. Microtubule Orientation in Neurons Before and After Polarization.*

- (A) Schematic representation of the microtubule LS procedure in a neurite. P indicates the proximal region and D the distal region.
- (B) A representative DIV1 cortical neuron expressing GFP–MT+TIP, followed by the maximum projection and stills from a time-lapse recording of the indicated neurite. The dashed cyan line represents the region of LS, and the cyan arrow indicates the moment of laser severing. Green and red arrows mark selected plus- and minus-end-out microtubules, respectively.
- (C–E) Kymographs and illustration of microtubule tracings from representative time-lapse recordings of a neurite (C) from a nonpolarized neuron, dendrite (D), and axon (E) of a polarized neuron. Green lines represent plus-end-out microtubules and red lines minus-end-out microtubules. Cyan asterisk and arrow indicate time and location of LS.
- (F, G) Quantification of anterograde (F) and retrograde (G) growing GFP–MT+TIP comets, with and without LS ( $n = 10–18$  neurons) in DIV1 cortical neurons.
- (H) Percentage of microtubules with their minus ends out in unpolarized and polarized DIV1 neurons, before (black columns) and after (gray columns) LS;  $n = 10–18$  neurons.
- (I) Representative images of nonpolarized (top) and polarized (bottom) DIV1 hippocampal neurons stained for both CAMSAP2 (left; I, L) and  $\alpha$ -tubulin (right).
- (J) Representative images of stage 2 neurons transfected with GFP and control pSuper (top) or CAMSAP2 shRNA (bottom) and stained for both GFP (left) and CAMSAP2 (right).
- (K), Quantification of CAMSAP2 intensity in neurites in control and CAMSAP2 shRNA transfected neurons ( $n = 19$  neurites). \*\*\* $p < 0.001$  using  $t$  test.
- (L) Quantification of CAMSAP2 localization in hippocampal neurons before and after polarization ( $n > 100$  neurites). CAMSAP2 distribution within the neurites is classified in indicated categories.
- (M–O) Representative examples of endogenous CAMSAP2 intensity profiles in neurites (M), before polarization, dendrites (N), and axons (O) from DIV1 hippocampal neurons. Scale bars: B, 2 and 10  $\mu\text{m}$ ; C–E, I, J, 5  $\mu\text{m}$ ; I, J, 20  $\mu\text{m}$ . Error bars indicate SEM.

## Chapter 6

plus-end tracking proteins and minus-end targeting proteins (Akhmanova and Steinmetz, 2008; Akhmanova and Hoogenraad, 2015), microtubule-associated proteins (Dehmelt and Halpain, 2005; Subramanian and Kapoor, 2012), enzymes that sever preexisting microtubules (Roll-Mecak and McNally, 2010; Sharp and Ross, 2012), and tubulin-modifying enzymes that through posttranslational modifications can regulate microtubule stability (Janke and Kneussel, 2010). Future studies should focus on the mechanisms responsible for setting up and selectively stabilizing minus-end-out microtubules during dendrite development.

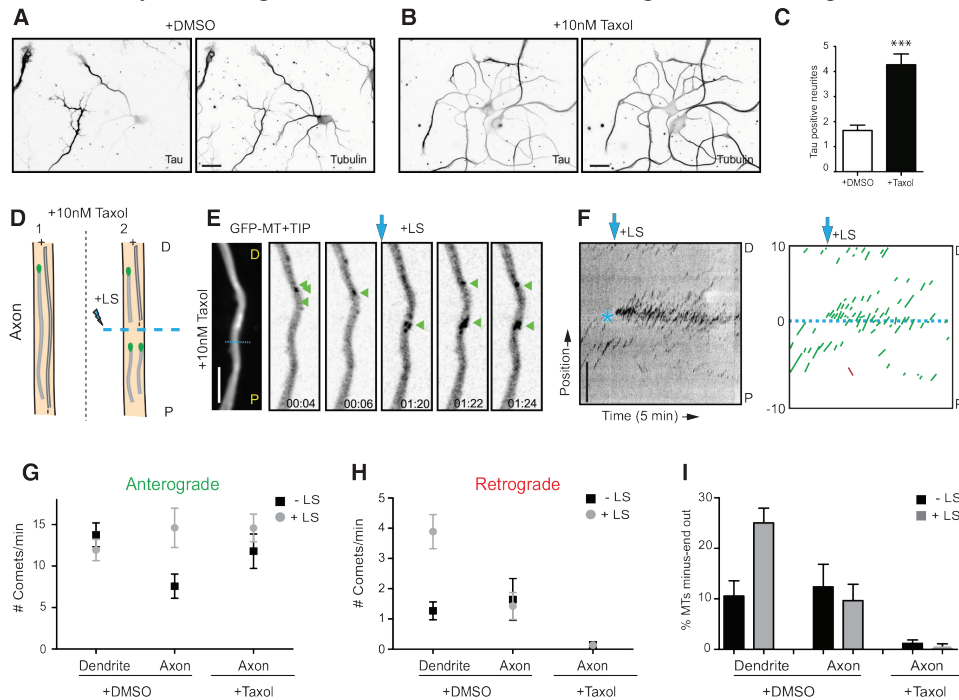


**Figure 7. Microtubule Orientation Changes in Neurons After Taxol Treatment.**

(A, B) Representative examples of DIV4 neurons treated for 72 h with DMSO (A) or 10nM taxol (B) and stained for both Tau (left) and  $\beta$ III-tubulin (right).

(C) Quantification of Tau-positive neurites in control and taxol-treated neurons. Neurons treated with taxol showed a significant increase in the number of Tau-positive neurites (\*\*\*)  $p < 0.001$  using *t* test).

(D) Schematic representation of the microtubule LS procedure in an axon, after taxol treatment. P indicates the proximal region and D the distal region.

(E) Maximum projection and stills from a representative time-lapse recording of a hippocampal neuron expressing GFP-MT+TIP and treated with taxol for 72 h.

(F) Kymographs and schematic tracings from a representative time-lapse recording of an axon after taxol treatment. Green lines represent plus-end-out microtubules and red lines minus-end-out microtubules. Cyan asterisk and arrow indicate time and location of LS.

(G, H) Quantification of GFP-MT+TIP moving anterograde (G) and retrograde (H), with (black squares) and without (gray circles) LS in DIV4 hippocampal neurons treated with DMSO or 10 nM taxol for 72 h.

(I) Percentage of minus-ends-out microtubules in control and taxol-treated neurons, before (black columns) and after (gray columns) LS.  $n=14$  axons and 31 dendrites in control neurons, and  $n=27$  axons after taxol treatment (> 3 axons analyzed per neuron). Scale bars: A, B, 50  $\mu$ m; E, F, 5  $\mu$ m. Error bars indicate SEM.

### **Mixed microtubules are present in neurites before neuronal polarization**

Using the same hook-decoration technique, it was found that, in nonpolarized cells, the microtubule orientation in the newly formed neurites was plus-end-out and that only after axon initiation and neuronal polarization minus-end-out microtubules appeared in dendritic processes (Baas et al., 1989). The EM data suggested that formation of mixed microtubule organization is important for differentiation into dendrites and establishing neuronal polarity (Baas and Lin, 2011). However, this model has never been tested in living neurons at early stages of development. Our results reveal that mixed polarity microtubules are already present in neurites before the neuron becomes polarized. We found that nonpolarized neurons contain ~20% minus-end-out microtubules in their neurites. At stage 3 neurons, directly after axon outgrowth, the polarity orientation of microtubules in axons changed: 10% of the axonal microtubules are oriented minus-end-out, whereas 20% of the minor neurites microtubules remain minus-end-out. Taxol treatments confirmed this observation and also showed a marked reduction of retrograde microtubules in newly induced axonal processes. At later stages of development, the difference in microtubule orientation in axons and dendrites is even more extreme: almost all minus-end-out microtubules in the axon disappear and minus-end-out microtubules in dendrites increase up to ~45%. These different microtubule orientations have been shown to facilitate polarized cargo trafficking in mature neurons (Kapitein and Hoogenraad, 2011; Rolls, 2011). For instance, uniform plus-end-out microtubules in axons facilitate the selective sorting of kinesin-driven vesicles, whereas minus-end-out microtubules allow dynein motors to drive specific cargo to dendrites (Nakata and Hirokawa, 2003; Kapitein et al., 2010b). Importantly, a recent study argued against a contribution of dynein to dendrite-specific transport because selective (non-axonal) transport was observed already in stage 3, during which microtubule orientations were long believed to be uniformly plus-end-out (Petersen et al., 2014). However, in this study, we show the following: (1) nonpolarized stage 2 neurons already contain a significant number of minus-end-out microtubules in their neurites, allowing for dynein-based transport at all developmental stages; and (2) axons reduce the number of stable minus-end-out microtubules in stage 3 neurons by ~50%, allowing dynein motors to exclude dendritic cargos from the axon and drive polarized cargo transport into future dendrites.

The observation that neurites in nonpolarized neurons contain a mixed population of microtubules raises several other questions. First, how are minus-end-out microtubules generated in these newly growing neurites? It is possible that microtubules are (1) nucleated at the centrosome, subsequently released, and transported into the neurites, (2) severed by local katanin or spastin activity, or (3) nucleated at noncentrosomal sites, such as Golgi membranes, local  $\gamma$ -tubulin complexes, or from preexisting microtubules (Kuijpers and Hoogenraad, 2011). In addition, several motor proteins have been reported to contribute to the establishment or maintenance of the minus-end-out microtubule organizations in dendrites. For instance, depletion of kinesin-5 increases the proportion of dynamic minus-end-out microtubules in neurons, whereas downregulation of kinesin-6 or kinesin-12 reduces the number of retrograde microtubules in dendrites (Lin et al., 2012; Kahn et al., 2015). Moreover, kinesin-1 and kinesin-2 have been reported to establish the uniform minus-end-out microtubules in *C. elegans* and *Drosophila*, respectively (Mattie et al., 2010; Yan et al., 2013). Second, how are uniform plus-end-out microtubules formed in axons? It is likely that axons eliminate their minus-end-out microtubules. Retrograde axonal microtubules may be specifically depolymerized, selectively destabilized, or actively severed. Interestingly, it has been demonstrated that Tau can regulate microtubule severing via controlling spastin and katanin activity (Yu et al., 2008; Zempel et al., 2013). Alternatively, it is possible that axons selectively stabilize their plus-end-out microtubules. Microtubule stabilization in axons is

consistent with previous reports in which high levels of acetylated tubulin and stable axonal microtubules are observed in stage 3 neurons (Witte et al., 2008). Most importantly, it has been shown that local stabilization of microtubules using a photoactivatable analog of the microtubule-stabilizing drug taxol induces axon formation in unpolarized neurons (Witte et al., 2008). Consistently, we found that treatment of cultured neurons with low doses of taxol generates uniform plus- end-out microtubules by reducing the number of retrograde microtubules in the newly formed axonal processes. We propose a model in which the selective formation of uniform plus-end-out microtubules in the axon is a critical processes underlying neuronal polarization. A major challenge for future research is to determine the multiple molecular players that associate with the microtubule cytoskeleton and directly control selective microtubule organization, stabilization, and remodeling to drive axon formation and neuronal polarization.

### ACKNOWLEDGEMENTS

This work was supported by the Netherlands Organization for Scientific Research (NWO-ALW-VICI; C.C.H.; NWO-ALW-VIDI; L.C.K.), the Netherlands Organization for Health Research and Development (ZonMW-TOP; C.C.H.), the European Science Foundation (ESF-EURYI; C.C.H.), the European Research Council (ERC-StG; L.C.K.), Swiss National Science Foundation Grant 31003A\_135631 (A.H.), the National Centre of Competence in Research (NCCR) SYNAPSY financed by Swiss National Science Foundation Grant 51AU40\_125759 (A.H., S.P.), the International Foundation for Research on Paraplegia (A.H.), and the Hans Wilsdorf Foundation (A.H., S.P.). P.S. is supported by an FP7 European Union Marie Curie postdoctoral fellowship and a fellowship of the Swiss National Science Foundation. E.T. received support by the Spanish Education Ministry and a FP7 European Union Marie Curie postdoctoral fellowship. We thank Dr. Akhmanova for helpful discussions and Phebe Wulf for help with cloning constructs. We are grateful to Dr. Didier Trono and Dr. Isabel Bade for providing pSIN-TRE-mSEAP-hPGK-rtTA2sM2 lentivirus vector.

### REFERENCES

- Akhmanova A, Hoogenraad CC (2015) Microtubule minus-end-targeting proteins. *Curr Biol* 25:R162–R171.
- Akhmanova A, Steinmetz MO (2008) Tracking the ends: a dynamic protein network controls the fate of microtubule tips. *Nat Rev Mol Cell Biol* 9:309–322.
- Baas PW, Lin S (2011) Hooks and comets: the story of microtubule polarity orientation in the neuron. *Dev Neurobiol* 71:403–418.
- Baas PW, White LA, Heidemann SR (1987) Microtubule polarity reversal accompanies regrowth of amputated neurites. *Proc Natl Acad Sci U S A* 84:5272–5276.
- Baas PW, Deitch JS, Black MM, Banker GA (1988) Polarity orientation of microtubules in hippocampal neurons: uniformity in the axon and non-uniformity in the dendrite. *Proc Natl Acad Sci U S A* 85:8335–8339.
- Baas PW, Black MM, Banker GA (1989) Changes in microtubule polarity orientation during the development of hippocampal neurons in culture. *J Cell Biol* 109:3085–3094.
- Baas PW, Slaughter T, Brown A, Black MM (1991) Microtubule dynamics in axons and dendrites. *J Neurosci Res* 30:134–153.
- Botvinick EL, Venugopalan V, Shah JV, Liaw LH, Berns MW (2004) Controlled ablation of microtubules using a picosecond laser. *Biophys J* 87:4203–4212.
- Burton PR (1988) Dendrites of mitral cell neurons contain microtubules of opposite polarity. *Brain Res* 473:107–115.
- Cane M, Maco B, Knott G, Holtmaat A (2014) The relationship between PSD-95 clustering and spine stability in vivo. *J Neurosci* 34:2075–2086.
- Colombelli J, Reynaud EG, Rietdorf J, Pepperkok R, Stelzer EH (2005) In vivo selective cytoskeleton dynamics quantification in interphase cells induced by pulsed ultraviolet laser nanosurgery. *Traffic* 6:1093–1102.
- Conde C, Cáceres A (2009) Microtubule assembly, organization and dynamics in axons and dendrites. *Nat Rev Neurosci* 10:319–332.
- Dehmelt L, Halpain S (2005) The MAP2/Tau family of microtubule-associated proteins. *Genome Biol* 6:204.
- De Paola V, Arber S, Caroni P (2003) AMPA receptors regulate dynamic equilibrium of presynaptic terminals in

- mature hippocampal networks. *Nat Neurosci* 6:491–500.
- Dombeck DA, Kasischke KA, Vishwasrao HD, Ingelsson M, Hyman BT, Webb WW (2003) Uniform polarity microtubule assemblies imaged in native brain tissue by second-harmonic generation microscopy. *Proc Natl Acad Sci U S A* 100:7081–7086.
- Dotti CG, Sullivan CA, Banker GA (1988) The establishment of polarity by hippocampal neurons in culture. *J Neurosci* 8:1454–1468.
- Goodwin PR, Sasaki JM, Juo P (2012) Cyclin-dependent kinase 5 regulates the polarized trafficking of neuropeptide-containing dense-core vesicles in *Caenorhabditis elegans* motor neurons. *J Neurosci* 32:8158–8172.
- Hammond JW, Huang CF, Kaech S, Jacobson C, Banker G, Verhey KJ (2010) Posttranslational modifications of tubulin and the polarized transport of kinesin-1 in neurons. *Mol Biol Cell* 21:572–583.
- Hill SE, Parmar M, Gheres KW, Guignet MA, Huang Y, Jackson FR, Rolls MM (2012) Development of dendrite polarity in *Drosophila* neurons. *Neural Dev* 7:34.
- Hirokawa N, Niwa S, Tanaka Y (2010) Molecular motors in neurons: transport mechanisms and roles in brain function, development, and disease. *Neuron* 68:610–638.
- Honnappa S, Gouveia SM, Weisbrich A, Damberger FF, Bhavesh NS, Jawhari H, Grigoriev I, van Rijssel FJ, Buey RM, Lawera A, Jelesarov I, Winkler FK, Wu<sup>†</sup> thrich K, Akhmanova A, Steinmetz MO (2009) An EB1-binding motif acts as a microtubule tip localization signal. *Cell* 138:366–376.
- Huang CF, Banker G (2012) The translocation selectivity of the kinesins that mediate neuronal organelle transport. *Traffic* 13:549–564.
- Janke C, Kneussel M (2010) Tubulin post-translational modifications: encoding functions on the neuronal microtubule cytoskeleton. *Trends Neurosci* 33:362–372.
- Jaworski J, Kapitein LC, Gouveia SM, Dortland BR, Wulf PS, Grigoriev I, Camera P, Spangler SA, Di Stefano P, Demmers J, Krugers H, Defilippi P, Akhmanova A, Hoogenraad CC (2009) Dynamic microtubules regulate dendritic spine morphology and synaptic plasticity. *Neuron* 61:85–100.
- Kahn OI, Sharma V, González-Billault C, Baas PW (2015) Effects of kinesin-5 inhibition on dendritic architecture and microtubule organization. *Mol Biol Cell* 26:66–77.
- Kapitein LC, Hoogenraad CC (2011) Which way to go? Cytoskeletal organization and polarized transport in neurons. *Mol Cell Neurosci* 46:9–20.
- Kapitein LC, Hoogenraad CC (2015) Building the neuronal microtubule cytoskeleton. *Neuron* 87:492–506.
- Kapitein LC, Schlager MA, van der Zwan WA, Wulf PS, Keijzer N, Hoogenraad CC (2010a) Probing intracellular motor protein activity using an inducible cargo trafficking assay. *Biophys J* 99:2143–2152.
- Kapitein LC, Schlager MA, Kuijpers M, Wulf PS, van Spronsen M, MacKintosh FC, Hoogenraad CC (2010b) Mixed microtubules steer dynein-driven cargo transport into dendrites. *Curr Biol* 20:290–299.
- Kapitein LC, Yau KW, Gouveia SM, van der Zwan WA, Wulf PS, Keijzer N, Demmers J, Jaworski J, Akhmanova A, Hoogenraad CC (2011) NMDA receptor activation suppresses microtubule growth and spine entry. *J Neurosci* 31:8194–8209.
- Kleele T, Marinković P, Williams PR, Stern S, Weigand EE, Engerer P, Naumann R, Hartmann J, Karl RM, Bradke F, Bishop D, Herms J, Konnerth A, Kerschensteiner M, Godinho L, Misgeld T (2014) An assay to image neuronal microtubule dynamics in mice. *Nat Commun* 5:4827.
- Kollins KM, Bell RL, Butts M, Withers GS (2009) Dendrites differ from axons in patterns of microtubule stability and polymerization during development. *Neural Dev* 4:26.
- Kuijpers M, Hoogenraad CC (2011) Centrosomes, microtubules and neuronal development. *Mol Cell Neurosci* 48:349–358.
- Kwan AC, Dombeck DA, Webb WW (2008) Polarized microtubule arrays in apical dendrites and axons. *Proc Natl Acad Sci U S A* 105:11370–11375.
- Lin S, Liu M, Mozgova OI, Yu W, Baas PW (2012) Mitotic motors coregulate microtubule patterns in axons and dendrites. *J Neurosci* 32:14033–14049.
- Maday S, Twelvetrees AE, Moughamian AJ, Holzbaur EL (2014) Axonal transport: cargo-specific mechanisms of motility and regulation. *Neuron* 84:292–309.
- Maniar TA, Kaplan M, Wang GJ, Shen K, Wei L, Shaw JE, Koushika SP, Bargmann CI (2012) UNC-33 (CRMP) and ankyrin organize microtubules and localize kinesin to polarize axon-dendrite sorting. *Nat Neurosci* 15:48–56.
- Mattie FJ, Stackpole MM, Stone MC, Clippard JR, Rudnick DA, Qiu Y, Tao J, Allender DL, Parmar M, Rolls MM (2010) Directed microtubule growth, +TIPs, and kinesin-2 are required for uniform microtubule polarity in dendrites. *Curr Biol* 20:2169–2177.
- Nakata T, Hirokawa N (2003) Microtubules provide directional cues for polarized axonal transport through interaction with kinesin motor head. *J Cell Biol* 162:1045–1055.
- Nakata T, Niwa S, Okada Y, Perez F, Hirokawa N (2011) Preferential binding of a kinesin-1 motor to GTP-tubulin-rich microtubules underlies polarized vesicle transport. *J Cell Biol* 194:245–255.
- Page<sup>s</sup> S, Cane M, Randall J, Capello L, Holtmaat A (2015) Single cell electroporation for longitudinal imaging of synaptic structure and function in the adult mouse neocortex in vivo. *Front Neuroanat* 9:36.
- Petersen JD, Kaech S, Banker G (2014) Selective microtubule-based transport of dendritic membrane proteins arises

## Chapter 6

---

- in concert with axon specification. *J Neurosci* 34:4135–4147.
- Roll-Mecak A, McNally FJ (2010) Microtubule-severing enzymes. *Curr Opin Cell Biol* 22:96–103.
- Rolls MM (2011) Neuronal polarity in *Drosophila*: sorting out axons and dendrites. *Dev Neurobiol* 71:419–429.
- Sharp DJ, Ross JL (2012) Microtubule-severing enzymes at the cutting edge. *J Cell Sci* 125:2561–2569.
- Stepanova T, Slemmer J, Hoogenraad CC, Lansbergen G, Dortland B, De Zeeuw CI, Grosveld F, van Cappellen G, Akhmanova A, Galjart N (2003) Visualization of microtubule growth in cultured neurons via the use of EB3-GFP (end-binding protein 3-green fluorescent protein). *J Neurosci* 23:2655–2664.
- Stone MC, Roegiers F, Rolls MM (2008) Microtubules have opposite orientation in axons and dendrites of *Drosophila* neurons. *Mol Biol Cell* 19: 4122–4129.
- Stoppini L, Buchs PA, Muller D (1991) A simple method for organotypic cultures of nervous tissue. *J Neurosci Methods* 37:173–182.
- Subramanian R, Kapoor TM (2012) Building complexity: insights into self-organized assembly of microtubule-based architectures. *Dev Cell* 23:874–885.
- Witte H, Neukirchen D, Bradke F (2008) Microtubule stabilization specifies initial neuronal polarization. *J Cell Biol* 180:619–632.
- Yan J, Chao DL, Toba S, Koyasako K, Yasunaga T, Hirotsune S, Shen K (2013) Kinesin-1 regulates dendrite microtubule polarity in *Caenorhabditis elegans*. *eLife* 2:e00133.
- Yau KW, van Beuningen SF, Cunha-Ferreira I, Cloin BM, van Battum EY, Will L, Schätzle P, Tas RP, van Krugten J, Katrukha EA, Jiang K, Wulf PS, Mikhaylova M, Harterink M, Pasterkamp RJ, Akhmanova A, Kapitein LC, Hoogenraad CC (2014) Microtubule minus-end binding protein CAMSAP2 controls axon specification and dendrite development. *Neuron* 82:1058–1073.
- Yu W, Qiang L, Solowska JM, Karabay A, Korulu S, Baas PW (2008) The microtubule-severing proteins spastin and katanin participate differently in the formation of axonal branches. *Mol Biol Cell* 19:1485–1498.
- Zempel H, Luedtke J, Kumar Y, Biernat J, Dawson H, Mandelkow E, Mandelkow EM (2013) Amyloid-beta oligomers induce synaptic damage via Tau-dependent microtubule severing by TTL6 and spastin. *EMBO J* 32:2920–2937.

## Chapter 7

### General Discussion

#### Live-cell imaging of hippocampal neuron cultures

Since the discovery of CLIPs and EB proteins many advances have been made in the discovery of new +TIPs and the function of these proteins (Jiang et al., 2012). In neurons, for example, it has been shown that +TIPs can regulate dendritic spine morphology (Gu et al., 2008; Hu et al., 2008; Jaworski et al., 2009). In chapter 2 it is described how MT plus-ends in dendritic spines of hippocampal neuron cultures can be visualized with live-cell imaging. Both microscopy techniques have been regularly used in other studies (Efimov et al., 2007; Hu et al., 2008; Wang et al., 2008). The advantage of TIRF microscopy is that a high signal-to-noise ratio can be achieved. The imaging is however limited to the surface of the coverslip since the penetration depth of the evanescent wave drops exponentially. In neuron cultures most of the dendrites and axons are not residing close enough to the surface of the coverslip to allow efficient imaging with TIRF microscopy and leads to patchy images of samples. To circumvent this problem spinning disk confocal microscopy is used, which allows us to image deeper into the samples but at the cost of some loss in sensitivity. Another imaging technique such as light sheet fluorescence microscopy (LSFM) is a promising alternative in the future (Keller and Ahrens, 2015). As labs are developing better resolution and faster imaging times with LFSM, an improved commercial LFSM version in the future will most likely benefit the general cell biological community.

Using hippocampal neuron cultures to study microtubule organization is challenging in many ways. One of the hurdles to overcome is the efficient transfection of neurons (Karra and Dahm, 2010). Lipofectamine based transfection for example, decreases dramatically in transfection efficiency for older neuronal cultures (Wanisch et al., 2013). With a viral based infection system, neuron cultures can be infected and express the protein of interest without the worry of an inefficient infection rate. Together with the aid of an inducible protein expression system, neurons can be cultured for a longer amount of time after infection with the virus. Such an infection method and protein expression system is used successfully in chapter 6 to image MT +TIPs.

#### Neuronal activity dependent MTs

Neurons can release chemical transmitters. This occurs at the axonal presynaptic sites. The chemical signals are received at the dendritic post-synaptic site of the neuron. In previous studies it is shown that dendritic spine morphology is regulated by MTs (Gu et al., 2008; Hu et al., 2008; Jaworski et al., 2009). The question remains however, whether neuronal activity also has an effect on the MT cytoskeleton. In chapter 3 we investigated which type of glutamate receptor activation leads to alterations in the underlying MT cytoskeleton. Bath application of NMDA (Beattie et al., 2000; Colledge et al., 2003; Ehlers, 2000; Lee et al., 1998) showed that in particular NMDA receptor activation (chemical LTD protocol) is involved in redistribution of EB3 from MT plus-ends. The redistribution of EB3 happens within a minute and is most likely due to an increase of calcium concentration in the neuron as discussed in chapter 3. Because of this effect on the MTs we tested whether CAMSAP2 was also affected by NMDA bath application (chapter 5). Similar to the EB3 comets, CAMSAP2 was redistributed from the MTs in a manner dependent on the NR2B receptor. The time scale at which this happened differed from the redistribution of EB3 from MT plus-ends, and CAMSAP2 did not accumulate at different compartments in neurons. The redistribution of

CAMSAP2 did coincide with the time scale in which EB3 accumulates onto MAP2-positive MTs. The accumulation of EB3 on MAP2-decorated MTs is likely due to dephosphorylation of MAP2 (Halpain and Greengard, 1990). It would be interesting to test these classical NMDA bath application treatments in hippocampal cultures of MAP2 knockout mice and observe what happens with CAMSAP2 stretches.

Another way to influence neuronal activity is by inducing LTP. In chapter 3 chemical LTP is used to observe whether there is a change in the number of MT plus-ends after chemical stimulation with glycine and KCl. In our hands, there was no significant change in the number of MT plus-ends before and after chemical LTP treatment. Others however did find an activity dependent MT invasion in spines (Gu et al., 2008; Hu et al., 2008). Gu et al. showed that this happened only in the presence of a low concentration of taxol during addition of BDNF. Hu et al. showed with KCl treatment that more spines were invaded, and the same lab has also shown that the dynamic MTs promoted spine enlargement via NMDA receptors. Future experiments with knockouts of different NMDA receptor subunits might elucidate which type of NMDA receptor is involved in this process.

Next to the experiments performed in chapter 5, additional studies need to be performed to test whether synaptic activity can influence CAMSAP2. It would also be interesting to investigate if CAMSAP2 has an effect in the synaptic transmission. A study performed in *C. elegans* did show that synapses are affected in ptrn-1 (CAMSAP/Patronin homolog) mutants. Presynaptic varicosities were significantly affected in size and appeared to be retracted in some cases, suggestion that PTRN-1 is involved in maintaining the presynaptic varicosities (Marcette et al., 2014). Furthermore, evidence from *C. elegans* experiments showed that neuronal morphology and synaptic vesicle localization were affected in ptrn-1 mutants. Activation of the DLK-1 MAP3 kinase pathway was shown to be able to alter neuronal morphology. Ptrn-1 seems to act upstream of DLK-1 activation affecting neuronal morphology in ptrn-1 mutants (Marcette et al., 2014; Richardson et al., 2014). This suggested that PTRN-1 is important for stabilizing microtubules in neurons, since microtubule depolymerization can activate the DLK-1 MAP3 kinase pathway and lead to aberrant neuronal morphology. In cultured hippocampal neurons DLK-1 was shown to affect the axonogenesis (Oliva et al., 2006; Tedeschi and Bradke, 2013). These data coincide with the results described in chapter 5, which show that CAMSAP2 is required for axon formation in cultured neurons and axon initiation and neuronal polarity in vivo. However in chapter 5 there was also a difference in dendrite morphology, which has not been described by the DLK-1 MAP3 kinase pathway. It would also be interesting to test whether the MAP kinase and CAMSAP pathway is conserved in mammalian neurons.

### **Noncentrosomal microtubules**

#### *The Golgi apparatus*

Mature hippocampal neurons do not have a microtubule organizing center (MTOC) like cultured fibroblasts. Moreover neurons have different MT orientations in different compartments. In dendrites MTs are mixed and in axons most MTs are unidirectionally oriented with the plus end away from the soma (Baas et al., 1988). It is believed that in the axon MT fragments are present that aid in the growth of new MTs in axonal branches (Yu et al., 1994). Dynein is suggested to play a role in organizing these microtubules in the axon (Zheng et al., 2008). As MT fragments might play a role in the growth of new MTs, this leads to the question how MTs are maintained and organized in neurons. It was believed that when MTs were not anchored or stabilized, MTs would depolymerize from their minus ends (Vorobjev et al., 1999). Previous studies showed in RPE1 cells that MTs emanated from the

Golgi. This was independent from the centrosome but did require  $\gamma$ -tubulin. Other candidates were also identified to play a role in Golgi originating MTs. For instance it was shown that GCC185, situated at the trans-Golgi network, was responsible for the recruitment of CLASP (Efimov et al., 2007).

In addition to the former mentioned studies, a study performed in *Drosophila* class IV dendritic arborization (da) neurons, showed that Golgi outposts in dendrites could nucleate noncentrosomal MTs. This was in contrast to other organelles such as Rab11-positive endosomes and mitochondria which did not correlate with EB1 comet formation (Ori-McKenney et al., 2012).  $\gamma$ -tubulin and AKAP450 are supposed to play a role in the nucleation of MTs at the Golgi and also regulate neuronal dendrite morphology. However, a more recent study showed that  $\gamma$ -tubulin is not associated with the Golgi outposts (Nguyen et al., 2014). In this study the Golgi was pulled away from their existing sites in dendrites. After pulling away the Golgi,  $\gamma$ -tubulin still remained in the dendrites. Nguyen, McCracken et al. thus concluded that Golgi outposts are not directly involved in MT nucleation. Ori-McKenney et al. however did point out that only static Golgi outposts nucleate MTs. In mammalian neurons Golgi outposts are also known to exist (Horton and Ehlers, 2003a, b; Quassollo et al., 2015), MT nucleation from Golgi outposts in mammalian neurons have not yet been reported.

#### *MT severing*

Another way to generate noncentrosomal MTs is by severing the existing ones. Katanin and spastin are severing enzymes that have different roles in neurons (Sharp and Ross, 2012). Initial reports about katanin inhibition with antibodies in cultured rat neurons showed that axon outgrowth was diminished and MT length was increased in the cell body of neurons. In addition, there was an increase in the number of centrosome-associated MTs (Ahmad et al., 1999). In chapter 4 we described that knockdown of CAMSAP2 in HeLa cells caused a more radial array of MTs during interphase. This is also supported by another study performed in epithelial cells (Tanaka et al., 2012). These results about a role for CAMSAP in regulating noncentrosomal MTs are interesting, since inhibition of katanin shows a similar result in sympathetic neurons (Ahmad et al., 1999). In chapter 4 it is furthermore described that there is a conserved binding site in CAMSAP2/3 for the interaction with katanin P60 subunit. Depleting the P60 subunit shows elongated CAMSAP2 stretches in HeLa cells. However the molecular details of that mechanism have yet to be discovered.

In chapter 5 it is described that CAMSAP2 stretches elongate over time during the development of neurons. During initial stages of neuronal development, CAMSAP2 puncta are present and at later stages longer stretches develop. In HeLa cells an increase in length of CAMSAP2 stretches can be observed when katanin P60 subunit is depleted. It would be interesting to see if there is a correlation between katanin P60 subunit activity/expression and the length of CAMSAP2 stretches in hippocampal neurons. What is furthermore striking in our observations of CAMSAP2 stretches in neurons is that most of the stretches are quite stationary. It will be interesting to see if there are more dynamic CAMSAP2 stretches during certain stages of development and/or neuronal plasticity.

In *Drosophila* neurons the dendritic arborization is affected when katanin P60 is overexpressed in class IV neurons (Mao et al., 2014). Although only axonal phenotypes have been described after spastin depletion (less branching and shorter length) (Yu et al., 2008), it would be interesting to conduct similar experiments for dendritic morphology in hippocampal neurons. Other studies have been performed on katanin and spastin showing that their overexpression decreases the total length of neuronal processes up to DIV7 (Yu et al., 2005). These results show the impact that MT severing proteins may have on neuronal development. Furthermore, MT severing enzymes may also have an important role in Alzheimer's disease

(AD) (Wang and Liu, 2008). For instance, Zempel et al. show that excess MT severing by spastin causes MT loss in AD.

Interestingly, amyloid beta oligomer treatment of cultured hippocampal neurons initially shows an increase in intracellular calcium through NMDA receptors (Zempel et al., 2013). A similar intracellular calcium increase is achieved in chapters 3 and 5. NMDA treatment causes a rise in intracellular calcium and eventually suppresses MT growth and spine entry, a reduction in MT density and loss of CAMSAP2-positive MTs in dendrites. It is interesting to note that in the study of Zempel et al., they found that spastin is a cause for the decrease in MT density. A follow up study with spastin depletion might give insight into whether or not spastin is also involved in suppressing MT growth induced by NMDA treatment and loss of CAMSAP2.

**Mixed microtubule organization in dendrites**

Chapter 6 shows that minus-end outward pointing MTs in dendrites are conserved in multiple neuron culture systems and in vivo. However the exact number of MTs in dendrites at the cross section of each position needs to be investigated more thoroughly. Laborious electron microscopy sectioning methods (Kubota et al., 2011; Yu and Baas, 1994) could give a more complete picture of MTs in dendrites and axons. Several other studies also demonstrate that dendritic hippocampal neurons have a mixed MT organization (Baas et al., 1988; Dotti and Banker, 1991; Heidemann and Euteneuer, 1982; Kapitein et al., 2010). EM studies by Baas et al. however also show that the mixed MT organization gradually turns into a plus-end out MT organization in dendrites.

The hook-decoration assay has previously been used to determine the orientation of MTs in neurons (Baas et al., 1989; Baas et al., 1988). With the hook-decoration assay lateral sheets of tubulin form onto existing MTs. In addition to the lateral sheets, pre-existing MTs can also polymerize and elongate. The latter effect causes a bias in the observed number of uniform MTs at the distal end of the dendrite. This explains the difference from our findings in chapter 6 that dendrites have equal ratios of mixed MTs throughout the dendrite. Furthermore we observed mixed MTs throughout the development of hippocampal neuron dendrites in vitro and in vivo. It should be noted, however, that some studies indicate a unidirectional MT organization using second harmonics generation (Dombeck et al., 2003; Kwan et al., 2008).

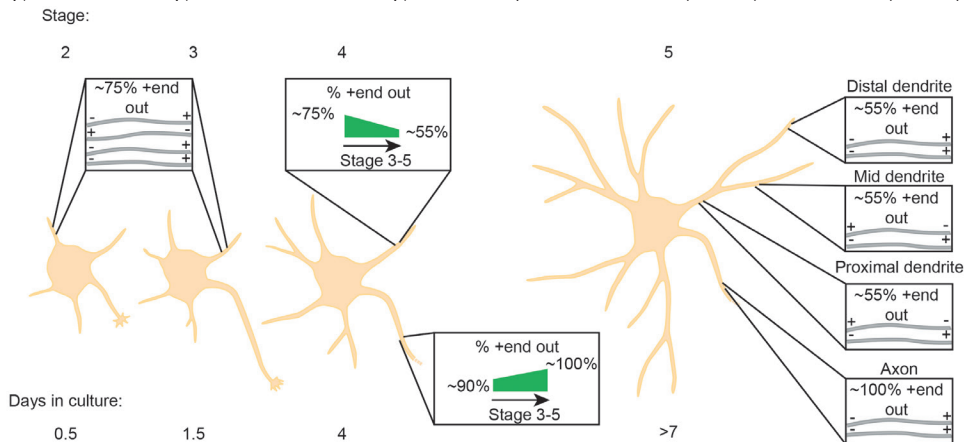


Figure 1. Microtubule organization during developmental stages of hippocampal neurons in culture. Proposed model adjusted to the new findings resulting from this thesis.

**Dynein-dependent transport throughout dendritic development**

Previously it is shown that mixed MTs steer dynein driven cargo into dendrites (Kapitein et al., 2010). In other model systems such as *C. elegans* and *D. melanogaster* the MT organization in dendrites is unidirectional with the MT plus end oriented toward the soma (Chalfie and Thomson, 1979; Hill et al., 2012; Stone et al., 2008; Yan et al., 2013). Differences between mammalian and invertebrate MT organization in dendrites has yet to be explained. However, a common MT dependent transport mechanism into dendrites for all model systems might be dynein (Liu et al., 2000; Zheng et al., 2008). Targeted manipulation of MT organization in dendrites could confirm existence of this MT dependent regulation of cargo. For example, uncaging taxol selectively near the tips of dendrites can make dendritic ends selectively more MT plus-end out. This will most likely lead to less dynein dependent dendritic cargo distributed to the dendritic tip.

A recent study by Petersen et al. shows that selective dendritic transport coincides with axon specification (Petersen et al., 2014). It is also shown however that even before axon specification, selective transport of transferrin and rab11b vesicles and accumulation of constitutively active kinesin-1 occurs in tips of neurites. These accumulations of kinesin-1 appear at different tips of neurites in a short time period. The accumulation at different tips might be due to the changes in the underlying MT organization. This can be performed by transporting MTs and sliding them into different areas of the neuron. Alternatively changes in MT modification could also affect the directional transport at that time scale (Boucher et al., 1994; Hammond et al., 2010; Jacobson et al., 2006). Further observations by Petersen et al. of bidirectional runs in stage 3 neuronal dendrites also support our findings shown in chapter 6. We report that stage 3 neuronal dendrites exhibit mixed MTs, which suggests that dynein dependent transport into the dendrite is possible at that stage, Figure 1. In addition, even before axon specification we show that there is a mixed MT organization, which could facilitate early dynein dependent transport. Moreover, with these findings we suggest that the formation of a uniform MT organization specifies axon formation.

### **Concluding remarks:**

The first live-cell imaging experiments of MTs have been published in 1953 (Desai and Mitchison, 1997; Inoue, 1953; Waterman-Storer, 1998). Thanks to advances in imaging technology, dynamic instability of individual MTs was observed some years later (Sammak and Borisy, 1988a, b). MTs were also studied using electron microscopy on neurons. MTs were then suggested to play a role in dendritic spines (Westrum et al., 1980). Another use of electron microscopy was on the MT organization of neurons, which showed the different MT organization in axons and dendrites (Baas et al., 1988). Late in 2008, a function of MT +TIPs in dendritic spines was reported (Gu et al., 2008; Hu et al., 2008; Jaworski et al., 2009) and increasingly more +TIPs have been discovered ever since (Honnappa et al., 2009; Jiang et al., 2012).

In this thesis, we have used state of the art microscopy techniques, which allowed us to further study MT organization in neurons using live-cell imaging. Technological advances allow the use of light-induced activation of proteins of interest (van Bergeijk et al., 2015). This technique might be used to activate proteins that play a role in the organization of MTs in neurons. It can also be used to selectively direct transport and to test the robustness of the MT organization.

In chapter 4 and 5 we have shown that CAMSAP stretches are dynamic, elongating with the growing MT minus-end. Although in chapter 4 katanin is identified as a regulator of the length of CAMSAP stretches, in neurons this is not yet shown. However, katanin depletion does have an axonal phenotype and it may be interesting to investigate the length of axonal CAMSAP2 stretches. In dendrites, the CAMSAP2 stretches are less likely to be affected, as katanin is not known to play a role in dendrites of rat hippocampal cultures. Also, CAMSAP2 stretches in dendrites are far longer than those in HeLa cells. Further characterization of CAMSAP2 stretches in developing neurons should give insight into the distribution of CAMSAP2 in neurons. While it is shown that CAMSAP2 stretches generally increase in length during development, the transport of CAMSAP2 stretches has not been studied.

In chapter 6 it is also shown that different model systems, such as cell cultures, brain slices and *in vivo* models complement each other. Future developments will surely increase the use of more *in vivo* systems. Further improvements and development of other live-cell imaging techniques will benefit the scientific community, by approaching biological questions from different perspectives.

In this thesis we have furthermore shown that CAMSAP2 stabilizes noncentrosomal MTs, while others have also been focussing on the Golgi apparatus as a nucleation site for noncentrosomal MTs (Efimov et al., 2007; Miller et al., 2009). Currently, there is no consensus yet on whether Golgi dependent MT nucleation plays a role in neurons (OrimcKenney, Jan et al. 2012; Nguyen et al., 2014). There are other ways to create new MTs in neurons, such as MT severing (Ahmad et al., 1999; Mao et al., 2014; Yu et al., 2005). CAMSAP2 plays a role in rescuing the severed MT by accumulating at the MT minus-end. This is supported by the fact that CAMSAP2 stretches in neurons start out to be very short in the early developmental stages and longer stretches are observed in older neurons. The early stabilization of noncentrosomal MTs shown in chapter 5 appears to be involved in axon specification and neuronal polarization.

In addition to the findings on MT organization in neurons and stabilization of noncentrosomal MTs, chapters 3 and 5 also show a relation between neuronal activity and MT dynamics. Although the displacement of EB3 and CAMSAP2 from the MT after NMDA treatment did not coincide with each other, the displacement of CAMSAP2 did coincide with the redistribution of EB3 onto MAP2 positive MTs. The displacement of CAMSAP2 from the MT minus-end could destabilize MTs, which explains the decrease in the MT density

observed in chapter 3.

The results from chapter 6, together with the results from chapter 5 show that neuronal polarization is regulated by early stabilization of noncentrosomal MTs and uniform MT plus-end-out organization in neurons. Additional regulators are probably involved to support local activation and/or global inhibition for axon formation (Takano et al., 2015). Future studies on MT organization and the role of MT severing enzymes in neurons might aid in understanding neurological disorders (Zempel et al., 2013).

## REFERENCES

- Ahmad, F.J., Yu, W., McNally, F.J., and Baas, P.W. (1999). An essential role for katanin in severing microtubules in the neuron. *The Journal of cell biology* 145, 305-315.
- Baas, P.W., Black, M.M., and Banker, G.A. (1989). Changes in microtubule polarity orientation during the development of hippocampal neurons in culture. *The Journal of cell biology* 109, 3085-3094.
- Baas, P.W., Deitch, J.S., Black, M.M., and Banker, G.A. (1988). Polarity orientation of microtubules in hippocampal neurons: uniformity in the axon and nonuniformity in the dendrite. *Proceedings of the National Academy of Sciences of the United States of America* 85, 8335-8339.
- Beattie, E.C., Carroll, R.C., Yu, X., Morishita, W., Yasuda, H., von Zastrow, M., and Malenka, R.C. (2000). Regulation of AMPA receptor endocytosis by a signaling mechanism shared with LTD. *Nature neuroscience* 3, 1291-1300.
- Boucher, D., Larcher, J.C., Gros, F., and Denoulet, P. (1994). Polyglutamylation of tubulin as a progressive regulator of in vitro interactions between the microtubule-associated protein Tau and tubulin. *Biochemistry* 33, 12471-12477.
- Chalfie, M., and Thomson, J.N. (1979). Organization of neuronal microtubules in the nematode *Caenorhabditis elegans*. *The Journal of cell biology* 82, 278-289.
- Colledge, M., Snyder, E.M., Crozier, R.A., Soderling, J.A., Jin, Y., Langeberg, L.K., Lu, H., Bear, M.F., and Scott, J.D. (2003). Ubiquitination regulates PSD-95 degradation and AMPA receptor surface expression. *Neuron* 40, 595-607.
- Desai, A., and Mitchison, T.J. (1997). Microtubule polymerization dynamics. *Annual review of cell and developmental biology* 13, 83-117.
- Dombeck, D.A., Kasischke, K.A., Vishwasrao, H.D., Ingelsson, M., Hyman, B.T., and Webb, W.W. (2003). Uniform polarity microtubule assemblies imaged in native brain tissue by second-harmonic generation microscopy. *Proceedings of the National Academy of Sciences of the United States of America* 100, 7081-7086.
- Dotti, C.G., and Banker, G. (1991). Intracellular organization of hippocampal neurons during the development of neuronal polarity. *Journal of cell science Supplement* 15, 75-84.
- Efimov, A., Kharitonov, A., Efimova, N., Loncarek, J., Miller, P.M., Andreyeva, N., Gleeson, P., Galjart, N., Maia, A.R., McLeod, I.X., et al. (2007). Asymmetric CLASP-dependent nucleation of noncentrosomal microtubules at the trans-Golgi network. *Developmental cell* 12, 917-930.
- Ehlers, M.D. (2000). Reinsertion or degradation of AMPA receptors determined by activity-dependent endocytic sorting. *Neuron* 28, 511-525.
- Gu, J., Firestein, B.L., and Zheng, J.Q. (2008). Microtubules in dendritic spine development. *The Journal of neuroscience : the official journal of the Society for Neuroscience* 28, 12120-12124.
- Halpain, S., and Greengard, P. (1990). Activation of NMDA receptors induces rapid dephosphorylation of the cytoskeletal protein MAP2. *Neuron* 5, 237-246.
- Hammond, J.W., Huang, C.F., Kaech, S., Jacobson, C., Banker, G., and Verhey, K.J. (2010). Posttranslational modifications of tubulin and the polarized transport of kinesin-1 in neurons. *Molecular biology of the cell* 21, 572-583.
- Heidemann, S.R., and Euteneuer, U. (1982). Microtubule polarity determination based on conditions for tubulin assembly in vitro. *Methods in cell biology* 24, 207-216.
- Hill, S.E., Parmar, M., Gheres, K.W., Guignet, M.A., Huang, Y., Jackson, F.R., and Rolls, M.M. (2012). Development of dendrite polarity in *Drosophila* neurons. *Neural development* 7, 34.
- Honnappa, S., Gouveia, S.M., Weisbrich, A., Damberger, F.F., Bhavesh, N.S., Jawhari, H., Grigoriev, I., van Rijssel, F.J., Buey, R.M., Lawera, A., et al. (2009). An EB1-binding motif acts as a microtubule tip localization signal. *Cell* 138, 366-376.
- Horton, A.C., and Ehlers, M.D. (2003a). Dual modes of endoplasmic reticulum-to-Golgi transport in dendrites revealed by live-cell imaging. *The Journal of neuroscience : the official journal of the Society for Neuroscience* 23, 6188-6199.

- Horton, A.C., and Ehlers, M.D. (2003b). Neuronal polarity and trafficking. *Neuron* 40, 277-295.
- Hu, X., Viesselmann, C., Nam, S., Merriam, E., and Dent, E.W. (2008). Activity-dependent dynamic microtubule invasion of dendritic spines. *The Journal of neuroscience : the official journal of the Society for Neuroscience* 28, 13094-13105.
- Inoue, S. (1953). [Polarization optical studies of the mitotic spindle. I. The demonstration of spindle fibers in living cells]. *Chromosoma* 5, 487-500.
- Jacobson, C., Schnapp, B., and Banker, G.A. (2006). A change in the selective translocation of the Kinesin-1 motor domain marks the initial specification of the axon. *Neuron* 49, 797-804.
- Jaworski, J., Kapitein, L.C., Gouveia, S.M., Dortland, B.R., Wulf, P.S., Grigoriev, I., Camera, P., Spangler, S.A., Di Stefano, P., Demmers, J., et al. (2009). Dynamic microtubules regulate dendritic spine morphology and synaptic plasticity. *Neuron* 61, 85-100.
- Jiang, K., Toedt, G., Montenegro Gouveia, S., Davey, N.E., Hua, S., van der Vaart, B., Grigoriev, I., Larsen, J., Pedersen, L.B., Bezstarosti, K., et al. (2012). A Proteome-wide screen for mammalian SxIP motif-containing microtubule plus-end tracking proteins. *Current biology : CB* 22, 1800-1807.
- Kapitein, L.C., Schlager, M.A., Kuijpers, M., Wulf, P.S., van Spronsen, M., MacKintosh, F.C., and Hoogenraad, C.C. (2010). Mixed microtubules steer dynein-driven cargo transport into dendrites. *Current biology : CB* 20, 290-299.
- Karra, D., and Dahm, R. (2010). Transfection techniques for neuronal cells. *The Journal of neuroscience : the official journal of the Society for Neuroscience* 30, 6171-6177.
- Keller, P.J., and Ahrens, M.B. (2015). Visualizing whole-brain activity and development at the single-cell level using light-sheet microscopy. *Neuron* 85, 462-483.
- Kubota, Y., Karube, F., Nomura, M., Gullledge, A.T., Mochizuki, A., Schertel, A., and Kawaguchi, Y. (2011). Conserved properties of dendritic trees in four cortical interneuron subtypes. *Scientific reports* 1, 89.
- Kwan, A.C., Dombeck, D.A., and Webb, W.W. (2008). Polarized microtubule arrays in apical dendrites and axons. *Proceedings of the National Academy of Sciences of the United States of America* 105, 11370-11375.
- Lee, H.K., Kameyama, K., Huganir, R.L., and Bear, M.F. (1998). NMDA induces long-term synaptic depression and dephosphorylation of the GluR1 subunit of AMPA receptors in hippocampus. *Neuron* 21, 1151-1162.
- Liu, Z., Steward, R., and Luo, L. (2000). *Drosophila* Lis1 is required for neuroblast proliferation, dendritic elaboration and axonal transport. *Nature cell biology* 2, 776-783.
- Mao, C.X., Xiong, Y., Xiong, Z., Wang, Q., Zhang, Y.Q., and Jin, S. (2014). Microtubule-severing protein Katanin regulates neuromuscular junction development and dendritic elaboration in *Drosophila*. *Development* 141, 1064-1074.
- Marcette, J.D., Chen, J.J., and Nonet, M.L. (2014). The *Caenorhabditis elegans* microtubule minus-end binding homolog PTRN-1 stabilizes synapses and neurites. *eLife* 3, e01637.
- Miller, P.M., Folkmann, A.W., Maia, A.R., Efimova, N., Efimov, A., and Kaverina, I. (2009). Golgi-derived CLASP-dependent microtubules control Golgi organization and polarized trafficking in motile cells. *Nature cell biology* 11, 1069-1080.
- Nguyen, M.M., McCracken, C.J., Milner, E.S., Goetschius, D.J., Weiner, A.T., Long, M.K., Michael, N.L., Munro, S., and Rolls, M.M. (2014). Gamma-tubulin controls neuronal microtubule polarity independently of Golgi outposts. *Molecular biology of the cell* 25, 2039-2050.
- Oliva, A.A., Jr., Atkins, C.M., Copenagle, L., and Banker, G.A. (2006). Activated c-Jun N-terminal kinase is required for axon formation. *The Journal of neuroscience : the official journal of the Society for Neuroscience* 26, 9462-9470.
- Ori-McKenney, K.M., Jan, L.Y., and Jan, Y.N. (2012). Golgi outposts shape dendrite morphology by functioning as sites of acentrosomal microtubule nucleation in neurons. *Neuron* 76, 921-930.
- Petersen, J.D., Kaech, S., and Banker, G. (2014). Selective microtubule-based transport of dendritic membrane proteins arises in concert with axon specification. *The Journal of neuroscience : the official journal of the Society for Neuroscience* 34, 4135-4147.
- Quassollo, G., Wojnacki, J., Salas, D.A., Gastaldi, L., Marzolo, M.P., Conde, C., Bisbal, M., Couve, A., and Caceres, A. (2015). A RhoA Signaling Pathway Regulates Dendritic Golgi Outpost Formation. *Current biology : CB* 25, 971-982.
- Richardson, C.E., Spilker, K.A., Cueva, J.G., Perrino, J., Goodman, M.B., and Shen, K. (2014). PTRN-1, a microtubule minus end-binding CAMSAP homolog, promotes microtubule function in *Caenorhabditis elegans* neurons. *eLife* 3, e01498.
- Sammak, P.J., and Borisy, G.G. (1988a). Detection of single fluorescent microtubules and methods for determining their dynamics in living cells. *Cell motility and the cytoskeleton* 10, 237-245.
- Sammak, P.J., and Borisy, G.G. (1988b). Direct observation of microtubule dynamics in living cells. *Nature* 332, 724-726.
- Sharp, D.J., and Ross, J.L. (2012). Microtubule-severing enzymes at the cutting edge. *Journal of cell science* 125,

- 2561-2569.
- Stone, M.C., Roegiers, F., and Rolls, M.M. (2008). Microtubules have opposite orientation in axons and dendrites of *Drosophila* neurons. *Molecular biology of the cell* 19, 4122-4129.
- Takano, T., Xu, C., Funahashi, Y., Namba, T., and Kaibuchi, K. (2015). Neuronal polarization. *Development* 142, 2088-2093.
- Tanaka, N., Meng, W., Nagae, S., and Takeichi, M. (2012). Nezha/CAMSAP3 and CAMSAP2 cooperate in epithelial-specific organization of noncentrosomal microtubules. *Proceedings of the National Academy of Sciences of the United States of America* 109, 20029-20034.
- Tedeschi, A., and Bradke, F. (2013). The DLK signalling pathway--a double-edged sword in neural development and regeneration. *EMBO reports* 14, 605-614.
- van Bergeijk, P., Adrian, M., Hoogenraad, C.C., and Kapitein, L.C. (2015). Optogenetic control of organelle transport and positioning. *Nature* 518, 111-114.
- Vorobjev, I.A., Rodionov, V.I., Maly, I.V., and Borisy, G.G. (1999). Contribution of plus and minus end pathways to microtubule turnover. *Journal of cell science* 112 ( Pt 14), 2277-2289.
- Wang, J.Z., and Liu, F. (2008). Microtubule-associated protein tau in development, degeneration and protection of neurons. *Progress in neurobiology* 85, 148-175.
- Wang, Z., Edwards, J.G., Riley, N., Provance, D.W., Jr., Karcher, R., Li, X.D., Davison, I.G., Ikebe, M., Mercer, J.A., Kauer, J.A., and Ehlers, M.D. (2008). Myosin Vb mobilizes recycling endosomes and AMPA receptors for postsynaptic plasticity. *Cell* 135, 535-548.
- Wanisch, K., Kovac, S., and Schorge, S. (2013). Tackling obstacles for gene therapy targeting neurons: disrupting perineural nets with hyaluronidase improves transduction. *PLoS one* 8, e53269.
- Waterman-Storer, C.M. (1998). Microtubules and microscopes: how the development of light microscopic imaging technologies has contributed to discoveries about microtubule dynamics in living cells. *Molecular biology of the cell* 9, 3263-3271.
- Westrum, L.E., Jones, D.H., Gray, E.G., and Barron, J. (1980). Microtubules, dendritic spines and spine apparatuses. *Cell and tissue research* 208, 171-181.
- Yan, J., Chao, D.L., Toba, S., Koyasako, K., Yasunaga, T., Hirotsune, S., and Shen, K. (2013). Kinesin-1 regulates dendrite microtubule polarity in *Caenorhabditis elegans*. *eLife* 2, e00133.
- Yu, W., Ahmad, F.J., and Baas, P.W. (1994). Microtubule fragmentation and partitioning in the axon during collateral branch formation. *The Journal of neuroscience : the official journal of the Society for Neuroscience* 14, 5872-5884.
- Yu, W., and Baas, P.W. (1994). Changes in microtubule number and length during axon differentiation. *The Journal of neuroscience : the official journal of the Society for Neuroscience* 14, 2818-2829.
- Yu, W., Qiang, L., Solowska, J.M., Karabay, A., Korulu, S., and Baas, P.W. (2008). The microtubule-severing proteins spastin and katanin participate differently in the formation of axonal branches. *Molecular biology of the cell* 19, 1485-1498.
- Yu, W., Solowska, J.M., Qiang, L., Karabay, A., Baird, D., and Baas, P.W. (2005). Regulation of microtubule severing by katanin subunits during neuronal development. *The Journal of neuroscience : the official journal of the Society for Neuroscience* 25, 5573-5583.
- Zempel, H., Luedtke, J., Kumar, Y., Biernat, J., Dawson, H., Mandelkow, E., and Mandelkow, E.M. (2013). Amyloid-beta oligomers induce synaptic damage via Tau-dependent microtubule severing by TTL6 and spastin. *The EMBO journal* 32, 2920-2937.
- Zheng, Y., Wildonger, J., Ye, B., Zhang, Y., Kita, A., Younger, S.H., Zimmerman, S., Jan, L.Y., and Jan, Y.N. (2008). Dynein is required for polarized dendritic transport and uniform microtubule orientation in axons. *Nature cell biology* 10, 1172-1180.



## **Addendum**

Summary  
Samenvatting  
CV  
List of Publications  
Acknowledgements

### Summary

Neurons are highly polarized cells consisting of a dendritic part and axonal part. Dendrites receive signals from other cells while axons transmit signals to other cells. In this thesis, mostly hippocampal neurons from rat embryos are used to study fundamental aspects of the microtubule organization in neurons, with the aid of molecular biology and microscopy techniques. Some of these techniques have been described in chapter 2.

Previously it was shown that microtubules can regulate the spine morphology in dendrites and regulate synaptic plasticity. However, little was known about neuronal receptor activation and the effect on the underlying microtubule cytoskeleton. In chapter 3, we have shown that neuronal activity affects the microtubule dynamics in neurons and redistributed EB3 to MAP2 positive microtubules. In chapter 5 another protein, CAMSAP2, was shown to be mislocalized from its initial position on microtubules after glutamate receptor activation. These results indicate a role for neuronal activity on microtubule binding proteins that influences the dynamics of microtubules.

As neurons develop into highly polarized cells, the neuronal microtubule organization also develops into a highly polarized structure. To create and maintain this polarized structure, a neuron needs to be able to stabilize its microtubules as it does not have a microtubule organizing centre. In chapter 5 we have shown that CAMSAP2 plays a role in stabilizing the free minus ends of microtubules in neurons. Further characterization on the function of the family of CAMSAP proteins and interaction with a microtubule severing protein, katanin, has been performed in chapter 4. We have shown that the stabilization of microtubules by CAMSAP2 in neurons is needed in order to control neuronal polarity and dendrite development.

In the past, studies using electron microscopy have shed light on the neuronal microtubule organization during neuronal development. Those studies are however based on static images from samples that have undergone fixation assays, which may influence the overall mixed polarity of microtubules in dendrites. We used live-cell imaging to visualize dynamic microtubule plus ends. Together with a laser microsurgery technique we were able to probe the neuronal microtubule organization during different developmental stages in hippocampal cultures and brain slices. In vivo imaging also confirmed the bidirectional microtubule organization in dendrites. We have shown that during the different developmental stages of hippocampal neurons in culture, a mixed microtubule organization is observable.

Taken together we show that neuronal activity plays a role in microtubule dynamics. Furthermore, our results on the development of neuronal microtubule organization show a mixed microtubule organization throughout dendritic development. This suggests a model in which the selective formation of uniform plus-end-out microtubules initiates neuronal polarization. In addition, CAMSAP2 is shown to be playing a major role in axon specification and dendrite development.

## Samenvatting

Neuronen zijn zeer sterk gepolariseerde cellen, die bestaan uit een dendritisch gedeelte en axonaal gedeelte. Met de dendrieten worden signalen van andere cellen ontvangen en met het axon worden signalen naar andere cellen verzonden. Voor dit proefschrift zijn voornamelijk hippocampale neuronenu gebruikt van ratembryo's om fundamentele aspecten van het neuronale microtubulus organisatie te bestuderen met behulp van moleculair biologische technieken en microscopie technieken. Sommige van deze technieken zijn beschreven in hoofdstuk 2 van dit proefschrift.

In het verleden is aangetoond, dat microtubuli spine-morfologie en synaptische plasticiteit kunnen reguleren. Er was toen nog weinig bekend over neuronale receptor activatie en het daarop volgende effect op het onderliggende microtubulus cytoskelet. In hoofdstuk 3 hebben we laten zien dat neuronale activiteit effect heeft op microtubulus dynamica, na glutamaat stimulatie en zorgt voor herlokalisatie van EB3 naar MAP2 positieve microtubuli. Daarnaast hebben we in hoofdstuk 5 laten zien dat CAMSAP2 ook niet meer op de originele positie blijft na activatie van glutamaat receptoren. Deze resultaten laten zien dat neuronale activiteit effect heeft op microtubulus bindende eiwitten wat daarnaast ook invloed heeft op de dynamiek van microtubuli.

Tijdens de ontwikkeling van neuronenu verandert ook de microtubulus organisatie. Om dit te bewerkstelligen en te onderhouden zijn er mechanismen nodig om microtubuli te stabiliseren, aangezien een neuron geen microtubulus organiserend centrum heeft. In hoofdstuk 5 hebben we laten zien dat CAMSAP2 een grote rol speelt in het stabiliseren van microtubuli in neuronenu en belangrijk is voor de neuronale polarisatie en ontwikkeling van de dendrieten. Verdere karakterisatie van de CAMSAP familie eiwitten en interactie met een microtubulus afbrekende eiwit, katanin, is beschreven in hoofdstuk 4.

Voorheen is onderzoek gedaan naar de microtubulus organisatie in neuronenu met behulp van elektronen microscopie. Deze onderzoeken zijn gebaseerd op statische beelden en maken gebruik van fixatieven op de te onderzoeken monsters, die invloed kunnen hebben op de verhouding van de orientatie van microtubuli in dendrieten. Wij gebruikten fluorescentie microscopie op levende cellen om de dynamische microtubulus plus eind te visualiseren. Door dit samen te gebruiken met een microchirurgische laser techniek, waren wij in staat om de microtubulus organisatie van neuronenu gedurende de ontwikkeling in hippocampale kweken te onderzoeken. Daarnaast hebben we ook in breincoupen en in levende muizen laten zien dat er sprake is van een bidirectionele microtubulus organisatie in dendrieten.

Alles samengenomen laten we in dit proefschrift laten zien dat neuronale activiteit ook een effect kan hebben op de dynamiek van een microtubulus. Verder is het stabiliseren van neuronale microtubuli een belangrijke factor voor de ontwikkeling van een neuron. Ook is de orientatie van de microtubuli tijdens de ontwikkeling gekarakteriseerd. En suggereren we dat het vormen van een axon wordt geïnitieerd door parallel lopende microtubuli.

### **Curriculum Vitea**

Kah Wai Yau was born on the 31<sup>st</sup> of May 1985 in Heemskerk, the Netherlands. In 2003 he graduated from the Bonhoeffer college in Castricum (VWO, atheneum) following two educational profiles (Natuur & Techniek and Natuur & Gezondheid). After that he started his multidisciplinary education, Medical Natural Sciences, at the VU University Amsterdam. He obtained his bachelor's degree in 2007 during which he also performed two short internships. The first internship was performed under supervision of dr. Lukas Kapitein (VU University Amsterdam, Physics of complex systems) in the group of prof. dr. ir. Erwin Peterman. The second internship was performed under supervision of dr. Irene Bijnsdorp (VUmc, Medical Oncology) in the group of prof. dr. Frits Peters. In 2009 Kah Wai obtained his master's degree, during which he performed two internships. His major intership of 9 months was performed under supervision of dr. Yves Bollen (VU University Amsterdam, Structural biology) and dr. Siet van den Wildenberg (VU University Amsterdam, Physics of complex systems) in the group of prof. dr. ir. Erwin Peterman. His minor internship of 6 months was performed under supervision of dr. Matthijn Vos (NKI-AVL Amsterdam, Tumorbiology) in the group of prof. dr. Peter Peters. After obtaining his master's degree Kah Wai started his PhD with prof. dr. Casper Hoogenraad and dr. Lukas Kapitein resulting in this thesis. From November 2014 Kah Wai has been working at Janssen Biologics in Leiden.

---

## List of Publications

1. **Microtubule Dynamics in Dendritic Spines**  
Lukas C. Kapitein, [Kah Wai Yau](#), and Casper C. Hoogenraad  
*Methods Cell Biol.* 2010;97:111-32
2. **NMDA Receptor Activation Suppresses Microtubule Growth and Spine Entry**  
Lukas C. Kapitein, [Kah Wai Yau](#), Susana Montenegro Gouveia, Wouter A. van der Zwan, Phebe S. Wulf, Nanda Keijzer, Jeroen Demmers, Jacek Jaworski, Anna Akhmanova, and Casper C. Hoogenraad  
*J Neurosci.* 2011 Jun 1;31(22):8194-209
3. **Microtubule Minus-End Stabilization by Polymerization-Driven CAMSAP Deposition**  
Kai Jiang, Shasha Hua, Renu Mohan, Ilya Grigoriev, [Kah Wai Yau](#), Qingyang Liu, Eugene A. Katrukha, A.F. Maarten Altelaar, Albert J.R. Heck, Casper C. Hoogenraad, and Anna Akhmanova  
*Dev Cell.* 2014 Feb 10;28(3):295-309
4. **Microtubule Minus-End Binding Protein CAMSAP2 Controls Axon Specification and Dendrite Development**  
[Kah Wai Yau](#), Sam F.B. van Beuningen, Inês Cunha-Ferreira, Bas M.C. Cloin, Eljo Y. van Battum, Lena Will, Philipp Schätzle, Roderick P. Tas, Jaap van Krugten, Eugene A. Katrukha, Kai Jiang, Phebe S. Wulf, Marina Mikhaylova, Martin Harterink, R. Jeroen Pasterkamp, Anna Akhmanova, Lukas C. Kapitein, and Casper C. Hoogenraad  
*Neuron.* 2014 Jun 4;82(5):1058-73
5. **Dendrites In Vitro and In Vivo Contain Microtubules of Opposite Polarity and Axon Formation Correlates with Uniform Plus-End-Out Microtubule Orientation**  
[Kah Wai Yau](#)<sup>\*</sup>, Philipp Schätzle<sup>\*</sup>, Elena Tortosa, Stéphane Pagès, Anthony Holtmaat, Lukas C. Kapitein, and Casper C. Hoogenraad  
*J Neurosci.* 2016 Jan 27;36(4):1071-85

<sup>\*</sup>Authors with equal contribution

### Acknowledgements

Het pad van een promovendus wordt zelden alleen bewandeld. Ook op mijn route ben ik menig persoon verschuldigd, die mij geholpen heeft om op het juiste pad te blijven en/of mijn reis nog leuker te maken. In dit deel van het proefschrift wil ik de mensen bedanken, die daaraan hebben bijgedragen.

Allereerst gaat mijn dank uit naar mijn promotor, Casper Hoogenraad. Vanaf ons eerste gesprek wist ik al dat ik bij jou in de groep in Rotterdam wilde werken. Naast het uitdagende werk, in een voor mij nieuw vakgebied, was het een heel mooi aanzicht om de squashracket in de hoek van jouw kantoor te zien. Bewonderingswaardig was het dan ook dat je naast je gezin ook vele uren en weekenden op het lab in Rotterdam was en ook nog wekelijks te zien was op de donderdagavond om te squashen. Jouw tomeloze inzetbaarheid in en rond het lab, motiverende houding en het denken in oplossingen was voor mij dan ook steeds iets waarop ik kon rekenen als het even tegen zat. De verhuizing met de groep naar Utrecht, halverwege mijn promotie, was denk ik het beste wat er had kunnen gebeuren. Nieuw labapparatuur en een nog nauwere samenwerking met de groep van Anna heeft tot vele resultaten van dit proefschrift geleid. Hopelijk blijft de synergie tussen de groepen nog lang bestaan, want daar kan alleen maar iets goeds uitkomen. Bedankt voor de mogelijkheid voor het doen van de promotieonderzoek, want zoals je al zei: “Trouwen doe je misschien een keer in je leven, maar promoveren doe je écht maar één keer”.

Mijn dank is ook groots naar mijn co-promotor, Lukas Kapitein. Vanaf het eerste moment was jij een inspirerende factor. Hoe jij met je toespraken een ieder in een *geëxciteerde* toestand brengt is ongekend. Tijdens onze microscoopsessies heb je vanuit jouw biofysische oogpunt laten zien hoe te kijken naar wat er in cellen gebeurt. Het is mooi om te zien, hoe jij je hebt ontwikkeld in het uitzonderlijke niche, waar je je nu in bevindt. Ik ben erg benieuwd naar hoe je je verder zal ontwikkelen en ben er van overtuigd dat je werk nog mooie vruchten zal afwerpen met zo'n ijzeren discipline. Iedere maandag stampotdag, mijn vrouw heeft het er nog over.

Anna Akhmanova, jouw kritische opmerkingen hebben ook bijgedragen aan dit proefschrift. Bedankt daarvoor en bedankt dat je deel uitmaakt van de lees-en promotiecommissie. Ook de andere leden wil ik graag bedanken: Marc Baldus, Jeroen Pasterkamp, Geert Kops en Erwin Peterman.

Erwin, toch best bijzonder dat je hier deelneemt aan de commissie en eigenlijk ook logisch. Vooral omdat je tijdens elk van mijn academische mijlpalen als een soort academisch checkpoint hebt gefungeerd voor mij van BSc. naar nu.

Jeroen, bedankt voor jouw bijdrage en die van Eljo aan het CAMSAP2 paper.

Ook Chris de Zeeuw bedankt voor de mogelijkheid om op de afdeling neurowetenschappen in Rotterdam te beginnen met mijn promotietraject.

Oude Rotterdam club: Dick, Bjorn, Alexander, Max, Rick, Nanda, Babet, Susanna, Vera en Samantha, fijn om jullie als collega's te hebben gehad.

Esther, de uren die jij elke dag op het lab draaide was indrukwekkend. Ook in Utrecht zette je deze trend voort, wat ook een inspiratie was voor mij. Bedankt voor de gezellige tijd in Rotterdam en Utrecht! Ik wens jou en Chris het beste.

Corette, ook zo'n sterke dame op de afdeling, op het lab als op het veld tijdens een sportdag van de UU. Ik wens jou en je groep heel veel succes!

Ook een aantal andere groepsleiders (en hun groepen) van de 5<sup>e</sup> verdieping van het Kruyt gebouw, Paul, Sander, Mike en Inge bedankt voor jullie bijdrage tijdens afdelingsmeetings. Voor mij waren de groepsoverstijgende meetings een goede toevoeging, die een andere kijk en inspiratie geven op je dagelijkse experimenten. En natuurlijk Fons ook bedankt!

De homies van N502. Mariella, overbuurvrouw. Ook mee gemigreerd vanuit Rotterdam en deels MNW. Wat leuk om je dan ook hier te treffen in het Hoogenraadlab. Verstandig dat je vaak uit de vele (verhitte) discussies tussen mij, Sam en Phebe bent gebleven, als muren konden praten...

Sam, bedankt voor jouw essentiële inzet/bijdrage tijdens het CAMSAP2 paper en het vertrouwen om in jouw auto te mogen rijden met jou als passagier. Ik denk dat ik met weinig andere AIO's zoveel heb gedeeld, inclusief hotelkamers, kampeerbusje, kantooplekje en tripjes naar een gay bar om dingen te regelen. Bedankt dat je mijn paranimf wilt zijn.

Phebe, de kern van het lab en de go-to voor alle zaken. Voor velen ben je de vraagbaak van het lab en zo ook voor mij. Jouw bijdrage aan dit boekje en mijn de rest van mijn promotie was onmisbaar. Bedankt voor je hulp/geduld/gezelligheid in en buiten het lab en dat je mijn paranimf wilt zijn.

Thanks to the technical support team. Ilya, your skills in handling microscopes and photoshop is unrivalled. Thanks for your help in Rotterdam and Utrecht. Ook gaat mijn dank uit naar Bart en Karin. Frits, nog bedankt voor het helpen maken van de foto's op de cover.

Best wishes and good luck go out to the Postdocs Inês, Benjamin, Amélie, Laura, Martin, Kai, Eugene, Anael, Harold, Maud, Wilco, Sabrina, Gabi, Dusan, Ankit, Ruddi, Philipp, Elena, Lena. In general I want to thank you all for your Postdoc wisdom. Special thanks to:

Lena, you've been working like a machine on the revisions of our CAMSAP2 paper, thanks for your super effort!

Kai, if there were a few more couples like you and your wife, Shasha, within the department there would probably be nothing much to do for the rest of us. Thanks for sharing a passion for the minus end of microtubules and your help that also resulted in a great part of this thesis.

Inês (the second Portuguese I gave guidance on how to ride a bike), also thanks for your crucial contribution on the CAMSAP2 paper, it was a delight working together with you. Best wishes to you and Roland, your wedding was a blast!

Phil, our joint effort to look at the plus end of microtubules in neurons paid off very well I would say! I hope you and your family are doing well in Switzerland. Immediate thanks also go out to Elena, Stéphane and Anthony for your help with publishing chapter 6.

Martin, jouw onderzoek met wormen heeft mij tijdens onze maandelijkse meetings altijd gefascineerd. Het is uiteindelijk toch best gaaf om in een volledig organisme te kijken naar plus eindjes van microtubuli.

Eugene, thank you for always sharing your knowledge on microtubules and interest in PUSA.

To the fellow PhD students that are ongoing, I wish you good luck and thanks for the nice years, Max, Amol, York, Robert, Bas, Marleen, Michael, Cátia, Hai Yin, Anne, Feline, QingYang, Ivar, XingXiu, Sybren, Robin, Helma, Ruben, Marta, Riccardo, Roderick, Dieudonné, JingChao, Chao, Yujie! Special thanks to:

Roderick and Bas, thanks for your contribution on the CAMSAP2 paper too! Bas, another thanks for the squash lessons.

Cátia, thanks for the great company during a late lunch and dinners in the lab. Especially when some of us had to work late again. Also the Portuguese treats were always very welcome!

Marta, you probably come close to Sam as to sharing stuff with me. I hope that sharing the apartment in Rotterdam made you feel a bit at home. I still remember the day I helped

## Addendum

---

you pick a bike. Epic.

I would also like to thank the people who already left the lab in Utrecht, Robert, Myrrhe, Marijn, Josta, Carol, Andrea, Joanna, Marina, Karin, Hari and Renu. I wish you all good luck in the next steps in your career and life. Marina, thanks for your contribution on the CAMSAP2 paper. Too bad that your dragon scales didn't make the cover ;)

Buiten mijn direct wetenschappelijke gemeenschap waren er ook andere mensen, die een belangrijke rol speelden op mijn pad richting het einde van mijn promotietraject.

Bram, Felix, Boy en Nienke, wat een genot was het elke keer als we weer eens konden afspreken om samen te eten. Uniek vond ik het hoe onze paden elkaar vonden, overlaptten en nu weer ieder zijn eigen weg gaat. De meesten van jullie zijn nu in Amerika en ik ben erg benieuwd naar wat jullie volgende stappen zijn. Boy en Lizeth gaan jullie ook het kikkerlandje verlaten? Hopelijk komen we weer eens samen om herinneringen op te halen en verhalen te delen onder het genot van een hapje en drankje. Ook ben ik tijdens mijn promotie een aantal keer verhuisd. Boy, jij was hierin elke keer aanwezig om te helpen en speelde vooral een cruciale rol bij de verhuizing richting Utrecht, mijn dank is groots daarvoor!

Stuart en CK, jullie had ik volgens mij voor het eerst in Haarlem ontmoet en vanaf toen kwamen de museumnachten, stedentripjes naar Brussel, Wenen (was Marco ook bij!), Milaan en Berlijn. Was ik naast de talloze etentjes in sterrenrestaurants nog iets vergeten? Manon en Jorge, jullie horen eigenlijk ook in dit rijtje. Zeker nadat jullie als gids hadden gespeeld in Lissabon en omgeving, geweldig! Dank voor jullie welkome onderbrekingen.

Kevin, ook jij hebt mij van de nodige onderbrekingen voorzien. Tripje naar Dubai en alsof dat niet genoeg was ook maar even naar New York tijdens 4th of July en ons laatste bestemming, Oslo. Ik ben blij dat jij nu van je welverdiende vrije weekenden geniet.

Kah Kih en Stephanie, nooit gedacht dat wonen in Amsterdam-Noord leuk kon zijn, maar jullie zijn volgens mij het bewijs.

Kah Kin en Esmeralda, wat hebben jullie alles goed op een rijtje en twee geweldige kids op de wereld gezet. De plek waar jullie wonen is wat ver, maar dat maakt het uitje wel leuker wanneer we die kant op gaan.

Pa en ma bedankt voor jullie altijd aanwezige stimulans om dingen in het leven te bereiken. Het lijkt me leuk pap om samen nog eens een reisje te maken zoals jij dat ook met opa hebt gedaan.

LieveLing, bedankt dat je me al die jaren niet voor gek hebt verklaard, zeker wanneer ik weer eens tot laat in het lab was of achter de computer werkte. Ook jij hebt me altijd gesteund als ik weer eens moest werken, maar bezorgde me ook de nodige breaks, aangezien jij de constante factor was tussen alle uitjes en stedentripjes. Ondertussen wonen we samen en zijn we getrouwd, want van bruiloft komt bruiloft (bedankt Patricia en Filippo...!). Op naar ons volgende avontuur.

